UCLA
UCLA Electronic Theses and Dissertations

Title
Calibrated Fragility Functions for Seismic Loading of Sacramento-San Joaquin River Delta Levees

Permalink
https://escholarship.org/uc/item/0j02h8bx

Author
Yang, Yang

Publication Date
2021

Peer reviewed|Thesis/dissertation

eScholarship.org Powered by the California Digital Library
University of California

UNIVERSITY OF CALIFORNIA

Los Angeles

Calibrated Fragility Functions for Seismic Loading of Sacramento-San Joaquin River Delta Levees

A dissertation submitted in partial satisfaction of

the requirements for the degree of Doctor of Philosophy

in Civil Engineering

by

Yang Yang

2021

© Copyright by

Yang Yang

2021

ABSTRACT OF THE DISSERTATION

Calibrated Fragility Functions for Seismic Loading of Sacramento-San Joaquin River Delta Levees

by

Yang Yang

Doctor of Philosophy in Civil Engineering

University of California, Los Angeles, 2021

Professor Scott Joseph Brandenberg, Chair

The Sacramento-San Joaquin River Delta, referred to as the Delta, is of great significance to California in numerous aspects. As one of the largest estuaries in the western United States, the Delta is vital to California's water supply system. Essential lifelines such as the transportation lines and transmission lines lie across the Delta. Across the Delta, there is also an extensive levee system which helps to maintain the islands and waterways. The levees are at the risk of failure, which have brought great attention because the levee failures could cause severe damage to both economy and environment. Although the levees at the Delta have not been shaken by extremely strong earthquake events, the risk is still high considering that there are quite a few active faults near the Delta. Therefore, it is of great importance to get a better understanding of the seismic fragility of levees in the Delta region.

Case histories of Japanese levees are first studied to validate the analysis approach. Three instrumented levee sites are selected where instrumental data and field performance data are available, including Nakashimo site, Yamazaki site and Kozuka site. For each site, a two-dimensional (2D) numerical model is constructed and calibrated using OpenSees. The 2D model is shaken by recorded earthquake events, and the response predicted by the finite element model is compared with recorded response. It is found that the predicted surface motions at the levee crest matches well with the recorded surface motion to a great extent with their response spectra compared. The predicted crest settlement for large earthquake events also agrees well with the reported settlement data. But for small earthquake events, it is unclear if the finite element model over-predicts the crest settlement when there is no reported damage report. At the Nakashimo site, a predicted pore water pressure response is also compared with the actual recording, and the comparison indicates that the finite element is able to predict the building-up of the pore water pressure that is consistent with the recorded response, and the predicted rate of dissipation is slightly faster than the measured rate of dissipation.

PGV-based fragility curves are then derived from a large number of numerical simulations by following a calibrated approach of developing fragility function. The derived fragility functions are also compared with empirical fragility functions developed by Kwak et al. (2016). A comparison study shows that the median of the log-normal CDFs for the fragility curve obtained from numerical simulations is quite close to the median of the fragility functions proposed by Kwak et al. (2016), while the standard deviation is slightly smaller. This is likely due to the fact that the approach of deriving fragility functions from numerical simulations does not account for all sources of uncertainty that the empirical fragility functions incorporated.

With the analysis approach validated, the levees in the Delta, specifically at the McDonald Island are analyzed. A 2D levee model is constructed following a generic levee cross-section profile, and soil

properties are determined from available geotechnical data and geophysical measurements. A group of ground motions are selected to be consistent with seismic hazard at McDonald Island. A ground motion intensity measure selection study shows that PGV of the crest motion from a one-dimensional (1D) model without liquefaction is favored in the fragility function derivations.

PGV-based fragility curves are also derived from numerical simulations, and it is found that the medians of the log-normal CDFs for PGV-based fragility curves are found to be smaller than what was proposed in Kwak et al. (2016). This indicates that levees at the McDonald Island are more fragile than Japanese levee sites mostly due to a much higher water level and the peat materials beneath the levee fill. The standard deviation of the log-normal CDFs of the fragility curve, after accounting for motion-to-motion variability, within-cross-section variability, and section-to-section varaibility, corresponds quite well with what was proposed by Kwak et al. (2016).

In addition, considering that natural soils are usually heterogeneous, the spatial variablity of soil is often characterized and modeled by a spatially correlated random field. Traditional methods like Cholesky decompostion can be computationally expensive for a random field exceeding certain size. An algorithm that combines both Cholesky decomposition and Kriging is proposed to save some computational cost. Example applications are also introduced to validate the algorithm.

The dissertation of Yang Yang is approved.

Jonathan Paul Stewart

Yousef Bozorgnia

Henry J. Burton

Scott Joseph Brandenberg, Committee Chair

University of California, Los Angeles

2021

TABLE OF CONTENTS

ABSTRACT OF THE DISSERTATION ii

LIST OF FIGURES x

LIST OF TABLES xx

ACKNOWLEDGEMENTS xxiii

CURRICULUM VITA xxv

1 Introduction 26

1.1 Background 26

1.2 Motivation 30

1.3 Organization 31

2 Analysis Approach 33

2.1 Finite Element Modeling Approach 33

2.1.1 Mesh Configuration 34

2.1.2 Material Models 36

2.1.3 Analysis Stages 44

2.2 Fragility Functions Development 51

2.2.1 Literature Review 53

2.2.2 Calibrated Numerical Approach to Developing Fragility Functions 56

3 SPATIAL VARIABILITY IN THE LEVEE SYSTEMS 62

3.1 Introduction 62

3.2 Random Fields 64

3.3 Literature Review 67

3.3.1 Previous Studies of Soil Properties as Random Fields 67
3.3.2 Existing Methods of Numerically Computing Gaussian Random Fields 71
3.4 Hybrid Method Combining Cholesky Decomposition with Kriging 72
3.5 Example Application of Random Field Algorithm to a Levee 81
3.6 Validation of Random Field Generator Using Bearing Capacity Problem 84
3.7 Summary 89
4 Validation of Analysis using Case Histories in Japan 91
4.1 Instrumented Sites 91
4.2 Nakashimo Site 95
4.2.1 Site Conditions 95
4.2.2 Recorded Response and Reported Performance 96
4.2.3 Finite Element Model Setup 100
4.2.4 Analysis Results 106
4.3 Yamazaki Site 116
4.3.1 Site Conditions 116
4.3.2 Recorded Response and Reported Performance 118
4.3.3 Finite Element Model Setup 125
4.3.4 Analysis Results 129
4.4 Kozuka Site 142
4.4.1 Site Conditions 142
4.4.2 Recorded Response and Reported Performance 144
4.4.3 Finite Element Model Setup 147
4.4.4 Analysis Results 152
4.5 Fragility Functions 163
4.5.1 Ground Motion Selection 164

4.5.2 Two Groundwater Cases 166
4.5.3 Fragility Curves 167
4.5.4 The Effect of Magnitude 172
4.5.5 Heteroscedasticity 174
4.5.6 The Effect of Within-Section Spatial Variability 177
4.5.7 The Effect of Mean Relative Density 181
4.6 Conclusions 185
5 McDonald Island Levees 188
5.1 Characterization of McDonald Island Levees 189
5.1.1 Levee Geometry 189
5.1.2 Stratigraphy and Soil Properties 194
5.1.3 Ground Motion Selection 201
5.2 Simulations 210
5.2.1 Finite Element Model Setup 210
5.2.2 Example Realizations 213
5.3 Fragility Functions 222
5.3.1 Ground Motion Intensity Measure Selection 223
5.3.2 Motion-to-Motion Variability 225
5.3.3 The Effect of Magnitude 228
5.3.4 The Effect of Within-Section Spatial Variability 233
5.3.5 The Effect of Mean Relative Density 238
5.3.6 Recommended Fragility Functions 245
6 Conclusions and Recommendations 247
6.1 Conclusions 247
6.2 Recommendations for future work 249

References **253**

LIST OF FIGURES

Figure 1.1 Levee Failure Mechanisms (Zina Deretsky, National Science Foundation, 2010) .. 26

Figure 1.2 Map of the Sacramento and San Joaquin Delta Region (USGS) 27

Figure 1.3 A map of pipelines in the Delta Region (California Energy Commission, Energy map) 28

Figure 1.4 Major Faults near the Delta Region (URS/JBA, 2008) 29

Figure 2.1 An example of simple levee model with mesh configured using GiD 34

Figure 2.2 A mesh example of real levee model from a levee site in Japan 36

Figure 2.3 G/G_{max} versus γ_c relationship from regression model by Kishida (2009) 39

Figure 2.4 Kσ relationship derived from model simulations compared to relationship by Idriss and Boulanger (Khosravifar et al. 2018) 40

Figure 2.5 Kα relationship simulated from model compared to relationship by Harder and Boulanger (Khosravifar et al. 2018) 41

Figure 2.6 Element test of model response in undrained cyclic simple shear loading for $(N_1)_{60}$ = 5 41

Figure 2.7 Model response in undrained cyclic simple shear loading for $(N_1)_{60}$ = 5 in OpenSees 42

Figure 2.8 Drucker-Prager and Mohr-Coulomb yield surfaces (Khatibinia et al. 2015) 43

Figure 2.9 Modulus reduction curve for sand recommended by EPRI (1993) 44

Figure 2.10 A simple levee model setup in Phase 2 47

Figure 2.11 Pressure head distribution after a steady state seepage analysis 47

Figure 2.12 Probabilities of exceeding damage levels above one for different conditions. CDFs are fit to data using standard deviations for the damage level above zero case and added means (Kwak et al. 2016) 55

Figure 2.13 Comparison of fragility curves for probabilities of exceeding any damage level evaluated for Hokkaido levees and Shinano levees. (Tsai, 2018) 56

Figure 2.14 An example of crest settlement versus PGV of a reference motion..... 57

Figure 2.15 A sketch showing the approach of developing fragility curves 59

Figure 3.1 Uncertainty in soil property estimates (Phoon and Kulhawy 1999)..... 63

Figure 3.2 Markov and Gaussian correlation function 66

Figure 3.3 $(N1)_{60cs}$ values in the 12-m-thick liquefiable foundation alluvium (Boulanger and Montgomery 2016) 68

Figure 3.4 Estimated mean bearing capacity factor as a function of (a) C. O. V. cu (b) Θcu (Fenton and Griffiths, 2002) 70

Figure 3.5 Estimated coefficient of variation of the bearing capacity factor as a function of C. O. V. cu and Θcu(Fenton and Griffiths, 2002)..... 70

Figure 3.6 The approach to dealing with different correlation length in random field 72

Figure 3.7 Screenshot of the documentation page 1 75

Figure 3.8 Screenshot of the documentation page 2 76

Figure 3.9 A sketch of nodes that are used in Cholesky decomposition and or Kriging..... 77

Figure 3.10 Spatially correlated random fields (a) using full Cholesky decomposition and (b) using Cholesky decomposition on a decimated set of grid points combined with Kriging interpolation (b), and (c) the differences between two random fields..... 78

Figure 3.11 Residuals versus sampling coarseness..... 79

Figure 3.12 Influence of sampling coarseness on time required to develop spatially correlated random field..... 80

Figure 3.13 RS2 finite element model of a levee's cross section..... 82

Figure 3.14 A contour plot of the discrete undrained shear strength..... 83

Figure 3.15. Uniform model result of maximum shear strain..... 83

Figure 3.16. Model with discrete undrained strength results 84

Figure 3.17 A sketch of bearing capacity problem with the finite element mesh 85

Figure 3.18 Bearing pressure versus displacement of the footing 86

Figure 3.19 One realization of undrained shear strength profile 87

Figure 3.20 Mean bearing factor as a function of θ/B and C. O. VSu 88

Figure 3.21 Coefficient of variation of the bearing factor as a function of θ/B and C. O. VSu .. 89

Figure 4.1 Map view of instrumented levees in Japan (Zimmaro et al. 2019) 92

Figure 4.2 Cross-section, stratigraphy under the levee, boring log locations and sensors locations at Nakashimo site (Zimmaro et al. 2019) 95

Figure 4.3 Detailed blow counts profile at boring log locations of Nakashimo site 96

Figure 4.4 Shear wave velocity profile at borehole H9-No.5 (left) and H7-2-1-A (right) 96

Figure 4.5 Acceleration time series recorded during event 2 97

Figure 4.6 Acceleration time series recorded during event 4 98

Figure 4.7 Acceleration time series recorded during event 9 98

Figure 4.8 Acceleration time series recorded during event 10 99

Figure 4.9 Pore water pressure recorded during event 2011 Tohoku-oki event 100

Figure 4.10 Mesh configuration using GiD 101

Figure 4.11 Mesh configuration in Phase 2 for seepage analysis 102

Figure 4.12 Pressure head distribution after the steady state seepage analysis 103

Figure 4.13 Acceleration time series to be applied at the base of the model and respective response spectrum for event 2, 4, 9 and 10 105

Figure 4.14 Predicted and measured surface motion at crest comparison for event 2, 4, 9 and 10 108

Figure 4.15 Predicted pore water pressure response compared with recordings during 2011 event 110

Figure 4.16 Profiles of PGA, PGV and peak shear strain for event 2 and 4..... 112

Figure 4.17 Profiles of PGA, PGV and peak shear strain for event 9 and 10..... 113

Figure 4.18 Crest settlement versus recorded PGV at levee crest 115

Figure 4.19 Cross-section, stratigraphy under the levee, boring log locations and sensors locations at Yamazaki site (Zimmaro et al. 2019) 116

Figure 4.20 Detailed blow counts profile at boring log locations of Yamazaki site 117

Figure 4.21 Shear wave velocity profile at borehole H25-No.1, H25-No.3 and YF-PB-1 118

Figure 4.22 Acceleration time series recorded during event 2 and 3..... 120

Figure 4.23 Acceleration time series recorded during event 4 and 5..... 121

Figure 4.24 Acceleration time series recorded during event 9 and 11..... 122

Figure 4.25 Acceleration time series recorded during event 13 and 17..... 123

Figure 4.26 Acceleration time series recorded during event 20 and 21..... 124

Figure 4.27 Mesh configuration using GiD 125

Figure 4.28 Acceleration time series to be applied at the base of the model and respective response spectrum for event 2, 3, 4 and 5..... 127

Figure 4.29 Acceleration time series to be applied at the base of the model and respective response spectrum for event 9, 11, 13 and 17..... 128

Figure 4.30 Acceleration time series to be applied at the base of the model and respective response spectrum for event 20 and 21..... 129

Figure 4.31 Predicted and measured surface motion at crest comparison for event 2, 3, 4 and 5 131

Figure 4.32 Predicted and measured surface motion at crest comparison for event 9, 11, 13 and 17 132

Figure 4.33 Predicted and measured surface motion at crest comparison for event 20 and 21133

Figure 4.34 Profiles of PGA, PGV and peak shear strain for event 2, 3 and 4..... 136

Figure 4.35 Profiles of PGA, PGV and peak shear strain for event 5, 9 and 11..... 137

Figure 4.36 Profiles of PGA, PGV and peak shear strain for event 13, 17 and 20..... 138

Figure 4.37 Profiles of PGA, PGV and peak shear strain for event 21 139

Figure 4.38 Crest settlement versus recorded PGV at levee crest 141

Figure 4.39 Cross-section, stratigraphy under the levee, boring log locations and sensors locations at Kozuka site (Zimmaro et al. 2019)..... 142

Figure 4.40 Detailed blow counts profile at boring log locations of Kozuka site 143

Figure 4.41 Shear wave velocity profile at borehole H26-No.1, H26-No.2, and K-PB-1..... 143

Figure 4.42 Acceleration time series recorded during event 3, 4, 9 and 10..... 145

Figure 4.43 Acceleration time series recorded during event 11, 12, 15 and 16..... 146

Figure 4.44 Acceleration time series recorded during event 22, 24 and 25..... 147

Figure 4.45 Mesh configuration using GiD 148

Figure 4.46 Acceleration time series to be applied at the base of the model and respective response spectrum for event 3, 4, 9 and 10..... 150

Figure 4.47 Acceleration time series to be applied at the base of the model and respective response spectrum for event 11, 12, 15 and 16..... 151

Figure 4.48 Acceleration time series to be applied at the base of the model and respective response spectrum for event 22, 24 and 25..... 152

Figure 4.49 Predicted and measured surface motion at crest comparison for event 3, 4, 9 and 10 154

Figure 4.50 Predicted and measured surface motion at crest comparison for event 11, 12, 15 and 16 155

Figure 4.51 Predicted and measured surface motion at crest comparison for event 22, 24 and 25 156

Figure 4.52 Profiles of PGA, PGV and peak shear strain for event 3, 4 and 9..... 158

Figure 4.53 Profiles of PGA, PGV and peak shear strain for event 10, 11 and 12..... 159

Figure 4.54 Profiles of PGA, PGV and peak shear strain for event 15, 16 and 22..... 160

Figure 4.55 Profiles of PGA, PGV and peak shear strain for event 25 and 26..... 161

Figure 4.56 Crest settlement versus recorded PGV at levee crest 163

Figure 4.57 Response spectra of 40 ground motions, compared to the target response spectra predicted by GMM (Boore and Atkinson 2008: (a) log-log scale (b) linear scale (Baker et al. 2011) 165

Figure 4.58 River table location for two cases: LGW and HGW 166

Figure 4.59 Phreatic surface from Phase 2 for the HGW case 166

Figure 4.60 Crest settlement versus PGV of input motion for both LGW and HGW cases ... 168

Figure 4.61 Crest settlement versus PGV of input motion for LGW case and regressed straight line (axis in natural log) 169

Figure 4.62 Crest settlement versus PGV of input motion for HGW case and regressed straight line (axis in natural log) 169

Figure 4.63 Fragility curve for DL>1 comparisons 171

Figure 4.64 Residuals from regressed line versus Magnitude for LGW case 172

Figure 4.65 Fragility curves of DL > 1 for different magnitudes 174

Figure 4.66 Residuals versus PGV for both LGW and HGW cases..... 175

Figure 4.67 Standard deviation versus mean PGV from bin method and regressed curve 176

Figure 4.68 Fragility curves comparison after the heteroscedasticity correction 177

Figure 4.69 An example of spatially correlated random field of soil properties 178

Figure 4.70 Ground motion record selected and its response spectra..... 179

Figure 4.71 Crest settlement distribution over 500 realizations 180

Figure 4.72 A Q-Q plot for the logged values of crest settlement..... 181

Figure 4.73 Crest settlement versus PGV of input motion for two different relative density cases 183

Figure 4.74 Fragility curves of DL > 1 for three different relative density..... 185

Figure 5.1 Map of the Sacramento and San Joaquin Delta Region (USGS) 189

Figure 5.2 Bathymetry and LiDAR data at McDonald Island, location of boring logs and reaches 190

Figure 5.3 Geometry profiles of reaches 1-7 (LiDAR data only)..... 191

Figure 5.4 Geometry profiles of reaches 8-14 (LiDAR data only)..... 192

Figure 5.5 Geometry profiles of reaches 15-21 (LiDAR data only)..... 192

Figure 5.6 Map of two boring logs locations at McDonald Island 193

Figure 5.7 Geometry profiles at boring log Mcd-Tra-22..... 194

Figure 5.8 Geometry profiles at boring log Mcd-Tra-24..... 194

Figure 5.9 Combined geometry profile using both LiDAR and bathymetry data 194

Figure 5.10 Map of locations of three survey sites that have shear wave velocity measurement 195

Figure 5.11 Stratigraphy profile of boring log (a) Mcd-Tra-25, (b) Mcd-Tra-23, (c) Mcd-Tra-24 196

Figure 5.12 A complete cross-section layout including the stratigraphy..... 197

Figure 5.13 A shear wave velocity profile at levee crest including stratigraphy, four SPT blow count profile and shear strength profile over depth 198

Figure 5.14 Seismic velocity profile at Site 1 from combined active and passive surveys (M.Craig and K.Hayashi)..... 199

Figure 5.15 Seismic velocity profile at Site 2 from combined active and passive surveys (M.Craig and K.Hayashi)..... 199

Figure 5.16 Seismic velocity profile at Site 3 from combined active and passive surveys (M.Craig and K.Hayashi)..... 199

Figure 5.17 Time-averaged shear velocity profile of upper 3m at Site 1 200

Figure 5.18 Variogram of the average shear wave velocity profile for upper 3m at Site 1..... 201

Figure 5.19 The location of four representative sites at McDonald Island..... 202

Figure 5.20 Hazard curve in terms of (a) PGA and (b) PGV 203

Figure 5.21 Deaggregation results at site 1 for a return period of 10 years..... 204

Figure 5.22 Deaggregation results at site 1 for a return period of 50 years..... 205

Figure 5.23 Deaggregation results at site 1 for a return period of 225 years..... 205

Figure 5.24 Deaggregation results at site 1 for a return period of 475 years..... 206

Figure 5.25 Deaggregation results at site 1 for a return period of 975 years..... 206

Figure 5.26 Deaggregation results at site 1 for a return period of 2475 years..... 207

Figure 5.27 Scenarios of magnitude and distance combinations from deaggregation results . 208

Figure 5.28 Response spectra of 30 ground motions, compared to the target response spectra predicted by GMM model (M = 6.5, R= 10km) 209

Figure 5.29 Histogram of PGV for the selected ground motions 209

Figure 5.30 Model setup in Phase2 for seepage analysis..... 210

Figure 5.31 Pressure head distribution after seepage analysis in Phase2 211

Figure 5.32 Mesh configuration using GiD for McDonald Island levee 211

Figure 5.33 Input ground motion record of event 1 and its response spectra 214

Figure 5.34 Crest motion time series under the shaking of event 1 and its response spectra .. 214

Figure 5.35 Vertical displacement contour plots after (a) gravity (b) shaking (c) post-shaking reconsolidation under event 1 215

Figure 5.36 Pore water distribution plots after (a) gravity (b) shaking (c) post-shaking reconsolidation under event 1 216

Figure 5.37 Excess pore water pressure ratio over time during shaking event 1 217

Figure 5.38 Crest settlement over time during shaking event 1 217

Figure 5.39 Input ground motion record of event 2 and its response spectra 218

Figure 5.40 Crest motion time series under the shaking of event 2 and its response spectra .. 218

Figure 5.41 Vertical displacement contour plots after (a) gravity (b) shaking (c) post-shaking reconsolidation under event 2 219

Figure 5.42 Pore water distribution plots after (a) gravity (b) shaking (c) post-shaking reconsolidation under event 2 220

Figure 5.43 Excess pore water pressure ratio over time during shaking event 2 221

Figure 5.44 Crest settlement over time during shaking event 2 221

Figure 5.45 Vertical column from 2D model and reconstructed 1D model 224

Figure 5.46 Crest settlement versus PGV of reference motion 225

Figure 5.47 Fragility curve for DL>1 comparisons with different reference motions 228

Figure 5.48 Residuals from regressed line versus magnitude using crest motion 1D NoLiq as the reference motion 229

Figure 5.49 Scaling factor versus the magnitude for the selected scaled ground motions 230

Figure 5.50 Crest settlement versus PGV in the natural logarithm scale using unscaled motions 231

Figure 5.51 Residuals from regressed line versus magnitude using unscaled motions 231

Figure 5.52 Fragility curves of DL > 1 for three different magnitudes 233

Figure 5.53 An example of spatially correlated random field of soil properties 234

Figure 5.54 Ground motion record selected and its response spectra..... 235

Figure 5.55 Crest settlement distribution over 500 realizations 235

Figure 5.56 A Q-Q plot of crest settlement with the natural logarithm taken 236

Figure 5.57 Crest settlement versus PGV for three different relative density using crest motion from 1D model..... 239

Figure 5.58 Fragility curves of DL > 1 for three different relative density 241

Figure 5.59 Fragility curves of DL > 1 for three different relative density cases and three different magnitudes 244

Figure 5.60 Integrated crest settlement data versus PGV of crest motion from 1D model in the natural logarithm scale..... 245

LIST OF TABLES

Table 2.1 A reference table of model parameters used in PIMY material model (Yang et al. 2008) 37

Table 2.2 PDMY03 material model input parameters (Khosravifar et al. 2018) 43

Table 2.3 Boundary conditions for six different stages 45

Table 2.4 A reference table of permeability values for different types of soil (Yang et al. 2008) 48

Table 2.5 Analysis commands used in the study 50

Table 2.6 Analysis methods and data employed (Porter et al. 2007) 52

Table 2.7 Damage levels classification (Kwak et al. 2016) 54

Table 2.8 Moments of log-normal CDFs for PGV- and PGA-based fragility curves (Kwak et al. 2016) 54

Table 2.9 Damage level classification 58

Table 3.1 Summary of scale of fluctuation of some geotechnical properties (Phoon and Kulhawy 1999) 67

Table 4.1 List of earthquakes recorded at the instrumented levee sites (Zimmaro et al. 2019) 93

Table 4.2 Instrumentation configuration for each levee site (Zimmaro et al. 2019) 94

Table 4.3 List of data available at seven sites (Zimmaro et al. 2019) 94

Table 4.4 Material properties used based on available data and assumptions 101

Table 4.5 PGA and PGV of measured and predicted surface motion at levee crest and residual term 109

Table 4.6 Settlement and damage level comparison 114

Table 4.7 Damage levels classification 115

Table 4.8 Material properties used based on available data and assumptions 126

Table 4.9 PGA and PGV of measured and predicted surface motion at levee crest and residual term 134

Table 4.10 Settlement and damage level comparison..... 140

Table 4.11 Material properties used based on available data and assumptions..... 148

Table 4.12 PGA and PGV of measured and predicted surface motion at levee crest and residuals 157

Table 4.13 Settlement and damage level comparison..... 162

Table 4.14 Slope, intercept and standard deviation of the regressed line for both cases..... 170

Table 4.15 Moments of log-normal CDFs of exceeding different damage levels for both LGW and HGW cases, and results from Kwak et.al. 2016 171

Table 4.16 Coefficients and standard deviation of residuals from multiple linear regression with and without accounting for magnitude effect 173

Table 4.17 Coefficients of the regressed curve of standard deviation for two cases..... 177

Table 4.18 Coefficients and standard deviation of residuals from multiple linear regression accounting for PGV, magnitude and relative density 183

Table 4.19 Moments of log-normal CDFs of exceeding different damage levels for three different relative density cases for events with a magnitude of 6..... 184

Table 4.20 Moments of log-normal CDFs of exceeding different damage levels for three different relative density cases for events with a magnitude of 7..... 184

Table 4.21 Moments of log-normal CDFs of exceeding different damage levels for three different relative density cases for events with a magnitude of 8..... 184

Table 5.1 Material properties used based on available data and assumptions..... 212

Table 5.2 Slope, intercept and standard deviation of the regressed line for three reference motions 226

Table 5.3 Moments of log-normal CDFs of exceeding different damage levels for three reference motions..... 226

Table 5.4 Moments of log-normal CDFs of exceeding different damage levels from Kwak et al. (2016) 226

Table 5.5 Coefficients and standard deviation of residuals from multiple linear regression with and without accounting for magnitude effect 232

Table 5.6 Settlement from uniform model, mean and standard deviation of settlement from 500 realizations 237

Table 5.7 Coefficients and standard deviation of residuals from multiple linear regression accounting for both PGV and relative density 240

Table 5.8 Moments of log-normal CDFs of exceeding different damage levels for three different relative density cases accounting for both PGV and relative density 240

Table 5.9 Coefficients and standard deviation of residuals from multiple linear regression accounting for PGV, magnitude and relative density 242

Table 5.10 Moments of log-normal CDFs of exceeding different damage levels for three different relative density cases for events with a magnitude of 4 242

Table 5.11 Moments of log-normal CDFs of exceeding different damage levels for three different relative density cases for events with a magnitude of 6 243

Table 5.12 Moments of log-normal CDFs of exceeding different damage levels for three different relative density cases for events with a magnitude of 8 243

Table 5.13 Regression constants, their standard errors and standard deviation of the residuals 245

ACKNOWLEDGEMENTS

This project was mainly funded by the California Energy Commission (CEC). The Department of Civil and Environmental Engineering at UCLA also generously offered me fellowships and teaching opportunities which I truly appreciate. I would not have been able to complete my Ph.D study without these great funding opportunities given my humble background.

I would like to first thank my advisor Professor Scott J. Brandenberg for the endless guidance and support throughout my Ph.D study. I certainly could not have wished for a better advisor than Scott. Thank you Scott for taking the time to meet with me weekly and for always steering me in the right direction and getting me back on track. I have learned a great deal from your knowledge and insights, which will benefit me for the rest of my life and also help me become a better equipped geotechnical engineer. I would also like to thank Professor Jonathan P. Stewart for all the insightful advice you have provided for me during our meetings. Your dedication to your work and your students has always been inspiring. Thank you Jon for hosting dinner at your house on multiple occasions and welcoming us. I also would like to thank the rest of my committee: Professor Yousef Bozorgnia and Professor Henry Burton for all the valuable suggestions.

I will always be grateful for the collaborative environment the geotechnical group of students have formed. Thank you Paolo for kindly sharing your data on Japanese case histories and Margo for all your guidance on helping me start off on using OpenSees. Thank you Yi Tyan for always being supportive and offering kind advice. Special thanks to Pengfei for showing tremendous patience in helping me solve research-related problems. You and Junhui have also shown great hospitality by frequently inviting me over for dinner. Much thanks to other colleagues, Sean, Mandro, Grace, Claudia, Victor, Tatiana, Kenneth, Ebuka and Zehan for all your support and friendships.

I am also greatly thankful for the group of friends that I have made at Austin, Texas amid the coronavirus pandemic. Thank you Qining, Zhichao, Yutian, Ronghuo and Yiwei (Eric) for all the company you have provided during the uneasy times. As true friends, you have brought me nothing but countless happiness, and thank you all for always believing in me. I am so blessed to have known all of you who are like family to me now.

Last but not the least, I owe my greatest thanks to my family. I met my wife, Yuwan, at UCLA in 2017 and we have been with each other since then. Thank you for being my best friend and supporting me throughout my Ph.D journey. I could never imagine how difficult this journey would have been without you by my side, and I am grateful that you always have my back. I would also like to thank my parents, who have never doubted me all these years. It is your support and understanding that have made my study abroad possible.

CURRICULUM VITA

2016	B.S. in Hydraulic Engineering Tsinghua University
2017	M.S. in Civil Engineering, University of California - Los Angeles
2017-2021	Graduate Research Assistant, Department of Civil and Environmental Engineering University of California - Los Angeles
2017-2020	Teaching Assistant, Department of Civil and Environmental Engineering University of California - Los Angeles

Publications

Yang, Y., and Brandenberg, S. (2021). "An Efficient Algorithm for Generating Spatially Correlated Random Fields using Cholesky Decomposition and Ordinary Kriging", Computers and Geotechnics, 2021 (Under review)

Brandenberg, S., J., & Yang, Y. (2021). 'ucla_geotech_tools: A set of Python packages developed by the UCLA geotechnical group' (Version 1.0.2) [Computer software]. https://doi.org/10.5281/zenodo.5621169

Awards

TA of the year, Civil & Environmental Engineering Department, UCLA, 2020-201

1 INTRODUCTION

1.1 BACKGROUND

Levees are earthen embankments that rest along the margin of a floodplain to provide flood protection. They can be formed from natural alluvial processes, or constructed from fill. Levees can experience failure in a number of ways, as illustrated in Figure 1.1. When a levee does fail, the soil becomes heavily eroded leaving an opening for water to flood the land.

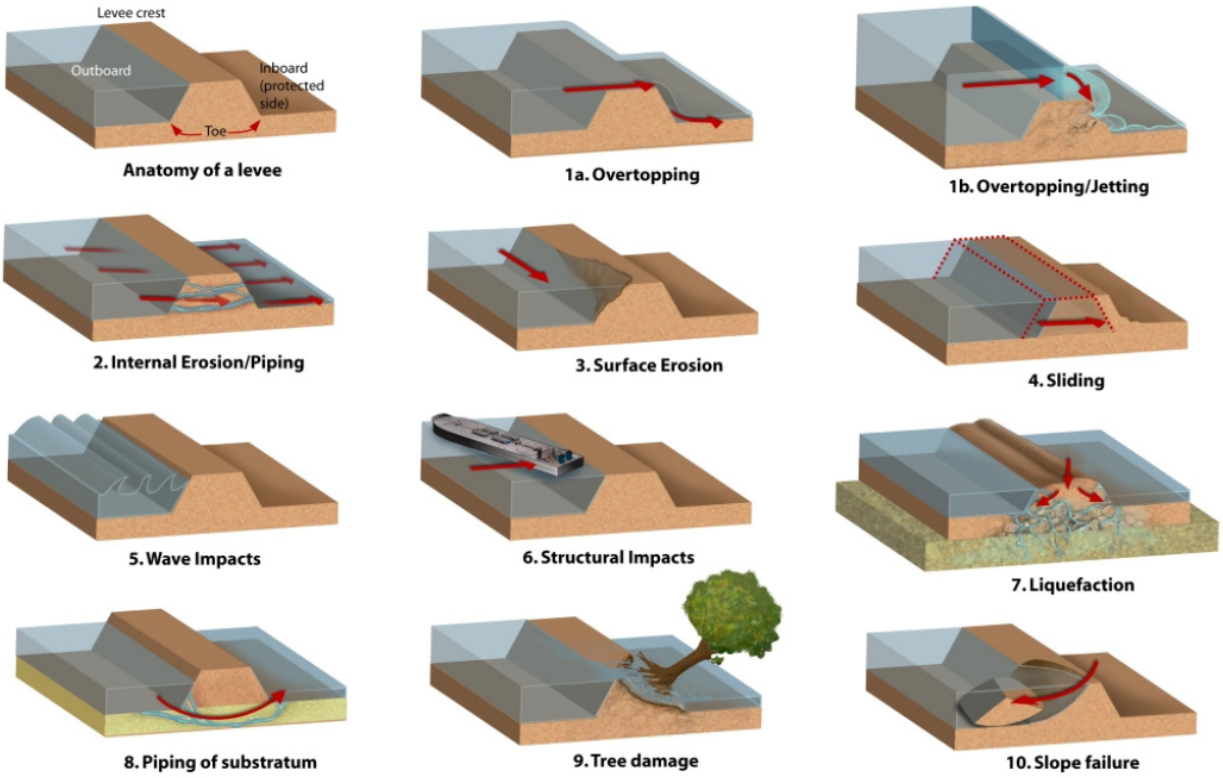


Figure 1.1 Levee Failure Mechanisms (Zina Deretsky, National Science Foundation, 2010)

According to the U.S. Army Corps of Engineers' (USACE) National Levee Database (NLD), approximately two-thirds of Americans live in counties with at least one levee, while the average age

of levees in the U.S. is 50 years (ASCE, 2017). A large number of levees were also constructed in early 20th century in response to the flooding problems. The levees in the Sacramento–San Joaquin River Delta region are especially well-known due to its unique significance.

The Sacramento–San Joaquin River Delta, referred to herein as the Delta region or simply as the Delta, is located south of Sacramento and east of San Francisco Bay, and it is of great importance to California in a number of ways. Due to the confluence of the Sacramento river and San Joaquin river, the Delta region came into being at the western edge of Central Valley. Figure 1.2 is shows the approximate location and area of the Delta region, across which an extensive levee system about 1300 miles long helps to maintain the islands and waterways that define the Delta.

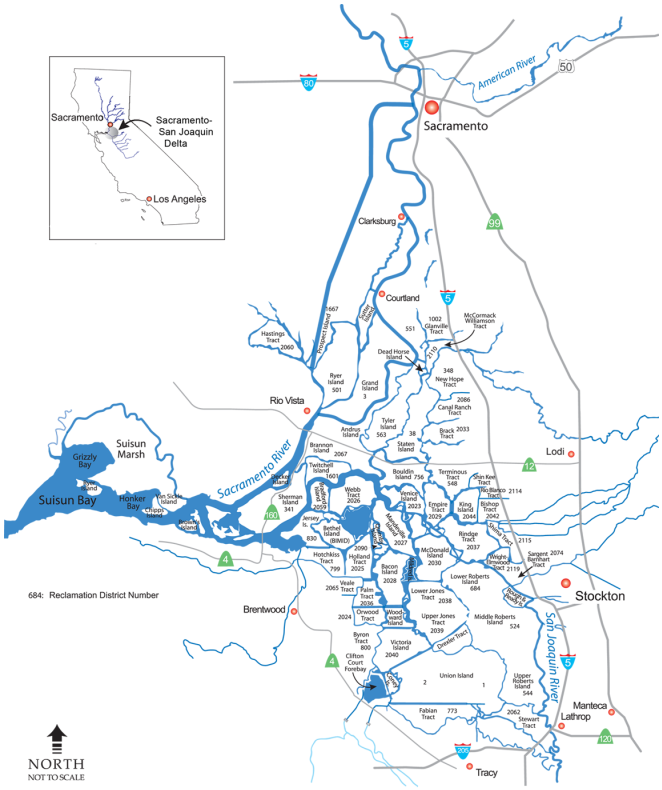


Figure 1.2 Map of the Sacramento and San Joaquin Delta Region (USGS)

The Delta Region is the largest estuary in the western United States, and provides an important estuarine habitat for both plants and animal species. It's also vital to California's water supply system.

Essential lifelines such as transportation and transmission lines also lie across the Delta Region. Figure 1.3 shows the major natural gas pipelines built in the Delta region. The damage caused by pipeline explosion can be very substantial under certain circumstances, and factors such as landslide or earthquake pose high risk to pipeline damage. With all things considered, it's without doubt that the levees that were constructed to protect the Delta region play a critical role in the economy and environment of California.

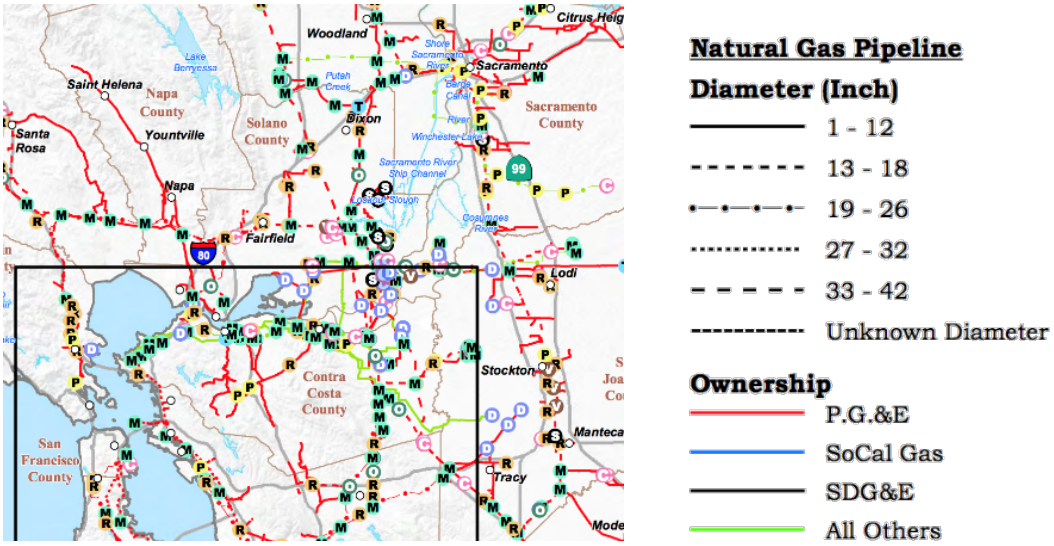


Figure 1.3 A map of pipelines in the Delta Region (California Energy Commission, Energy map)

The levees in the Delta Region are at risk of failure for a number of factors, whose occurrence will lead to severe damage to both the economy and environment. Since 1900, there have been over 160 levee failures in the Sacramento–San Joaquin River Delta. The most recent examples of levee failure in the Delta region occurred in June 2004 when a levee breach flooded the entire island of Jones Tract (Burton and Cutter, 2009).

Aging is one of the reasons that lead to the failure of the levees in the Delta Region. As the time goes by, many of the levees in the region that were built in late 1800s and early 1900s without modern engineering practices. Although these levees have been maintained by local reclamation districts, the

original un-engineered levee fills remain in place with newer fills placed on top. Levee failures also occurred during high water or dry weather events, flooding some of the islands in the Delta Region multiple times. Flooding problem is particularly critical in the Delta Region, considering that much of the land there were experiencing subsidence due to the frequent agricultural activities performed in the Central Delta islands. Though peat soils in those islands may provide a great opportunity to agriculture, they are also responsible for the serious land subsidence problem in the Delta region.

Although the levees in the Delta Region haven't yet experienced a large earthquake, the risk of a major earthquake occurring is still high since there exist quite a few active faults in the San Francisco Bay area and the Delta Region. Figure 1.4 shows the locations of major faults near those two regions. The U.S. Geological Survey estimates that an earthquake of magnitude 6.7 or greater has a 62 percent probability of occurring in the San Francisco Bay Area between 2003 and 2032. If such earthquake does happen and the Delta levees are shaken strongly enough, it is likely that it will cause multiple levee failures in the Delta Region, which could result in great economic loss, interruption of water supply, ecosystem consequences and infrastructure damage like the leak of pipelines.

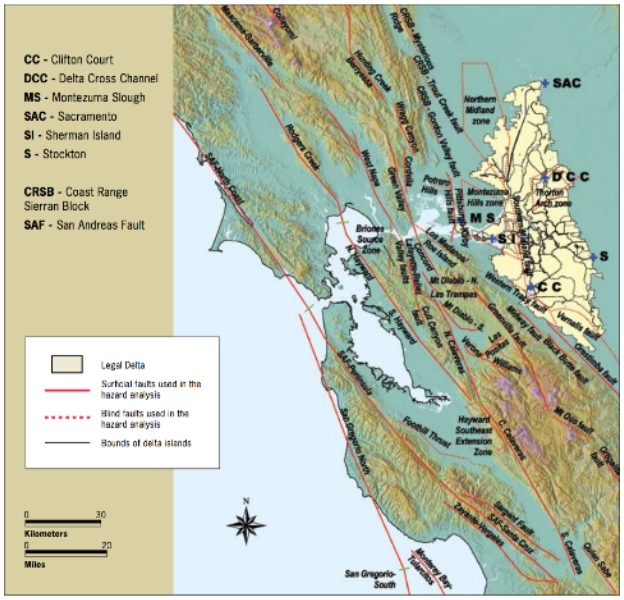


Figure 1.4 Major Faults near the Delta Region (URS/JBA, 2008)

1.2 MOTIVATION

The primary motivation of the research presented in this dissertation is to better understand the seismic fragility of levees in the Sacramento-San Joaquin Delta. My research builds upon previous research and risk assessments. Namely, the Delta Risk Management Strategy (DRMS) conducted over a decade ago utilized fragility functions based on finite element models and expert judgment (URS/JBA, 2008). The influence of levee length on system reliability was included in an ad hoc manner that did not consider spatial correlation of capacity or demand. Importantly, the DRMS study utilized uniform hazard shaking levels, which is now known to be inappropriate for spatially distributed infrastructure systems like levees.

Kwak et al. (2016) developed fragility functions for levees in Japan that were shaken by two strong earthquakes. Damage observations following those earthquakes were combined with ground motion interpolation methods to develop empirical fragility functions. This was the first set of empirical fragility functions developed for quantifying seismic effects on levees. Furthermore, Kwak et al. (2016b) inferred spatial correlation of levee capacity from autocorrelation of demand and damage. The levees studied by Kwak et al. (2016) were founded on inorganic soil. Tsai (2018) developed fragility functions for levees in Hokkaido for which peat soils were present beneath the levees. These levees resting on peat were found to be more susceptible to earthquake-induced damage than the levees founded on inorganic soils. These fragility functions and their spatial correlations were later incorporated by Zimmaro et al. (2019) into a system reliability analysis procedure in which spatial correlation of capacity and demand are considered directly in computing the probability of failure for a levee system.

The empirical method utilized to develop fragility functions for Japanese levees is not feasible for Delta levees because, fortunately, they have not been shaken by strong ground motion during past earthquakes. There are reasons to believe that Delta levees are likely more fragile than the levees studied by Kwak et al. (2016). Levees in Japan are traditional flood control levees that are high and dry most of the year, and only impound water during a high water event. By contrast, Delta levees constantly impound water and therefore much more soil is saturated and susceptible to liquefaction, which is a primary driver of earthquake-induced levee deformations. For this reason, I do not recommend directly utilizing fragility functions from Japan for analysis of Delta levees.

The approach adopted herein is to calibrate numerical models to reasonably match observations of levee damage in Japan, and then exercise those models to develop fragility functions for Delta levees. I include analysis of instrumented Japanese levees where ground motion and in some cases pore water pressure were measured during past earthquakes that damaged some of the levees. I then compare fragility functions derived from these simulations with those developed by Kwak et al (2016). I then analyze Delta levees, accounting for motion-to-motion variability, within cross-section soil variability, and differences in average soil properties along the length of the levee system. My study site is McDonald Island, in the Central Delta, which protects important gas infrastructure.

1.3 ORGANIZATION

This dissertation consists of 5 main chapters, and is organized in the following manner:

Chapter 2 presents two analysis approaches that are used in this study. The finite element modeling approach section introduces general procedures of running finite element analysis in OpenSees with an example of a simple levee model. The element type and material model type used in the finite element analysis are described in detail. The boundary conditions and analysis type for different

analysis stages are also summarized. The fragility function development section, on the other hand, first provided a brief overview on previous studies regarding the empirical fragility function of levees. And a calibrated numerical approach of deriving fragility function is proposed by relating the crest settlement to a ground motion intensity measure. This approach is used extensively in both Chapter 4 and Chapter 5.

Chapter 3 focuses on modeling soil spatial variability as a spatially correlated random field. Using common methods like Cholesky decomposition to create random field realizations is computationally expensive. Finite elements are often small relative to the scale of fluctuation of the random field, and therefore some computational efficiency is achieved by combining Cholesky decomposition and ordinary Kriging. The algorithm is published as a Python package through GitHub, and is validated by example applications.

Chapter 4 first presents case histories of Japanese sites using the finite element modeling approach. Three sites are analyzed, and the surface motions at the levee crest are compared with regard to the response spectra. A pore water pressure response is recorded at one of the sites, and is compared with the predicted pore water pressure response. The predicted crest settlements are also compared with reported performance data. PGV-based fragility functions derived from finite element simulation results are presented.

Chapter 5 is focused on evaluating the seismic performance of levees at McDonald Island through finite element analysis. By accouting for motion-to-motion variability, within-cross-section-section soil variability and section-to-section variablity, PGV-based fragility functions are derived and recommended fragility functions are summarized. Chapter 6 concludes major findings from this study and provides recommendations for future research work.

2 ANALYSIS APPROACH

2.1 FINITE ELEMENT MODELING APPROACH

Finite element method is a commonly used method for solving physical problems in engineering analysis and design (Bathe 2007). It has been applied in various fields including electromagnetics, heat transfer, fluid flow, structural analysis et cetera. Generally, a domain of interest will be divided into small elements, referred to as finite elements, to solve a problem. For typical geotechnical problems, the finite element method is often used to simulate the response of geotechnical systems.

There are a number of different geotechnical finite element software packages available to conduct finite element analysis. I choose to use the Open System for Earthquake Engineering Simulation (OpenSees), which is an open-source software frame work for simulating the seismic response of structural and geotechnical systems (McKenna et al. 2000). OpenSees has been known to be capable of modeling and analyzing the nonlinear response of structural and geotechnical systems using a wide range of material models, elements, and analysis algorithms (McKenna et al. 2000).

In order to conduct a finite element analysis successfully in OpenSees, there are some generalized procedures that need to be followed. First of all, the user is required to select element type and construct the finite element model accordingly depending on what type of structural system that is of interest to the user. Meanwhile, the user should specify what type of material model to use. Appropriate material properties are then assigned to constructed elements given the material model and calibrated material parameters. Moreover, boundary conditions need to be properly defined before any analysis starts. The last step is for the user to determine the type of analysis that needs to be conducted on this well-defined and constrained finite element model. Depending on the type of analysis, the analysis parameters and

solution algorithms used to compile the analysis will vary as well. Considering that the main subject of interest is levee systems, I decided to demonstrate the fore-mentioned procedures with the example of a simple levee model.

2.1.1 Mesh Configuration

For systems that have a simple geometry and relatively small size, it is easy to build the mesh by manually creating nodes and construct elements. However, this seems almost impossible if the system has an irregular shape of geometry and especially when a large number of elements are required. One way to solve this problem is to use the so-called pre and post processors such as GiD and STKO, which are designed specifically for OpenSees. In this study, GiD has always been used to help generate the mesh. Figure 2.1 is an example of a simple levee model, and the mesh is generated using GiD. Even with such simple geometry, it is still clear to see how time consuming it would have been if the nodes and elements were to defined manually.

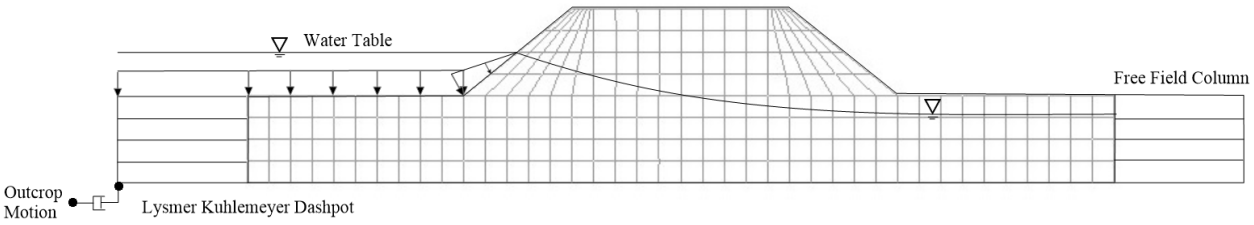


Figure 2.1 An example of simple levee model with mesh configured using GiD

The elements used in this mesh are called SSPquadUP element. The SSPquadUP element is an extension of SSPquad element, which is a four-node quadrilateral element using physically stabilized single-point integration (SSP). The mixed displacement-prssure (u-p) formulation is based on the Biot's theory of porous medium and extended by Zienkiewicz and Shiomi (1984). The benefit of using SSP is that the physical stabilization allows for reduced integration and also results in an element which is free from volumetric and shear locking (McGann el at., 2012). For SSPquadUP elements, each node

has three degrees of freedom (DOF): DOF 1 and 2 for solid displacement in horizontal and vertical directions, and DOF 3 for fluid pressure.

When constructing a SSPquadUP element, a stabilizing parameter α needs to be included in the element construction. According to McGann et al. (2012), the parameter α can be computed as:

$$\alpha = 0.25 * (h^2)/(\rho * c^2) \tag{2.1}$$

where h is the element size, ρ is the mass density of the solid phase, and c is the speed of shear wave propagation in the solid phase. A preliminary study indicates that the value obtained from this equation often needs to be adjusted to produce reasonable results.

As shown in Figure 2.1, there are two wide columns on either side of the model, which are referred to as free-field columns. The presence of these two free-field columns ensures that free-field conditions exist at the horizontal boundaries of the model. These free-field columns are utilized instead of harmonic boundary conditions because, as indicated in Fig. 2.2, the domain may have different heights at the left and right boundary, and/or it may have different material properties. These two columns are usually far away from the levee so that the critical regions in the main mesh are not affected by them. Figure 2.2 is a mesh example of a real levee model from a levee site in Japan, which will be addressed in detail in Chapter 4. As shown in Figure 2.2, the two free-field columns are sufficiently far away from the interior mesh so that the wave reflections interaction between the interior mesh and free-field columns will have negligible impact on the levee response. Meanwhile, the elements in these two free-field columns are also given increased thickness (in the out of plane direction) to ensure that they are significantly more massive than the elements in the interior of the mesh.

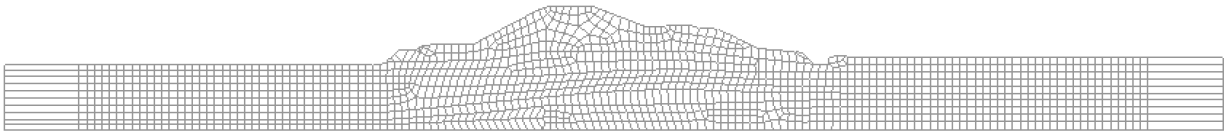


Figure 2.2 A mesh example of real levee model from a levee site in Japan

2.1.2 Material Models

2.1.2.1 PressureIndependMultiYield Material

As we know, some commonly found soil materials in the levee fill and foundation soils include silt, clay, peat, and sand materials. For the former three soil materials, I decide to use PressureIndependMultiYield (PIMY) material model (Elgamal et al. 2003). The PIMY material model is typically used to simulate monotonic or cyclic response of material whose shear behavior is insensitive to the confinement change. A reference table of parameter values is summarized in Table 2.1 (Yang et al. 2008). As recommended by Yang et al. (2008), this table should be used with great caution and the parameter values should get adjusted based on available information.

Table 2.1 A reference table of model parameters used in PIMY material model (Yang et al. 2008)

	Soft Clay	Medium Clay	Stiff Clay
rho	1.3 ton/m^3 or 1.217x10^{-4} (lbf)(s^2)/in^4	1.5 ton/m^3 or 1.404x10^{-4} (lbf)(s^2)/in^4	1.8 ton/m^3 or 1.685x10^{-4} (lbf)(s^2)/in^4
refShearModul	1.3x10^4 kPa or 1.885x10^3 psi	6.0x10^4 kPa or 8.702x10^3 psi	1.5x10^5 kPa or 2.176x10^4 psi
refBulkModul	6.5x10^4 kPa or 9.427x10^3 psi	3.0x10^5 kPa or 4.351x10^4 psi	7.5x10^5 kPa or 1.088x10^5 psi
cohesi	18 kPa or 2.611 psi	37 kPa or 5.366 psi	75 kPa or 10.878 psi
peakShearStra	0.1	0.1	0.1
frictionAng	0	0	0
pressDependCoe	0	0	0

The yield surfaces of PIMY material models are of the Von Mises type. The desired undrained shear strength is modelled by the outer yield surface and the modulus reduction curve is modelled by the inner yield surfaces. The Darendeli (2001) modulus reduction curve equation is applied to obtain the modulus reduction curve for different clay or silt layers. The equation is defined as:

$$\frac{G}{G_{max}} = \frac{1}{1+\left(\frac{\gamma}{\gamma_r}\right)^{\alpha}} \tag{2.2}$$

where G/G_{max} is normalized modulus, γ is the shearing strain, γ_r is the reference strain and α is the curvature coefficient. As recommended by Darendeli (2001), $\alpha = 0.92$ and $\gamma_f = (0.0352 + 0.001 * PI * OCR^{0.3246}) * \left(\frac{\sigma_0'}{p_a}\right)^{0.3483}$, and σ_0' is the mean effective stress and p_a is atmospheric pressure.

As for the peat layers, the PIMY material model is also adopted, but regression model by Kishida (2009) is applied for the modulus reduction curve calculation. Kishida (2009) proposed regression models for dynamic properties of highly organic soils based on a database that includes test results by triaxial, resonant column, torsional shear and direct simple shear apparatuses of samples mainly retrieved from the Sacramento-San Joaquin Delta. The secant shear modulus (G) and equivalent damping ratios (ξ) were modelled as variables related to shear strain amplitude (γ_c), consolidation stress (σ'_{vo}) and organic content (OC). Figure 2.3 shows the influence of σ'_{vo} and OC on G/G_{max} versus γ_c relationships. It is clear that for the low OC case, the G/G_{max} curves shift higher when σ'_{vo} is increasing. However, for the high OC case, variation in σ'_{vo} seems to have relatively little impact on G/G_{max} curves. This is inconsistent with some of the data in Kishida's dataset (e.g., tests performed by Wehling et al. 2003). However, I opt to use these regression equations anyway since they were proposed by the same UC Davis research team, and Kishida's relationship is more recent.

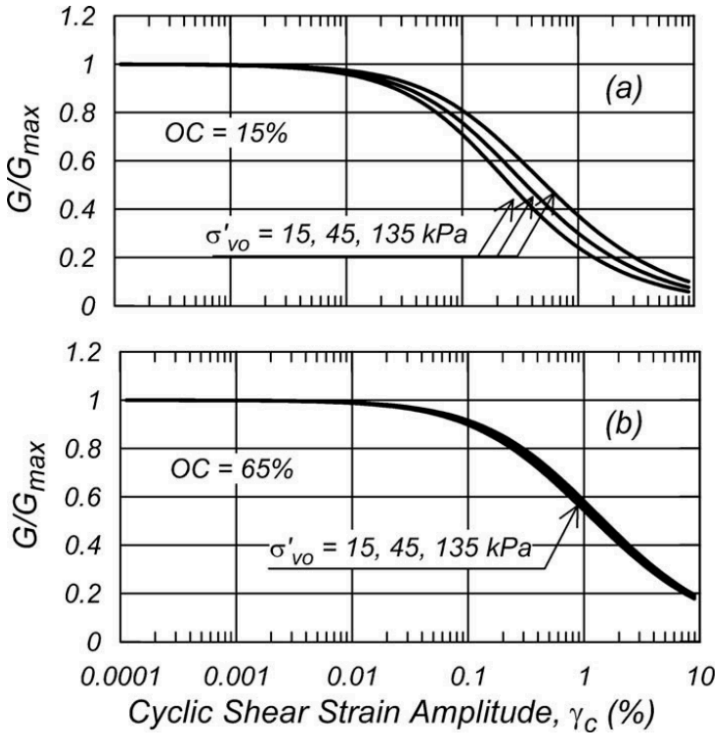


Figure 2.3 G/G_{max} versus γ_c relationship from regression model by Kishida (2009)

2.1.2.2 PressureDependMultiYield03 Material

PressureDependMultiYield03 (PDMY03) material model (Khosravifar et al. 2018) is adopted for the sand material. As a matter of fact, there are three PDMY material models available in OpenSees: PDMY, PDMY02 and PDMY03. Generally speaking, PDMY material is an elastic-plastic material for simulating the essential response characteristics of pressure sensitive soil materials under general loading conditions, which means that this material model can represent the sand materials that often exist in the levees. PDMY02 material model is modified from PDMY material to account for effective overburden stress effect, which is characterized by the overburden correction factor (K_σ), while PDMY03 material model is modified from PDMY02 material model to further account for static shear stress effect, which is characterized by static shear correction factor (K_α).

Figure 2.4 (Khosravifar et al. 2018) shows how simulated K_σ varies with effective overburden stress for sands with different $(N_1)_{60}$ values. As indicated by this figure, the model response agrees quite well with relationships by Idriss and Boulanger (2008). Figure 2.5 (Khosravifar et al. 2018), on the other hand, shows how simulated K_α varies with static shear stress ratio (α) for sands with different $(N_1)_{60}$ values under vertical effective stress of σ'_{vo} = 1 atm, and the results were compared with experimental results from Harder and Boulanger (1997). It can be observed from the figure that for loose sands, K_α will decrease as α increases, and the trend is opposite for denser sands.

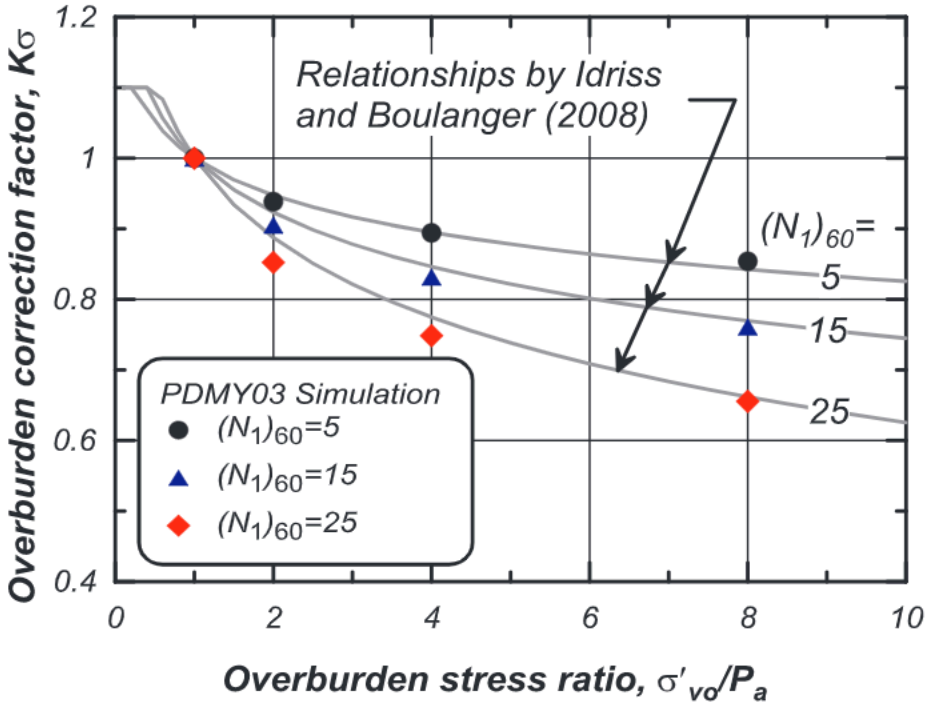


Figure 2.4 K_σ relationship derived from model simulations compared to relationship by Idriss and Boulanger (Khosravifar et al. 2018)

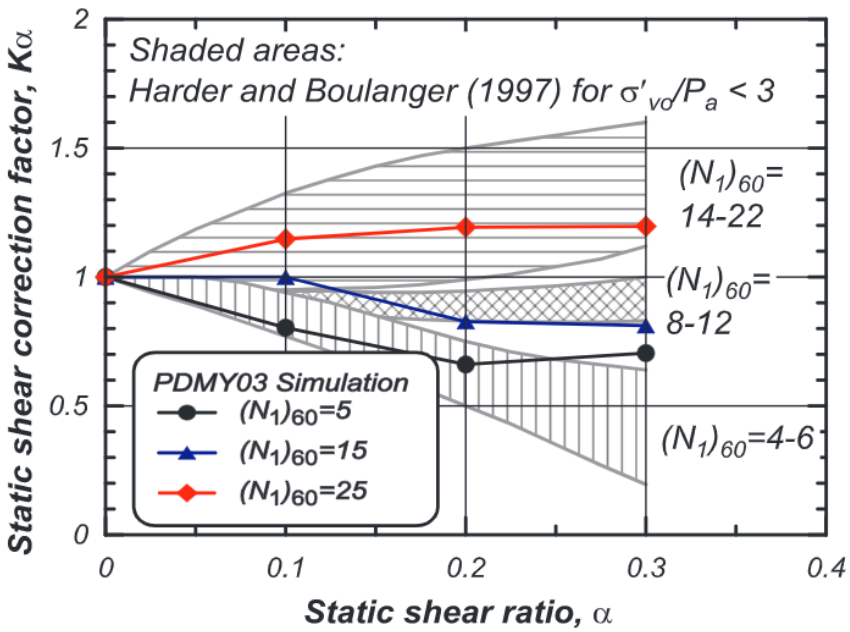


Figure 2.5 K_α relationship simulated from model compared to relationship by Harder and Boulanger (Khosravifar et al. 2018)

Khosravifar et al. (2018) also presented a single element test results with undrained cyclic shear loading on a sand with $(N_1)_{60}$ = 5 under the effective confining stress of 1 atm and no static shear stress (α = 0), which is shown in Figure 2.6. I was able to produce the same results in OpenSees shown in Figure 2.7 to ensure that this material model works well.

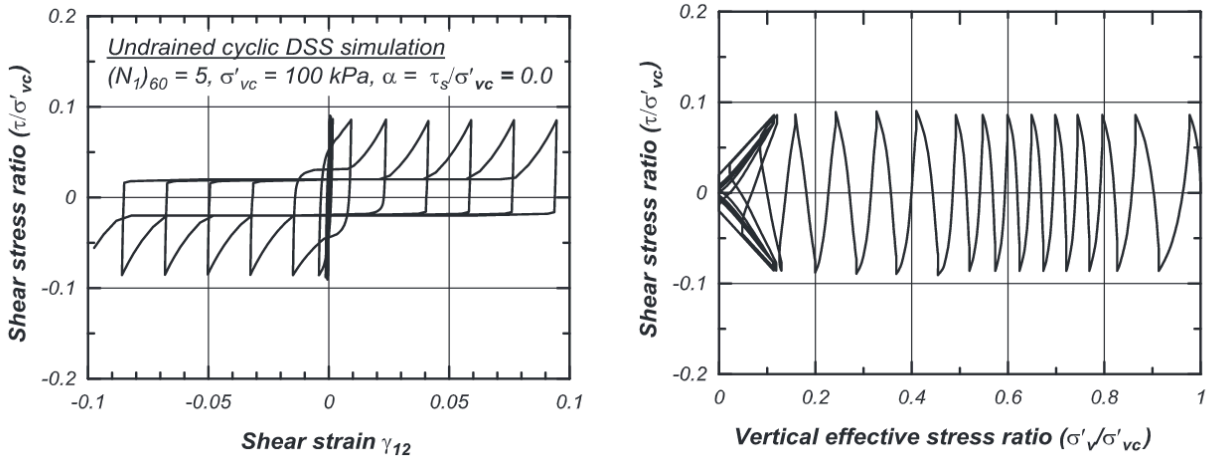


Figure 2.6 Element test of model response in undrained cyclic simple shear loading for $(N_1)_{60}$ = 5(Khosravifar et al. 2018)

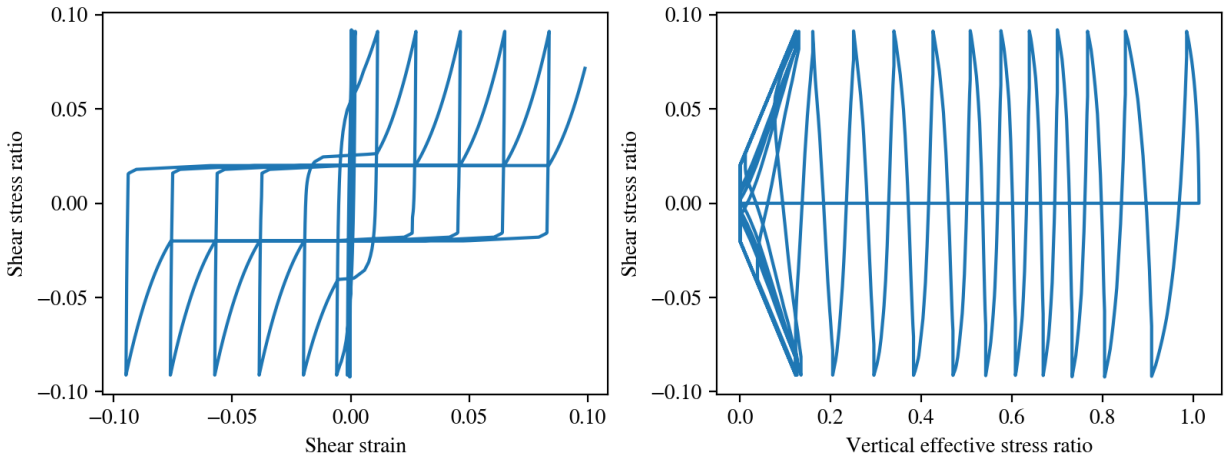


Figure 2.7 Model response in undrained cyclic simple shear loading for $(N_1)_{60} = 5$ in OpenSees

A reference table of parameter values for PDMY03 material model is summarized in Table 2.2 (Khosravifar et al. 2018). These values also need to be used with great caution and other information need to be incorporated when possible. The yield surfaces for this material model are of the Drucker-Prager type. Figure 2.8 shows a comparison of Drucker-Prager yield surfaces and Mohr-Coulomb yield surfaces. Generally speaking, Mohr-Coulomb has a hexagonal shape that is not very stable for multi-directional loading because of issues with return mapping near the corners of the yield surface. The input friction angle defines the size of the outmost yield surface, so it is important to adjust the user-defined modulus reduction curve to render the appropriate friction angle. The modulus reduction curve I used is recommended by EPRI (1993). Figure 2.9 shows the modulus curve and equivalent damping ratio relationships for sands at different depths, as recommended by EPRI (1993). As a matter of fact, another material model called PM4Sand (Boulanger and Ziotopoulo, 2017) material model simulates modulus reduction curve and equivalent damping ratio relationships that is consistent with empirical design relations, such as the ones by EPRI (1993) as well. I evaluated the PM4Sand material model as a candidate for this study, but the implementation in OpenSees failed to produce accurate results for complicated stress paths. Note that PM4Sand was implemented by its authors in FLAC, but UCLA has opted not to pay for an expensive FLAC license.

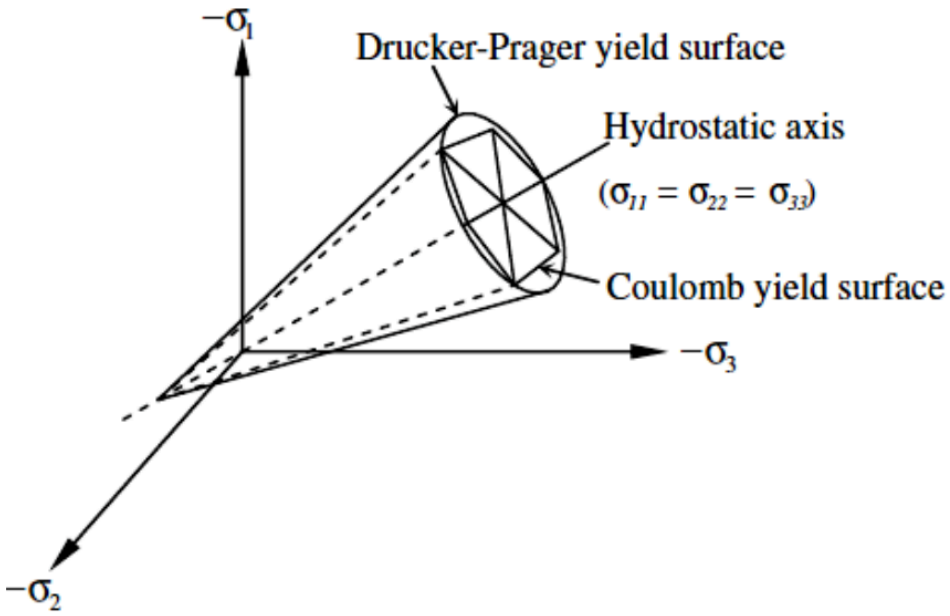


Figure 2.8 Drucker-Prager and Mohr-Coulomb yield surfaces (Khatibinia et al. 2015)

Table 2.2 PDMY03 material model input parameters (Khosravifar et al. 2018)

Model parameters	Loose sand	Medium dense sand	Dense sand	Very dense sand
$(N_1)_{60}$[a]	5	15	25	35
Relative density, D_R[a]	33%	57%	74%	87%
Cyclic resistance ratio, $CRR_{\sigma'_V=1,M=7.5}$[a]	0.09	0.16	0.29	N.A.
Density, ρ	1.94 t/m^3	1.99 t/m^3	2.03 t/m^3	2.06 t/m^3
Reference mean effective pressure, p'_r	101 kPa	101 kPa	101 kPa	101 kPa
Small-strain shear modulus at reference pressure, $G_{max,r}$	46.9 MPa	73.7 MPa	94.6 MPa	111.9 MPa
Maximum shear strain at reference pressure, $\gamma_{max,r}$	0.1	0.1	0.1	0.1
Bulk modulus at reference pressure, B_r	125.1 MPa	196.8 MPa	252.6 MPa	298.3 MPa
Pressure dependence coefficient, d	0.5	0.5	0.5	0.5
DSS friction angle, φ_{DSS}[a]	30°	35°	40°	45°
Model friction angle, φ	25.4°	30.3°	35.8°	42.2°
Phase transformation angle, φ_{PT}	20.4°	25.3°	30.8°	37.2°
Contraction coefficient, c_a	0.03	0.012	0.005	0.001
Contraction coefficient, c_b	5.0	3.0	1.0	0.0
Contraction coefficient, c_c	0.2	0.4	0.6	0.8
Contraction coefficient, c_d	16.0	9.0	4.6	2.2
Contraction coefficient, c_e	2.0	0.0	−1.0	0.0
Dilation coefficient, d_a	0.15	0.3	0.45	0.6
Dilation coefficient, d_b	3.0	3.0	3.0	3.0
Dilation coefficient, d_c	−0.2	−0.3	−0.4	−0.5
Number of yield surfaces, NYS	20	20	20	20
S_0	1.73 kPa	1.73 kPa	1.73 kPa	1.73 kPa

[a] These are not input parameters to the constitutive model, but rather parameters computed during model calibration.

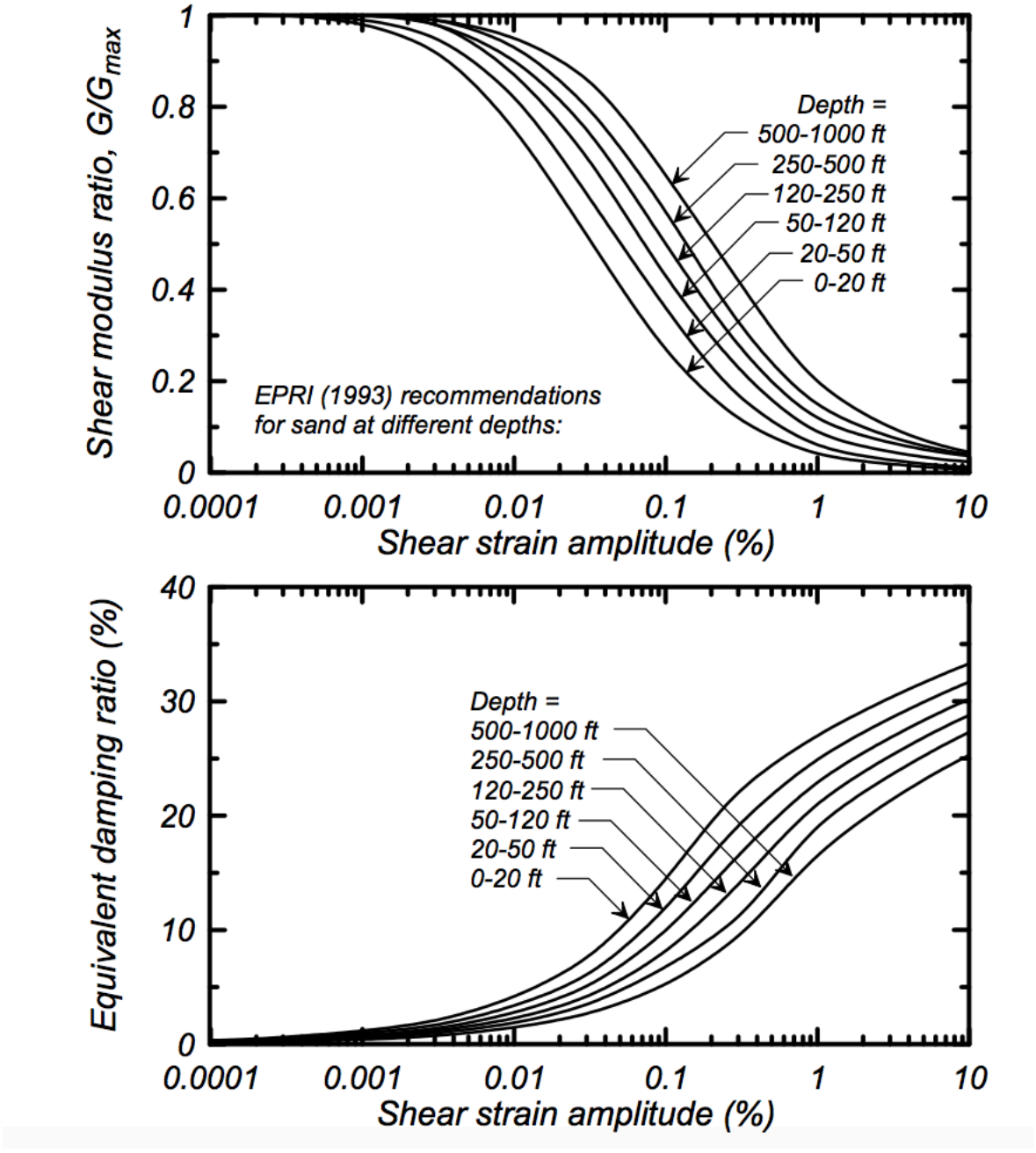


Figure 2.9 Modulus reduction curve for sand recommended by EPRI (1993)

2.1.3 **Analysis Stages**

In general, a model will go through six different stages before the finite element analysis completes. The boundary conditions for the model in different stages will sometimes vary and need to be properly defined in each stage. Gravity is usually applied to the model as the first step of the analysis. For gravity stage, the nodes at the base of the model are fixed in both horizontal and vertical directions so that they won't move physically. The third DOF of the base nodes is not constrained to create zero flow conditions. Two free-field columns exist at horizontal boundaries of the model as shown in Figure 2.1. The nodes on either side of the column are tied together and given equal displacements in both horizontal and vertical boundaries using the *equalDOF* command in OpenSees. These boundary conditions are all summarized in Table 2.3.

Table 2.3 Boundary conditions for six different stages

Stage Number	Stage Name	Horizontal BC - Base	Vertical BC - Base	Seepage BC - Base	Horizontal BC - Sides	Vertical BC - Sides	Seepage BC - Sides
1	Elastic Gravity	Fixed	Fixed	Zero Flow	Fixed	Free	Zero Flow
2	Plastic Gravity	Fixed	Fixed	Zero Flow	Fixed	Free	Zero Flow
3	Seepage - Uniform k	Fixed	Fixed	Zero Flow	Fixed	Free	Zero Flow
4	Seepage - Nonuniform k	Fixed	Fixed	Zero Flow	Fixed	Free	Zero Flow
5	Shaking	Lysmer-Kuhlemeyer	Fixed	Zero Flow	Harmonic for free-field columns	Free	Zero Flow
6	Post-shaking Reconsol	Lysmer-Kuhlemeyer	Fixed	Zero Flow	Harmonic for free-field columns	Free	Zero Flow

The soil elements are assumed to be linear elastic during initial gravity stage, and the material stage needs to be set as elastic stage first by using the *updateMaterialStage* command in OpenSees and setting the material stage to be zero. The permeability for all of the elements is initially set to 1.0 m/s to ensure that hydrostatic conditions occur quickly after the application of gravity in the model. If the permeability of a particular layer is too low, it may take many gravity analysis steps in order to reach hydrostatic pressure conditions.

During gravity stage, it is also important to incorporate the body of water into the model since Figure 2.1 clearly shows part of the left side of the model is submerged under water. Nodal loads are computed individually by integrating water pressure over element length due to water weight, and applied to each node under water given the water table. This is accomplished in OpenSees by using the *load* command in *Plain* pattern. The water pressure associated with each node needs to be applied as the velocity of the third DOF. An example of such procedure can be found in the OpenSees page: https://opensees.berkeley.edu/wiki/index.php/Simulating_a_Centrifuge_Test.

Figure 2.1 also shows the location of the phreatic surface, which means that all the nodes above the phreatic surface should be fixed in the third DOF so that the pore water pressure at these nodes are restricted as zero. Undesired negative pore water pressure will develop if the third DOF is not constrained at these nodes. However, there are also cases where the phreatic surface inside the model is unknown, and I find that it is more beneficial and convenient to conduct the seepage stage in RocScience Phase 2 to determine the phreatic surface. Phase 2 allows us to easily conduct a steady state seepage analysis, while OpenSees can only conduct a transient analysis for seepage analysis which will take a large number of steps to finish. Figure 2.10 shows the model setup in Phase 2. Permeability of soil materials, and boundary conditions need to be defined properly. Figure 2.11 shows the pressure head distribution after seepage analysis is finished, and the purple line indicates the location of phreatic surface. As a matter of fact, another benefit of conducting seepage analysis in

Phase 2 first is that the phreatic surface can be included as a type of boundary line in the mesh configuration so that it will be easier to figure out the nodes that are above the phreatic surface and to constrain the pore water pressure DOF at those nodes to be zero pressure accordingly.

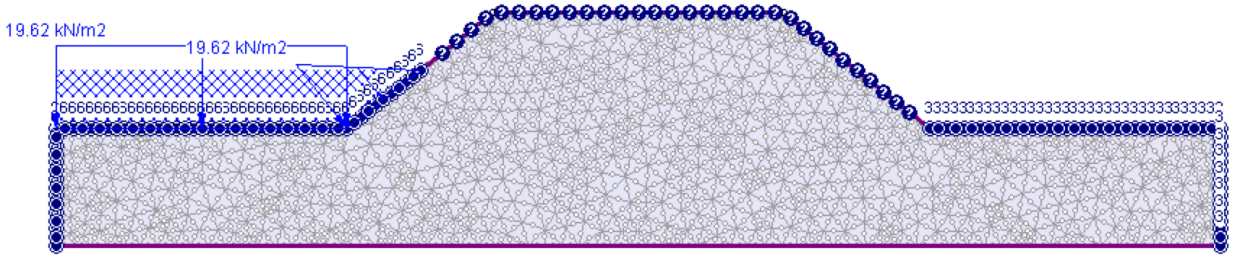


Figure 2.10 A simple levee model setup in Phase 2

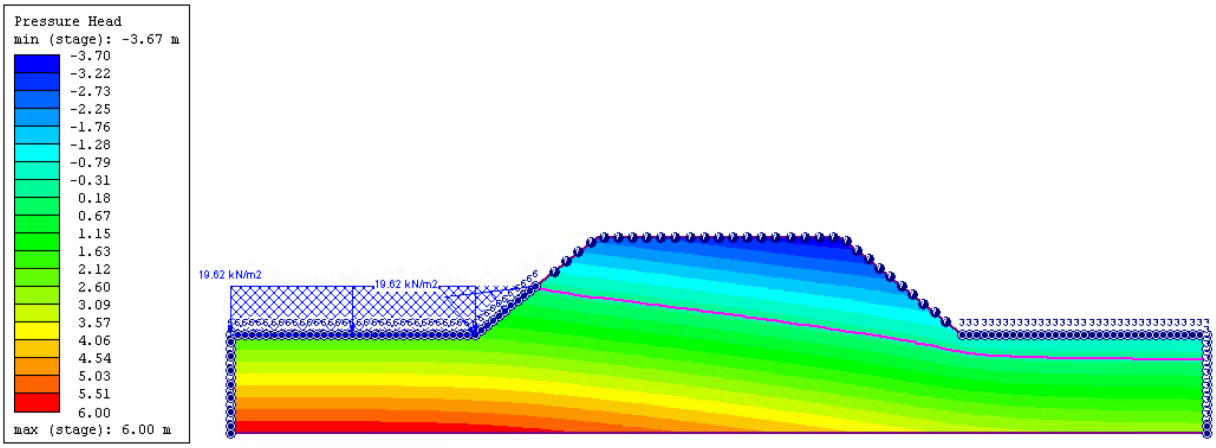


Figure 2.11 Pressure head distribution after a steady state seepage analysis

Following the elastic portion of the gravity analysis is the plastic gravity analysis in which the material stage needs to be updated to be one, also using the *updateMaterialStage* command in OpenSees. The plastic stage is usually run using smaller time steps to aid in convergence. After both elastic and plastic gravity analysis are finished, the permeability of each soil layer are updated using the *updateParameter* command to their respective assigned values so that pore pressure generation during the horizontal excitation is captured appropriately, and to allow the pore water pressure distribution to reach the new

equilibrium prior to the shaking. Table 2.4 lists some commonly used permeability values for different types of soil materials (Yang et al. 2008).

Table 2.4 A reference table of permeability values for different types of soil (Yang et al. 2008)

Gravel	Sand	Silty Sand	Silt	Clay
$>1.0x10^{-1}$ cm/s (or $3.94x10^{-2}$ in/s)	$1.0x10^{-3}$ cm/s (or $3.94\ x10^{-4}$ in/s) ~ $1.0x10^{-1}$ cm/s (or $3.94\ x10^{-2}$ in/s)	$1.0x10^{-5}$ cm/s (or $3.94\ x10^{-6}$ in/s) ~ $1.0x10^{-3}$ cm/s (or $3.94\ x10^{-4}$ in/s)	$1.0x10^{-7}$ cm/s (or $3.94\ x10^{-8}$ in/s) ~ $1.0x10^{-5}$ cm/s (or $3.94\ x10^{-6}$ in/s)	$<1.0x10^{-7}$ cm/s (or $3.94x10^{-8}$ in/s)

After the soil's pore water conditions reach equilibrium again, a ground motion record will be applied. The ground motion records usually include two horizontal components and one vertical component. Only the horizontal components of the ground motion record are used in this study. In order to make sure that the ground motion to be applied is transverse to the levee cross-section, two horizontal components are often needed to rotated to the direction desired. As for the boundary conditions during this shaking stage, the horizontal constraints at the base nodes need to be removed so that these nodes are still fixed in the vertical direction, but now can move freely in the horizontal direction. EqualDOF command is used for the base nodes for equal horizontal displacement so that these nodes will move simultaneously given the ground motion time series. If the ground motion is within motion (a downhole motion for example), the motion can be applied directly to the base nodes. However, a Lysmer-Kuhlemeyer (1969) dashpot will need to be used if the motion is outcrop motion. By using a Lysmer-Kuhlemeyer (1969) dashpot, it is assumed that the model is underlain by an elastic half-space, which allows part of the energy caused by the motion to be removed from the underlying layer beneath the base of the model.

A single zeroLength element is used to define the Lysmer-Kuhlemeyer (1969) dashpot, and the viscous uniaxial material is used to define the constitutive behavior of the Lysmer-Kuhlemeyer (1969) dashpot in the horizontal direction. The single zeroLength element is constructed by two nodes that will share

the same coordinates as the node in the lower left hand corner of the model. The viscous uniaxial material model requires a single input, the dashpot coefficient, c. Following the method of Joyner and Chen (1975), the dashpot coefficient is defined as the product of the mass density and shear wave velocity of the underlying medium. The dashpot coefficient must be scaled by the area of the base of the model to ensure that equivalent loading is applied. And it is important to account for the extra thickness (out of plane direction) of the two free-field columns when calculating the area of the base of the model.

Similar to the base nodes, both ends of the dashpot element are fixed against all displacements in the gravity analysis, but the horizontal constraints will be removed during shaking. While one end of the dashpot is applied with the ground motion time series, the other end is given equalDOF with the soil node in the lower left hand corner of the model and will move accordingly depending on the dashpot coefficient. The node in the lower left hand corner of the model will be the master node for the horizontal equalDOF assigned to the nodes at the base of the mesh.

The last stage is called post-shaking reconsolidation. After the earthquake loading, the excess pore water pressure might not have fully dissipated, and the soil will reconsolidate during this stage. This is typically done by allowing big time steps to let the soil fully reconsolidate. Even though OpenSees usually underestimates the post-shaking settlement, it is still necessary to incorporate this stage during the analysis.

Last but not the least, to create the analysis in OpenSees, it is important to understand how to aggregate analysis commands and perform the analysis depending on the analysis type. Table 2.4 lists a group of analysis commands that are used in this study.

Table 2.5 Analysis commands used in the study

Analysis Command Type	Analysis Command Selection
constraints	Transformation
numberer	RCM
system	ProfileSPD
test	NormDispIncr 10^{-3} 30 0
algorithm	Newton
integrator	Newmark 0.5 0.25
analysis	Transient
	VariableTransient

In general, the *constraints* command handles how the constraint equations or boundary conditions are enforced in the analysis, and we used the Transformation method. The *numberer* command determines the mapping between equation numbers and DOFs, and I used the Reverse Cuthill-McKee (RCM) Numberer in our analysis (Cuthill and McKee 1969). The *system* command specifies how to store and solve the system of equations (SOE)

in the analysis, and I used ProfileSPD to construct a profileSPD SOE linear system of equation object. The *test* command is used to determine if convergence has been achieved at the end of an iteration step, and I selected Norm Displacement Increment (NormDispIncr) test which uses the norm of the left hand side solution vector of the matrix equation to determine if convergence has been reached. A tolerance level and maximum number of iterations need to be specified. The *algorithm* command determines the sequence of steps taken to solve the non-linear equation, and the Newton algorithm I selected uses the Newton-Raphson algorithm to solve the nonlinear residual equation. The *integrator* command determines the meaning of the terms in the system of equation object, and the integrator varies depending on whether the analysis is static or transient. I used Newmark integrator which require a γ and β factor for the transient analysis. The *analysis* command determines the type of analysis that is to

be performed. In this study, I used Transient analysis for gravity and seepage stage, and used VariableTransient in dynamic analysis. The VariableTransient analysis commands allows the time step to be divided when the convergence is not achieved. During dynamic analysis, full Rayleigh damping is usually included by specifying the following two parameters defined by Eq. 2.3 and Eq. 2.4,

$$a_0 = \frac{2\xi_T \omega_1 \omega_2}{\omega_1 + \omega_2} \tag{2.3}$$

$$a_1 = \frac{2\xi_T}{\omega_1 + \omega_2} \tag{2.4}$$

where ξ_T is the target damping ratio, and ω_1, ω_2 are the angular frequencies associated with the target damping ratio. The Rayleigh damping is then computed as,

$$\xi_R = \frac{a_0}{2\omega} + \frac{a_1 \omega}{2} \tag{2.5}$$

2.2 FRAGILITY FUNCTIONS DEVELOPMENT

The Pacific Earthquake Engineering Research (PEER) center developed a performance-based earthquake engineering framework (Moehle and Deierlein, 2004) that has since been adapted by the Applied Technology Council for professional practice (Porter et al. 2007; FEMA 2012). The procedures integrate seismic hazard analysis with engineering demand parameters, damage analysis, and loss analysis, as defined by the following formula,

$$\lambda(\mathrm{DV}) = \iiint \mathrm{G}(\mathrm{DV}|\mathrm{DM})\, \mathrm{dG}(\mathrm{DM}|\mathrm{EDP})\, \mathrm{dG}(\mathrm{EDP}|\mathrm{IM})\, \mathrm{d}\lambda(\mathrm{IM}) \tag{2.6}$$

where DV stands for the decision variable, which is often related to direct losses, downtime or casualties; DM represents a damage measure, which describes the physical damage to a facility; EDP

is called engineering demand parameter, such as deformations, forces and strains of a structure; IM is an intensity measure used to characterize the ground shaking intensity, such as peak ground acceleration (PGA), spectral acceleration and peak ground velocity (PGV). The terms G(EDP|IM) and G(DM|EDP) give the probability that a certain damage state is exceeded given an IM or an EDP, and the dG(EDP|IM) and dG(DM|EDP) terms represent the slope of the functions with respect to IM or EDP. Furthermore, fragility functions traditionally defined as G(DM|EDP) can also sometimes be treated as G(DM|IM) by skipping the EDP parameter. Among the four analyses, the damage analysis uses fragility functions that produces the probability of exceeding a damage state given a EDP or IM, which will be the focus of this section.

Depending on how damage is assessed and characteristics of damage observations, fragility functions can be created in different ways. As shown in Table 2.6, Porter et al. (2007) summarized six methods for deriving fragility functions depending on whether data is available, the specimen damage, and the EDP imposed. Note that IM can be substituted for EDP as the conditioning variable. Considering that the focus of this study is levee systems, a brief literature review on the levee fragility functions is presented in the following section.

Table 2.6 Analysis methods and data employed (Porter et al. 2007)

Method name	Data used
A. Actual failure EDP	All specimens failed at observed values of EDP
B. Bounding EDP	Some specimens failed; maximum EDP for each is known
C. Capable EDP	No specimens failed; maximum EDP for each is known
D. Derived fragility	Fragility functions produced analytically
E. Expert opinion	Expert judgment is used
U. Updating	Enhance existing fragility functions with new method-B data

2.2.1 Literature Review

There have been some studies regarding the development of fragility functions for levees. For instance, part of the Delta Risk Management Strategy project (DRMS) involved assessing the seismic risk of levees in the Sacramento-San Joaquin Delta region. Fragility functions were developed for these levees using Monte Carlo simulations based on a series of vulnerability classes using factors that differentiate the performance of the levees (Salah-Mars et al. 2008), and method B from Table 2.6 was adopted. Rosidi (2007) analyzed the seismic risk of levees by assessing the dynamic response of a typical cross section of levees and computed the probability of failure using the fragility curve of levees.

Fragility functions have also been developed from empirical data for levees in Japan. Kwak et al. (2016) utilized field performance data of flood control levees along the Shinano River in Japan from two shallow crustal earthquakes, and developed both PGA and PGV based fragility functions. These levees are founded mostly on sands and gravels with low fines content. When developing fragility functions, geomorphic conditions, levee geometry, and groundwater conditions were also included as predictive variables correlated to damage. 3318 levee segments are defined along the river system and each segment is approximately 50m long. Kwak et al. (2016) defined five damage levels for these 3318 levee segments based on the crack depth and width, and crest settlement, which is shown in Table 2.7. Damage levels were then identified for different bins of the IMs, and based on that, the probabilities of exceeding different damage thresholds were derived and fitted with log-normal CDFs. Table 2.8 summarizes moments of log-normal CDFs including the mean and standard deviation, the standard deviation of residuals and ranges of PGA and PGV for damage levels larger than 0 (Kwak et al. 2016). For exceedance probabilities of higher damage levels, the mean for the log-normal CDF is adjusted while the standard deviation is kept the same, and the added means are shown in Figure 2.12. The standard deviations were kept the same because otherwise the fragility functions would cross over at

some point, resulting in a higher probability of a higher damage state than a lower damage state, which is logically impossible.

Table 2.7 Damage levels classification (Kwak et al. 2016)

Damage Level	Crack depth (cm)	Crack width (cm)	Subsidence (cm)	Description
0	0	0	0	No damage reported
1	0–100	0–10	0–10	Slight damage, small cracks
2	100–200	10–50	10–30	Moderate damage, cracks or small lateral spreading
3	200–300	50–100	30–100	Severe damage, lateral spreading
4	>300	>100	>100	Levee collapse

Table 2.8 Moments of log-normal CDFs for PGV- and PGA-based fragility curves (Kwak et al. 2016)

Model	*IM*	Condition	μ	e^{μ}	β	σ	Range
Model 1	*PGV*	All	4.64	104 cm/s	0.92	0.07	7–111 cm/s
	PGA	All	0.42	1.52 g	1.07	0.07	0.13–1.31 g
Model 2	*PGV*	G_N 1	6.42	611 cm/s	1.70	0.05	10–110 cm/s
		$D_W < -1.0$ m	4.69	108 cm/s	0.89	0.07	7–112 cm/s
		$D_W > -1.0$ m	4.43	84 cm/s	0.80	0.05	13–78 cm/s
	PGA	G_N 1	2.59	13.4 g	2.02	0.03	0.14–1.29 g
		$D_W < -1.0$ m	0.37	1.44 g	0.89	0.08	0.13–1.32 g
		$D_W > -1.0$ m	0.32	1.38 g	1.17	0.07	0.14–1.09 g

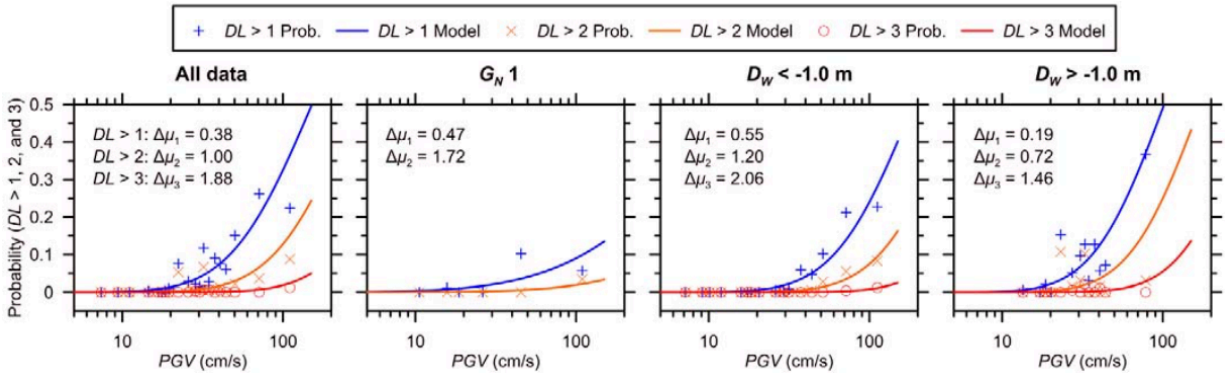


Figure 2.12 Probabilities of exceeding damage levels above one for different conditions. CDFs are fit to data using standard deviations for the damage level above zero case and added means (Kwak et al. 2016)

Moreover, Tsai (2018) developed PGA-based fragility functions empirically from field performance of levees along the Kushiro and Tokachi Rivers, where both peat levee foundations and inorganic levee foundations were considered. As shown in Figure 2.13, the Hokkaido levees have higher fragility curves for probability of any damage level (DL> 0) compared with fragility functions proposed by Kwatk et al. (2016) when PGA is above 0.25g. And the standard deviation is lower than what was proposed by Kwak et al. (2016). Levees resting on peat were also found to be more fragile than levees resting on inorganic soils.

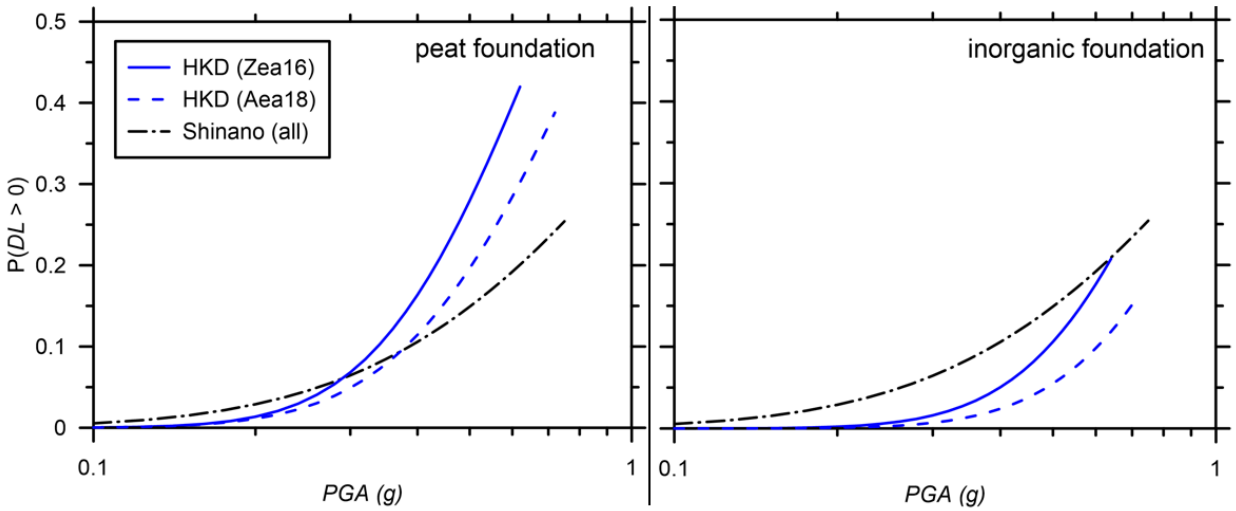


Figure 2.13 Comparison of fragility curves for probabilities of exceeding any damage level evaluated for Hokkaido levees and Shinano levees. (Tsai, 2018)

2.2.2 Calibrated Numerical Approach to Developing Fragility Functions

Instead of using field performance data to develop fragility functions as Kwak et al. (2016) and Tsai (2018) did, I adopt an approach in which I utilize numerical simulations calibrated with empirical fragility functions to derive fragility functions for Delta levees. These fragility functions are developed by analyzing the dynamic response of a two-dimensional levee cross-section model. Each levee model is analyzed with a number of ground motions of various intensities. For each ground motion, the average crest settlement is recorded together with an intensity measure of the ground motion (i.e. PGV). A preliminary study indicated that when plotting these two together, the logarithm of crest settlement is found to be approximately linearly related to the logarithm of PGV, as illustrated in Figure 2.13.

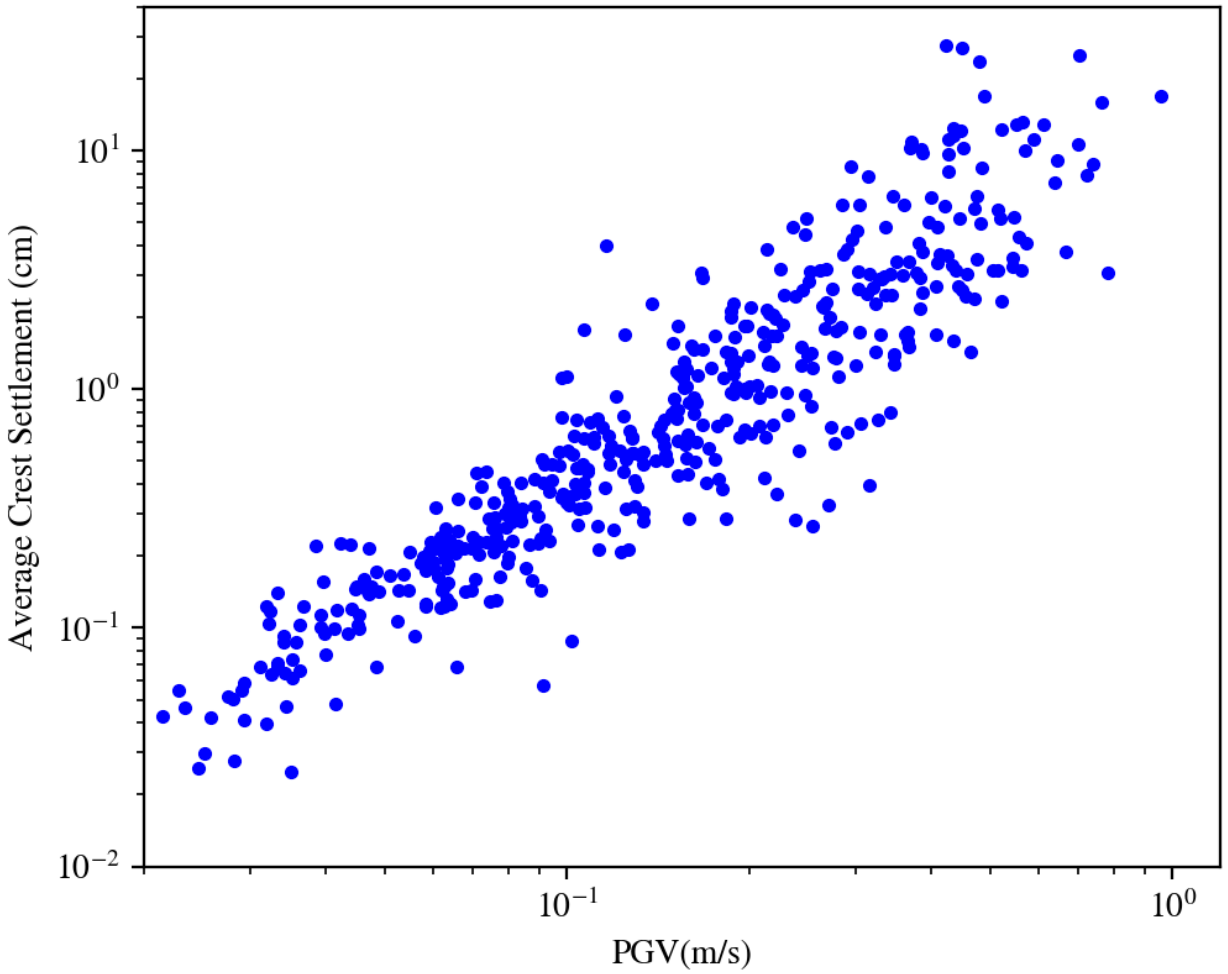


Figure 2.14 An example of crest settlement versus PGV of a reference motion

The linear relationship in Figure 2.14 can be defined by the equation below,

$$\ln(S) = m_0 + m_1 \cdot \ln(PGV) + \varepsilon \tag{2.7}$$

where S is the crest settlement; m_0 and m_1 represent the intercept and the slope of the fitted line, and ε is a normally distributed random variable with a mean of 0, and a standard deviation of σ. This also means that for each given PGV, the crest settlement is lognormally distributed, with a mean of μ_S, which is shown in Eq 2.8, and the standard deviation is σ.

$$\ln(\mu_S) = m_0 + m_1 \cdot \ln(PGV) \tag{2.8}$$

Based on Eq 2.7 and Eq 2.8, it is straightforward to compute the probability of exceeding a certain amount of settlement given the PGV or any other intensity measure using Eq. 2.9.

$$P(S > S_t|im) = 1 - \Phi[\frac{\ln(S_t) - \ln(\mu_S)}{\sigma}] \quad (2.9)$$

where S_t is the user-defined settlement threshold. By varying the intensity measure, a fragility curve will be developed, which shows how the probability of exceeding the settlement threshold changes with intensity measure. Similar to how Kwak et al. (2016) classified the damage level based on crack width, depth and settlement, I choose to use the following classification shown in Table 2.9. By changing the settlement threshold, different fragility curves can be computed. Figure 2.15 also illustrates how the fragility curve is derived by calculating the probability of exceeding certain settlement threshold given different IMs.

Table 2.9 Damage level classification

Damage Level	Settlement (cm)
0	0-1
1	1-10
2	10-30
3	30-100
4	>100

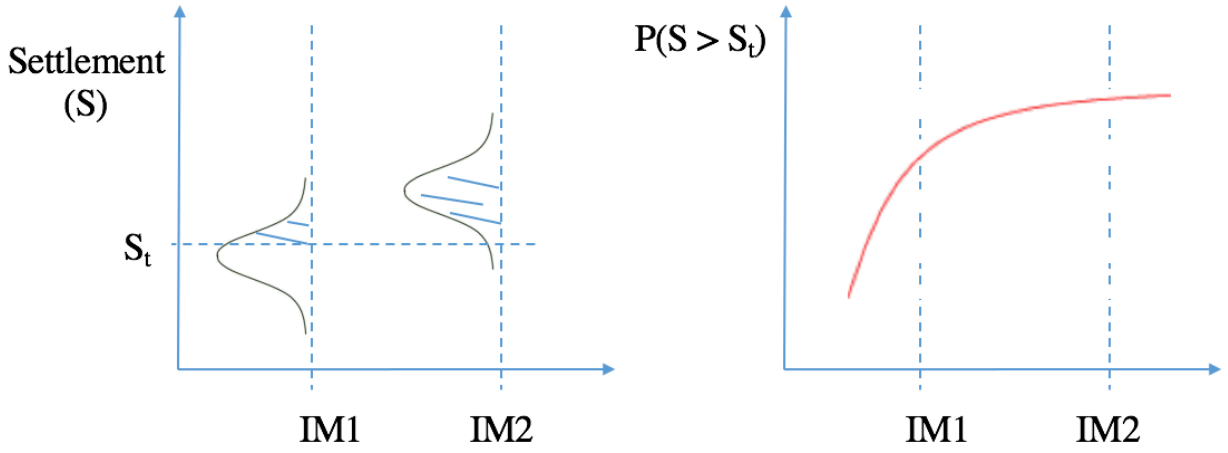


Figure 2.15 A sketch showing the approach of developing fragility curves

In addition, it is also possible to include more than one variable in Eq. 2.7 Duration is known to influence liquefaction, and liquefaction is a primary driver of earthquake-induced levee damage. Therefore, PGV is likely not a sufficient intensity measure for levee fragility. As a result, magnitude may be included by simply adding another term in Eq. 2.7, which is shown as follows,

$$\ln(S) = m_0 + m_1 \cdot \ln(PGV) + m_2 \cdot M + \varepsilon \tag{2.10}$$

where M represents the magnitude of the earthquake.

The primary advantage of the proposed numerical approach is that fragility functions can be developed for levees that have not been shaken by past earthquakes with ground motions of high enough intensity to induce damage. Another advantage is ground motions with a large range of intensity and duration can be considered, whereas empirical fragility functions are limited to the events for which damage was documented. However, a drawback is that the numerical simulations may not capture all of the conditions encountered in a real levee system. In deriving the fragility functions from numerical simulations, three factors are considered and summarized as follows:

1. Motion-to-motion variability, in which motions with the same intensity measure value may produce different crest settlements for the same model due to differences in spectral shape, frequency content, duration, or other attributes
2. Within-cross-section soil variability, in which modeling the soil properties as a spatially correlated random field results in differences in settlement relative to a uniform model for the same ground motion
3. Section-to-section variability, in which the mean value of the soil properties within a cross-section vary with distance along the length of the levee.

We can also classify these three different sources using the definition of aleatory variability and epistemic uncertainty. The aleatory variability is associated with the randomness in a process, which in this study can be quantified by considering motion-to-motion variability and within-cross-section soil variability. The section-to-section variability can be treated as a form of epistemic uncertainty, since it can be reduced if we have more available geotechnical information to refine the average soil properties along the length of the levee. There also exists modeling uncertainty, which is another kind of epistemic uncertainty and is not addressed in this study.

Another thing worth noting here is that for this approach, if only one variable is considered, it turns out the moments of the log-normal CDFs can be directly computed using the coefficients of the fitted straight line, which are shown by Eq. 2.11 and Eq. 2.12.

$$\mu = \frac{\ln(S_t) - m_0}{m_1} \tag{2.11}$$

$$\beta = \frac{\sigma}{m_1} \tag{2.12}$$

where μ and β represent the mean and the standard deviation of the log-normal CDF for the fragility curve. If more than one variable is included, Eq 2.11 can be modified to compute the mean of the log-normal CDFs, while the standard deviation can still be determined using Eq. 2.12.

3 SPATIAL VARIABILITY IN THE LEVEE SYSTEMS

3.1 INTRODUCTION

Soils can naturally be highly variable due to the method by which they are deposited. In 1915, Harris first provided evidence of the influence of substratum irregularities through field experiments. Spatial variability in soil properties, since then, has been studied from various perspectives for decades. Campbell (1976) claims that although variation within soil units has impact on the study of soil, it is still not formally and fully acknowledged in the soil descriptions. More research could be conducted to improve current understanding on soil variability and to give a better estimate of soil variability.

It is obvious that natural soils are rarely homogeneous, and heterogeneity is commonly found in soil structure. Soil heterogeneity can be classified into two types, which come from two sources. One source is lithological heterogeneity, and the other source is the so-called inherent spatial soil variability (Elkateb et al. 2002). Lithological heterogeneity often refers to the organization of different soil layers within a profile, and it is usually manifested in the form of thin soft layers embedded in the stiffer media or the inclusion of different lithology within a uniform soil mass (Elkateb et al. 2002). The inherent spatial soil variability, on the other hand, is associated with deposition conditions and loading histories, resulting in variation of soil properties in space.

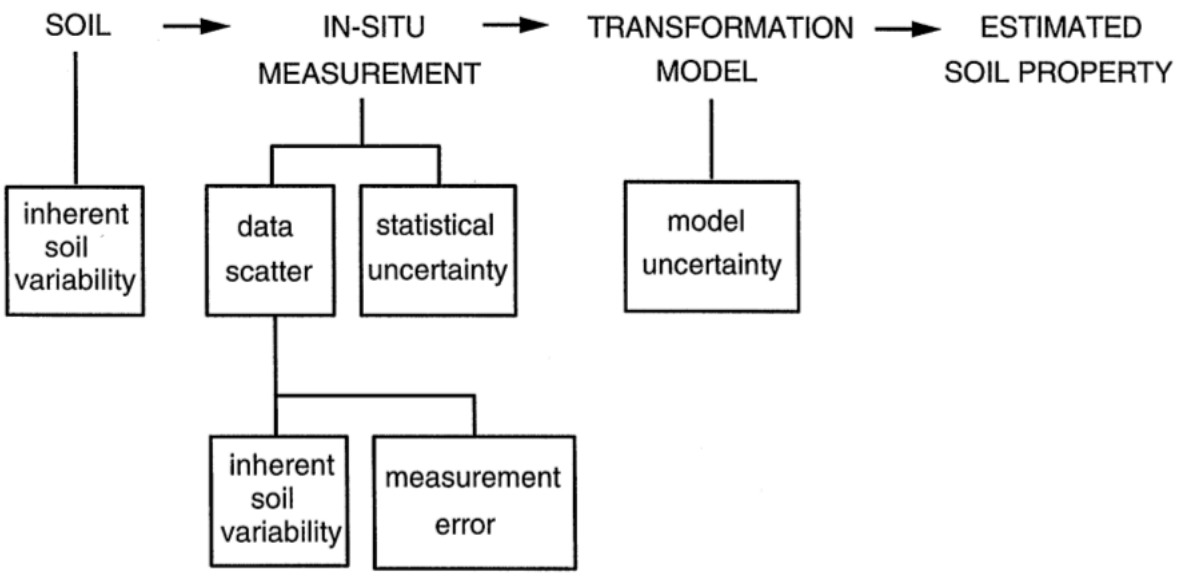


Figure 3.1 Uncertainty in soil property estimates (Phoon and Kulhawy 1999)

As a matter of fact, the inherent spatial soil variability is only one of the sources of geotechnical uncertainly when we consider the uncertainties in soil properties. As illustrated in Figure 3.1, measurement error and transformation uncertainty also contribute to the uncertainty in soil property estimates (Phoon and Kulhawy 1999). Transformation uncertainty occurs when measurements are transformed into design soil properties using empirical or other correlation models. Phoon and Kulhawy (1999) states that the relative contribution of different sources of uncertainty to the overall uncertainty clearly depends on the site conditions, degree of equipment and procedural control, and precision of the correlation model, which makes the estimates of soil property so complex.

Several studies have been successfully accomplished with regard to describing and modelling the spatial variability in soil properties. It is usual to model inherent soil variability as a random field, which can be effectively described by the distribution of the soil property of interest and its spatial correlation function (Phoon and Kulhawy 1999, ISSMGE-TC304 2021). The distribution function is generally parameterized by the mean μ and standard deviation σ. The coefficient of variation COV is defined as the standard deviation divided by the mean and quantifies the amplitude of fluctuations of

a soil property. The spatial correlation function is generally parameterized by the scale of fluctuation, defined as the integral of the spatial correlation function from minus infinity to plus infinity, which quantifies the spatial frequency of fluctuations.

3.2 RANDOM FIELDS

The random field theory (Vanmarcke 1977) has been widely adopted to model spatial variability of soil properties. A random field arises when a random variable is extended over a domain (generally space or time; this dissertation deals with spatial random fields). In addition to the parameters necessary to describe the distribution of the random field at a point (e.g., the mean and standard deviation for a normally distributed random variable), spatial correlation must also be specified. I restrict my discussion to stationary random fields here. A stationary random field is characterized by a constant distribution function (i.e., the mean and standard deviation are constant), and the spatial correlation between two points within the random field is a uniform function of separation distance and not of spatial position within the domain. Spatial correlation functions can either be specified as covariance versus separation distance, or as correlation versus separation distance. I adopt the latter here.

Commonly used correlation functions include the Markov function specified by Eq. 3.1 and the Gaussian function specified by Eq. 3.2, where τ is the distance between two points and θ is the correlation length (Vanmarcke 1984), which is a constant defined in Eq. 3.3. Note that constants other than θ are often used to define spatial correlation functions, in which case the normalizing constants (2 for Markov, π for Gaussian) may be different in some forms encountered in text books or academic papers. Sometimes these alternative constants are erroneously called "correlation length". To avoid this confusion, I prefer to use θ in the correlation functions.

$$\rho(\tau) = \exp\left\{-\frac{2|\tau|}{\theta}\right\} \tag{3.1}$$

$$\rho(\tau) = \exp\left\{-\pi\left(\frac{\tau}{\theta}\right)^2\right\} \tag{3.2}$$

$$\theta = \int_{-\infty}^{\infty} \rho(\tau) d\tau \tag{3.3}$$

Examples of Markov and Gaussian correlation functions are plotted in Figure 3.2. It can be observed from the figure that Gaussian correlation is mean square differentiable (Griffith and Fenton 2008), meaning that its second derivative is defined at $\tau = 0$. On the other hand, the Markov correlation function comes to a sharp point, and is not mean square differentiable. As a matter of fact, it is important for correlation functions to be mean square differentiable when using Rice's (1944) formula to solve level crossing statistics problems. For this reason, I adopt Gaussian correlation functions throughout the study.

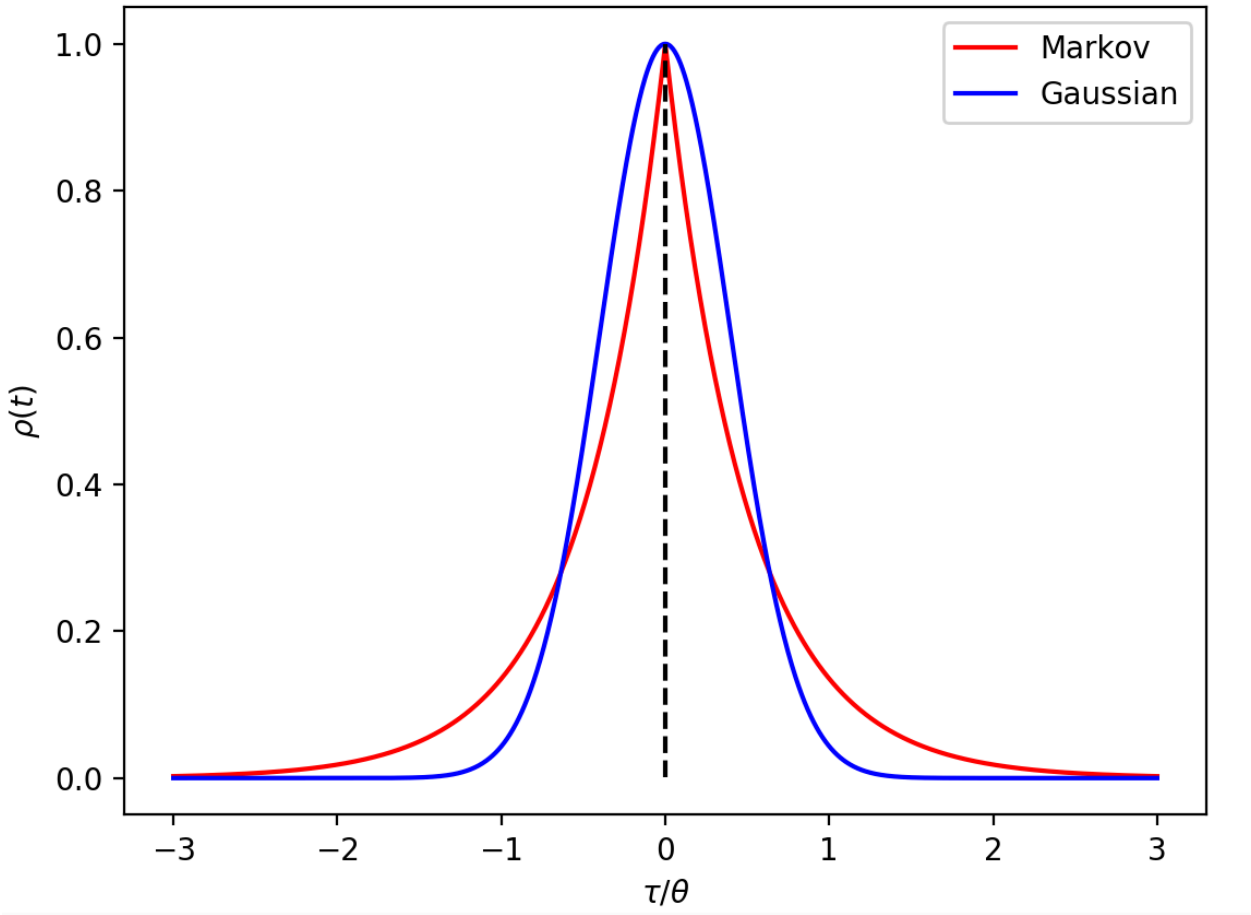


Figure 3.2 Markov and Gaussian correlation function

Correlation length (θ), sometimes called the scale of fluctuation, is often interpreted as the distance within which points are significantly correlated, implying that two points that having a distance of more than θ are essentially uncorrelated. While this interpretation assigns an intuitive meaning to θ, it is not very mathematically rigorous since the correlation function is actually constantly changing and does not resemble a Heavyside step function. I believe it is more insightful to consider correlation in a mathematically rigorous manner by treating θ as an input to an equation that defines a continuous function.

The correlation length in the horizontal direction is typically an order of magnitude or more than that in vertical direction, because soil tends to be deposited in thin layers. For example, Phoon and Kulhawy

(1999) summarized scales of fluctuation for the inherent variability of various soil properties, as reproduced in Table 3.1. Notice that the ratio of horizontal-to-vertical scale of fluctuation for cone tip resistance is approximately 50 times larger for sand and 150 times larger for clay.

Table 3.1 Summary of scale of fluctuation of some geotechnical properties (Phoon and Kulhawy 1999)

Property[a]	Soil type	No. of studies	Scale of fluctuation (m) Range	Mean
Vertical fluctuation				
s_u	Clay	5	0.8–6.1	2.5
q_c	Sand, clay	7	0.1–2.2	0.9
q_T	Clay	10	0.2–0.5	0.3
s_u(VST)	Clay	6	2.0–6.2	3.8
N	Sand	1	—	2.4
w_n	Clay, loam	3	1.6–12.7	5.7
w_L	Clay, loam	2	1.6–8.7	5.2
$\bar{\gamma}$	Clay	1	—	1.6
γ	Clay, loam	2	2.4–7.9	5.2
Horizontal fluctuation				
q_c	Sand, clay	11	3.0–80.0	47.9
q_T	Clay	2	23.0–66.0	44.5
s_u(VST)	Clay	3	46.0–60.0	50.7
w_n	Clay	1	—	170.0

[a] s_u and s_u (VST), undrained shear strength from laboratory tests and vane shear tests, respectively; $\bar{\gamma}$, effective unit weight.

3.3 LITERATURE REVIEW

3.3.1 Previous Studies of Soil Properties as Random Fields

The concept of modeling spatial variability in soil as random field has been implemented in different cases and applications. For instance, Boulanger and Montgomery (2016) modeled standard penetration test resistance, $(N1)_{60cs}$, within a liquefiable layer as a spatially correlated Gaussian random field, and

imposed ground motion at the base of the model. The resulting deformations were compared with models with the same geometry, but with uniform soil properties. Figure 3.3 gives an example of the spatial distribution of $(N1)_{60cs}$ values in a geotechnical model for embankment dam. Contours of $(N1)_{60cs}$ values and their values are plotted versus depth and position along the slope. The horizontal scale of variation was larger than the vertical scale to reflect the variability that arises naturally from alluvial deposition.

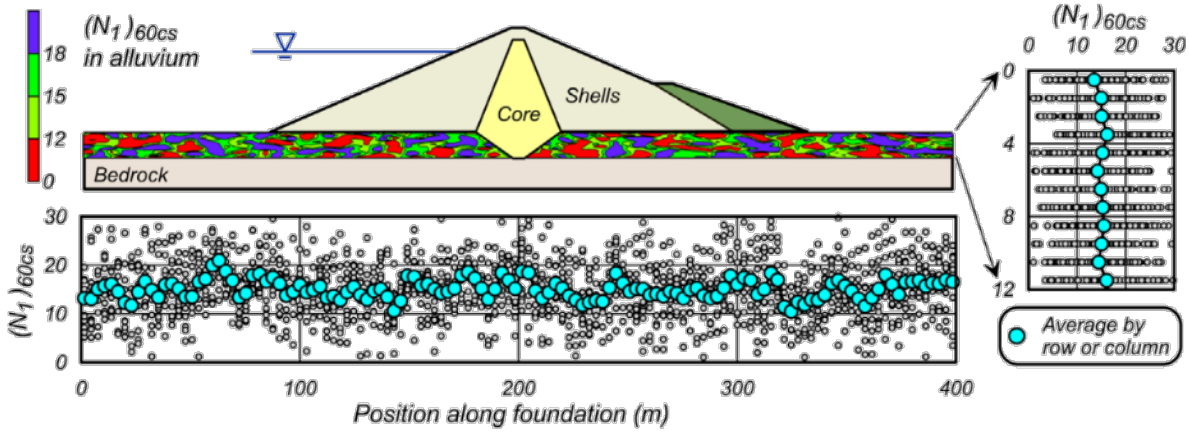


Figure 3.3 $(N1)_{60cs}$ values in the 12-m-thick liquefiable foundation alluvium (Boulanger and Montgomery 2016)

Individual $(N1)_{60cs}$ values mostly range from 5 to 25 and are randomly distributed with respect to depth and position along the slope. The horizontally averaged $(N1)_{60cs}$ values were between about 13.5 and 16.2 for all depths, while the vertically averaged $(N1)_{60cs}$ values were between 10.5 and 21.0 along the length of the model (Boulanger and Montgomery 2016). The "equivalent uniform" soil property, defined as the uniform model that produced the same deformation as the random field model, was found to be approximately the 30th percentile $(N1)_{60cs}$ value for loose sands, and about the 50th percentile value for dense sands. This was due to the deformations being concentrated in weaker zones in the loose models.

Another good example of modelling soil properties as random fields is the bearing capacity problem. Fenton and Griffiths (2001) first studied spatially random c-ϕ soils in a bearing capacity problem by modeling the soil parameters as random variables, performing Monte Carlo simulations on the random field realizations, and evaluating the extent to which spatial variability and cross-correlation in soil properties (c and ϕ) affect bearing capacity.

Subsequently, Fenton and Griffiths (2002) modeled the undrained shear strength of cohesive soil as a random field, and investigated how the spatial variation of undrained shear strength has an impact on the mean bearing capacity of a rough rigid strip footing through a parametric study. The spatial variability of the undrained shear strength is assumed to be characterized by a lognormal distribution with three parameters: mean (μ_{c_u}), standard deviation (σ_{c_u}) and spatial correlation length ($\theta_{\ln c_u}$). Figure 3.4 (a) and (b) together show how the mean bearing capacity factor (m_{N_c}) varies with $C.O.V._{c_u}$ and Θ_{c_u}, where $C.O.V._{c_u}$ is the coefficient of variation equal to σ_{c_u}/μ_{c_u}, and Θ_{c_u} is normalized spatial correlation length equal to $\theta_{\ln c_u}$/B, where B is the width of footing. It is clearly seen from Figure 3.4(a) that the mean bearing capacity factor is close to the deterministic value of 5.14 when $C.O.V._{c_u}$ is relatively small, but will decreases rapidly for higher $C.O.V._{c_u}$ values. Figure 3.5, on the other hand shows how the estimated coefficient of variation of the bearing capacity factor ($C.O.V._{N_c} = s_{N_c}/m_{N_c}$) varies with $C.O.V._{c_u}$ and Θ_{c_u}. s_{N_c} is the standard deviation of bearing capacity factor. As shown in Figure 3.5, $C.O.V._{N_c}$ increases steadily with $C.O.V._{c_u}$ for higher Θ_{c_u} values.

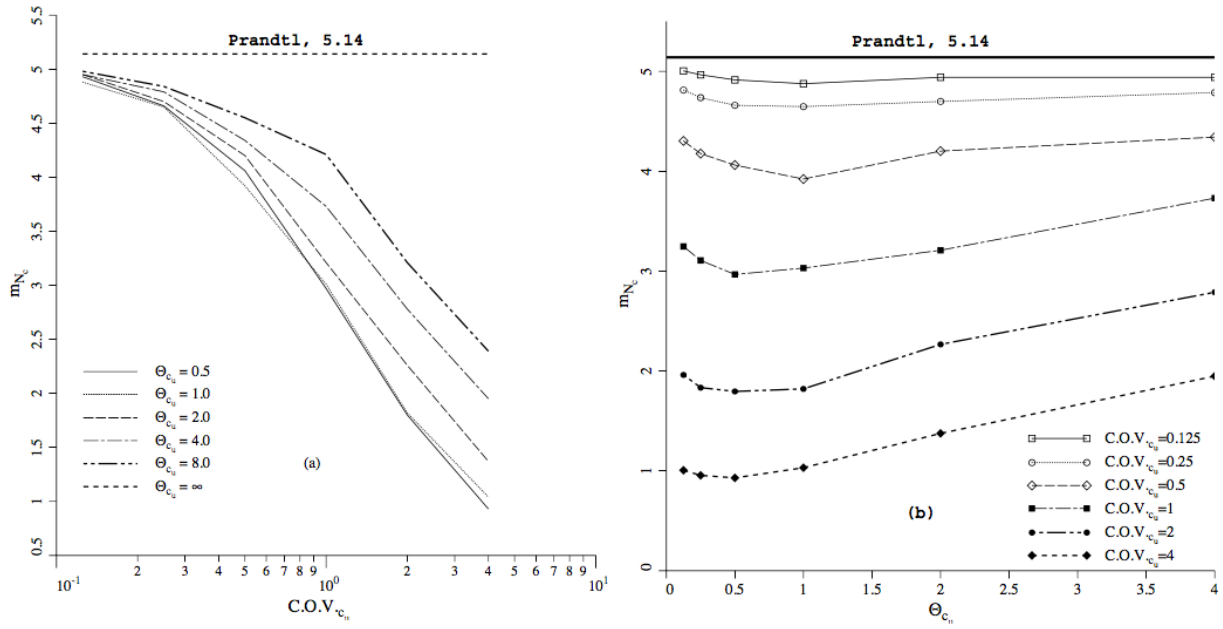


Figure 3.4 Estimated mean bearing capacity factor as a function of (a) $C.O.V._{c_u}$ (b) Θ_{c_u} (Fenton and Griffiths, 2002)

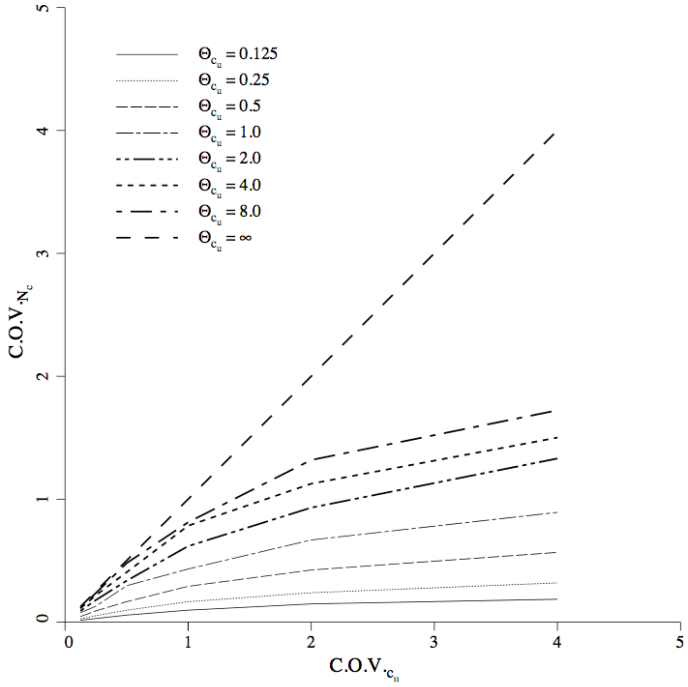


Figure 3.5 Estimated coefficient of variation of the bearing capacity factor as a function of $C.O.V._{c_u}$ and Θ_{c_u}(Fenton and Griffiths, 2002)

Fenton and Griffiths (2002) conclude that the mean bearing capacity of a footing on a soil with spatially varying shear strength is found to be always lower than that obtained for a uniform soil with strength equal to the mean value. This important observation is due to the linking up of weak elements beneath the footing, and shows that weak elements rather than strong elements tend to dominate the expected bearing capacity of a footing on spatially random soil.

3.3.2 Existing Methods of Numerically Computing Gaussian Random Fields

Realizations of Gaussian random fields are often needed to perform Monte Carlo simulations to assess the influence of soil variability on the statistics of an output of a problem (e.g., levee deformation). Methods for generating realizations from stationary homogeneous spatially correlated random fields include the spectral method (Mejía and Rodrígues-Iturbe 1974), the matrix decomposition method (Myers 1989), the turning-band method (Tompson et al. 1989), the local average subdivision method (Fenton and Vanmarcke 1990), and the sequential Gaussian simulation method (Johnson1987; Journel 1989). Among them, the matrix decomposition method is favored and used in this study.

The matrix decomposition method requires the user to define a discrete set of N points at which the random field will be sampled, and subsequently to construct a covariance matrix, C, quantifying the correlation between all of the sampling points. The size of C is therefore N x N. Cholesky decomposition is performed on the covariance matrix to obtain an upper, U, and lower, L, triangular matrix, which is shown in Eq. 3.4. A vector of correlated random variables, Y, is then computed by creating a vector, X, of uncorrelated random numbers from a unit normal distribution, computing LX, and subsequently multiplying by the standard deviation of the desired random field, σ, and adding the mean, μ

$$\boldsymbol{L}\boldsymbol{L}^{T} = \boldsymbol{C} \tag{3.4}$$

$$\boldsymbol{Y} = \sigma \boldsymbol{L} \boldsymbol{X} + \mu \tag{3.5}$$

Multi-dimensional random fields must be stationary, hence the correlation length must be isotropic. In cases where correlation is anisotropic, a coordinate transformation is required prior to computing C and performing Cholesky decomposition. Note that a random field with $\theta_x \neq \theta_y$ is not stationary because correlation is not a sole function of separation distance, but also the direction in which the distance is measured. The transformation given by Eq. 3.6 transforms an anisotropic two-dimensional random field into an isotropic, stationary two-dimensional random field, as illustrated in Figure 3.6.

$$X' = \frac{\theta_y}{\theta_x} X \tag{3.6}$$

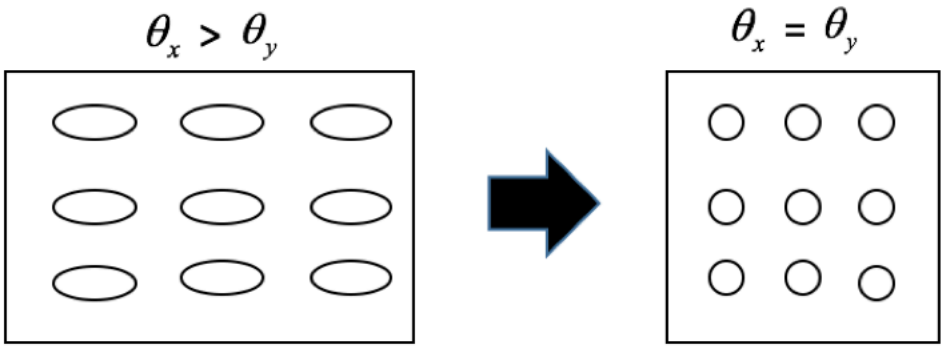


Figure 3.6 The approach to dealing with different correlation length in random field

3.4 Hybrid Method Combining Cholesky Decomposition with Kriging

Cholesky decomposition is regarded as an exact method, indicating that the simulated Gaussian random field follows an exact multivariate Gaussian distribution (Wood and Chan, 1994). While Cholesky decomposition provides a convenient means of obtaining spatially correlated random fields, it is computationally expensive when N becomes large. Sampling density must be selected to

adequately model the random field numerically. However, in many applications other factors may require N to be larger than it would need to be to model the random field. For example, in finite element modeling elements must be small relative to the domain to render accurate mechanical solutions. Generally, each element is assigned its own set of material constants, and sometimes tens of thousands of elements are included in a finite element simulation. This sampling density may be far in excess of what is required to accurately represent a particular random field.

On the other hand, we recognize that the sequential Gaussian method uses the Kriging technique to estimate each newly simulated node based on existing values of all previously simulated nodes, but the major issue of this technique is that the number of previously simulated nodes increases as the simulation progresses, which in turn makes it also computationally expensive. In such cases, we believe that computational complexity can be reduced by performing Cholesky decomposition on a subset of sampling points, and interpolating at the other sampling points using Kriging. A brief overview of Kriging is presented as follows.

Kriging (Krige 1951) is an interpolation technique extensively used in geostatistics (Cressie 1990; Fenton and Griffiths, 2008). The main purpose of Kriging is to give a best estimate of an unknown random variable at a location given known values at adjacent locations. Some commonly used linear Kriging methods include simple, ordinary and universal Kriging. Simple and ordinary Kriging require stationarity of the random field, while universal Kriging can be applied to smoothly varying non-stationary random fields. The ordinary Kriging method is adopted in this study.

In essence, the linear kriging method estimates a random variable at a desired point using a linear combination of the known data. For instance, a variable Z is unknown at a location of X_0, but the variable Z values are available at adjacent locations X_i. The Kriging technique estimates the value of Z at X_0 as a linear combination of the known values following Eq. 3.7, where n is the total number of

observation values, w_i are the n unknown weights associated with each observation point, and $\hat{Z}(X_0)$ is the value of Z estimated at location X_0.

$$\hat{Z}(X_0) = \sum_{i=1}^{n} w_i Z(X_i) \; with \; \sum_{i=1}^{n} w_i = 1 \tag{3.7}$$

The weights are computed by minimizing the variance at location X_0, which requires inversion of the covariance matrix at the known sampling points.

To my knowledge, no existing computational package exists for computing spatially correlated random fields using a combination of Cholesky decomposition and Kriging. For this reason, I have developed a new Python package that is documented at https://ucla-geotech-tools.readthedocs.io/en/latest/random_field_README.html. and can be installed using pip and run in any Python environment. Figure 3.7 and Figure 3.8 are the screenshots of the documentation page. This following section utilizes an example problem to describe the new algorithm, and to quantify the computational efficiency and interpolation errors associated with the hybrid algorithm.

» random_field Edit on GitHub

random_field

This function generates the random field using both Cholesky Decomposition method and Kriging

Installation

```
pip install ucla_geotech_tools.random_field
```

Functions

```
sort_nodes: sort the nodes to better separate cholesky nodes from kriging nodes
get_random_field: main function for generating the random field
get_C: get correlation matrix
get_chol_krig_nodes: group cholesky nodes and kriging nodes separately
get_C_chol_krig: get correlation matrix between cholesky nodes and kriging nodes
get_chol_field: generate the random field for cholskey nodes
get_krig_field: generate the random field for kriging nodes
```

Input Parameters for Main Function

```
x: x coordinates (list or array of x coordinates)
z: z coordinates (list or array of z coordinates)
mu: mean of random field
sigma: standard deviation of random field
theta_v: vertical scale of fluctuation
model: (optional) default is 0 for Guassian correlation matrix. Other intergers for Markovian c
```

Output Data

```
output : an array of values, and it has the same of order of the sorted nodes.
```

Usage

Figure 3.7 Screenshot of the documentation page 1

```
import ucla_geotech_tools.random_field as ugtrf
import matplotlib.pyplot as plt
import numpy as np

x = np.linspace(0.0,40,641)
z = np.linspace(0.0,10,161)
x,z = np.meshgrid(x,z)
x = x.reshape(np.prod(x.shape),) # create a vector of X coordinates
z = z.reshape(np.prod(z.shape),) # create a vector of Y coordinates

x,z = ugtrf.sort_nodes(x,z)      # sort nodes

RF = ugtrf.get_random_field(x=x,z=z,mu=50,sigma=10,theta_z = 1.25)

f,ax = plt.subplots(figsize=(10, 5))
cntr = ax.tricontourf(x,z,RF,20)
f.colorbar(cntr, ax=ax,shrink=0.5,aspect = 5)
ax.set_aspect('equal')
ax.set_frame_on(False)
```

Example

The Jupyter notebook example illustrates how to use the random_field package. Two examples are given in this Jupyter notebook, where random fields are generated using Gaussian and Markovian coorelation function, respectively. Feel free to modify the example to suit your own problem. Right click the link and use "Save link as".

random_field.ipynb

Figure 3.8 Screenshot of the documentation page 2

The example problem consists of a rectangular domain that is 40m long and 10m tall. Various sampling densities are utilized for this domain such that the total number of nodes (N) varies. Figure 3.9(a) displays all of the nodes that are used to perform Cholesky decomposition of the whole domain for N=451 (41x11 grid). The spacing of this grid of nodes is 1m in both horizontal and vertical direction. Figure 3.9(b), on the other hand, shows a sub-sampling method of grouping two sets of nodes for Cholesky decomposition and Kriging respectively. In this case, one of every four nodes in the horizontal and vertical directions are used for Cholesky decomposition while the remaining nodes are interpolated using Kriging. Therefore, Cholesky decomposition is only performed on a 14x 4 grid (N_{chol} = 56) while Kriging is performed on the rest of nodes (N_{krig} = 344).

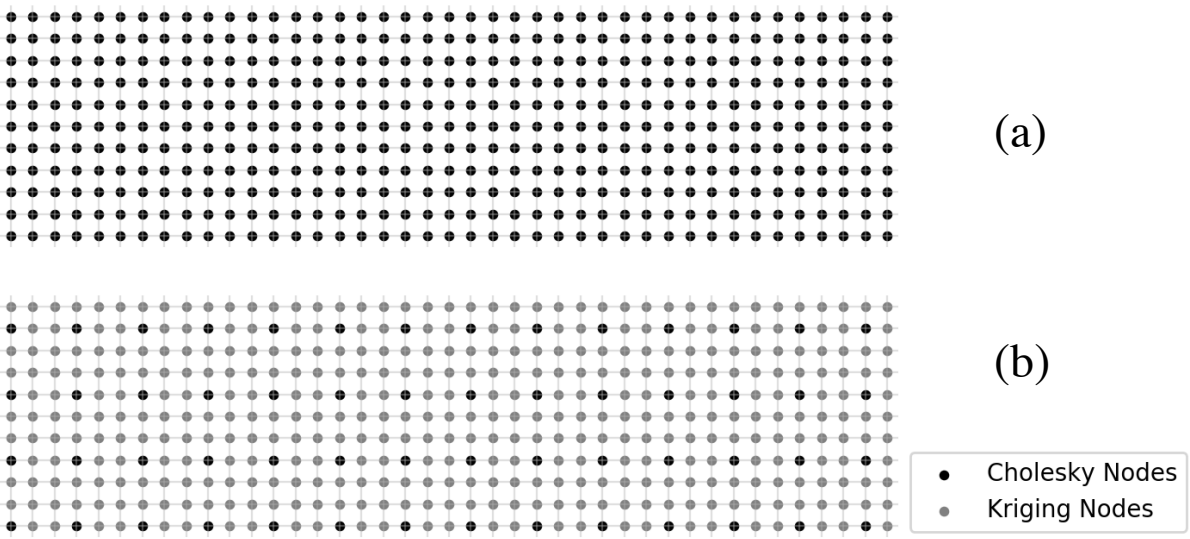


Figure 3.9 A sketch of nodes that are used in Cholesky decomposition and or Kriging

The key questions addressed here are (1) does the proposed hybrid method provide computational benefit compared with the full Cholesky decomposition method, and (2) if so, what are the errors associated with a particular selection of Kriging nodes and Cholesky nodes. Figure 3.11 illustrates two random field realizations for the example problem for N = 6601 (161 x 41 grid). The spacing of this grid of nodes in both horizontal and vertical direction is 0.25m. The random field represents undrained shear strength that is normally distributed with μ = 50 kPa, σ = 10 kPa, and follows a Gaussian spatial correlation function with $\theta_x = \theta_y$ = 1.25 m. Figure 3.10(a) represents a random field realization generated by performing Cholesky decomposition at all of the nodes (N_{chol} = 6601, N_{krig} = 0), while Figure 3.10(b) shows a case with N_{chol} = 756 and N_{krig} = 5845. The bottom image shows the error in Figure 3.10(b) relative to Figure 3.10(a). The random fields exhibit very similar characteristics and are visually indistinguishable. The mean error is 0.0%, and the standard deviation of the error is 2%.

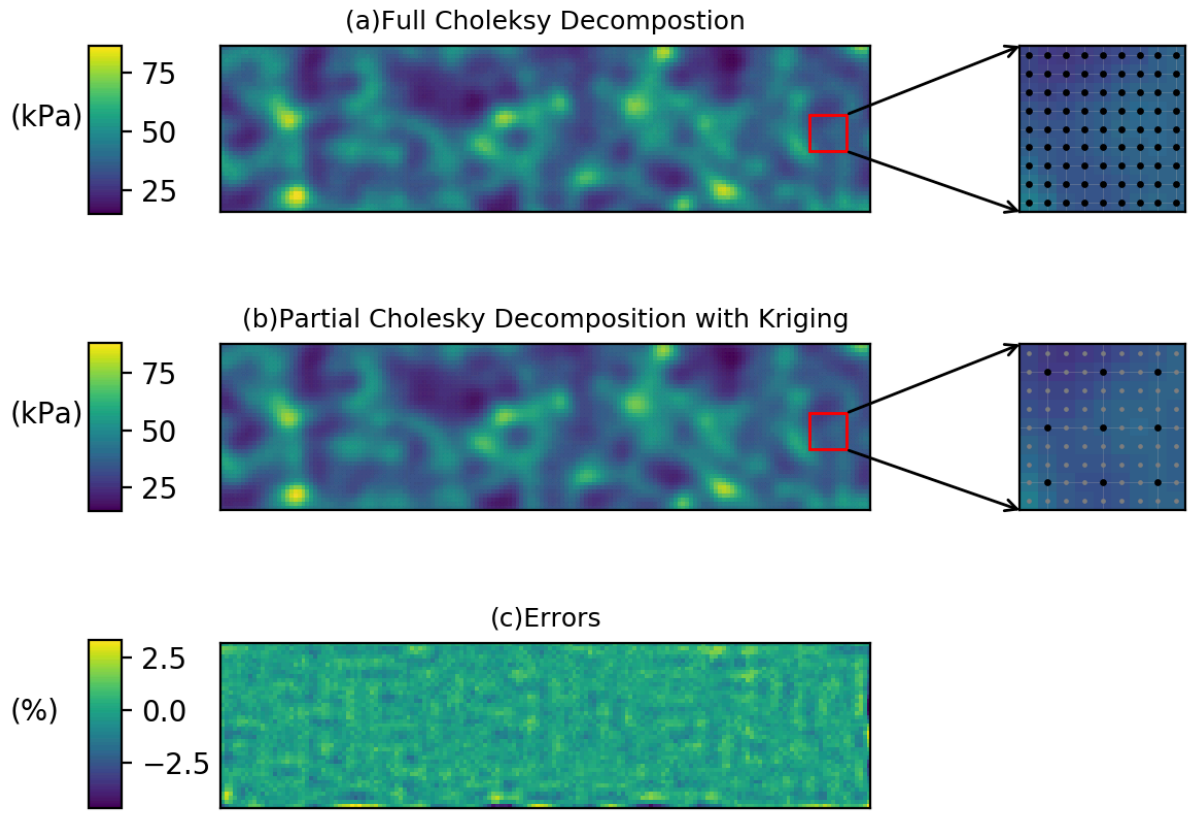


Figure 3.10 Spatially correlated random fields (a) using full Cholesky decomposition and (b) using Cholesky decomposition on a decimated set of grid points combined with Kriging interpolation (b), and (c) the differences between two random fields

Figure 3.10 has clearly shown that the hybrid algorithm can perform quite well. However, a key question is how many Cholesky decomposition points to use for a particular spatially correlated random field, and how many Kriging points to use. The algorithm is faster with more Kriging points, but errors are also larger. To quantify these errors and figure out what a proper sampling interval might be, the N=6601 domain is sub-sampled using various intervals quantified by the ratio $\Delta h_{chol}/\theta$, where Δh_{chol} is the horizontal and vertical sampling interval for the Cholesky decomposition nodes, and θ is the correlation length for the random field. This dimensionless quantity therefore represents Cholesky decomposition sampling frequency normalized by the scale of fluctuation, which is interpreted as a fundamental dimensionless parameter. Residuals, defined as the differences between two random

fields, are plotted versus sampling coarseness in Figure 3.11. As sampling coarseness increases, the standard deviation of the residuals increases as well, as indicated by the increase in the size of the box and whisker plots. Selection of an appropriate $\Delta h_{chol}/\theta$ is a judgmental call that depends on a specific application. I consider $\Delta h_{chol}/\theta = 0.6$ to be a reasonable value for many applications, and I adopt it as the baseline in the algorithm and use it throughout this dissertation.

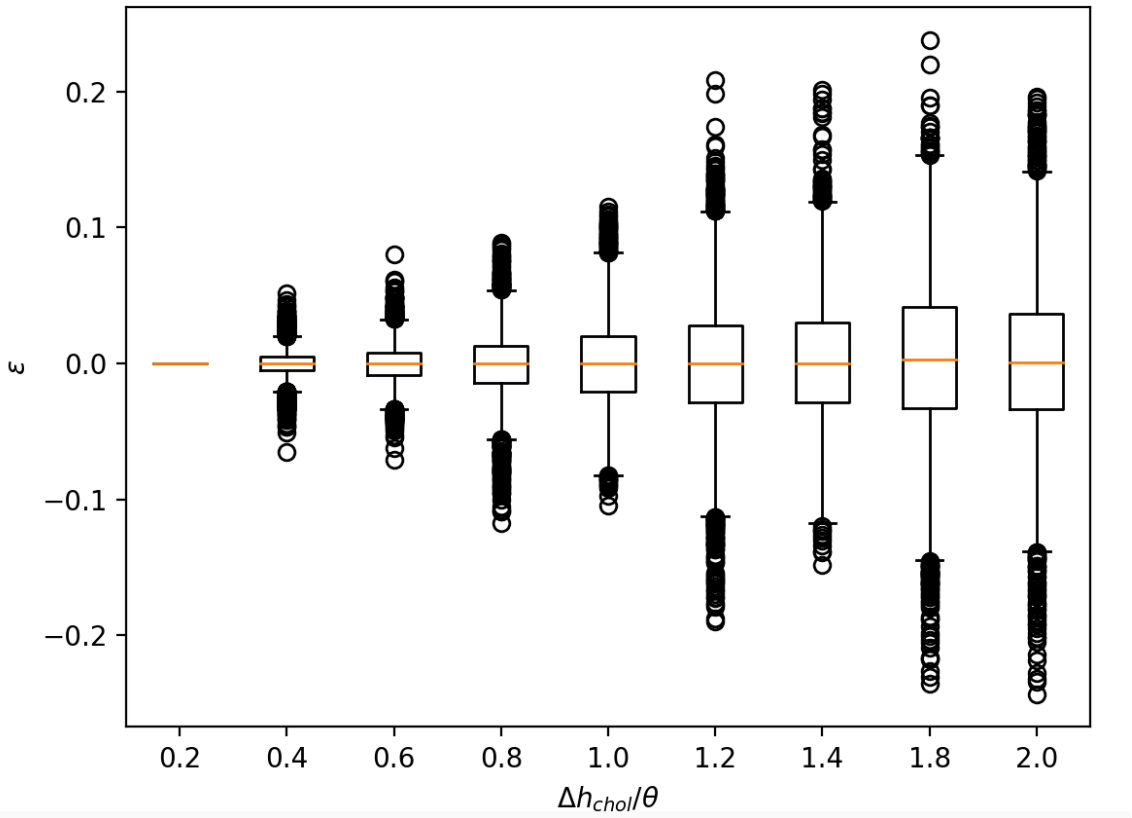


Figure 3.11 Residuals versus sampling coarseness

An assessment of the computational efficiency of the hybrid method is presented in Figure 3.12 for a total number of points N = [3000, 4000, 5000, 6000, 7000]. The horizontal axis is the ratio between the number of points used for Kriging versus total number of points (N_{krig}/N). The vertical axis is the normalized computation time, where t represents the computation time it takes to complete the procedure, while t_0 is the computation time required for full Cholesky decomposition. Figure 3.12

shows how the computation time decreases as the ratio of Kriging points relative to total number of points increases. As sampling coarseness increases, the computation time decreases significantly, particularly when a large number of total grid points are utilized. This trend appears to be consist in cases where total number of points are varied. Generally speaking, we conclude that this hybrid algorithm provides significant computational efficiency when there are more Kriging points being used. This algorithm will also work if the size of the correlation matrix becomes so large that full Kriging might not work. For cases where the total number of points is relatively small, it might not be necessary to use this algorithm when Cholesky decomposition method might have already satisfied the need.

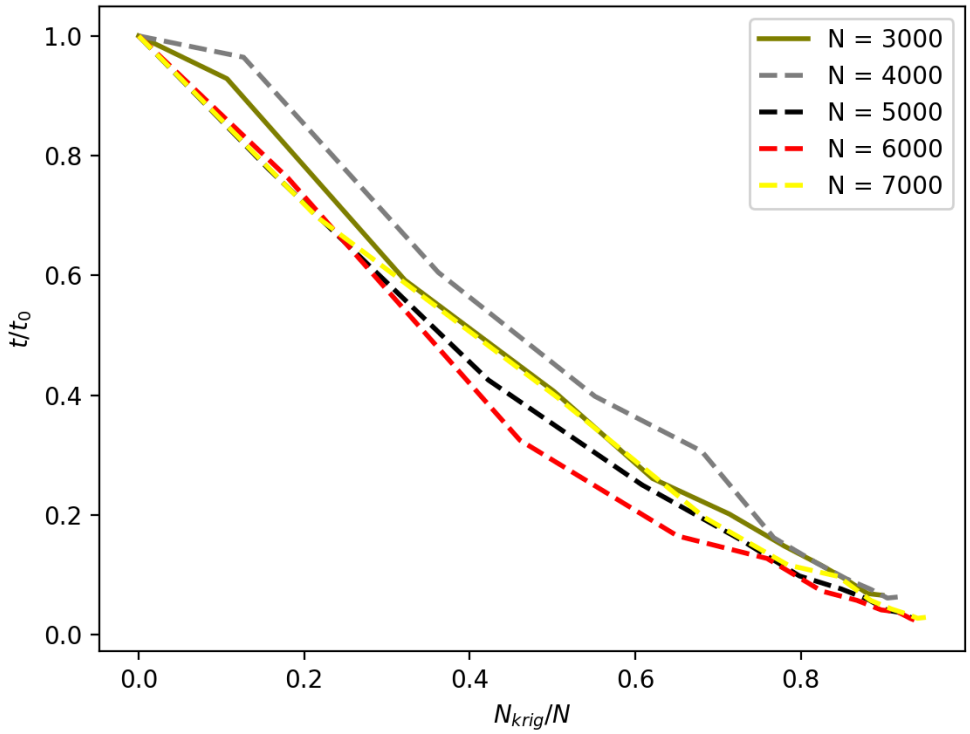


Figure 3.12 Influence of sampling coarseness on time required to develop spatially correlated random field

3.5 EXAMPLE APPLICATION OF RANDOM FIELD ALGORITHM TO A LEVEE

Slope stability is generally performed using limit equilibrium wherein a trial slip surface is postulated and divided into vertical slices, assumptions are made regarding inter-slice forces to render the problem statically determinant, and a factor of safety is computed. Many trial slip surfaces are evaluated, and the one that produces the lowest factor of safety is considered the most accurate and controls the design. A fundamental problem with limit equilibrium procedures is that the most critical failure surface might not be circular, non-circular search algorithms may be unable to identify the critical surface, and the resulting factor of safety may be over-estimated. This is particularly true for complicated geometries, and is also true when the soil strength is modeled as a spatially correlated random field. The problem is that the trial slip surface averages out the spatial variations in shear strength along the trial slip surface, whereas the actual failure mechanism tends to preferentially follow an interconnected network of weak soil.

In this study, the finite element method is adopted as an alternative to limit equilibrium procedures. The finite element modeling platform RS2 is utilized for this purpose. The output of an RS2 analysis is a field of deformations and stress, and not a factor of safety value required to evaluate slope stability. To evaluate the factor of safety, RS2 uses the Shear Strength Reduction (SSR) method, with the output being a critical shear strength reduction factor (SRF). This critical SRF is equivalent to the factor of safety in limit equilibrium analysis. The Shear Strength Reduction method follows these steps:

1. The strength parameters are reduced by a trial SRF, and stresses and deformations are computed.

2. This process is repeated for different SRF values

3. The critical SRF is taken as the SRF value at the point where the model becomes unstable (i.e., deformations exceed a tolerance).

An example is utilized to illustrate the strength reduction procedure (Figure 3.13). The dimensions of the levee indicated in the figure are in units of meters. The soil is assumed to have a mean undrained shear strength of S_u = 40kPa and is assumed to be normally distributed with a standard deviation of 10kPa.

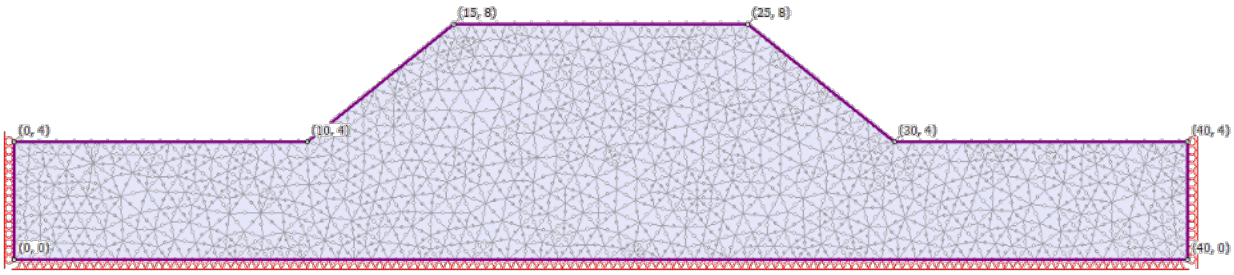


Figure 3.13 RS2 finite element model of a levee's cross section

Spatial correlation is assumed to follow a Gaussian correlation function with θ_x = 2.5m and θ_y = 0.25m. An individual realization may result in a mean value for undrained shear strength that is higher or lower than the mean value of the population. The realization was therefore adjusted so that the mean value of the undrained shear strength is 40 kPa. The undrained shear strength values are then input to RS2 as a grid of X, Y, S_u points. A realization of undrained strength arising from this procedure is shown in Figure 3.14. In addition to the random field, the analysis was repeated with uniform soil strength s_u = 40kPa for comparison.

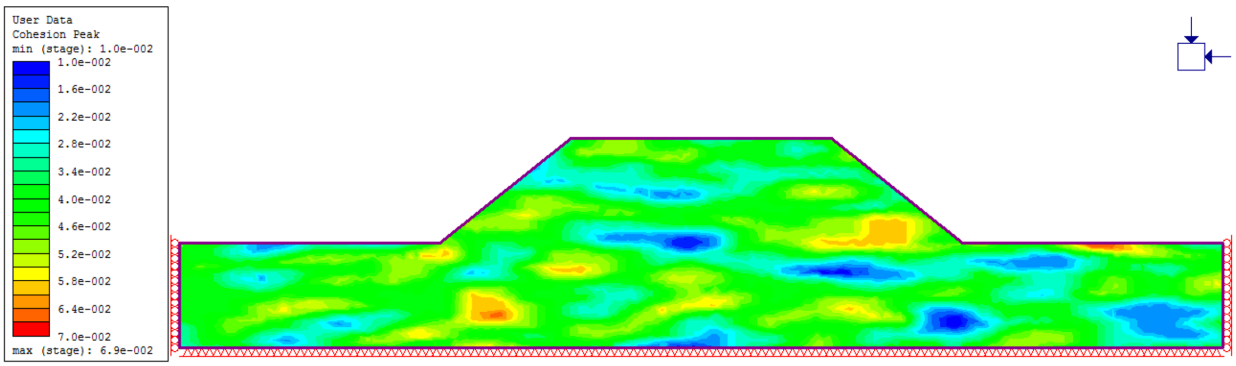


Figure 3.14 A contour plot of the discrete undrained shear strength

The model with uniform undrained shear strength produces a critical SRF of 1.96. As illustrated in Figure 3.15, the contours of maximum shear strain indicate that the deformations are symmetric in this case, which makes sense because the undrained shear strength is uniform and therefore the model is symmetric. The critical failure zone, corresponding to locations with high shear strain, is almost circular, which implies that limit equilibrium analysis with circular slip surfaces would likely to obtain a similar value for factor of safety.

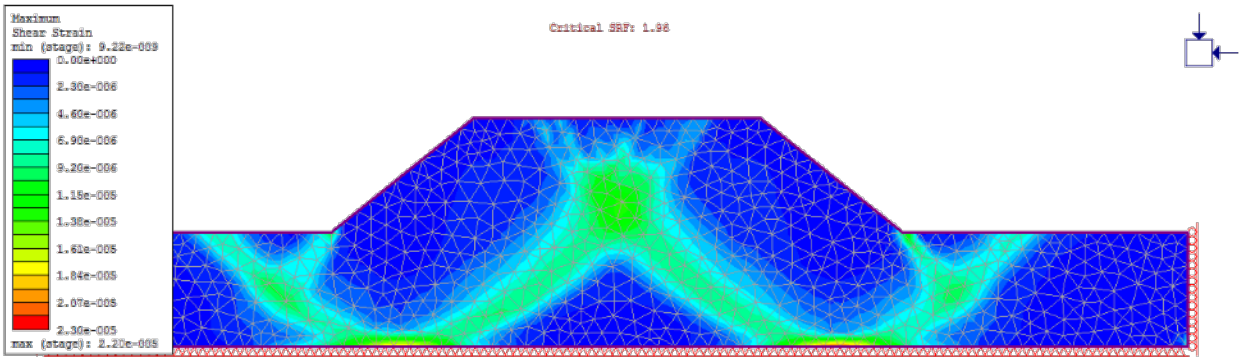


Figure 3.15. Uniform model result of maximum shear strain

The model with undrained shear strength modeled as a spatially correlated random field has a critical SRF of 1.64, which is significantly lower than the value of 1.96 obtained for the uniform model. The contours of maximum shear strain in Figure 3.16 indicate that a complicated failure mechanism occurs along two weak zones; one at an elevation near the base of the levee, and one tangent to the bottom of the model. The shallower failure surface occurs through an inter-connected network of weak soil, as

illustrated by the blue zones in Figure 3.14. This outcome demonstrates that spatial variability decreases the factor of safety, rendering a structure less safe than a model using uniform mean properties. In practice, undrained strength is often conservatively set to be less than the mean value, but there is no way to know a priori how conservative a particular selection of undrained strength is. Furthermore, selection of an appropriate "equivalent uniform" undrained strength depends on the scales of fluctuation. I therefore conclude that incorporating spatial variability is a crucial aspect of modeling the problem properly. The failure surfaces in Fig. 3.16 are also relatively circular, indicating that a limit equilibrium method would work well for this particular problem.

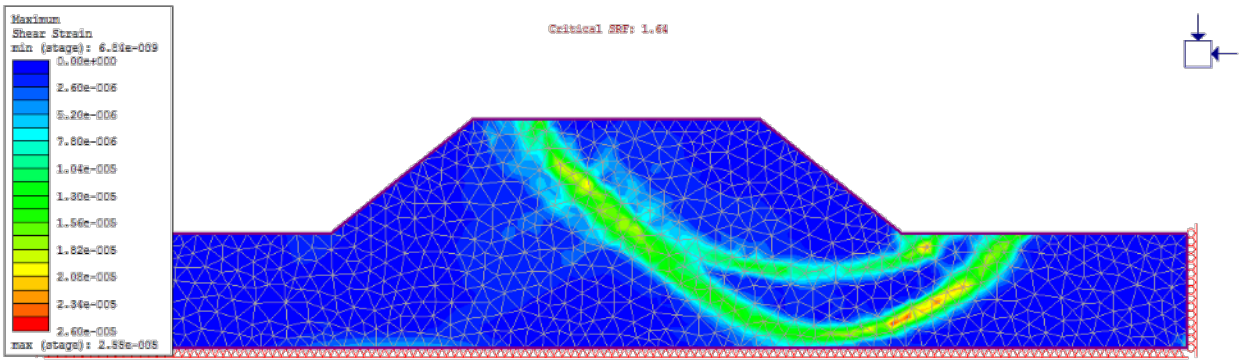


Figure 3.16. Model with discrete undrained strength results

3.6 VALIDATION OF RANDOM FIELD GENERATOR USING BEARING CAPACITY PROBLEM

The undrained bearing capacity problem studied by Fenton and Griffiths (2002) is utilized here to validate the random field generator tool. For undrained loading conditions with s_u = constant and ϕ_u = 0, the dimensionless bearing capacity factor N_c is defined as:

$$N_c = q_f / S_u \tag{3.8}$$

where q_f is the bearing capacity and s_u is the undrained shear strength of the soil beneath the footing. For a homogeneous soil with a uniform undrained shear strength, N_c equals 5.14 (Prandtl solution). As demonstrated by Fenton and Griffiths (2002), if undrained strength is modeled as a spatially correlated random field, N_c will change based on how the random field is spatially varied.

We choose to conduct this finite element analysis using OpenSees. A sketch of the simple vertical bearing capacity problem is shown in Figure 3.17. The model is 40m long and 10m tall, and a rigid 2m footing rests at the surface. The mesh consists of 400 four node quad elements in total, with 10 rows and 40 columns. The soil strength is modeled using a Drucker Prager material model. A vertical displacement of 0.2m is incrementally applied to the 2m strip footing vertically until the soil "fails". Our preliminary study indicates that 0.2m of vertical displacement is adequate to cause the bearing pressure to reach a limiting value. Uniform soil properties were first applied to all the elements with an undrained shear strength of 40kPa. The bearing factor was computed to be 5.2, which is in reasonable agreement with closed-form solutions. The bearing pressure is plotted against the vertical displacement of the footing in Figure 3.18.

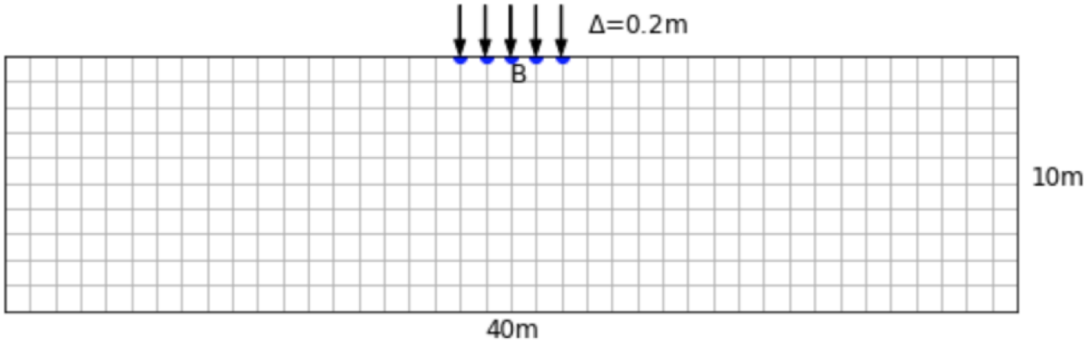


Figure 3.17 A sketch of bearing capacity problem with the finite element mesh

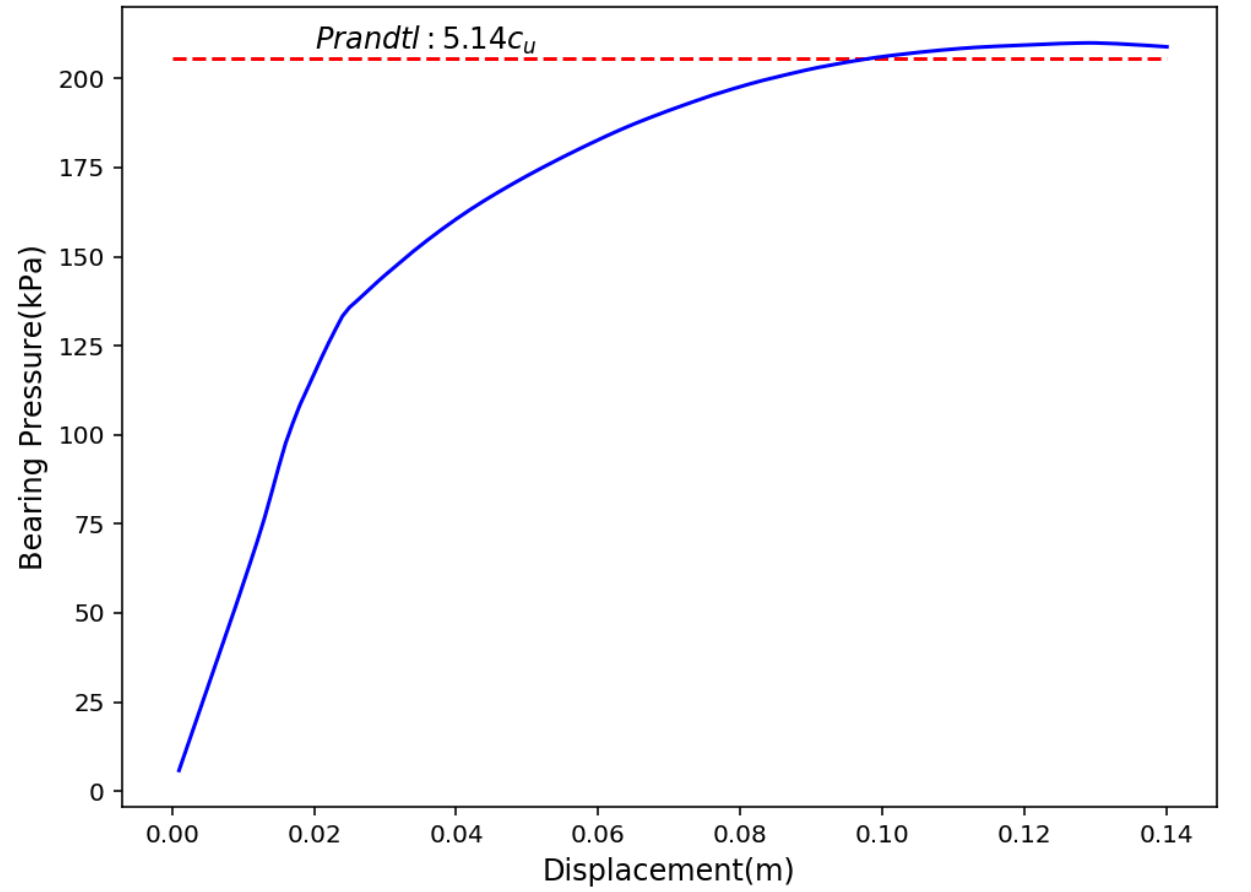


Figure 3.18 Bearing pressure versus displacement of the footing

The soil strength was then modeled as a spatially correlated random field and the mean bearing capacity factor was computed for 1000 realizations of undrained strength profiles. For each realization, the undrained strength is modeled as a lognormally distributed random variable with given mean (40kPa) and for various standard deviations. One realization of undrained shear strength profile is shown as an example in Figure 3.19. The profile might look a bit choppy mostly because the element size is relatively big. This is the same element size adopted by Fenton and Griffiths, so it is utilized here in this validation study. For each case, the mean value and the standard deviation of bearing factor based on the simulation results of 1000 realizations was obtained. Fenton and Griffiths (2003) varied both the correlation length (θ) and the COV of the undrained strength ($COV_{S_u} = \sigma_{S_u}/\mu_{S_u}$). To directly compare with their results, the same values of θ/B and COV_{S_u} are used here and are shown as follows:

θ/B = 0.125, 0.25, 0.5, 1.0, 2.0, 4.0, 8.0

COV_{S_u} = 0.125, 0.25, 0.5, 1.0, 2.0, 4.0

These turned out to be a large number of simulations that were performed on Stampede2 at the University of Texas, Austin through the DesignSafe cyberinfrastructure (Rathje et al. 2017). Parallel computing via OpenSeesMP was adopted to facilitate the process. OpenSeesMP is an OpenSees interpreter intended for parallel machines to perform parametric studies of large number of finite element simulations (McKenna 2007). The user will have control on different work that each parallel computer performs. All the simulations were successfully accomplished using OpenSeesMP.

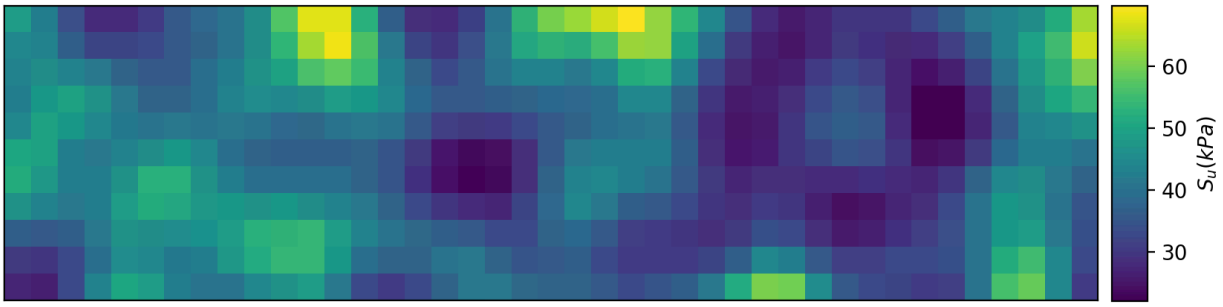


Figure 3.19 One realization of undrained shear strength profile

Figure 3.20 shows how the estimated mean bearing capacity factor varies with θ/B and COV_{S_u}. Solid lines in Figure 3.20 represented our simulation results, while the data points are from Fenton and Griffiths (2003). Good agreement is observed between the results of this study and their results, which I consider to provide validation of both the random field tool and my ability to run nonlinear simulations in OpenSees. The results show that the bearing factor decreases as COV increases, and the rate of decrease is more significant when correlation length is shorter. Furthermore, the influence of correlation length increases as COV increases (i.e., the lines become more separated). However, the results for the shortest correlation lengths are very similar. One explanation is that as the spatial

correlation length decreases, the weakest path becomes increasingly tortuous and its length correspondingly longer, which makes weakest path start to look for shorter routes cutting through higher strength material (Fenton and Griffiths, 2003).

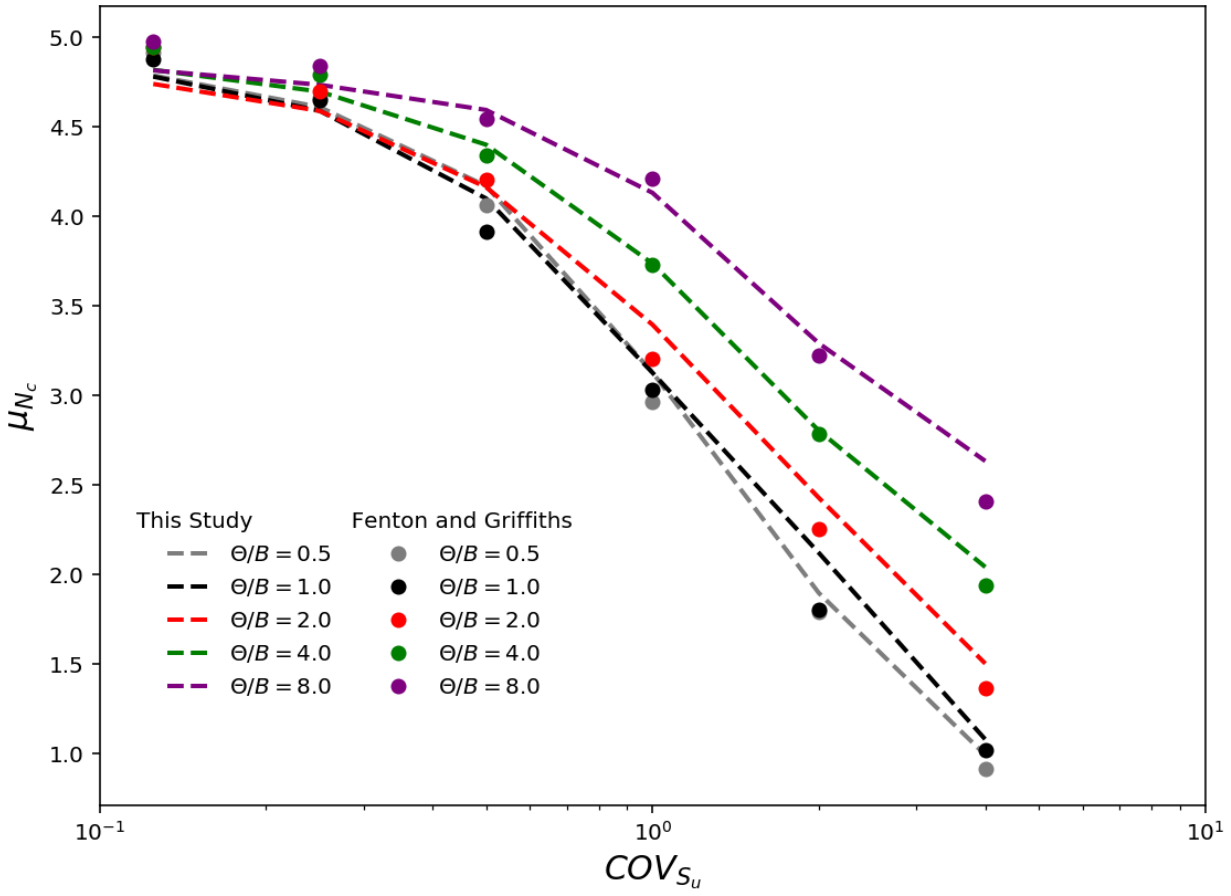


Figure 3.20 Mean bearing factor as a function of θ/B and $C.O.V_{S_u}$

Figure 3.21 shows that the coefficient of variation of the bearing factor increases as the coefficient of variation of undrained strength increases. When θ/B is small, COV_{N_c} is fairly small and not very sensitive to COV_{S_u}. However, when θ/B is higher, COV_{N_c} increases significantly. Our results again exhibited great extent of agreement with results from Fenton and Griffiths (2003) shown as points in Figure 3.21.

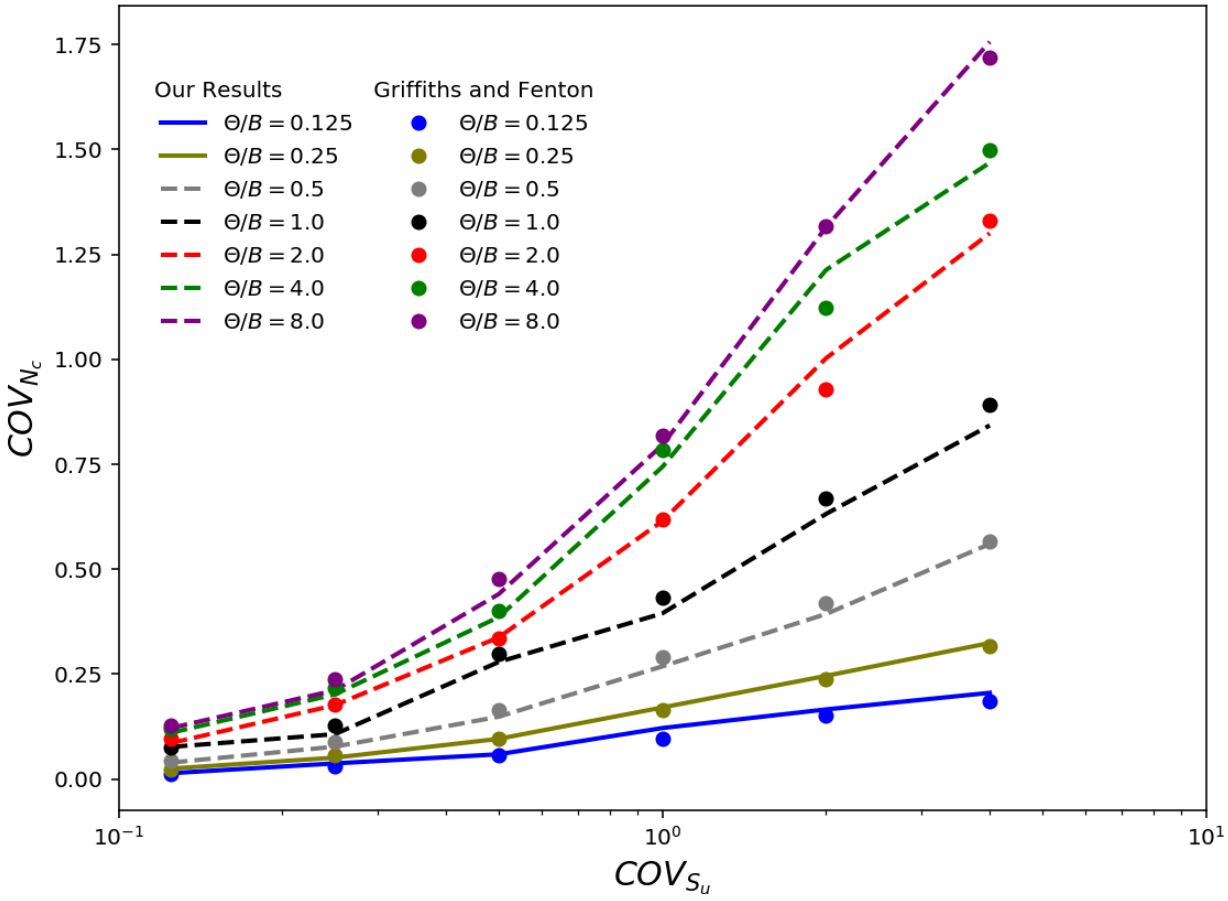


Figure 3.21 Coefficient of variation of the bearing factor as a function of θ/B and $C.O.V_{S_u}$

3.7 SUMMARY

Natural soils are rarely homogeneous, and heterogeneity is commonly found in soil structure. Soil heterogeneity can be classified into two types, which come from two sources. One source is lithological heterogeneity, and the other source is the so-called inherent spatial soil variability. The inherent spatial soil variability is often characterized and incorporated through random field implementation. And the lithological variability can be handled by creating separate random fields for each separate soil layer.

The random field can generally be described by its field mean, variance and spatial correlation. Regarding the spatial correlation, it is important to understand correlation length and correlation model. We usually consider spatial correlation length to be the distance within which points are significantly correlated, and the correlation length in the horizontal direction is often different from the correlation length in the vertical direction. The correlation length is also used in correlation models, which determines the correlation between two points depending on their relative positions. Some of the commonly used correlation models include Gaussian correlation model, Markovian correlation model (exponential correlation model).

Despite various methods of generating Gaussian random field, we recognize that some of the traditional methods have their own limitations. Therefore, a new algorithm of combining both Cholesky decomposition method and Kriging interpolation technique is proposed. This new algorithm was able to save the computational cost and render enough precision by carefully selecting relevant parameters.

One example of finite element analysis of a simple levee model is analyzed in order to examine how spatial variability is affecting the system stability. A spatially correlated random field of undrained shear strength generated by the proposed algorithm is implemented into the finite element analysis. The simulation result indicates that spatial variability decreases the factor of safety, rendering a structure less safe than a model using uniform mean properties, which concludes that incorporating spatial variability is a crucial aspect of modeling the problem properly. Subsequently, a comparison study with Fenton and Griffiths (2003) also validates the proposed algorithm.

4 VALIDATION OF ANALYSIS USING CASE HISTORIES IN JAPAN

4.1 INSTRUMENTED SITES

Japanese researchers have done substantial amount of work documenting the performance of their major federal flood control levees following earthquakes. Following earthquakes, the levees are inspected by technicians and any instances of cracking or other damage is documented. In this way, they have a rich archive of a range of field performance for a wide range of shaking conditions. In addition, several of these levees are instrumented. For instance, the Ministry of Land, Infrastructure, Transport and Tourism (MLIT) in Japan has established a national network of instrumented infrastructure. As of 2013, 56 levee sites at different locations in Japan were instrumented and monitored with a combination of triaxial accelerometers and in some cases piezometers (Zimmaro et al. 2019). Triaxial accelerometers at the surface and downhole are often installed at these levee sites, and pore pressure transducers, when present, are typically installed in liquefiable levee fill. Whenever an earthquake is recorded at these sites, the data are usually recovered by technicians either shortly after earthquake or during their monthly visits. Considering the fact that much of the data are locally stored in MLIT field offices on tapes and disks and have not been compiled, it would seem impractical to fully document all recorded data. Instead, Zimmaro et al. 2019 presented a database documenting instrumental data and related field performance data for seven prioritized levee arrays in Japan.

Zimmaro et al. 2019 proposed two criteria to prioritize whether information from a levee site is likely to be useful for engineering analysis, such as for validation studies of the types of finite element analyses discussed in Chapter 2. One is that there must be at least one event with strong shaking that

occurred at the levee site. The other one is that the site also experienced events with relatively weak shaking, which would be useful for the study of linear site response and potentially defining levee performance over the range of shaking intensity of engineering interest. Based on these two criteria, seven sites were identified and are shown in Figure 4.1 along with all other instrumented levee sites that existed in Japan.

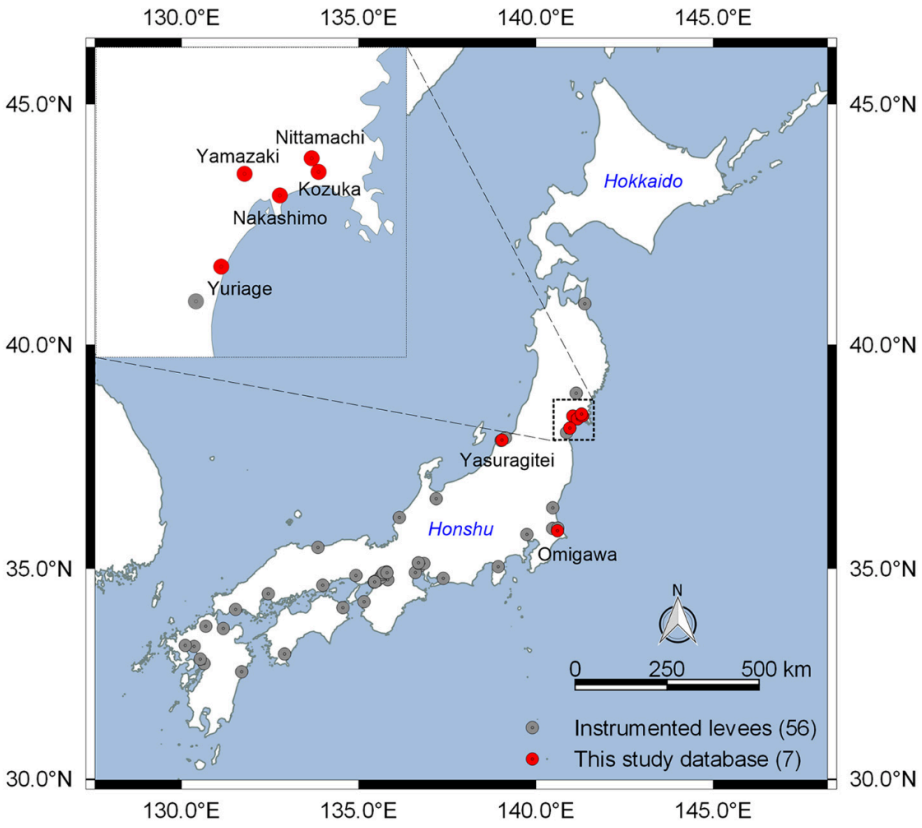


Figure 4.1 Map view of instrumented levees in Japan (Zimmaro et al. 2019)

Five events with strong shaking were identified and are listed rows 1 to 5 of Table 4.1. Events with relatively weak ground motion are listed in rows 6 to 25. All seven selected levee sites are instrumented with multiple accelerometers. Table 4.2 lists the identification number of sensors installed at each site, sensor locations and the number of recorded events. Only the Nakashimo site is instrumented with a pore pressure transducer. Table 4.3 also lists the type of accelerometer installed at each site as well as

available geotechnical data. As shown in Table 4.3, three levee sites (Nakashimo, Yamazaki and Kozuka) have detailed cross-sections along with boring logs and shear wave velocity profiles. Therefore, these three sites are more useful for validating the finite element analysis procedure.

Table 4.1 List of earthquakes recorded at the instrumented levee sites (Zimmaro et al. 2019)

Event number (ID)	Earthquake name	Timestamp	Moment magnitude (**M**)	Hypocentral depth (km)	Epicenter location
1	Near the west coast of Honshu	2004-10-23 08:56:00 UTC	6.6	16	37.226°N 138.779°E
2	Near the east coast of Honshu	2005-08-16 02:46:28 UTC	7.2	36	38.276°N 142.039°E
3	Eastern Honshu	2008-06-13 23:43:45 UTC	6.9	7.8	39.030°N 140.881°E
4	Tohoku-oki mainshock (near the east coast of Honshu)	2011-03-11 05:46:24 UTC	9.1	29	38.297°N 142.373°E
5	Near the east coast of Honshu	2011-04-07 14:32:43 UTC	7.1	42	38.276°N 141.588°E
6	Near the west coast of Honshu	2004-10-23 09:34:04 UTC	6.3	10	37.318°N 138.808°E
7	Near the east coast of Honshu	2005-04-10 22:22:15 UTC	5.9	43	35.604°N 140.401°E
8	Near the east coast of Honshu	2005-12-16 18:32:16 UTC	6.0	42.9	38.506°N 141.900°E
9	Eastern Honshu	2008-07-23 15:26:19 UTC	6.8	108	39.802°N 141.464°E
10	Near the east coast of Honshu	2010-03-14 08:08:03 UTC	6.5	32	37.745°N 141.590°E
11	Near the east coast of Honshu	2010-06-13 03:32:57 UTC	5.9	27	37.372°N 141.625°E
12	Near the east coast of Honshu	2011-03-09 02:45:20 UTC	7.3	32	38.435°N 142.842°E
13	Eastern Honshu	2011-03-11 08:40:56 UTC	5.9	39.5	37.447°N 140.984°E
14	Near the east coast of Honshu	2011-03-11 11:36:40 UTC	6.6	25.7	39.241°N 142.463°E
15	Near the east coast of Honshu	2011-03-24 08:21:00 UTC	5.8	27	39.079°N 142.084°E
16	Near the east coast of Honshu (1)	2011-03-25 11:36:24 UTC	6.2	39	38.772°N 141.880°E
17	Near the east coast of Honshu (2)	2011-03-27 22:23:58 UTC	6.2	19	38.415°N 142.011°E
18	Near the east coast of Honshu	2011-03-31 07:15:30 UTC	6.0	42	38.922°N 141.821°E
19	Near the east coast of Honshu (1)	2011-07-23 04:34:24 UTC	6.3	41	38.898°N 141.815°E
20	Near the east coast of Honshu (2)	2011-07-24 18:51:25 UTC	6.3	40	37.730°N 141.390°E
21	Near the east coast of Honshu (3)	2011-07-30 18:53:50 UTC	6.3	38	36.942°N 140.955°E
22	Near the east coast of Honshu (3)	2011-08-19 05:36:33 UTC	6.2	47	37.671°N 141.652°E
23	Near the east coast of Honshu	2012-06-17 20:32:20 UTC	6.3	36	38.919°N 141.831°E
24	ESE of Ishinomaki	2013-08-04 03:28:50 UTC	5.8	56	38.213°N 141.862°E
25	NE of Namie	2013-05-18 05:47:59 UTC	6.0	39	37.739°N 141.471°E

Table 4.2 Instrumentation configuration for each levee site (Zimmaro et al. 2019)

Levee site (site ID)	Sensor ID	Sensor type[a]	Sensor location[b]	Number of recorded events
Nakashimo (CG8274208)	CG827420801a	TA (up, 360, 090)	Bench (–10 m)	2
	CG827420802a	TA (up, 360, 090)	Bench (–5 m)	2
	CG827420803a	TA (up, 360, 090)	Bench	2
	CG827420804a	TA (up, 360, 090)	Crest (–13 m)	4
	CG827420805a	TA (up, 360, 090)	Crest	4
	CG8274208SCa	Piezometer	Crest (–8.94 m)	1
Yuriage (CG8274109)	CG827410901a	TA (up, 360, 090)	Crest[c]	1
	CG827410902a	TA (up, 360, 090)	Bench[c] (–10 m)	1
	CG827410903a	TA (up, 360, 090)	Bench[c] (–20 m)	1
Nittamachi (CG8274211)	CG827421101a	TA (up, 360, 090)	Crest (–77 m)	19
	CG827421102a	TA (up, 360, 090)	Crest	19
	CG827421103a	TA (up, 360, 090)	Crest (–7.8 m)	19
	CG827421104a	TA (up, 360, 090)	Crest	19
	CG827421105a	TA (up, 360, 090)	Crest (–8.3 m)	19
	CG827421106a	TA (up, 360, 090)	Crest	19
Yamazaki (CG8274210)	CG827421001a	TA (up, 360, 090)	Crest	10
	CG827421002a	TA (up, 360, 090)	Bench	10
	CG827421003a	TA (up, 360, 090)	Bench (–22 m)	10
Kozuka (CG8274209)	CG827420901a	TA (up, 360, 090)	Toe	11
	CG827420902a	TA (up, 360, 090)	Crest	11
	CG827420903a	TA (up, 360, 090)	Toe (–13 m)	11
	CG827420904a	TA (up, 360, 090)	Toe (–6 m)	11
	CG827420905a	TA (up, 360, 090)	Free-field area (landside)	1
Omigawa (CG8372103)	CG837210301a	TA (up, 360, 090)	Free-field area[c] (landside –10 m)	1
	CG837210302a	TA (up, 360, 090)	Free-field area[c] (landside –5 m)	1
	CG837210303a	TA (up, 360, 090)	Free-field area[c] (landside –1.5 m)	1
	CG837210304a	TA (up, 360, 090)	Free-field area[c] (landside –1.5 m)	1
	CG837210305a	TA (up, 360, 090)	Crest (–15 m)	1
	CG837210306a	TA (up, 360, 090)	Crest (–10 m)	1
	CG837210307a	TA (up, 360, 090)	Crest (–1.5 m)	1
Yasuragitei (CG8472701)	CG847270101a	TA (up, 360, 090)	Crest[c]	2
	CG847270102a	TA (up, 360, 090)	Free-field area[c] (landside –11.5 m)	2
	CG847270103a	TA (up, 360, 090)	Free-field area[c] (landside –11.5 m)	2
	CG847270104a	TA (up, 360, 090)	Free-field area[c] (landside)	2

[a]TA: triaxial accelerometers, numbers in parentheses indicate orientations (up/down, horizontal azimuths)

[b]Sensor locations for Nakshimo, Yamazai and Kozuka sites are shown in the following sections

[c]Based on sensor configuration description

Table 4.3 List of data available at seven sites (Zimmaro et al. 2019)

Name	Latitude/longitude	River system	Date of installation	Instrument type[a]	Recorded events (IDs)	Geotechnical data
Nakashimo	38.3814°N 141.1686°E	Naruse	March 1997	Acc: K2	2, 4, 9, 10	BSV
Yamazaki	38.4433°N 141.0395°E	Yoshida	April 1981	Acc: K2	2–5, 9, 11, 13, 17, 20, 21	BSV
Kozuka	38.4489°N 141.3099°E	Old Kitakami	March 1993	Acc: K2	3, 4, 9–12, 15, 16, 22, 24, 25	BSV
Nittamachi	38.4881°N 141.2848°E	Old Kitakami	March 2000	Acc: K2	2–5, 8–12, 14, 15, 17–20, 22–25	GS
Yuriage	38.1769°N 140.9543°E	Natori	February 1999	Acc: KSP-3K	2	NA
Omigawa	35.8675°N 140.6057°E	Tone	March 1999	Acc: KD01	7	DS
Yasuragitei	37.9120°N 139.0399°E	Shinano	March 1990	Acc: K2	1, 6	NA

NA: no data; GS: generalized cross-section but no boring logs; BSV: boring logs cross-section, and VS profiles; DS: detailed cross-section

[a]Instrument types listed here are those installed on the dates of the recordings listed in Table 4.1, which may not match the originally installed instrument types. K2:Kinemetrics Altus K2 triaxial accelerometers; KSP-3K: KD01: Katsushima-Datol 2001 triaxial accelerometer

4.2 NAKASHIMO SITE

4.2.1 Site Conditions

Figure 4.2 shows a detailed cross-section for the Nakashimo site. The levee fill was found to be mostly sandy soils. The two clay layers are approximately 2-3m in thickness. The ground water table was found to be approximately at the base of the levee fill at the time of site investigation trip. There are five accelerometers installed at this site, and one pore water pressure transducer that is located within a sandy layer below the crest of the levee. The center sand layer is expected to be liquefiable based on its location below the ground water and lack of plastic fines.

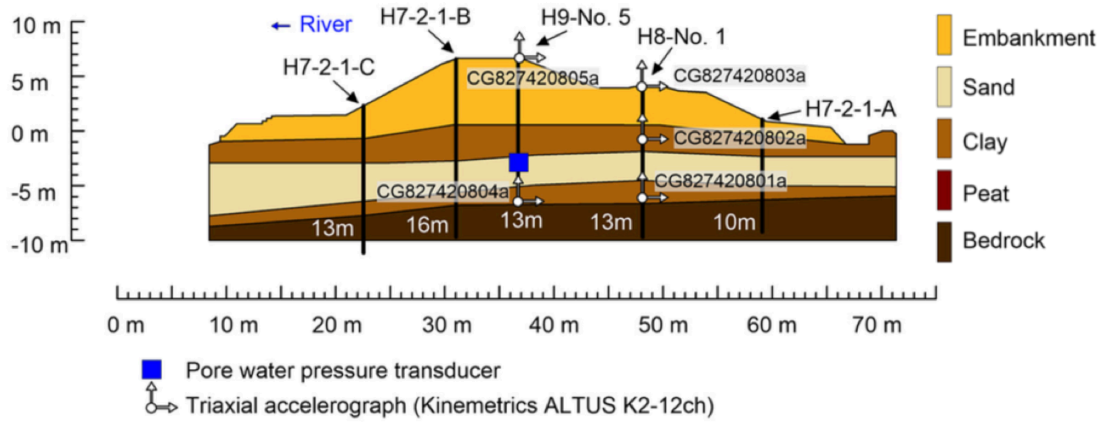


Figure 4.2 Cross-section, stratigraphy under the levee, boring log locations and sensors locations at Nakashimo site (Zimmaro et al. 2019)

As also shown in Figure 4.2, the Nakashimo site has multiple boring logs available across the cross-section. Figure 4.3 shows the blow counts for each existing boring log at this site, which are useful for estimation of relative density and soil state as required for the specification of material properties used in finite element modeling. Two shear wave velocity profiles are also available at this site. The locations are approximately at Borehole H9-No.5 and Borehole H7-2-1-A. These two profiles were obtained using suspension logging and are shown in Figure 4.4. The shear wave velocity profile is

directly related to the small-strain shear modulus which is another input parameter for the material model.

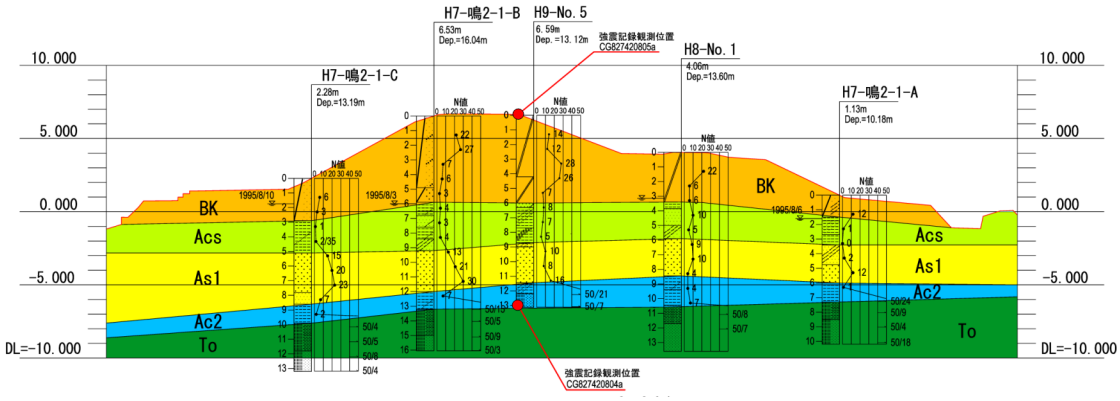


Figure 4.3 Detailed blow counts profile at boring log locations of Nakashimo site

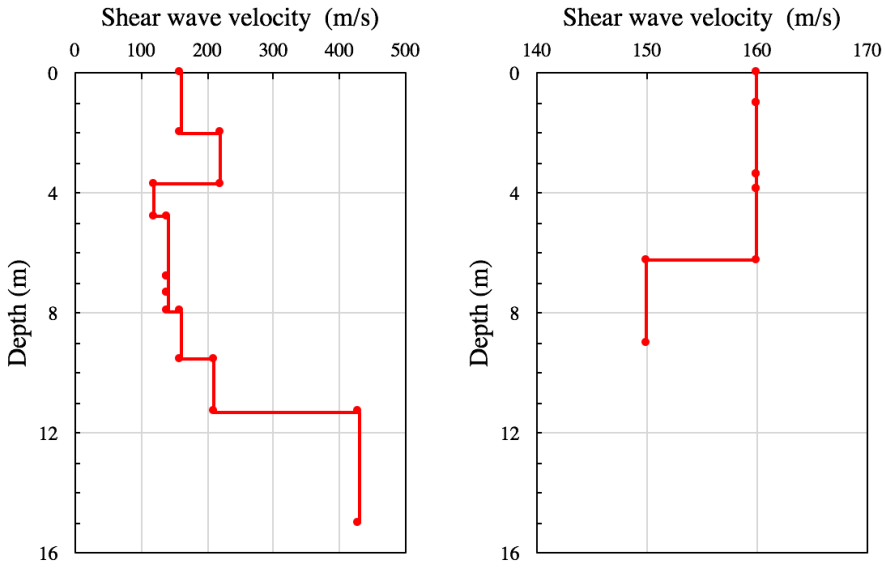


Figure 4.4 Shear wave velocity profile at borehole H9-No.5 (left) and H7-2-1-A (right)

4.2.2 **Recorded Response and Reported Performance**

As listed in Table 4.3, each site experienced various numbers of events including events with both strong shaking and relatively weak shaking, and specifically, events 2, 4, 9 and 10 were recorded at the Nakashimo site. Although there are five accelerometers installed at this site, I focus my attention here on the surface accelerometer at the crest (CG827420805a) and the downhole accelerometer at a

depth of 13m below the crest (CG827420804a). This is because the downhole record is used as an input to the finite element models presented later in this chapter, and the crest motions are compared as model validation. All four events are recorded by these two sensors.

Figures 4.5-4.8 are horizontal components of ground motion records at both the surface accelerometer (CG827420805a) and the downhole accelerometer (CG827420804a) during events 2, 4, 9 and 10. Their response spectra are also plotted in the same figures. Note that the motions shown in Figures 4.5-4.8 are only portions of the original records. The strongest event among all for the Nakshimo site is event 4, which is the **M** 9.1 2011 Tohoku-oki event.

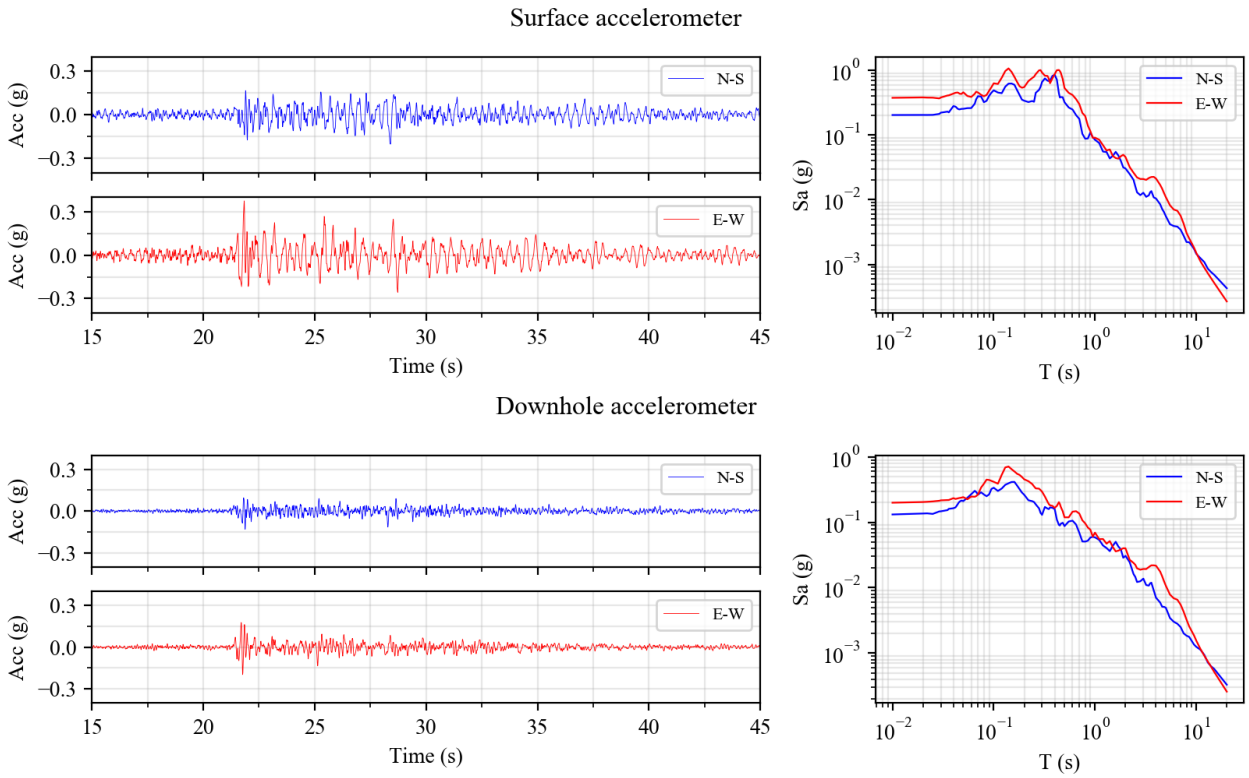


Figure 4.5 Acceleration time series recorded during event 2

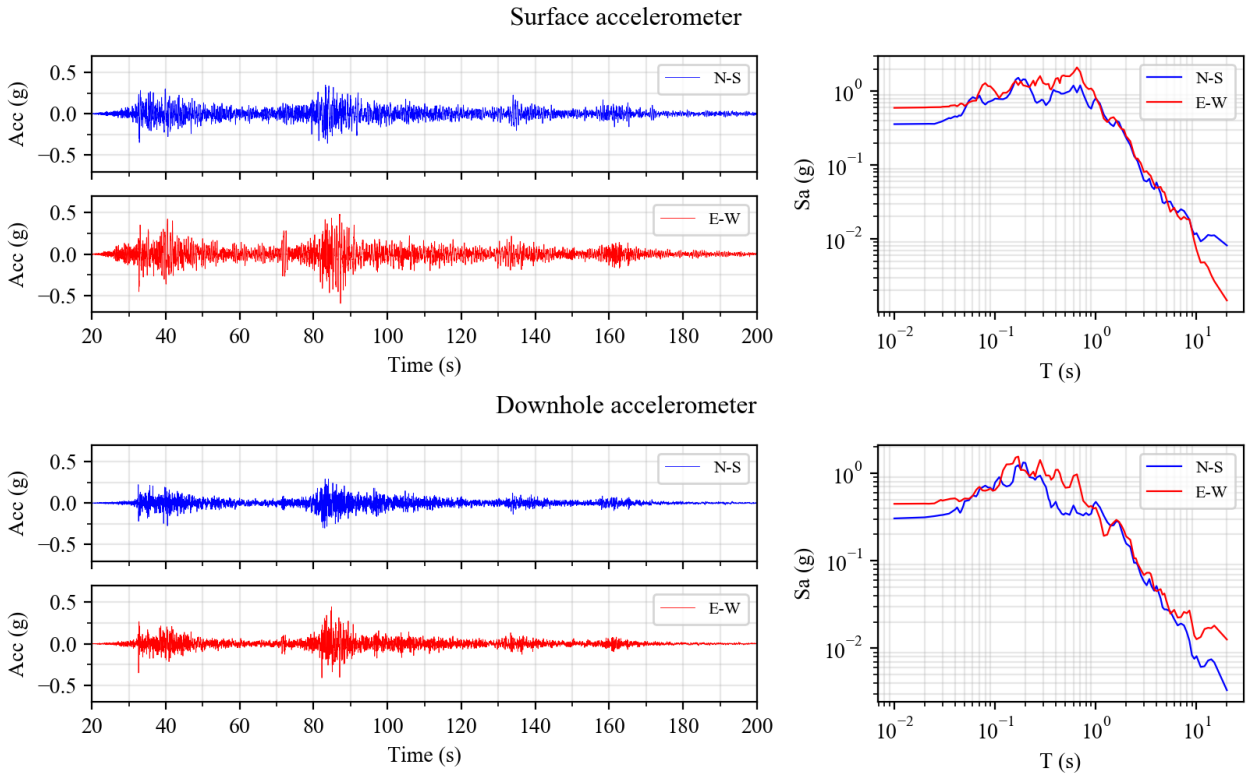


Figure 4.6 Acceleration time series recorded during event 4

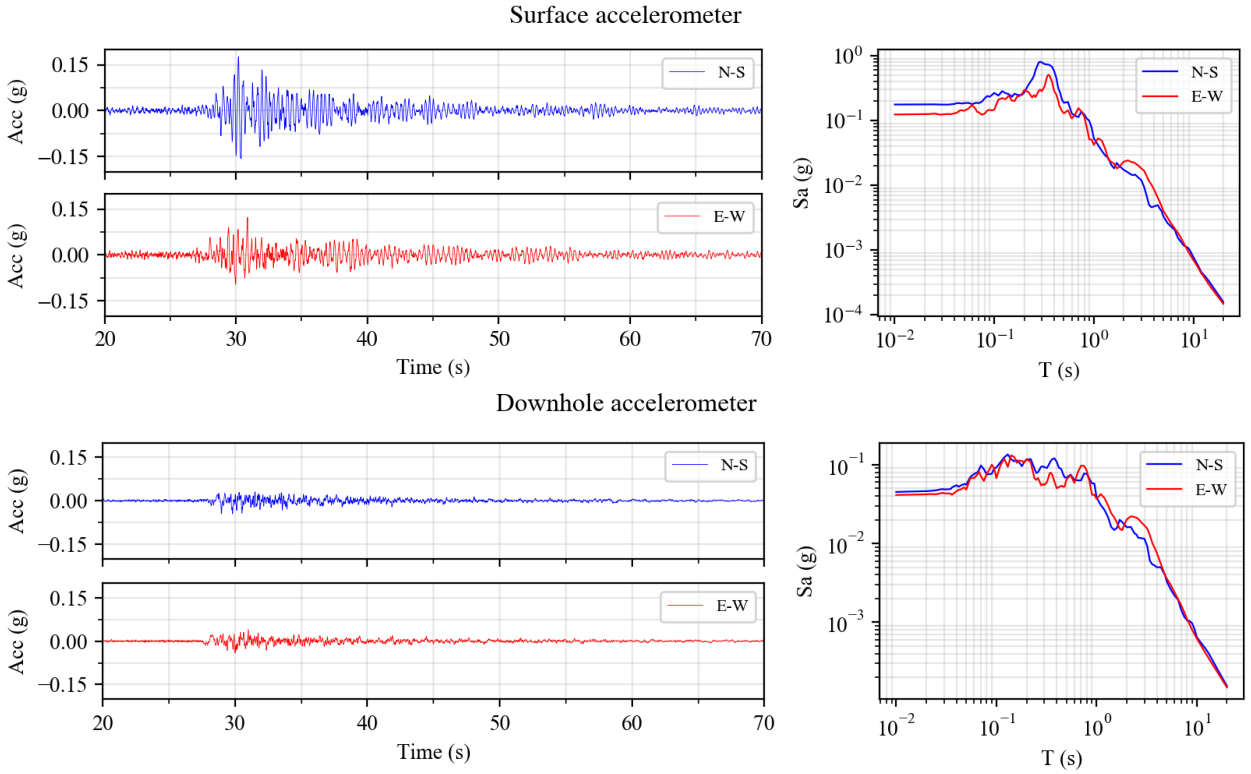


Figure 4.7 Acceleration time series recorded during event 9

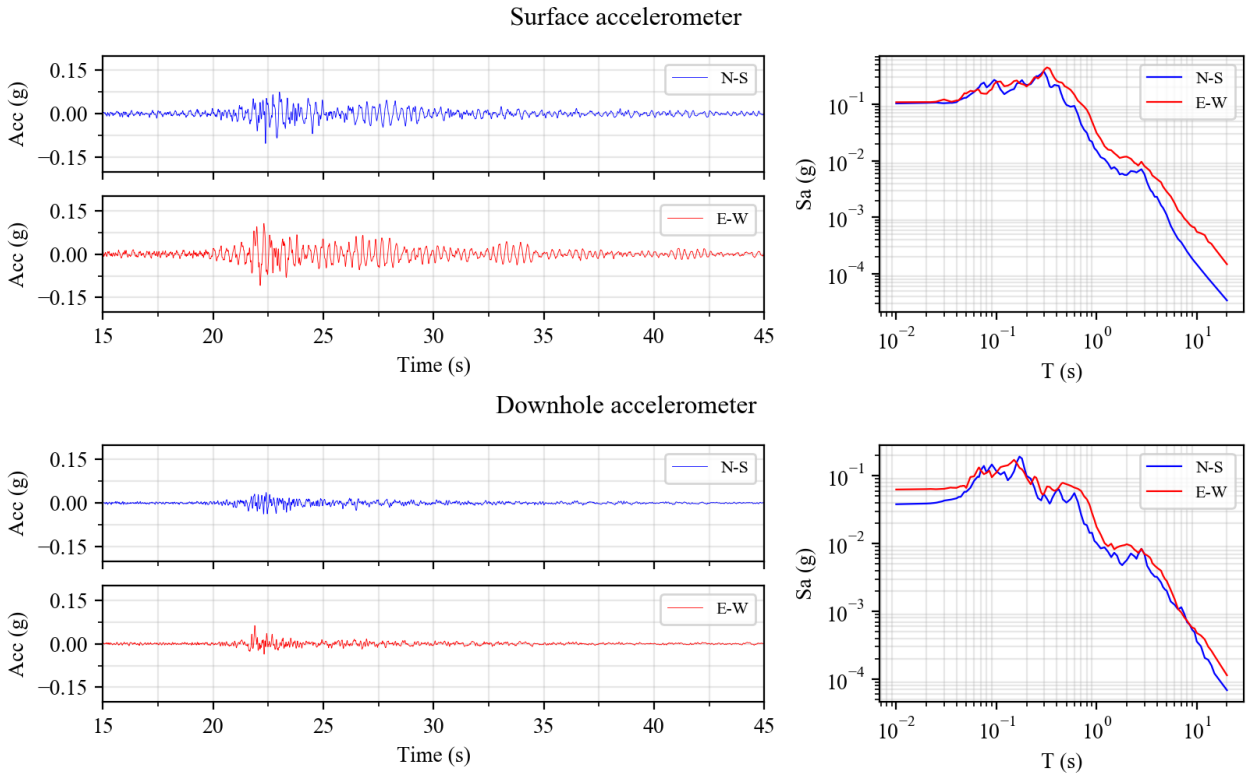


Figure 4.8 Acceleration time series recorded during event 10

As for the damage observations, none of the weak shaking events (event 2, 9 and 10) were strong enough to cause observable damage. The 2011 Tohoku-oki event also did not produce surface evidence of liquefaction, but it did cause vertical displacements of up to 10cm and damage to the concrete cover of the levee on the riverside over a length of about 70m along the levee. It also triggered a pore pressure response in the sand layer. The pore water pressure recording is plotted in Figure 4.10. The transducer has a measurement limit of 101.3kPa, which is also shown in the figure. Unfortunately, the transducer limit truncated the measured pore pressure.

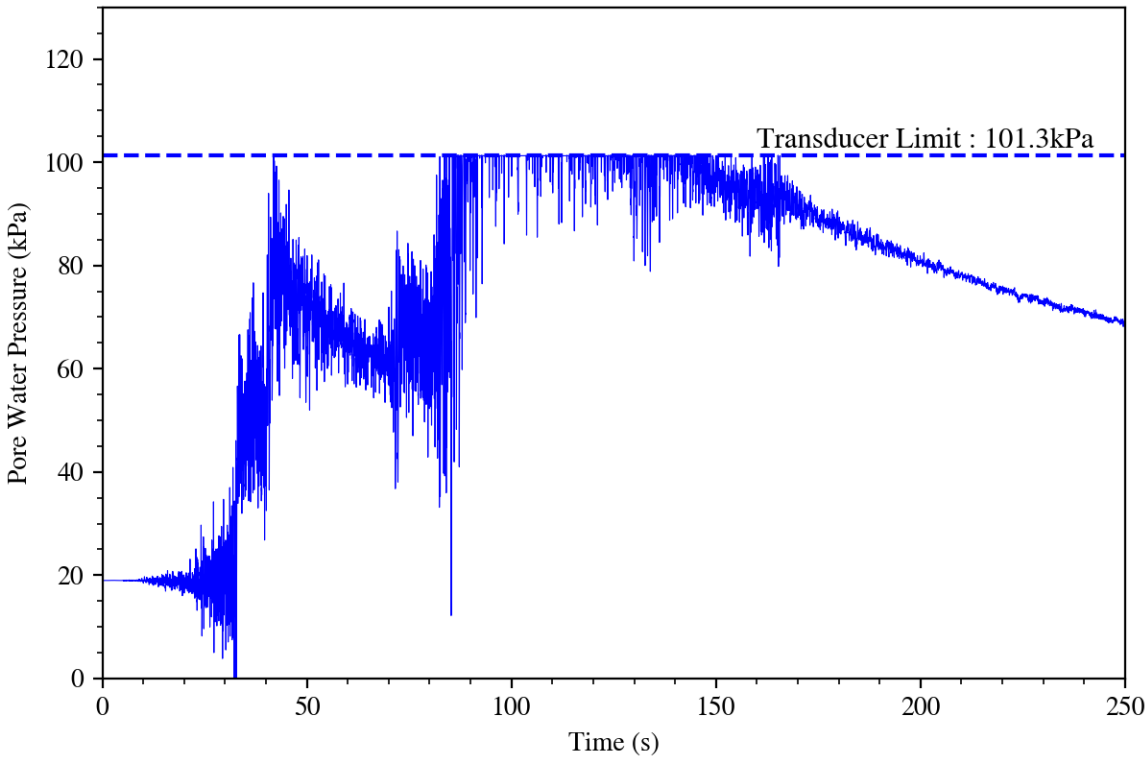


Figure 4.9 Pore water pressure recorded during event 2011 Tohoku-oki event

4.2.3 **Finite Element Model Setup**

Figure 4.10 shows the generated mesh after integrating information such as the geometry and material boundaries obtained from cross-section profile into GiD, and Table 4.4 contains the material properties for the different soil layers. The two thick columns on either side of the model are two free-field columns. As described in Chapter 2, the presence of these two free-field columns ensures that free-field conditions exist at the horizontal boundaries of the model, and they are sufficiently far away from the interior mesh so that the wave reflections between the interior mesh and free-field columns will have negligible impact on the levee response. After creating the mesh, the next step is to assign material properties to the elements. Table 4.4 summarizes some of the important parameters that are either directly used or related to material input parameters in OpenSees.

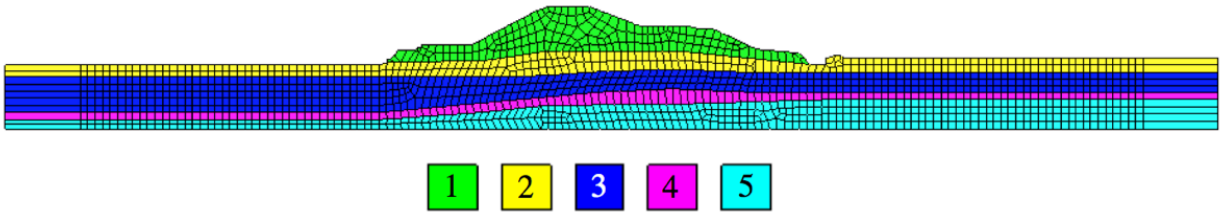


Figure 4.10 Mesh configuration using GiD

Table 4.4 Material properties used based on available data and assumptions

Soil Type	MD	Layer Tag	ρ (g/cm^3)	υ	V_S (m/s)	D_R	OCR	k_x (m/s)	k_y (m/s)
Sand	PDMY03	1	1.9	0.35	180	53%	NA	$5x10^{-7}$	$5x10^{-7}$
Clay	PIMY	2	1.8	0.4	140	NA	2	$5x10^{-9}$	$5x10^{-9}$
Sand	PDMY03	3	2.2	0.35	200	54%	NA	$5x10^{-7}$	$5x10^{-7}$
Clay	PIMY	4	1.8	0.4	210	NA	2	$5x10^{-9}$	$5x10^{-9}$
Bedrock	PIMY	5	2.7	0.25	430	NA	NA	$5x10^{-11}$	$5x10^{-11}$

The shear wave velocity is used to determine the small strain shear modulus, and the Poisson ratio is used to relate the shear modulus and bulk modulus. The relative density for the sand layer is based on the blow counts that exists at the boring log locations (Boulanger and Idriss, 2008) and computed as

$$D_R = \sqrt{\frac{(N_1)_{60}}{46}} \tag{4.1}$$

It was found that the two sand layers are both medium dense. The clay layers, on the other hand, are assumed to have an overconsolidation ratio of 2, and undrained shear strength is computed as (Ladd 1991):

$$s_u = 0.22 * \sigma'_v * OCR^{0.8} \tag{4.2}$$

where s_u is the undrained strength, σ'_v is the vertical effective stress and OCR is the overconsolidation ratio. Regarding OCR, since its correlations with SPT blow counts are pretty poor, and there is no CPT

data available at this site, so I assumed an OCR of 2 because it is clear that it is not reasonable for the clay to be normally consolidated due to the groundwater fluctuation. The permeability for different layers are varied based on the soil type.

Subsequently, it is important to figure out where the phreatic surface is by conducting a seepage analysis. OpenSees is poorly suited to seepage analysis because it can only perform transient seepage analysis and not the simpler steady-state analysis, so I utilized the RocScience program Phase 2 for this purpose. Figure 4.11 shows the model setup in Phase 2. The permeability of each material, and the water table on either side of the boundary needs to be defined in this analysis. Figure 4.12 shows the estimated pressure head distribution from seepage analysis and the purple line indicates the phreatic surface. The location of the phreatic surface is consistent with the site exploration observation that the ground water table was found to be at the base of the levee fill. This phreatic surface from Phase 2 is used to fix the pore water pressure DOF at the nodes on and above that surface as zero in OpenSees.

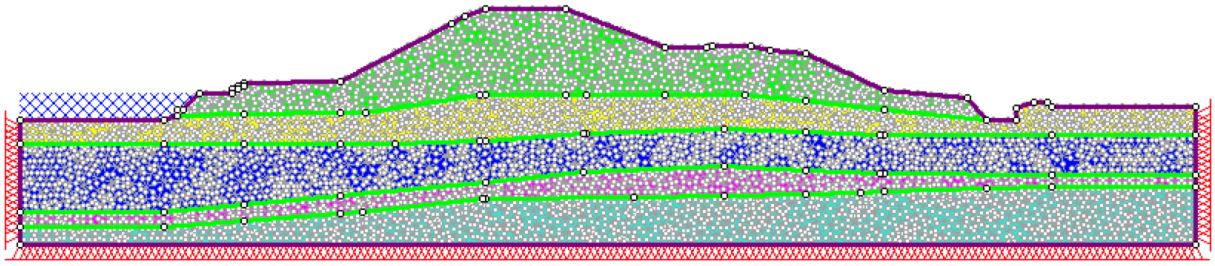


Figure 4.11 Mesh configuration in Phase 2 for seepage analysis

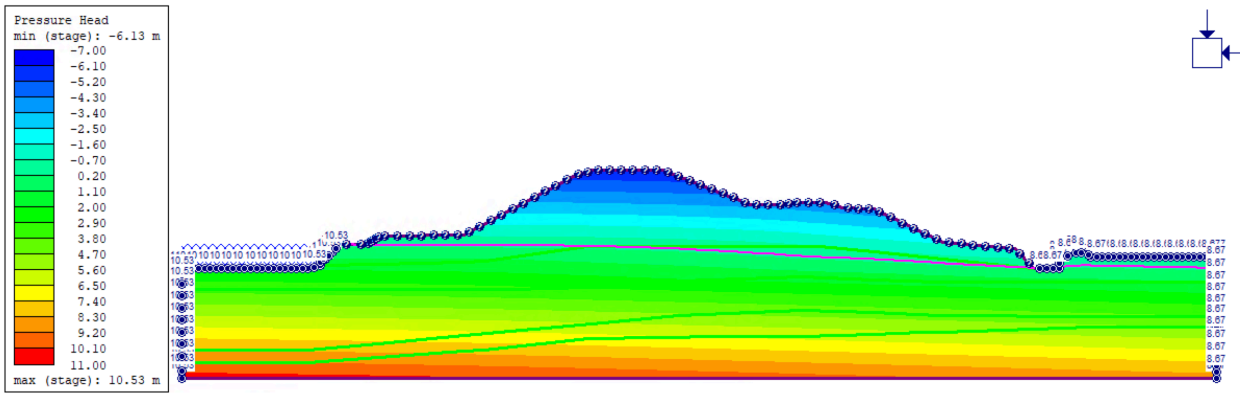


Figure 4.12 Pressure head distribution after the steady state seepage analysis

The last step is to apply the ground motion to the base of the model. The recorded downhole motion is used herein, therefore a dashpot at the base of the model is not needed to model reflected wave energy at that interface. The motion transverse to the levee cross-section (referred to as transverse) was computed by rotating the two horizontal components to the transverse direction azimuth. The base of the finite element model is deeper than the downhole sensor. Therefore, the ground motion recorded by the downhole sensor CG827420804a was deconvolved from the elevation of the measurement location to the base of the model. A transfer function was computed from the finite element model by taking the ratio of the Fourier amplitude of the predicted motion at sensor location to the motion at the base of the model, and that transfer function was then applied to the recorded motion to obtain a suitable input motion. The phase of the recorded motion was retained during the deconvolution analysis.

Figure 4.13 shows the acceleration time series that were applied at the base of the model within bedrock after the deconvolution analysis for the four earthquakes. The deconvolved motions are very similar to the recorded motions because the bottom of the model was only 2 m below the recorded downhole motion, and because the bedrock is fairly stiff. Note that the length of the ground motion record for event 4 is found to be about 800 seconds long. However, the acceleration time series indicates that most of the shaking occurred approximately before 250 seconds, so in order to save the computation

time for the finite element analysis, this ground motion record is windowed to exclude time intervals after 250 seconds when implemented into finite element modeling.

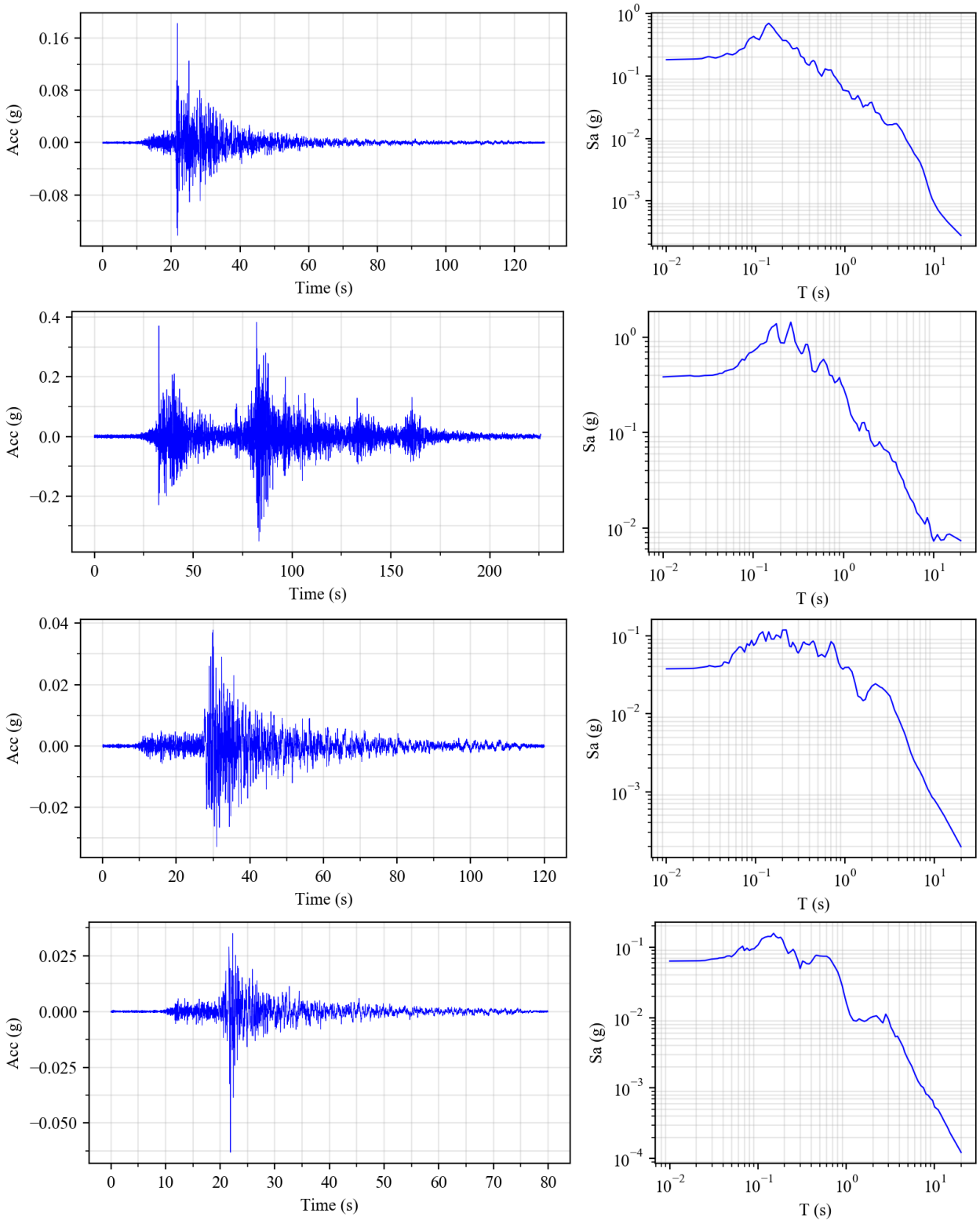


Figure 4.13 Acceleration time series to be applied at the base of the model and respective response spectrum for event 2, 4, 9 and 10

4.2.4 **Analysis Results**

This section compares results from the finite element simulations to recorded responses and reported performance. The predicted and recorded surface motion time series together with their respective response spectra are first compared. The predicted and measured pore water pressure response is also compared. Profiles of peak acceleration, velocity and shear strain at the location of boring logs are plotted for each ground motion. Lastly, I also compared the predicted levee crest settlement with reported damage observations.

4.2.4.1 Comparison of Surface Motions

At the Nakashimo site, I compared the surface crest motions at the location of sensor CG827420805a. As shown in Figure 4.14, the blue and red time series are the recorded and predicted motions, respectively. Their response spectra are also plotted in Figure 4.14. An error term (ε) is defined in Eq. 4.3 to quantify the difference between the two response spectra:

$$\varepsilon = \frac{\sum [\ln(PSA_{measured}) - \ln(PSA_{predicted})]^2}{n-1} \tag{4.3}$$

where n is the total number of periods in computing the response spectrum. The computed residual terms are summarized in Table 4.5. The periods used in computing the response spectrum ranges from 0.01s to 20s.

Table 4.5 summarizes the peak acceleration (PGA) and peak velocity (PGV) values for both measured and predicted surface motion. Overall, the response spectral shape match quite well, and the period and height of peaks of the response spectra are reasonably consistent. However, the error term slowly increases as the motions strengthen. For the strongest motion, which is from event 4 (2011 Tohoku-oki event), the predicted and measured PGAs are very close but the peaks of the response spectrum differ slightly. This might be due to the fact that the response becomes nonlinear when the shaking

intensity increases, and accurately predicting the nonlinearity is more complicated than matching the linear response. The other possible reason is that I only used the two horizontal components of the ground motion record as my input motion, while in reality the vertical component might also have some impact on the response of the levee system.

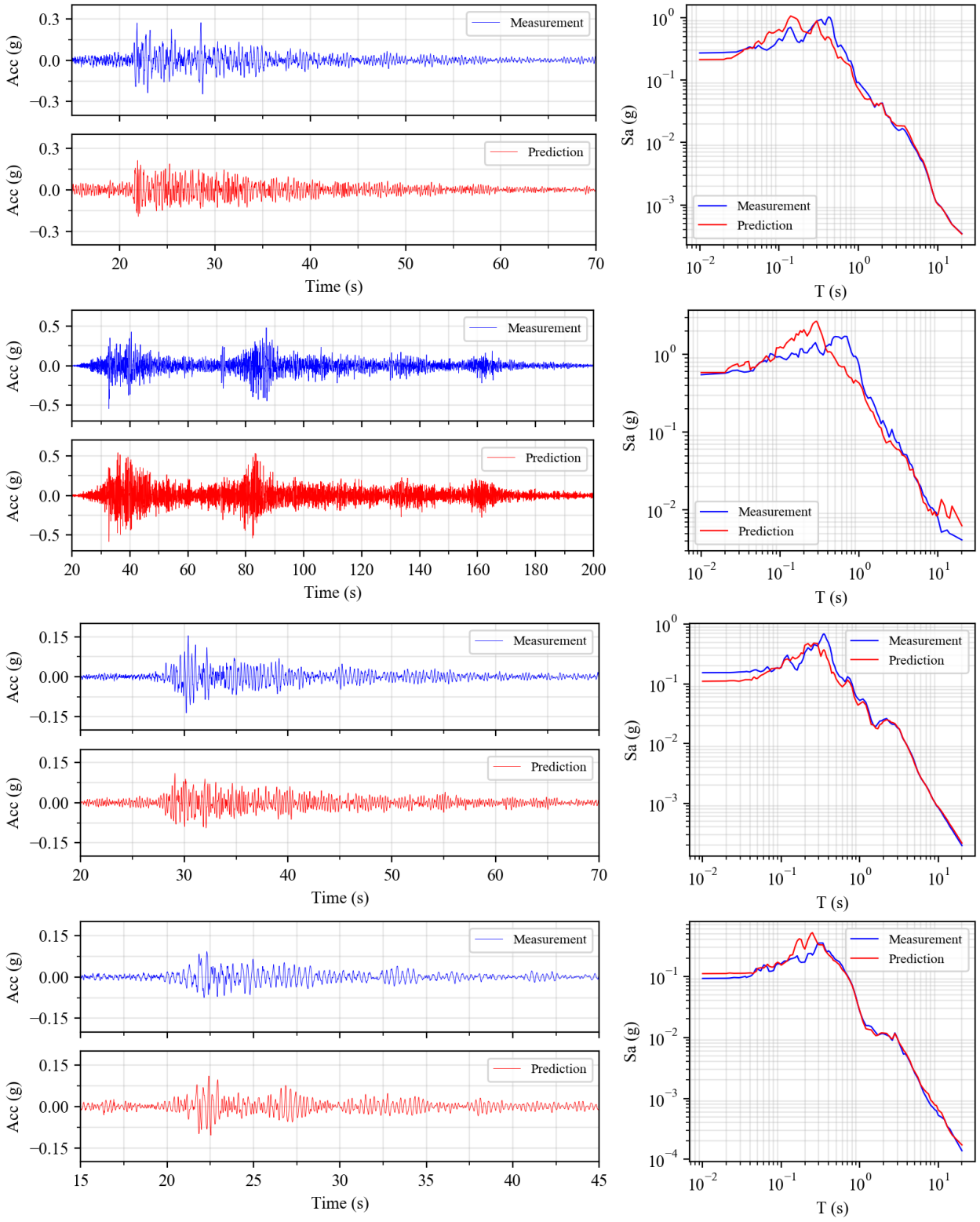


Figure 4.14 Predicted and measured surface motion at crest comparison for event 2, 4, 9 and 10

Table 4.5 PGA and PGV of measured and predicted surface motion at levee crest and residual term

Event ID	Year	Measured PGA at Crest (g)	Measured PGV at Crest (m/s)	Predicted PGA at Crest (g)	Predicted PGV at Crest(m/s)	ε
2	2005	0.273	0.142	0.212	0.131	0.106
4	2011	0.543	0.374	0.583	0.369	0.185
9	2008	0.154	0.101	0.11	0.079	0.07
10	2010	0.092	0.06	0.11	0.068	0.054

4.2.4.2 Pore Water Pressure Response Comparison

As mentioned earlier, the 2011 Tohoku-oki event triggered a pore water pressure response at this site, which is shown as the blue curve in Figure 4.15. Unfortunately, the piezometer installed at this site can only measure up to 101.3kPa, and the pore water pressure readings temporarily plateau when this level is reached (Unjoh et al. 2012).

To make a direct comparison, the pore water pressure was also recorded at the location of the pore water pressure transducer during the finite element analysis, which is shown as the red curve in Figure 4.15. The red dashed line indicates an approximate value of vertical total stress at the location of the transducer. This constitutes the maximum pore pressure that can occur in the absence of any vertical stress changes (which can occur due to rocking of the levee system). It is clear from the figure that the finite element model predicts that the foundation sand layer liquefies approximately between time t = 80 to 100s, which seems reasonable because this event contains two intervals of relatively strong shaking, and the second strong shaking interval started at approximately t = 80s. It can also be seen from the figure that the finite element model provides build-up of pore water pressure that is generally consistent with recorded responses. What is unclear is whether the measured pore pressure response reached σ_v since it was truncated at 101.3 kPa. The predicted rate of dissipation is faster than the measured rate. I adjusted the hydraulic conductivity to better match the observed dissipation rate, but

this caused the overall pore pressure response to be over-predicted. This is an interesting case study because the rate of dissipation is not insignificant compared with the duration of shaking, and the sand is partially drained.

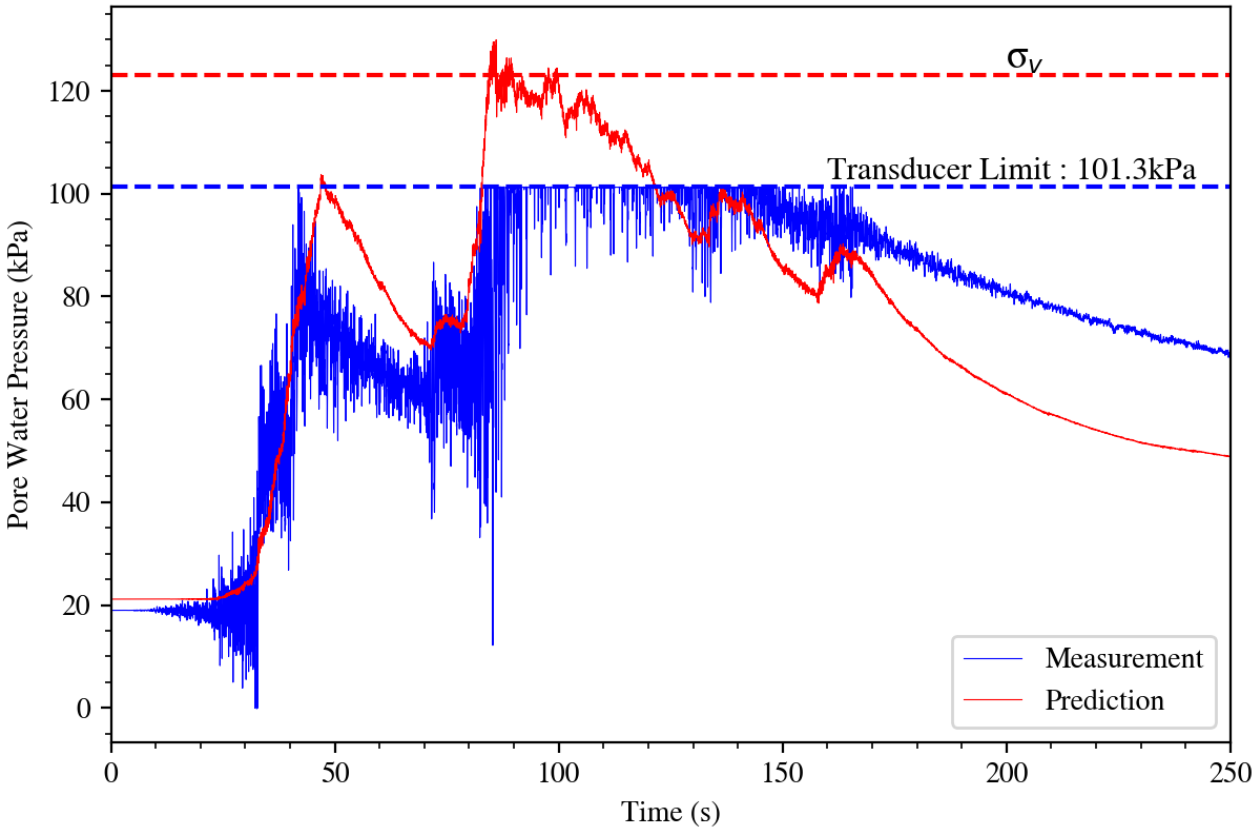


Figure 4.15 Predicted pore water pressure response compared with recordings during 2011 event

4.2.4.3 Profiles of Peak Acceleration, Velocity and Shear Strain

As shown in Figure 4.2, the two sensors that are of interest to this study (sensor CG827420804a and sensor CG827420805a) are located at boring log location H9-No.5. To show the depth-variations of peak accelation, velocity and shear strain, I recorded the response of a vertical array of elements at the location of the boring log at the levee crest.

Figure 4.16-4.17 are the profiles of peak acceleration (PGA), velocity (PGV) and shear strain for elements right under levee crest during these four events, where the blue triangles represent the actual

measurement from accelerometer recordings. The measured PGA at the top of bedrock agrees quite well the predicted PGA, which proves that the deconvolution analysis was done properly. Furthermore, the acceleration at the bottom is different from the acceleration at the transducer location, indicating that the deconvolution was necessary. A profile of shear strength is also plotted in the figures, where the drained shear strength is computed as $\sigma_v' \tan(\phi')$ for sand layers and undrained shear strengths are shown for clay layers.

Overall, the strains are fairly high in the sand layers, and lower in the clay layers. The strain is highest in the lower sand layer during the Tohoku event. This may be due to trapping of pore pressure in the sand beneath the low-permeability clay. PGA tends to decrease near the top of the lower sand layer for the stronger motions, whereas it increases throughout the profile for the weaker motions. This is the result of nonlinearity, and increased damping in event 4. Figure 4.16 shows that the largest shear strains occur in the foundation sand layer during the 2011 Tohoku-oki event, which is consistent with the finding that this layer liquefied during this event. The small change in the response of bedrock layer for strong vs. weak motions is reasonable and expected.

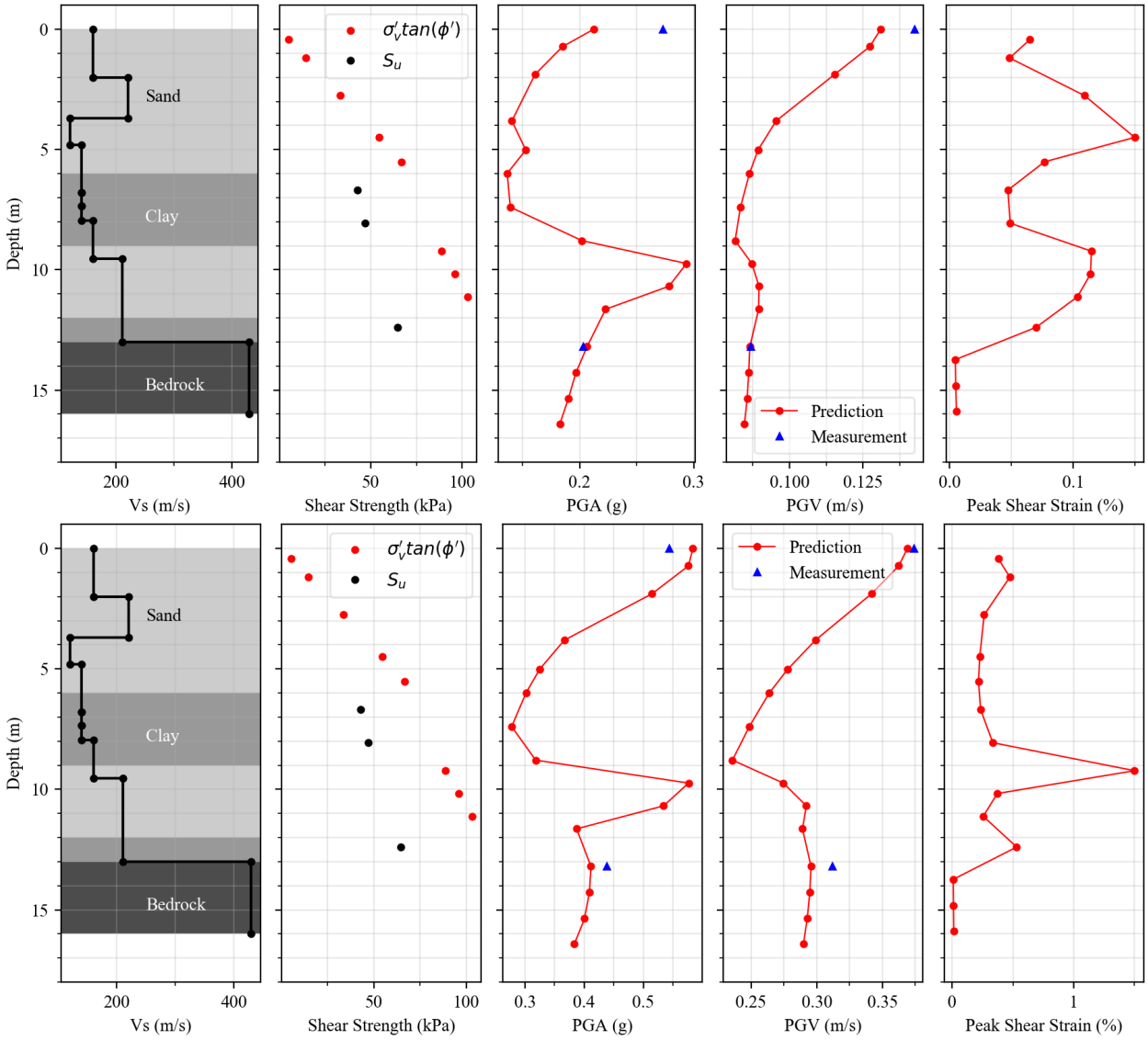


Figure 4.16 Profiles of PGA, PGV and peak shear strain for event 2 and 4

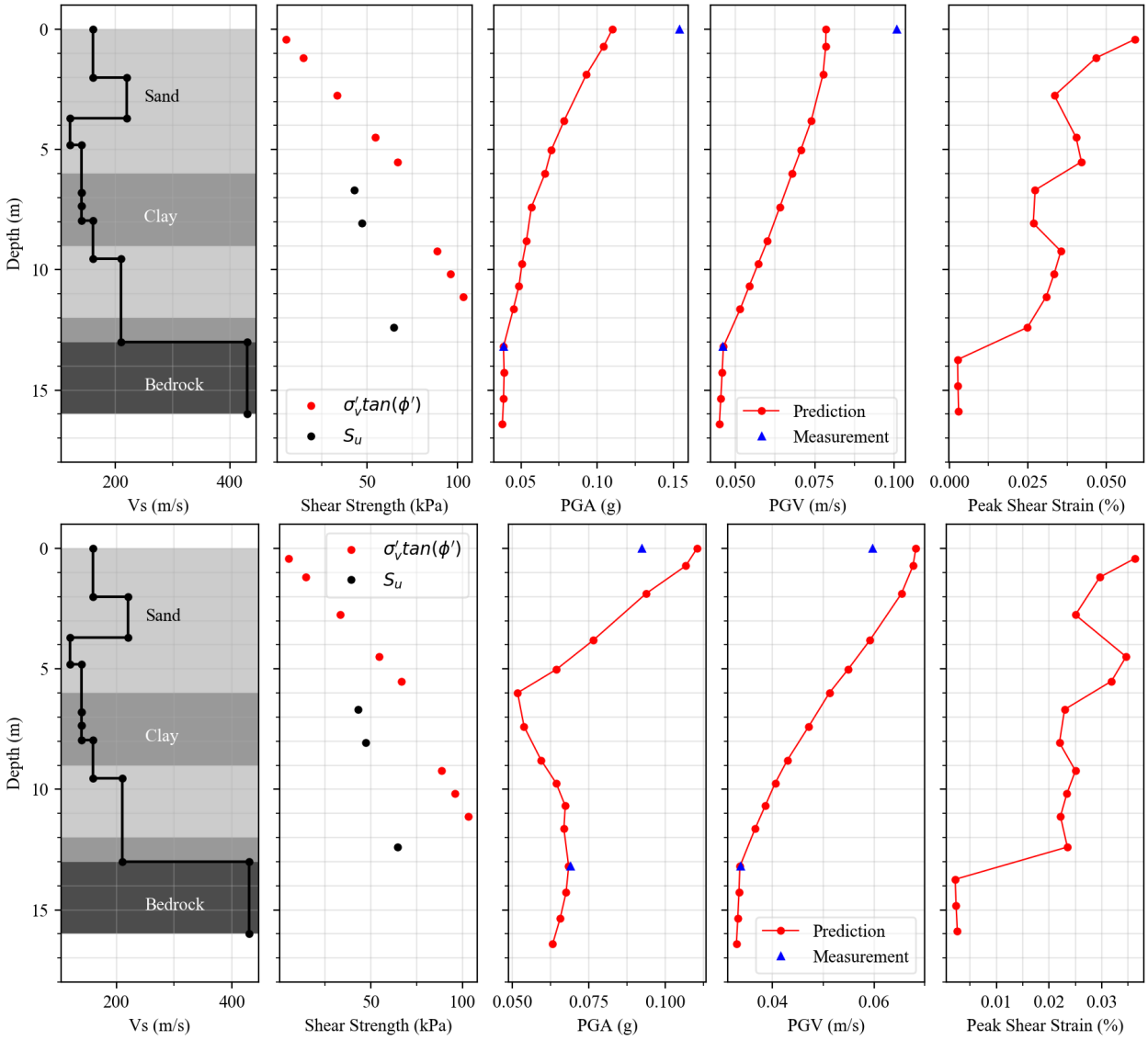


Figure 4.17 Profiles of PGA, PGV and peak shear strain for event 9 and 10

4.2.4.4 Observed Damage versus Predicted Damage

Reconnaissance performed after the 2011 Tohoku-oki event at the Nakashimo site identified subsidence of the levee crest of about 10cm, whereas no damage was reported for the other 3 events. The levees were inspected following each event, therefore no reported damage is an indication that settlements were small enough to not be visually apparent and reported by the inspector. These displacements are not necessarily zero, but they are interpreted as being small. I recorded the average crest settlement in the finite element analysis and compared the results with the reported settlement,

which are summarized in Table 4.6.The finite element model predicted approximately 15cm of crest settlement during the 2011 Tohoku-oki event, which is slightly higher than the observed settlement. For the two smallest motions, the finite element model predicts less than 1cm of crest settlement, which would likely be small enough that damage would not be noticed or reported. For event 2, 2.7cm of settlement was predicted, but no damage was reported. Overall, observed and predicted crest settlements match quite well. Table 4.6 also summarizes the damage level that is assigned based on the damage level classifications shown in Table 4.7. The damage level classification will be addressed more in detail in Chapter 5. Lastly, Figure 4.18 shows how the crest settlements change with the measured PGV at levee crest, and it is obvious that as the PGV of the crest motion increases, the settlement increases along with the associated damage level.

Table 4.6 Settlement and damage level comparison

Event ID	Year	Damage Observation	Recorded PGV at Crest (m/s)	Observed Damage Level	Predicted Settlement (cm)	Predicted Damage Level
2	2005	No damage reported	0.143	0	2.7	1
4	2011	Vertical settlement up to 10cm	0.371	2	15	2
9	2008	No damage reported	0.101	0	0.39	0
10	2010	No damage reported	0.06	0	0.28	0

Table 4.7 Damage levels classification

Damage Level	Settlement (cm)
0	0-1
1	1-10
2	10-30
3	30-100
4	>100

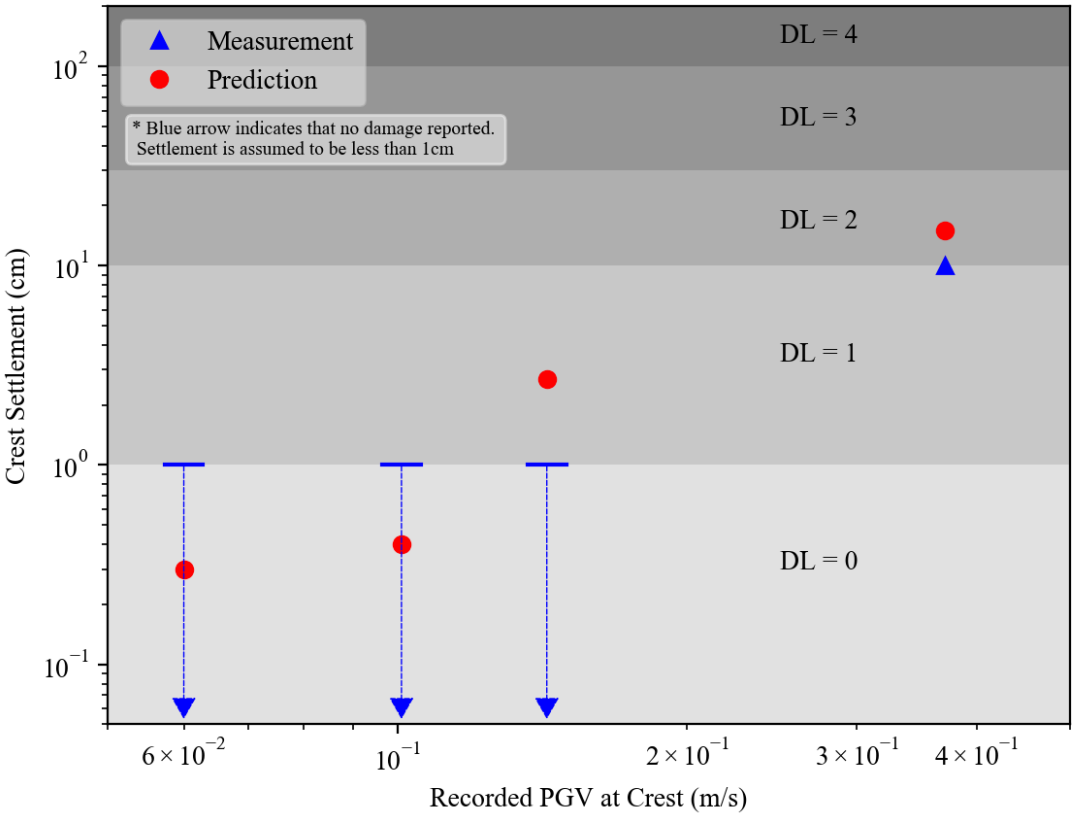


Figure 4.18 Crest settlement versus recorded PGV at levee crest

4.3 YAMAZAKI SITE

4.3.1 Site Conditions

The Yamazaki site is located along the Yoshida river, 15.8km upstream from the Naruse river mouth (Zimmaro et al. 2019). As shown in Figure 4.19, the levee is mainly constructed by fill, which consists of sandy materials, and it is founded on clay, sand, and peat layers. At one of the site explorations in 2004, the ground water was found approximately 2m above the base of the levee fill. Due to the presence of sandy material in the fill and the shallow ground water table, this site was expected to have relatively high liquefaction potential.

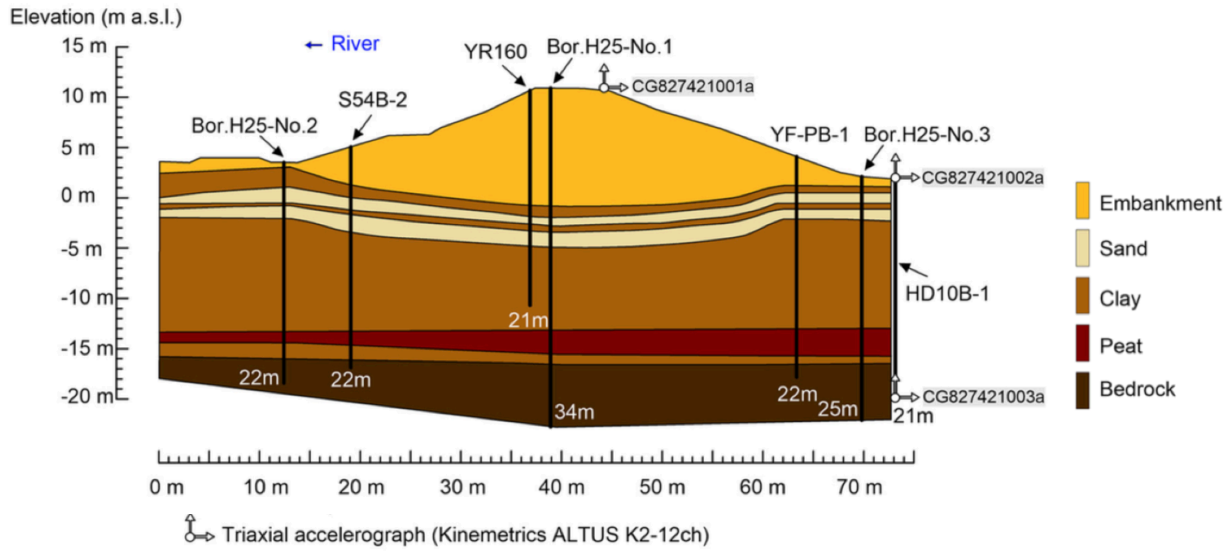


Figure 4.19 Cross-section, stratigraphy under the levee, boring log locations and sensors locations at Yamazaki site (Zimmaro et al. 2019)

There are three accelerometers installed at this site: one at the crest (CG827421001a), one at the toe (CG827421002a) and one downhole accelerometer (CG827421003a). There are multiple boring logs located at this site, which are indicated in both Figure 4.19 and Figure 4.20 (Zimmaro et al. 2019), and

these boring logs help define the layering of the strata beneath the levee crest. Figure 4.20 also shows more in details the blow counts profile for each existing boring log at this site. Again, these blow counts profile are extremely useful in terms of providing guidance on material properties input in finite element modeling since blow counts are directly related to relative density, for instance.

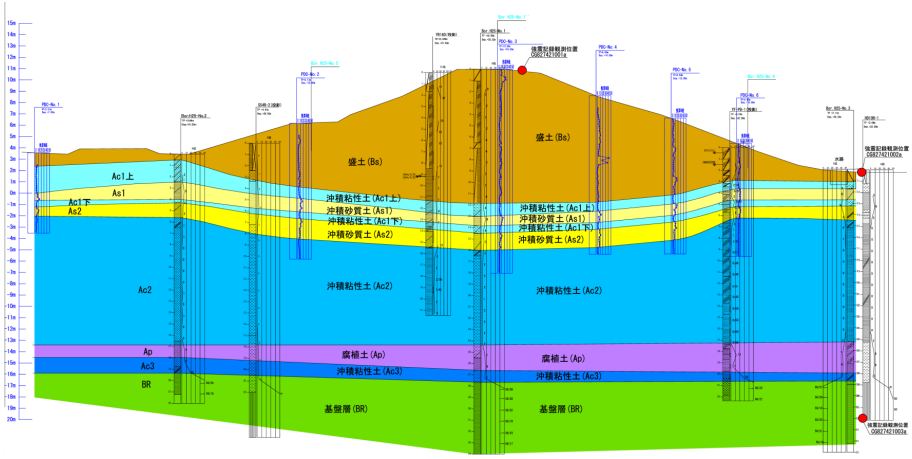


Figure 4.20 Detailed blow counts profile at boring log locations of Yamazaki site

Shear wave velocity profiles are also available at this site. At borehole H25-No.1 and borehole H25-No.3, shear wave velocities are obtained using both downhole method and suspension logging method. One shear wave profile obtained from suspension logging method is also available at borehole YF-PB-1. These shear wave velocity profiles are shown in Figure 4.21. Shear wave velocity profiles are useful as they are directly related to shear modulus which is an input parameter for the material model.

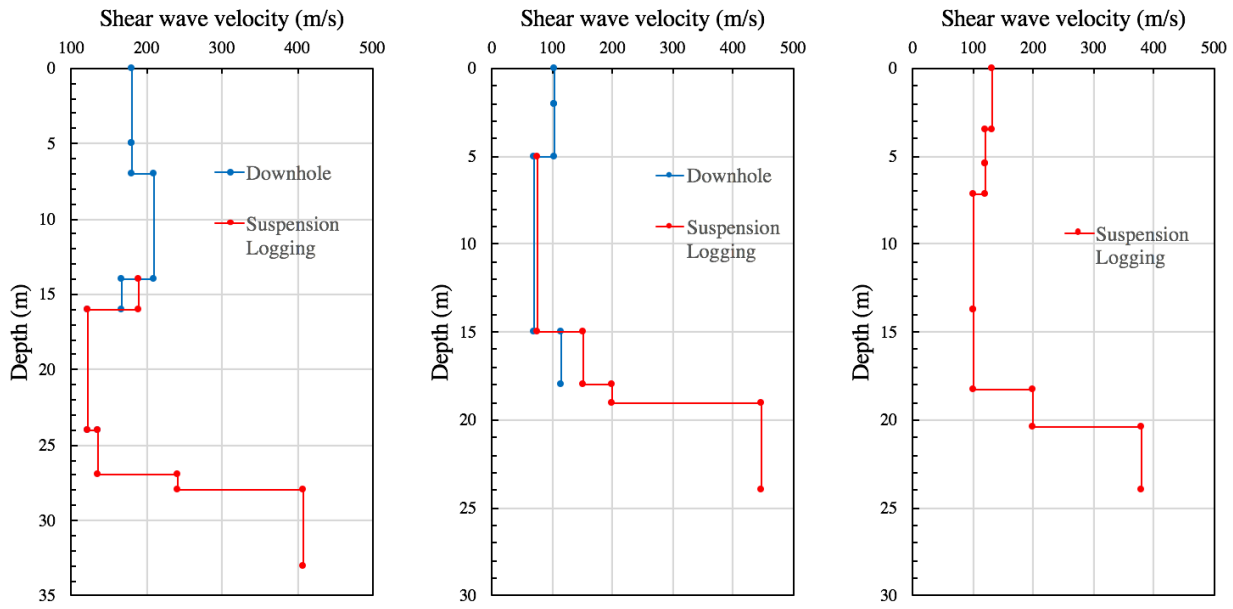


Figure 4.21 Shear wave velocity profile at borehole H25-No.1, H25-No.3 and YF-PB-1

4.3.2 **Recorded Response and Reported Performance**

As listed in Table 4.3, the Yamazaki site experienced ten earthquake events in total including four strong events and six relatively weak events. Although there are three accelerometers installed at this site, the surface accelerometer at the crest (CG827421001a) and the downhole accelerometer (CG827421003a) are of more interest to this study. The ground motion records at sensor CG827421003a can be directly used for finite element analysis in the subsequent section, and the surface motion records at the crest will be quite useful for the validating of the finite element model. All nine events are recorded by these two sensors.

Figures 4.22-4.26 are horizontal components of ground motion records at both surface accelerometer (CG827421001a) and downhole accelerometer (CG827421003a) during events 2-5, 9, 11, 13, 17, 20 and 21. Their response spectrums are also plotted in the same figures. Again, the strongest event among all for the Yamazaki site is also event 4, which is the 2011 Tohoku-oki event. The ground motion record for this event is also found to be about 800 seconds long, so in order to save the

computation time for the finite element analysis, this ground motion record is being chopped off around 250 seconds when implemented into finite element modeling.

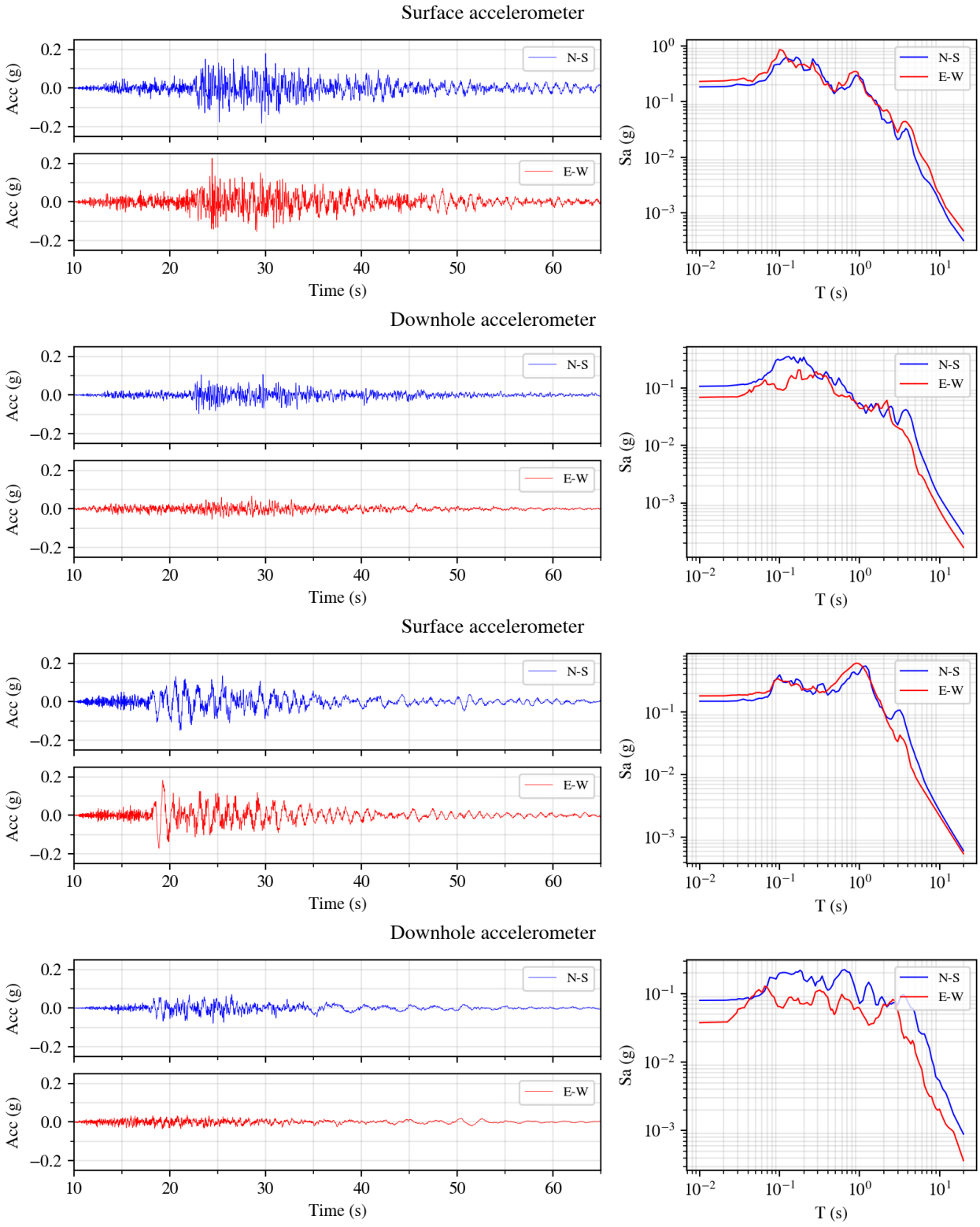


Figure 4.22 Acceleration time series recorded during event 2 and 3

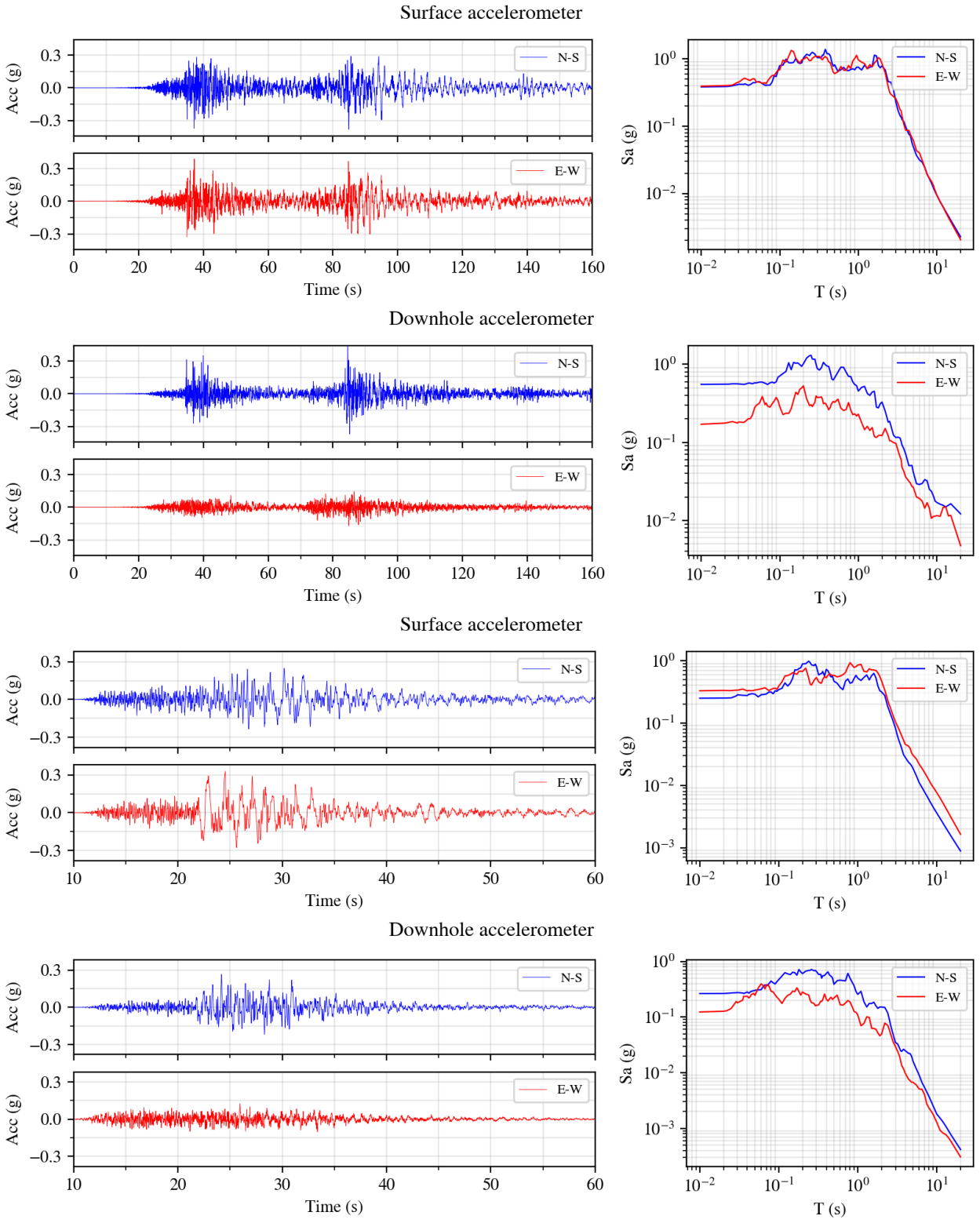


Figure 4.23 Acceleration time series recorded during event 4 and 5

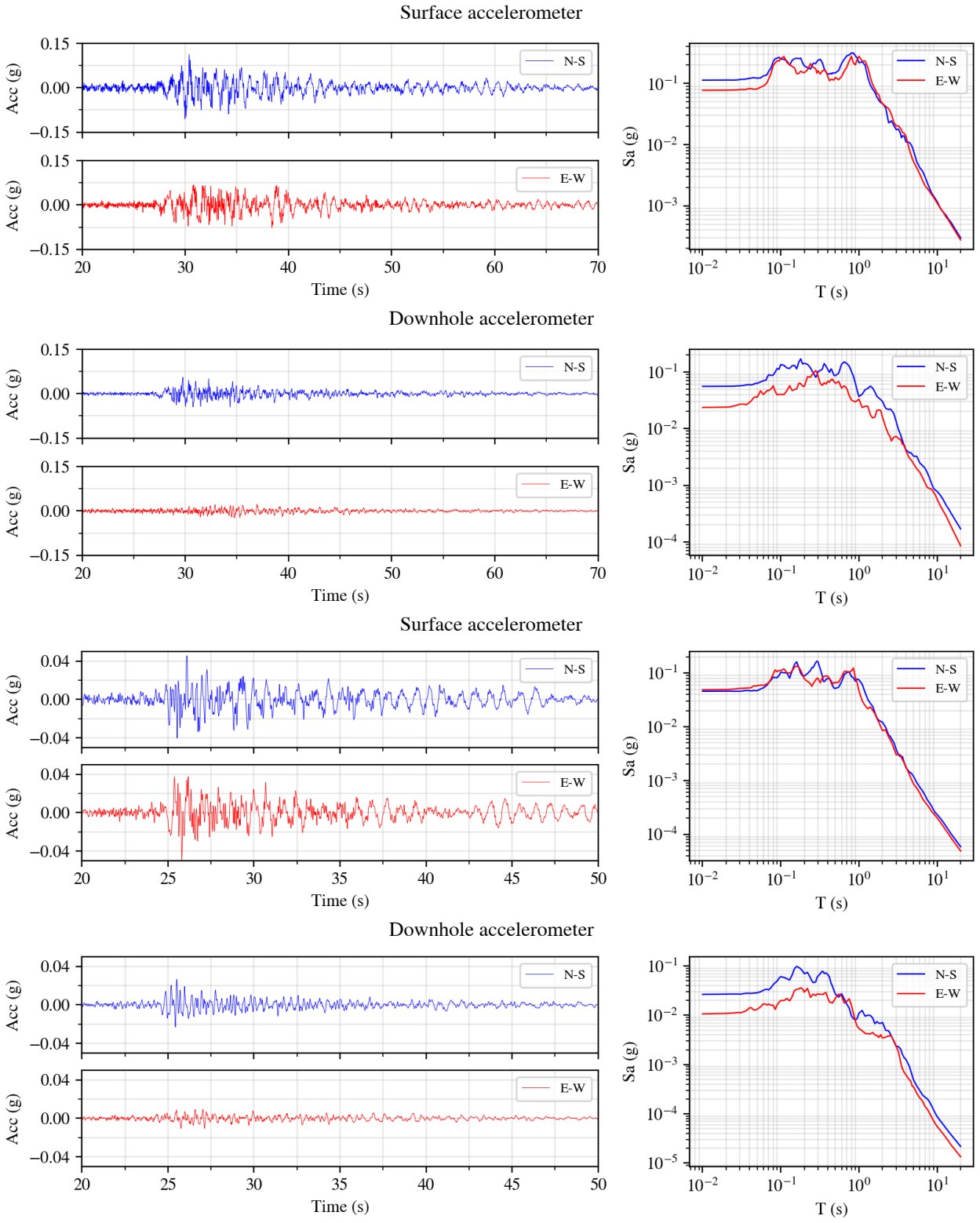


Figure 4.24 Acceleration time series recorded during event 9 and 11

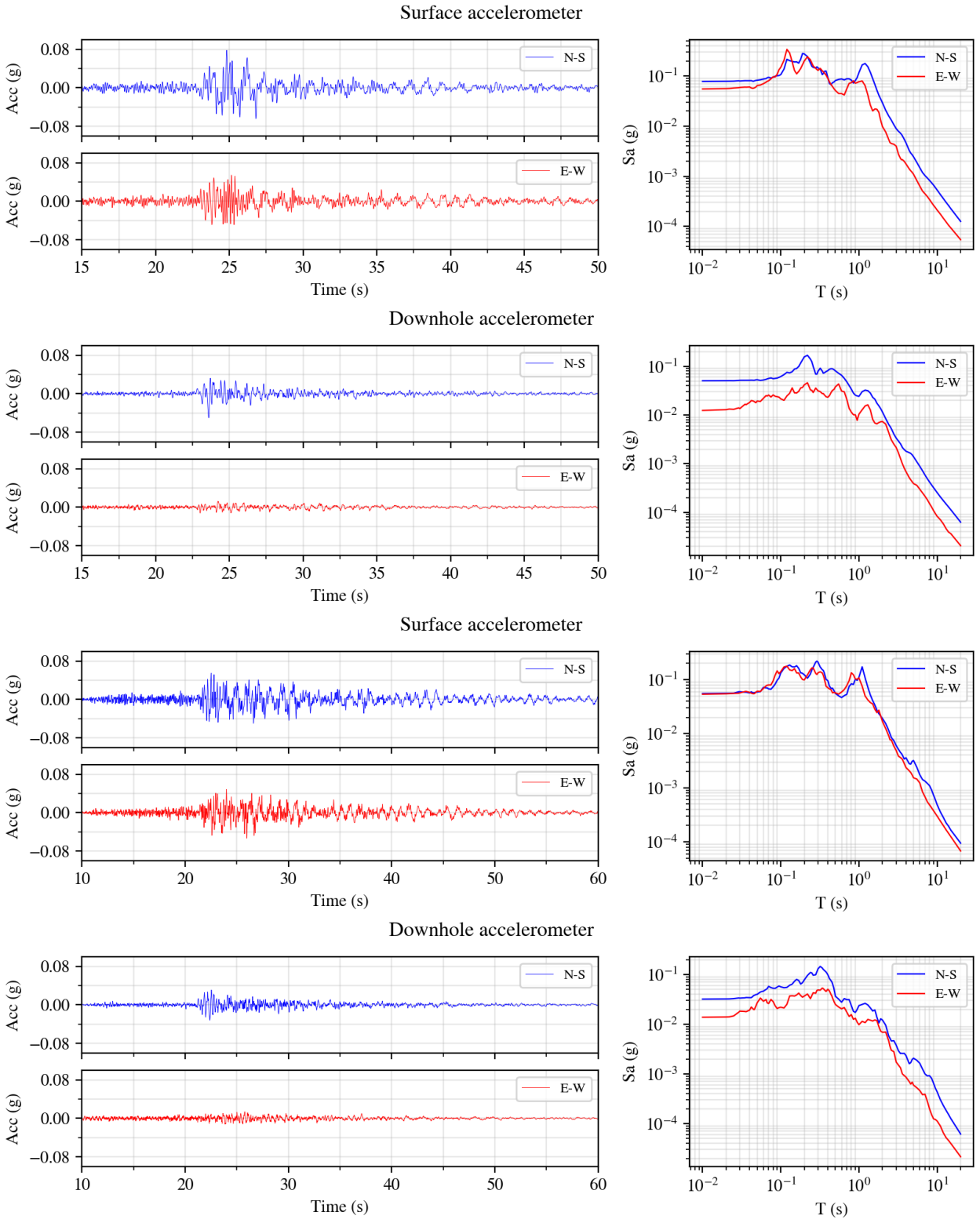


Figure 4.25 Acceleration time series recorded during event 13 and 17

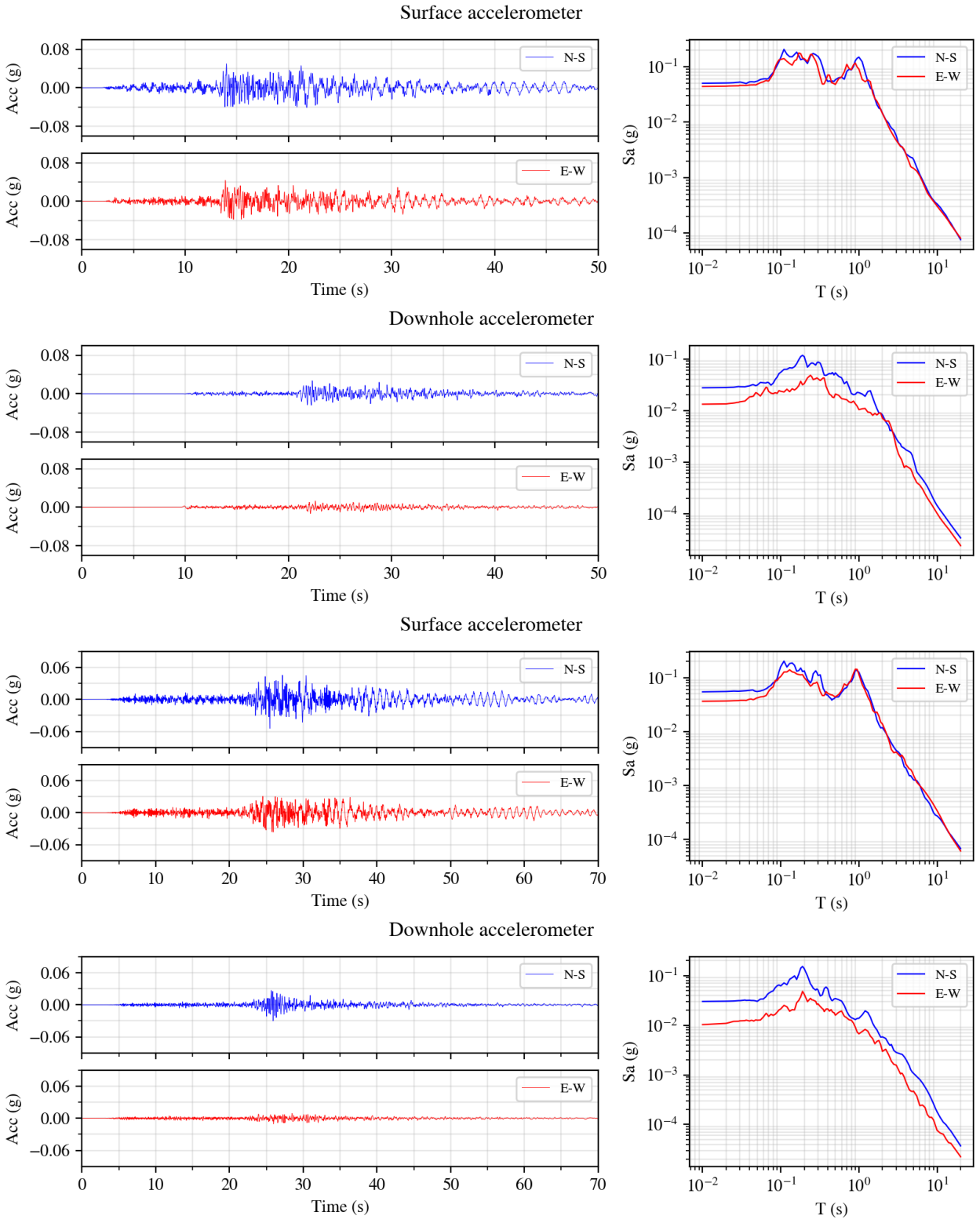


Figure 4.26 Acceleration time series recorded during event 20 and 21

As for the damage observations, none of the weak shaking events (event ID larger than 5) were strong enough to cause adequate damage to be observed and reported. However, the 2011 Tohoku-oki event did caused a vertical displacement at the levee crest of about 59cm. During the post-earthquake reconnaissance trip of the 2011 Tohoku-oki event, liquefaction was also observed, and there was evidence of sand boils near the riverside toe. Diffuse cracking was also found at the levee crest and both sides of the levee. The length is approximately 75m, and the width of the cracks ranged between 10 and 55cm (Zimmaro et al. 2019).

4.3.3 **Finite Element Model Setup**

Figure 4.27 shows the finite element mesh after integrating information such as the geometry and material boundaries obtained from cross-section profile into GiD. The two thick columns on either side of the model are two free-field columns. Different from the Nakashimo site, the phreatic surface was included when generating the mesh, which was shown as the material boundary between the green and yellow layers. The green layer is unsaturated fill above the phreatic surface, while the yellow layer is saturated fill below the phreatic surface. These two materials are otherwise the same. This is because the location of ground water table was recorded in the boring logs and the site exploration also reported that the ground water table was at 2m above the base of the levee. Pre-defining the phreatic surface makes it easier to create zero pressure conditions for nodes on and above the phreatic surface.

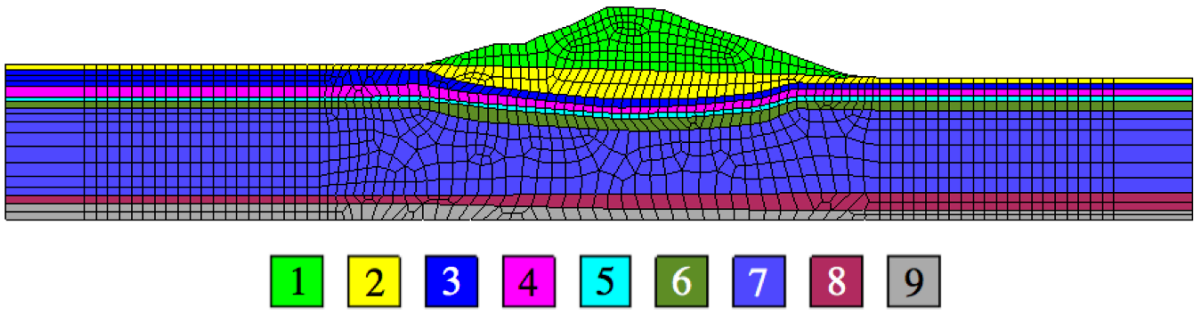


Figure 4.27 Mesh configuration using GiD

After creating the mesh, the next step is to assign proper material properties to the elements. Table 4.8 summarizes some of the important parameters that are either directly used or related to material input parameters in OpenSees. Similar to what I did with Nakashimo site, the shear wave velocity is used to determine the small strain shear modulus, and the Poisson ratio is used to relate the shear modulus and bulk modulus. The relative density for the sand layer is based on the blow counts that exists at the boring log locations (Idriss and Boulanger, 2008), and the undrained shear strength was determined based on the overconsolidation ratio and vertical effective stress. The permeability for different layers are varied based on the soil type, and are summarized in the table as well.

Table 4.8 Material properties used based on available data and assumptions

Soil Type	MD	Layer Tag	ρ (g/cm^3)	υ	V_S (m/s)	D_R	OCR	k_x (m/s)	k_y (m/s)
Sand	PDMY03	1	1.9	0.35	179	47%	NA	$5x10^{-7}$	$5x10^{-7}$
Sand	PDMY03	2	2.1	0.35	210	47%	NA	$5x10^{-7}$	$5x10^{-7}$
Clay	PIMY	3	1.8	0.4	130	NA	2	$5x10^{-9}$	$5x10^{-9}$
Sand	PDMY03	4	2.2	0.35	210	55%	NA	$5x10^{-7}$	$5x10^{-7}$
Clay	PIMY	5	1.8	0.4	210	NA	2	$5x10^{-9}$	$5x10^{-9}$
Sand	PDMY03	6	2.2	0.35	180	53%	NA	$5x10^{-7}$	$5x10^{-7}$
Clay	PIMY	7	1.8	0.4	121	NA	2	$5x10^{-9}$	$5x10^{-9}$
Peat	PIMY	8	1.1	0.35	134	NA	2	$5x10^{-8}$	$5x10^{-8}$
Clay	PIMY	9	1.8	0.4	240	NA	2	$5x10^{-9}$	$5x10^{-9}$

The last step is to apply the right ground motion to the base of the model. Since the motions used herein are within motions, there is no need to add a dashpot in this case. First of all, the motion recorded by the downhole accelerometer (CG827421003a) is directly used herein since the sensor is very close to the base of the model and it's at the bottom of the bedrock layer. Secondly, the two horizontal components need to be combined and rotated to be transverse to the levee cross-section. Figures 4.28-4.30 show all acceleration time series that will be applied at the base of the model. Response spectrums of the acceleration time series are also shown in the figure.

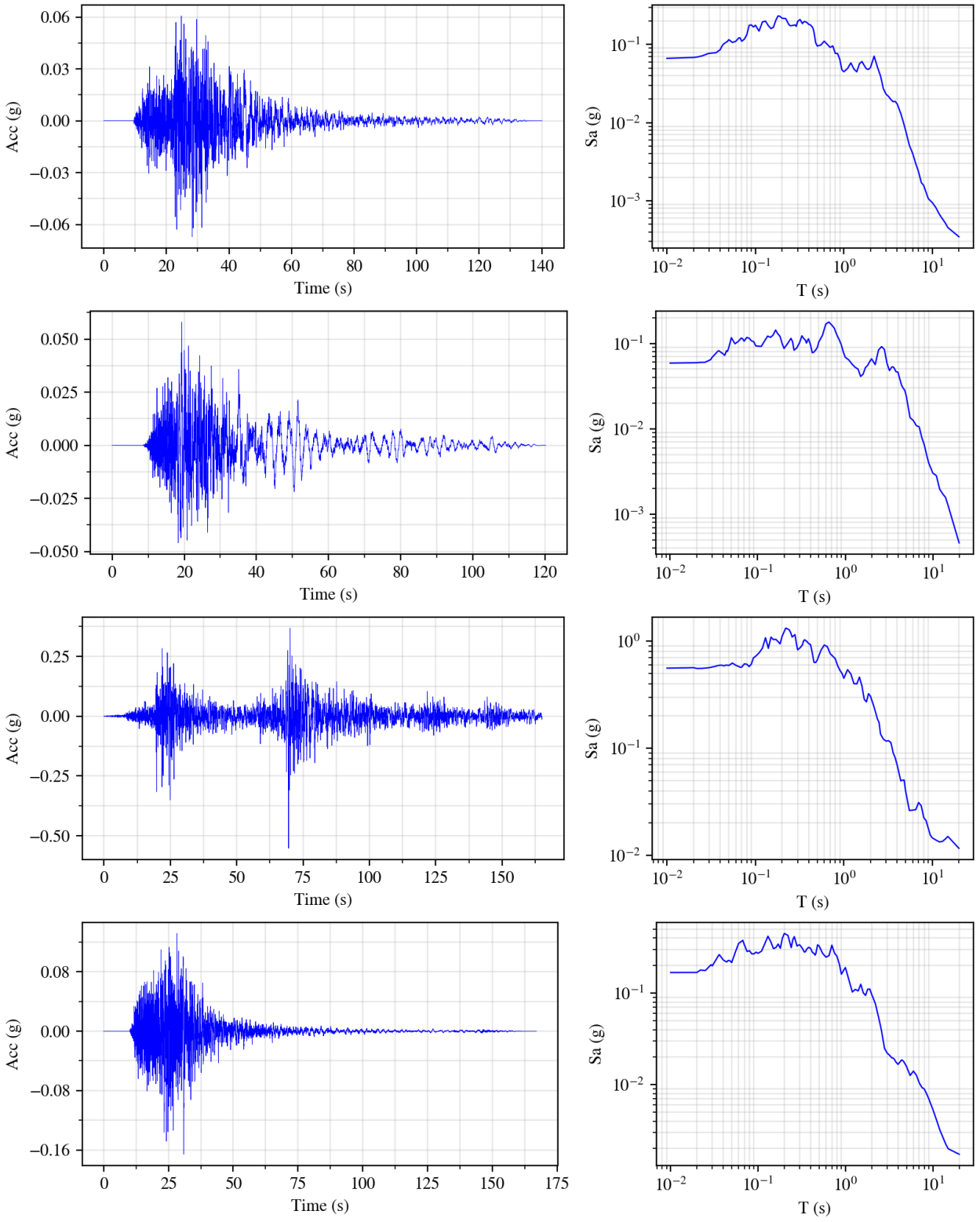


Figure 4.28 Acceleration time series to be applied at the base of the model and respective response spectrum for event 2, 3, 4 and 5

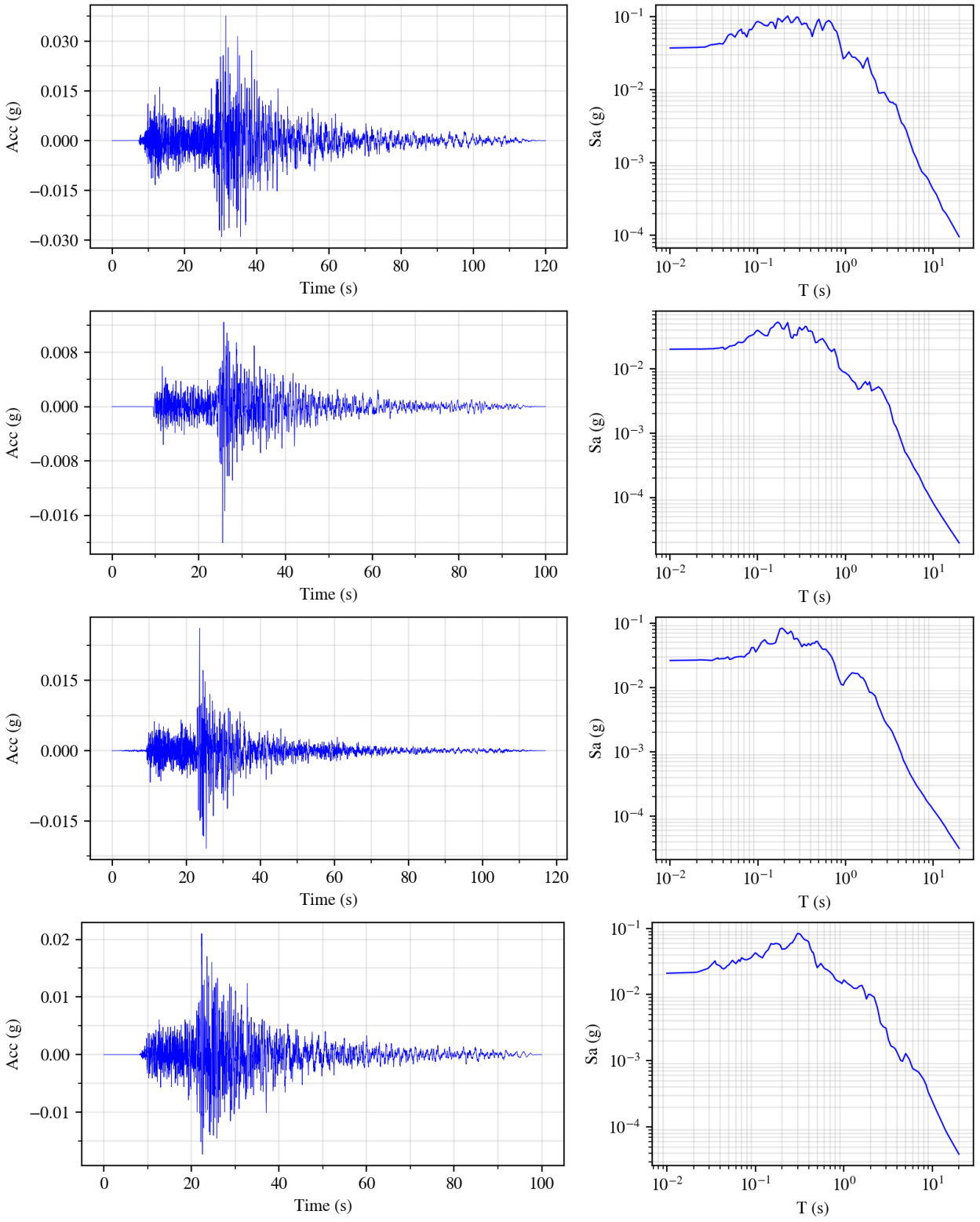


Figure 4.29 Acceleration time series to be applied at the base of the model and respective response spectrum for event 9, 11, 13 and 17

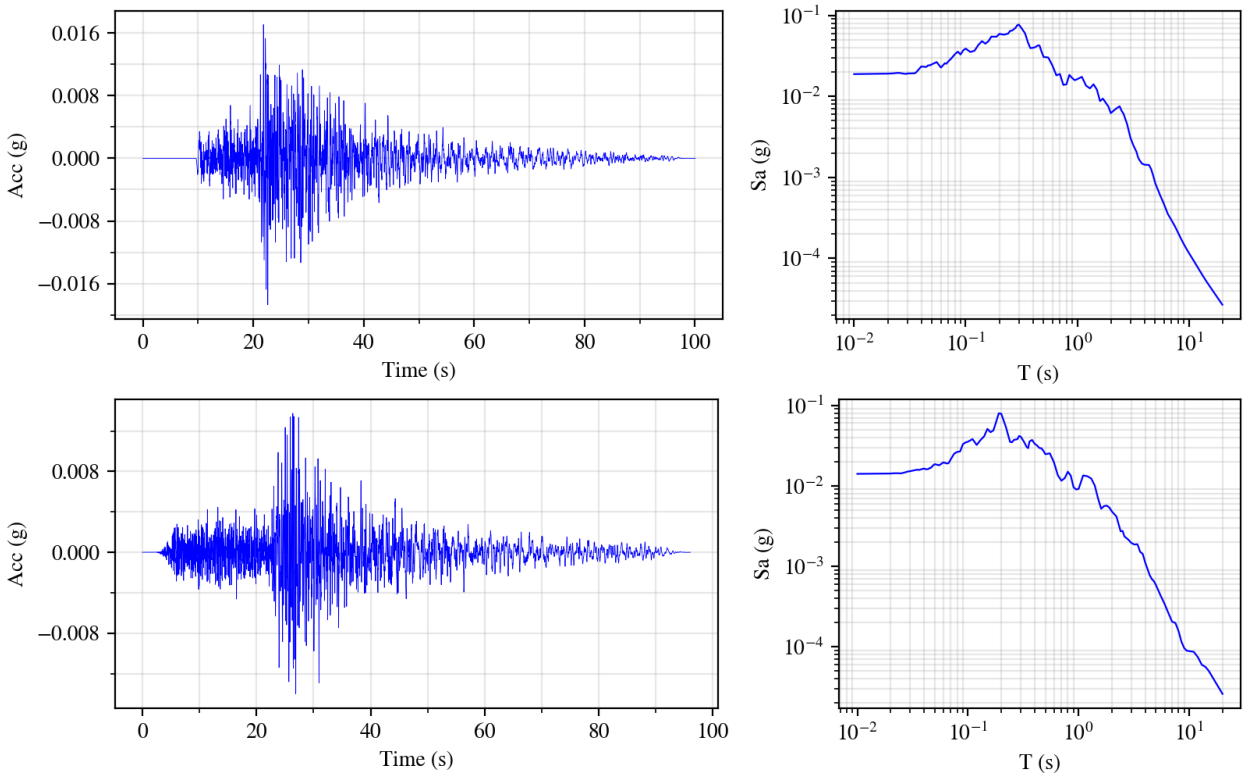


Figure 4.30 Acceleration time series to be applied at the base of the model and respective response spectrum for event 20 and 21

4.3.4 **Analysis Results**

Similar to what was performed at Nakshimo site, this section presents results for the finite element simulations compared with recorded response and reported performance data. The predicted and recorded surface motion time series together with their respective response spectrum are first compared. Profiles of peak acceleration, velocity and shear strain at the location of boring logs are plotted for each ground motion. Lastly, I also compared the predicted levee crest settlement with reported damage observations.

4.3.4.1 Comparison of Surface Motions

At Yamazaki site, I compared the surface crest motions at the location of sensor CG827421001a. As shown in Figures 4.31-4.33, the blue curve stands for the recorded response at Yamazaki site, and the

red curve represents the predicted response from finite element simulation results. Their response spectra are also plotted in the same figures. A residual term defined by Eq. 4.3 was computed to assess how well the response spectrum matches with each other, and all the residual terms are summarized in Table 4.9. Table 4.9 also summarized the peak acceleration (PGA) and peak velocity (PGV) values for both measured and predicted surface motion.

Generally speaking, the similar shape of response spectrum indicates that the response produced by finite element model matches quite well with the recorded response. The peaks of the response spectrum are also close to each other between the measurement and prediction. For Nakashimo site, it was observed that the residual term slowly increases as the motion gets stronger. But for the Yamzaki site, what seems to be interesting is that the residual terms for event 4 and 5, which are two strongest events among all, are relatively very small. This indicates that the finite element model performed quite well when the response gets nonlinear.

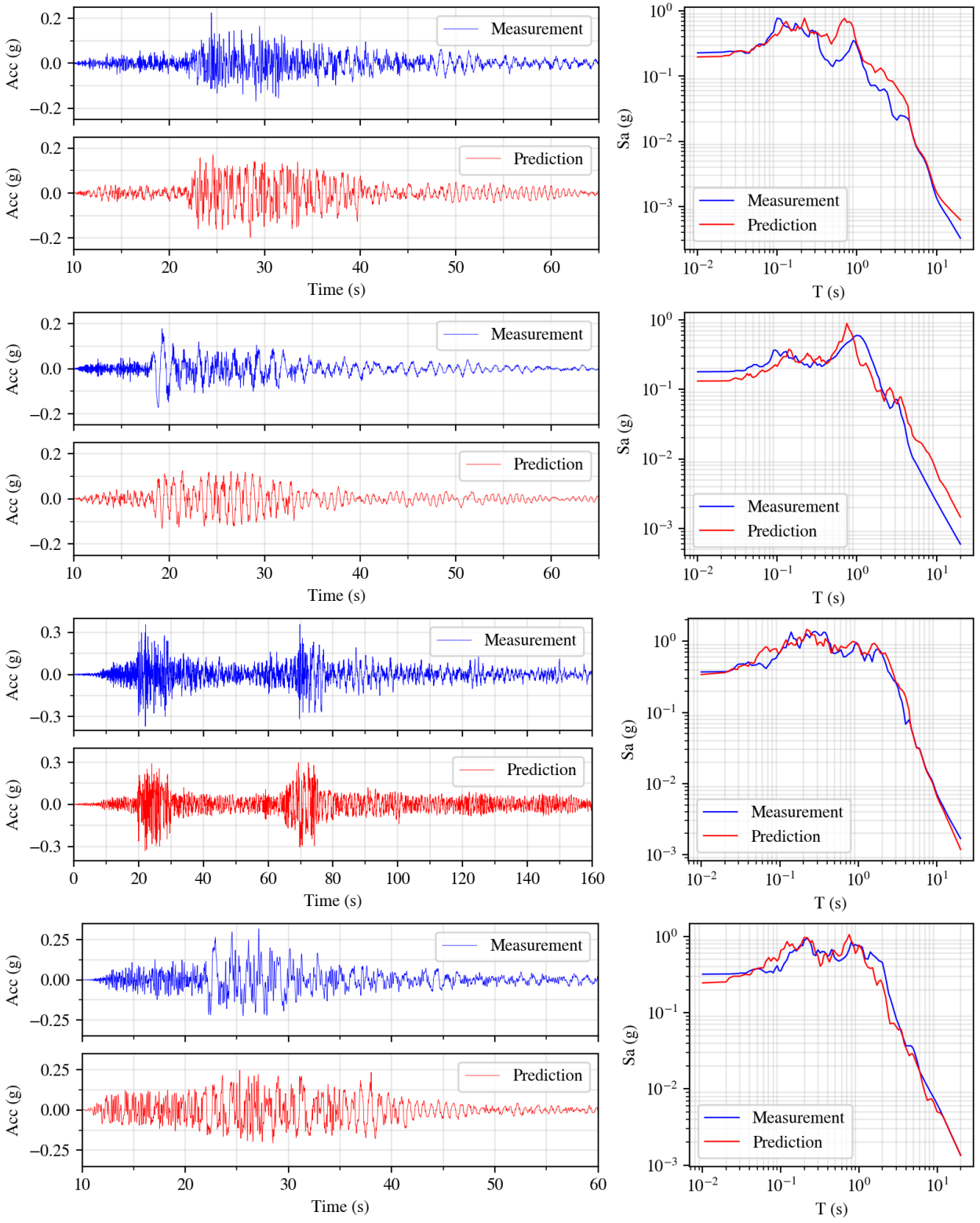


Figure 4.31 Predicted and measured surface motion at crest comparison for event 2, 3, 4 and 5

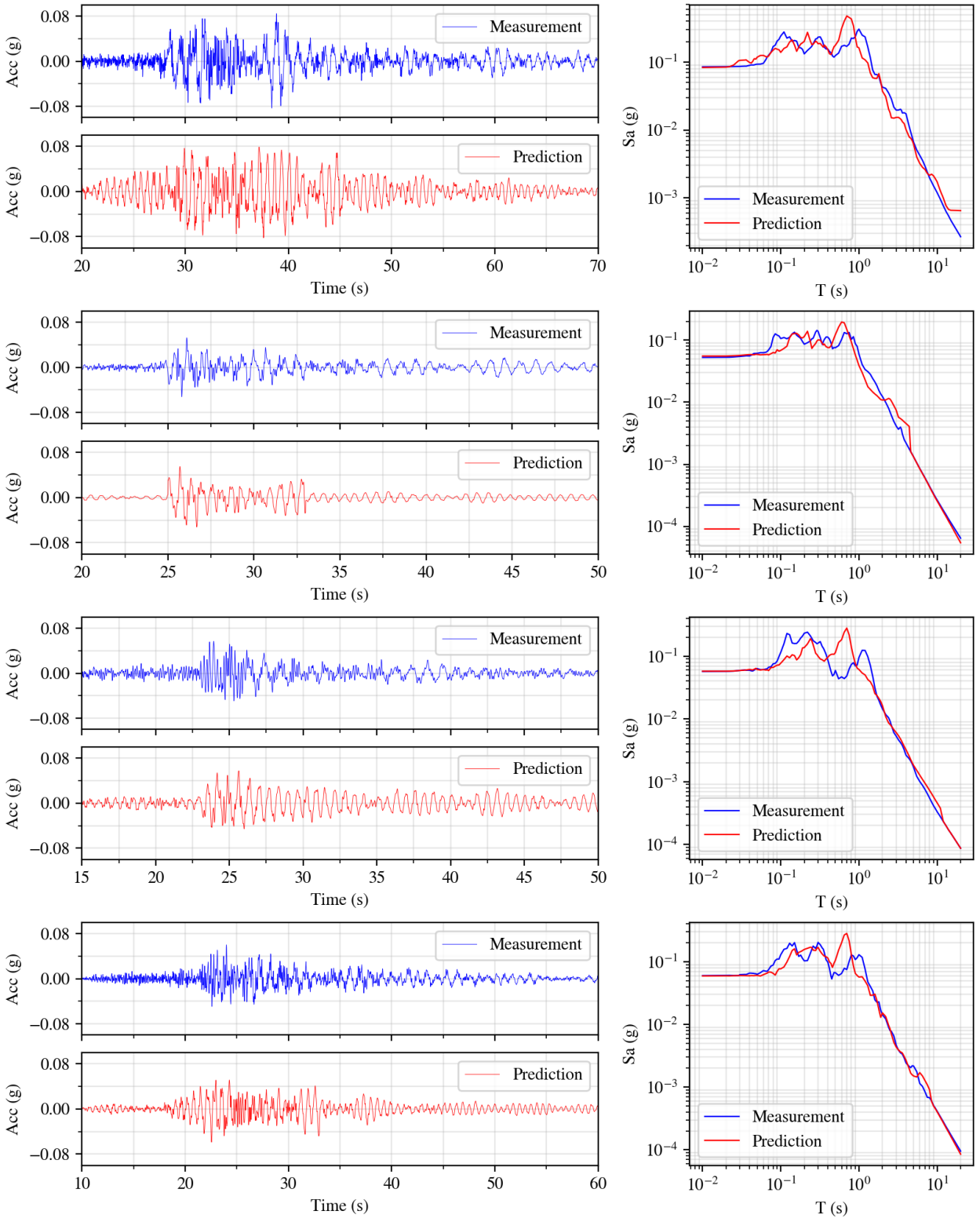


Figure 4.32 Predicted and measured surface motion at crest comparison for event 9, 11, 13 and 17

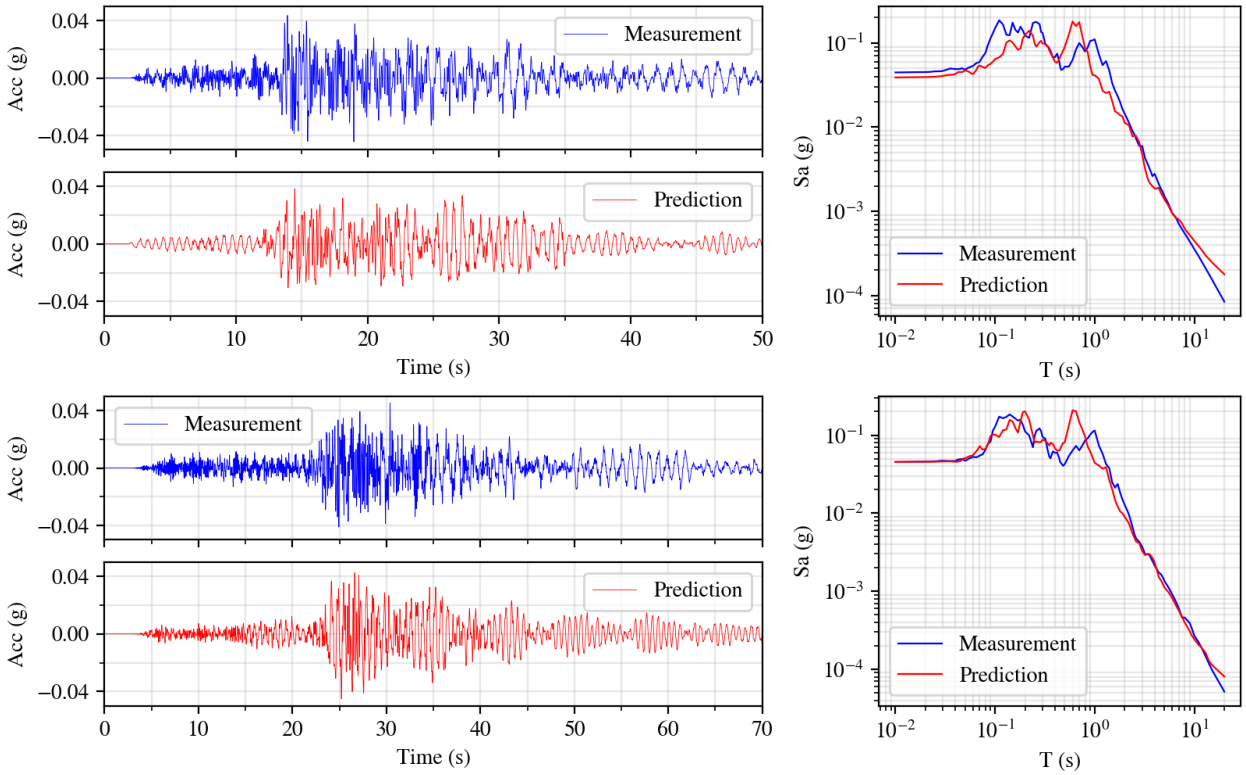


Figure 4.33 Predicted and measured surface motion at crest comparison for event 20 and 21

Table 4.9 PGA and PGV of measured and predicted surface motion at levee crest and residual term

Event ID	Year	Measured PGA at Crest (g)	Measured PGV at Crest (m/s)	Predicted PGA at Crest (g)	Predicted PGV at Crest(m/s)	ε
2	2005	0.226	0.111	0.189	0.099	0.28
3	2008	0.179	0.142	0.127	0.118	0.276
4	2011	0.37	0.470	0.345	0.453	0.066
5	2011	0.318	0.333	0.251	0.194	0.107
9	2008	0.085	0.096	0.083	0.074	0.123
11	2010	0.052	0.035	0.049	0.033	0.104
13	2011	0.057	0.046	0.056	0.049	0.226
17	2011	0.06	0.045	0.06	0.041	0.128
20	2011	0.044	0.035	0.04	0.034	0.171
21	2011	0.045	0.030	0.043	0.026	0.119

4.3.4.2 Profiles of Peak Acceleration and Peak Shear Strain

Similar to what was performed at the Nakashimo site, it will be interesting to see how the peak accelation, velocity and shear strain change over depth beneath the crest of the levee. Therefore, I recorded the response of a vertical array of elements at the location of the boring log, and plotted them versus depth.

Figure 4.34-4.37 are the profiles of peak acceleration (PGA), velocity (PGV) and shear strain for elements right under levee crest during these ten events, where the blue triangles represent the actual measurement from accelerometer recordings. A profile of shear strength is also plotted in the figures, where the shear strength is computed as $\sigma_v'\tan(\phi')$ for sand layers and undrained shear strength shown for clay layers. It appears that for most of the events, PGA slowly increases as it goes from the base to the surface of the model. The response gets more complicated for the two strongest events (event 4 and 5). It is obviously observed from these figures that shear strain occurs the most at the peat layer and the clay layer right above it, which seems reasonable because these two layers have relatively

low shear wave velocities as well, and the 2011 Tohoku-oki event caused significantly more shear strain among them all.

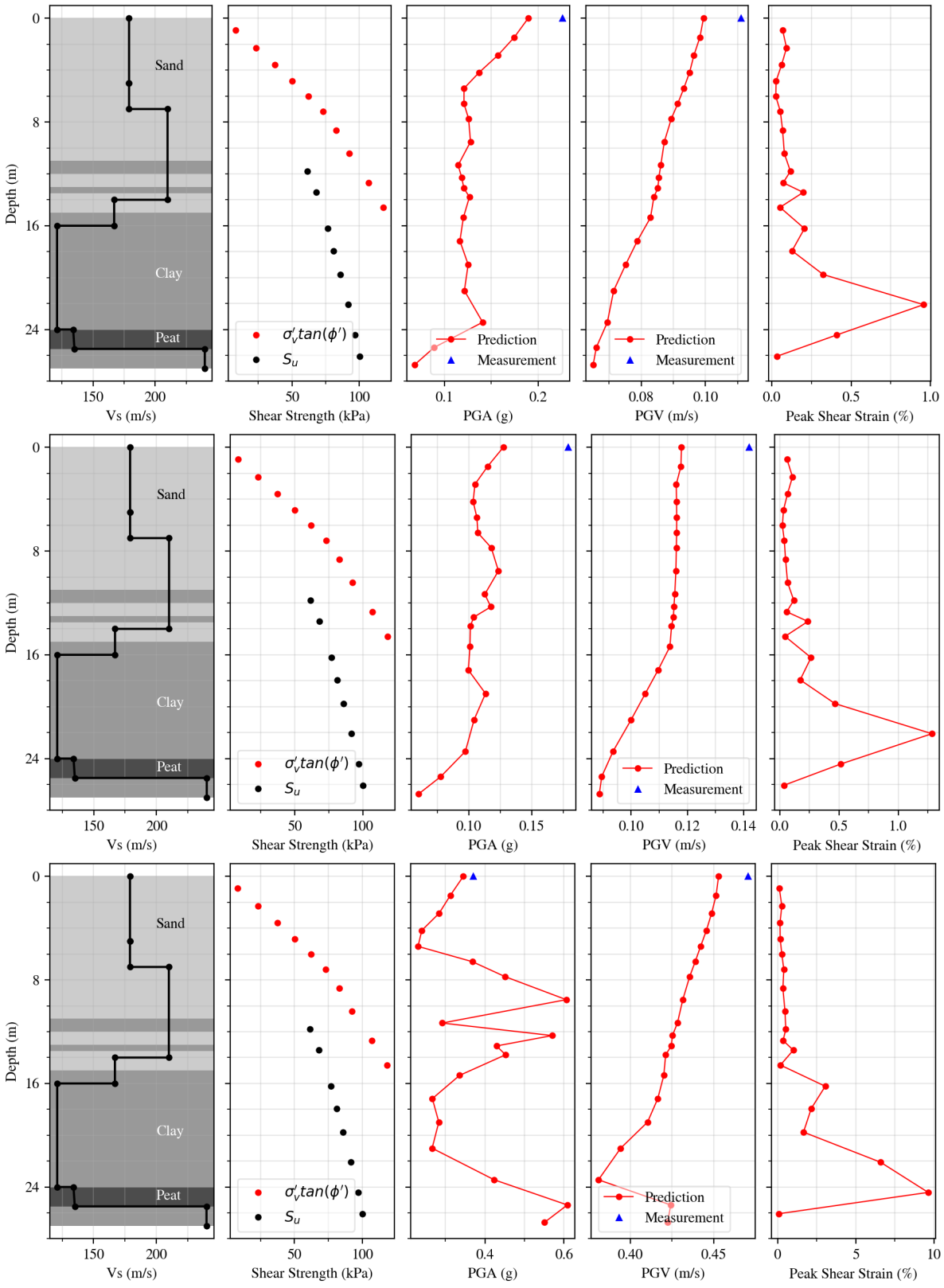


Figure 4.34 Profiles of PGA, PGV and peak shear strain for event 2, 3 and 4

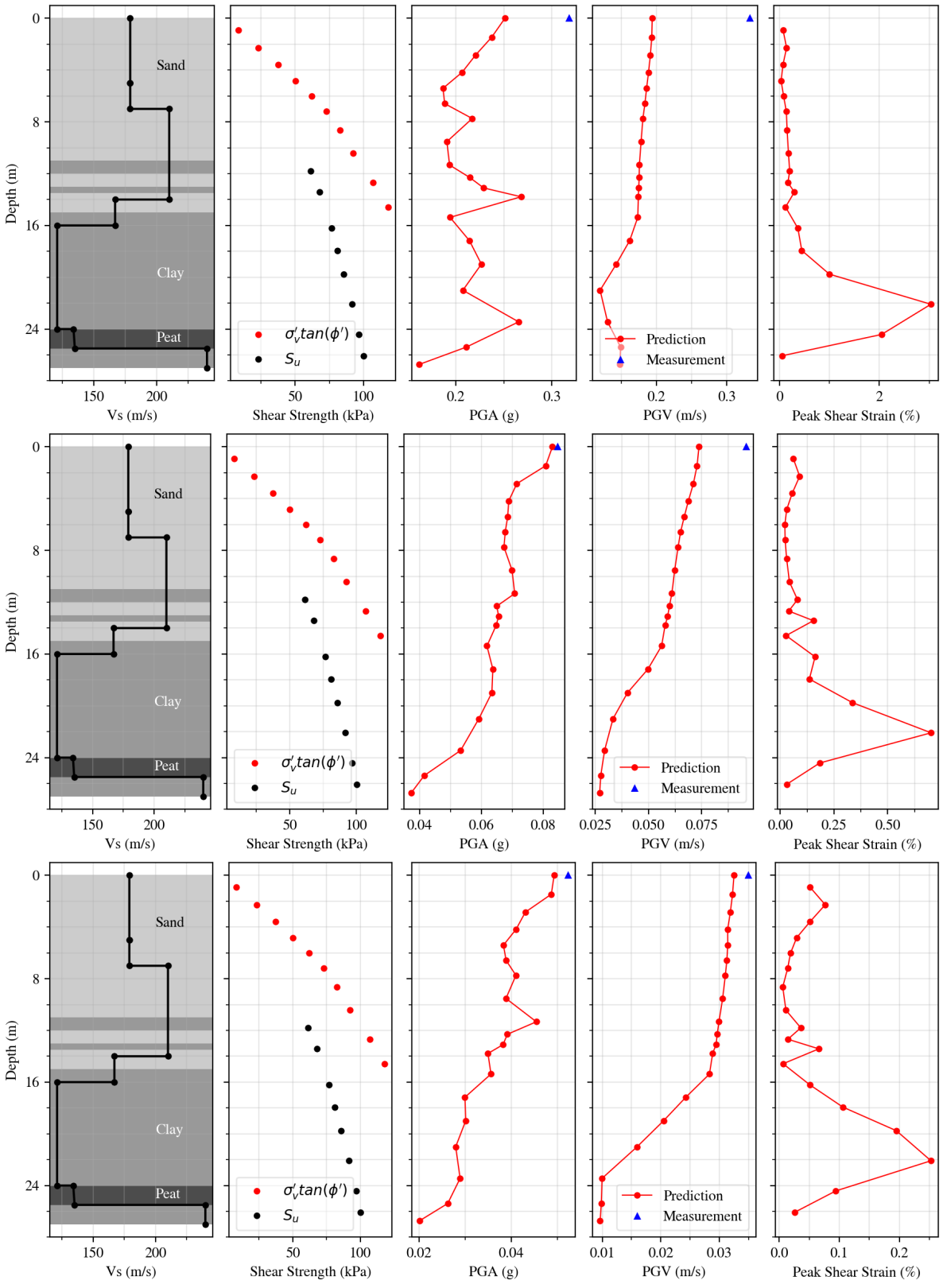


Figure 4.35 Profiles of PGA, PGV and peak shear strain for event 5, 9 and 11

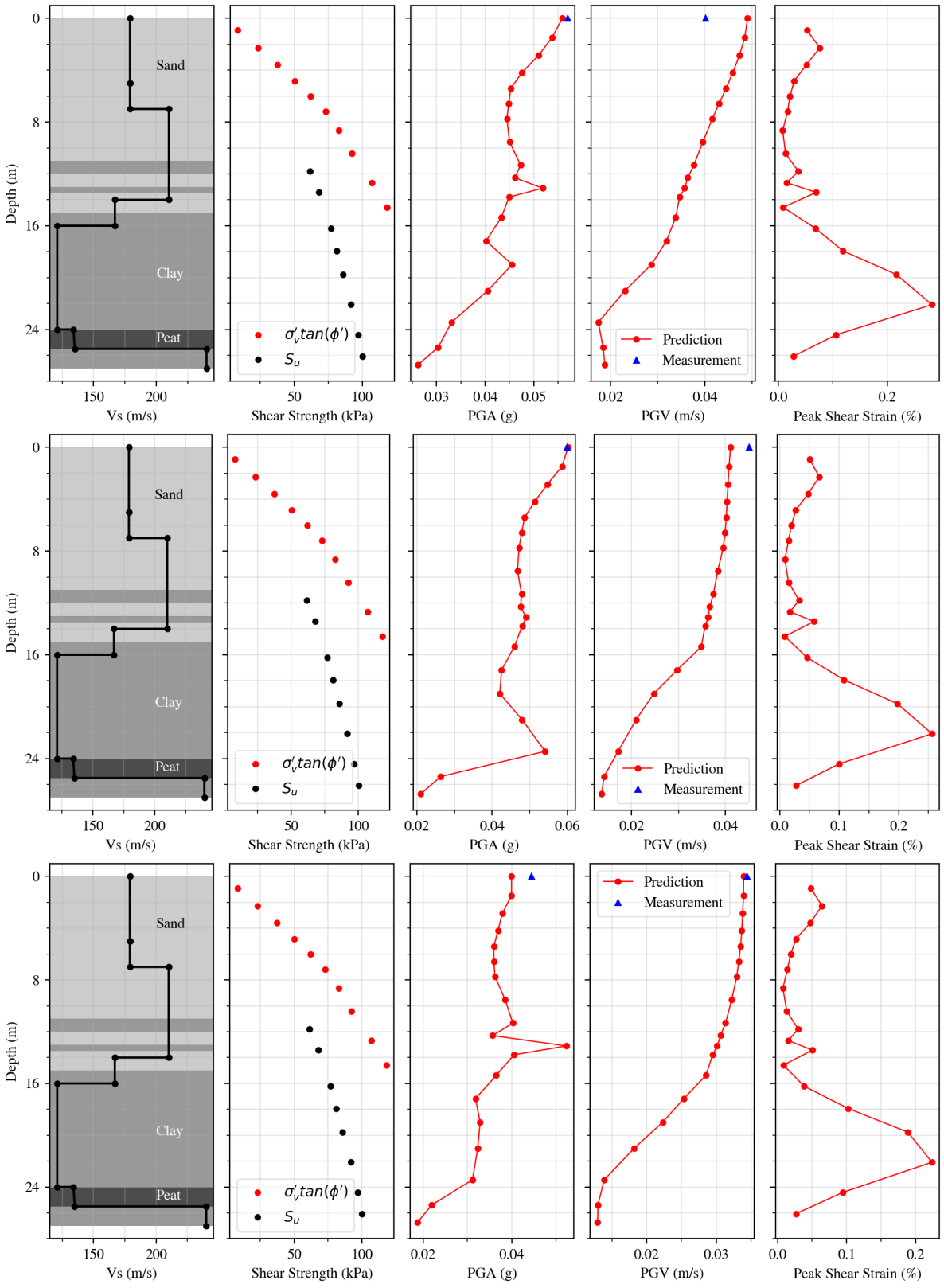


Figure 4.36 Profiles of PGA, PGV and peak shear strain for event 13, 17 and 20

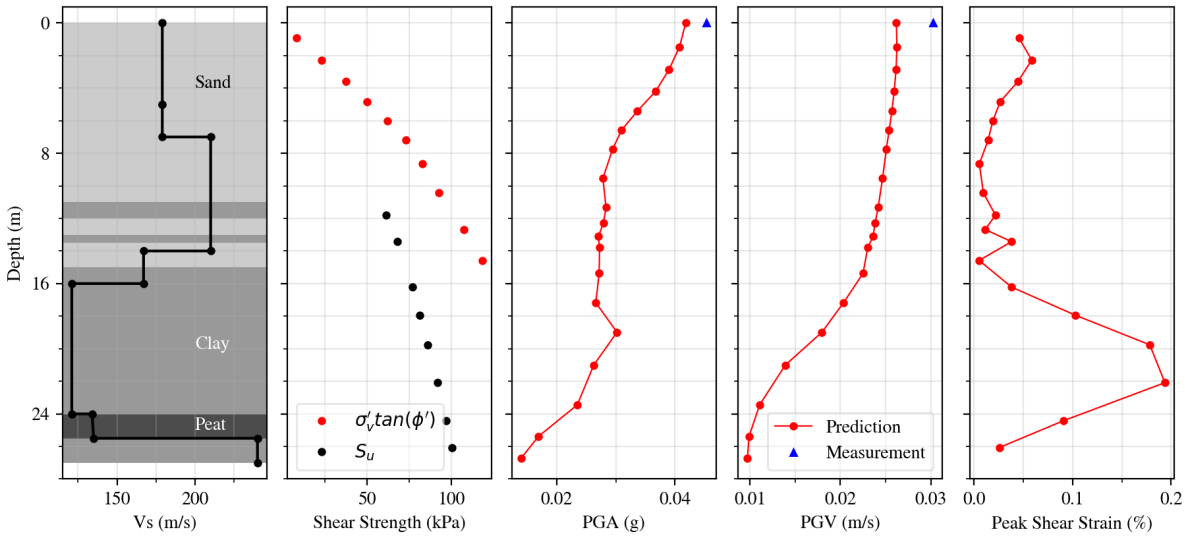


Figure 4.37 Profiles of PGA, PGV and peak shear strain for event 21

4.3.4.3 Observed Damage versus Predicted Damage

At the Yamazaki site, a post-earthquake reconnaissance reported a subsidence of levee crest of about 59cm after the 2011 Tohoku-oki event, and there is no reported damage for all the other events. Therefore, I recorded the average crest settlement in the finite element analysis and compared the results with the actual reported settlement, which are all summarized in Table 4.10. Table 4.10 shows that the finite element model predicted approximately 69 cm of crest settlement during the 2011 Tohoku-oki event, which is quite close to the actual reported settlement. Settlements were over-predicted for events 2, 3, 5, and 9, where damage level 1 was predicted, but no damage was reported. It is unclear what amount of settlement would be required to render a damage report. We have interpreted this to be 1.0cm, but it is conceivable that larger settlements could go unreported, particularly if the settlement was relatively uniform. Therefore it is unclear the extent to which these are actually over-predictions.

All things considered, the crest settlement prediction matches quite well with observed damage observation. Table 4.10 also summarizes the damage level that is determined based on the damage level classification shown in Table 4.7. Lastly, Figure 4.38 shows how the crest settlement changes

with the measured PGV at levee crest, and it is obvious that as the PGV of the crest motion increases, the settlement is also increasing as well as the associated damage level.

Table 4.10 Settlement and damage level comparison

Event ID	Year	Damage Observation	Measured PGV at Crest (m/s)	Observed Damage level	Predicted Settlement (cm)	Predicted Damage level
2	2005	No damage reported	0.111	0	1.84	1
3	2008	No damage reported	0.142	3	2.31	1
4	2011	Vertical settlement about 59 cm	0.470	0	69.26	3
5	2011	No damage reported	0.333	0	5.71	1
9	2008	No damage reported	0.096	0	1.23	1
11	2010	No damage reported	0.035	0	0.3	0
13	2011	No damage reported	0.046	0	0.37	0
17	2011	No damage reported	0.045	0	0.24	0
20	2011	No damage reported	0.035	0	0.2	0
21	2011	No damage reported	0.030	0	0.1	0

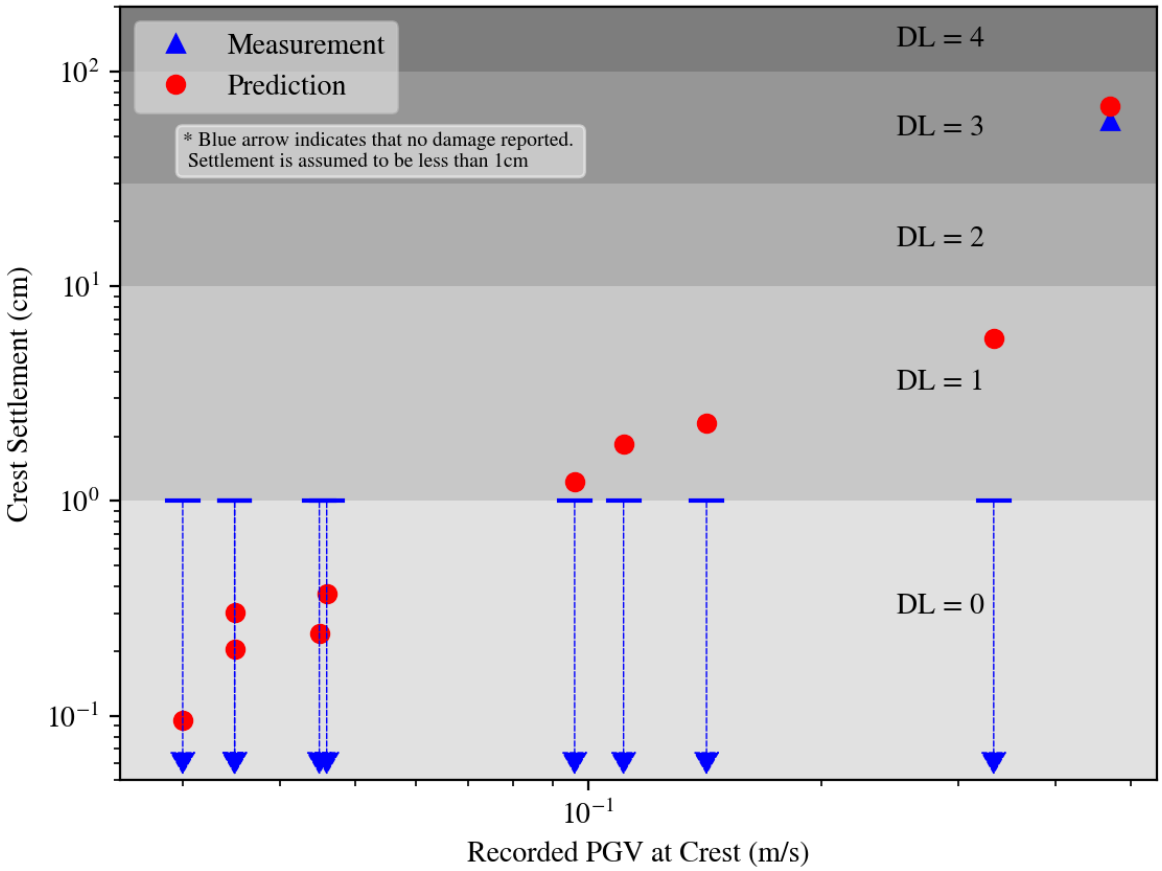


Figure 4.38 Crest settlement versus recorded PGV at levee crest

4.4 KOZUKA SITE

4.4.1 Site Conditions

The Kozuka site is located 5km upstream from the old Kitakami river mouth and on the north side of the river channel (Zimmaro et al. 2019). As shown in Figure 4.39, the levee is constructed by fill resting on clay and sand layers, overlying the bedrock. At one of the site explorations in 2004, the ground water was found approximately 2m below the base of the levee fill.

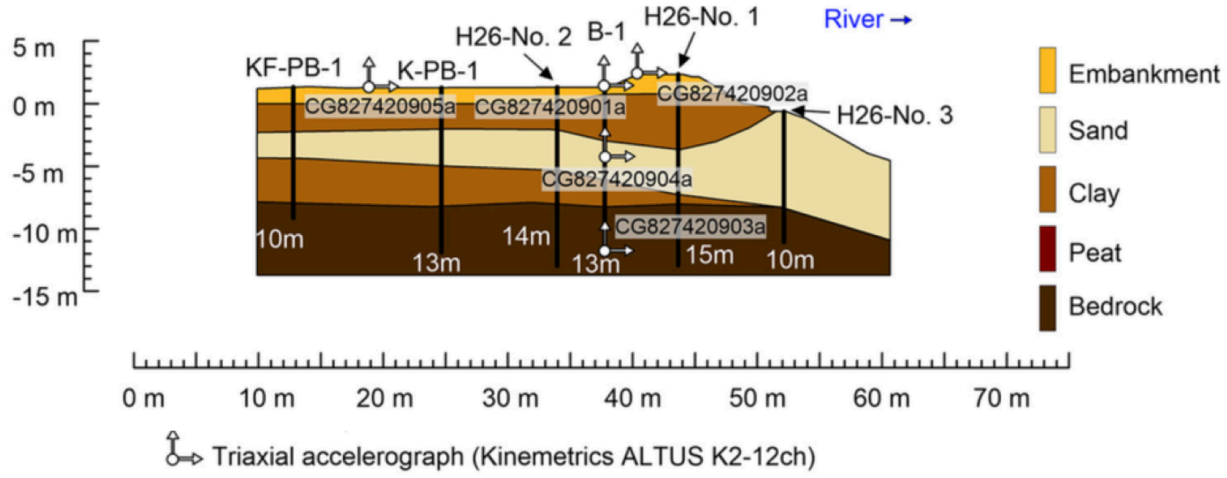


Figure 4.39 Cross-section, stratigraphy under the levee, boring log locations and sensors locations at Kozuka site (Zimmaro et al. 2019)

There are five accelerometers installed at this site: a vertical array of accelerometers at B-1(CG8274209021a, CG827420904a and CG827420903a), one at the levee crest (CG827420902a), one at the landside (CG827420905a). There are multiple boring logs located at this site, which are indicated in both Figure 4.39 and Figure 4.40 (Zimmaro et al. 2019), which help define the layering of the strata beneath the levee crest. The blow counts profiles for each existing boring log at this site are shown in Figure 4.40. Ground water elevation data are also available at these boring logs and indicated in the figure as well.

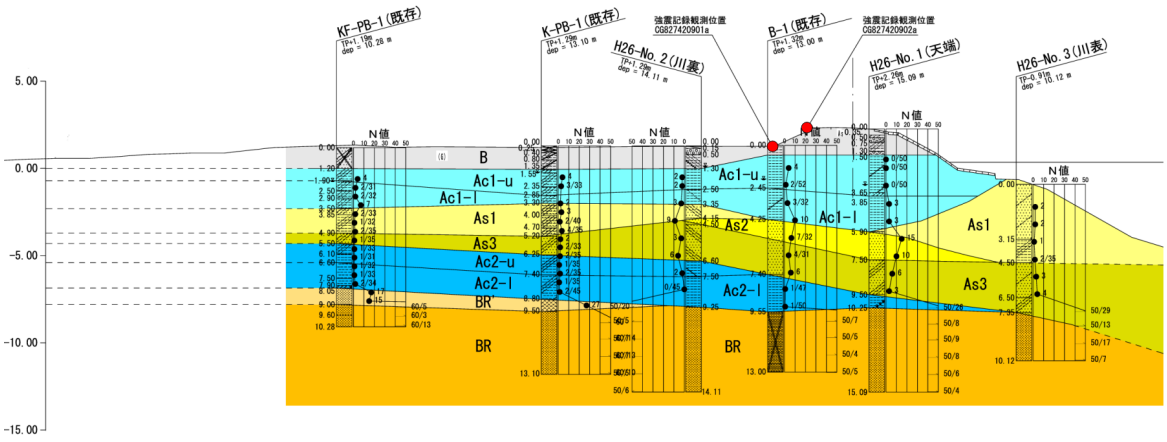


Figure 4.40 Detailed blow counts profile at boring log locations of Kozuka site

Shear wave velocity profiles are also available at this site. At borehole H26-No.1 and borehole H26-No.2, shear wave velocities are obtained using both downhole method and suspension logging method. One shear wave profile obtained from suspension logging method is also available at borehole K-PB-1. These shear wave velocity profiles are shown in Figure 4.21.

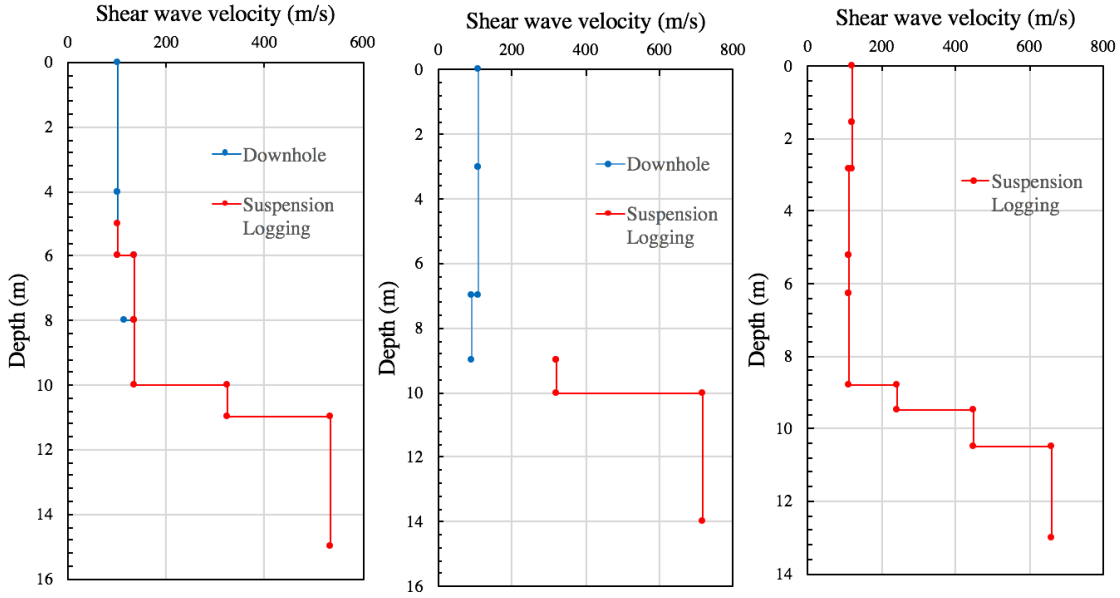


Figure 4.41 Shear wave velocity profile at borehole H26-No.1, H26-No.2, and K-PB-1

4.4.2 **Recorded Response and Reported Performance**

As listed in Table 4.3, Kozuka site experienced eleven earthquake events in total including two strong event and nine relatively weak events. Again, the surface motion records at the crest will be quite useful for the validating of the finite element model, so surface motions recorded by sensor CG827420902a are of more interest to this study. The downhole accelerometer (CG827420903a) would have been very useful as its recordings can be directly used as our input motion to the finite element model. However, it turns out the time series recorded by this sensor seem to only contain noises and could not be used at all. In this case, recordings by sensor CG827420904a or sensor CG827420901a need to be used for a deconvolution analysis. For this reason, only surface recordings at the crest are plotted in the following.

Figures 4.41-4.43 are horizontal components of ground motion records at surface accelerometer (CG827420902a) during events 3, 4, 9-12, 15, 16, 22, 24 and 25. Their response spectra are also plotted in the same figures. Again, the strongest event among all for the Kozuka site is also event 4, which is the 2011 Tohoku-oki event. The ground motion record for this event is being chopped off around 250 seconds when implemented into finite element modeling to save the computational cost. No surficial evidence of liquefaction was found and reported after the 2011 Tohoku-oki event, and no damage was reported after all the other events either.

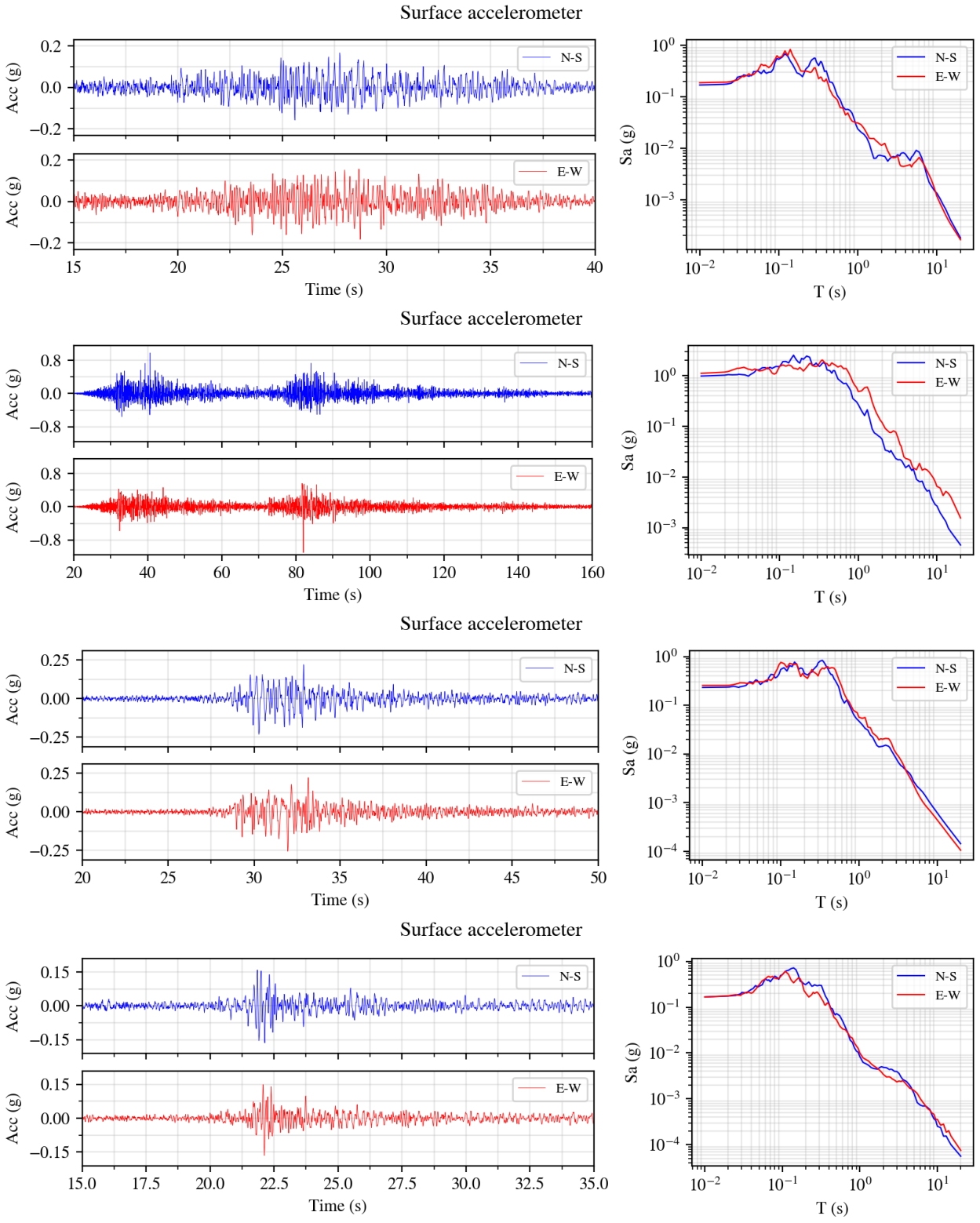


Figure 4.42 Acceleration time series recorded during event 3, 4, 9 and 10

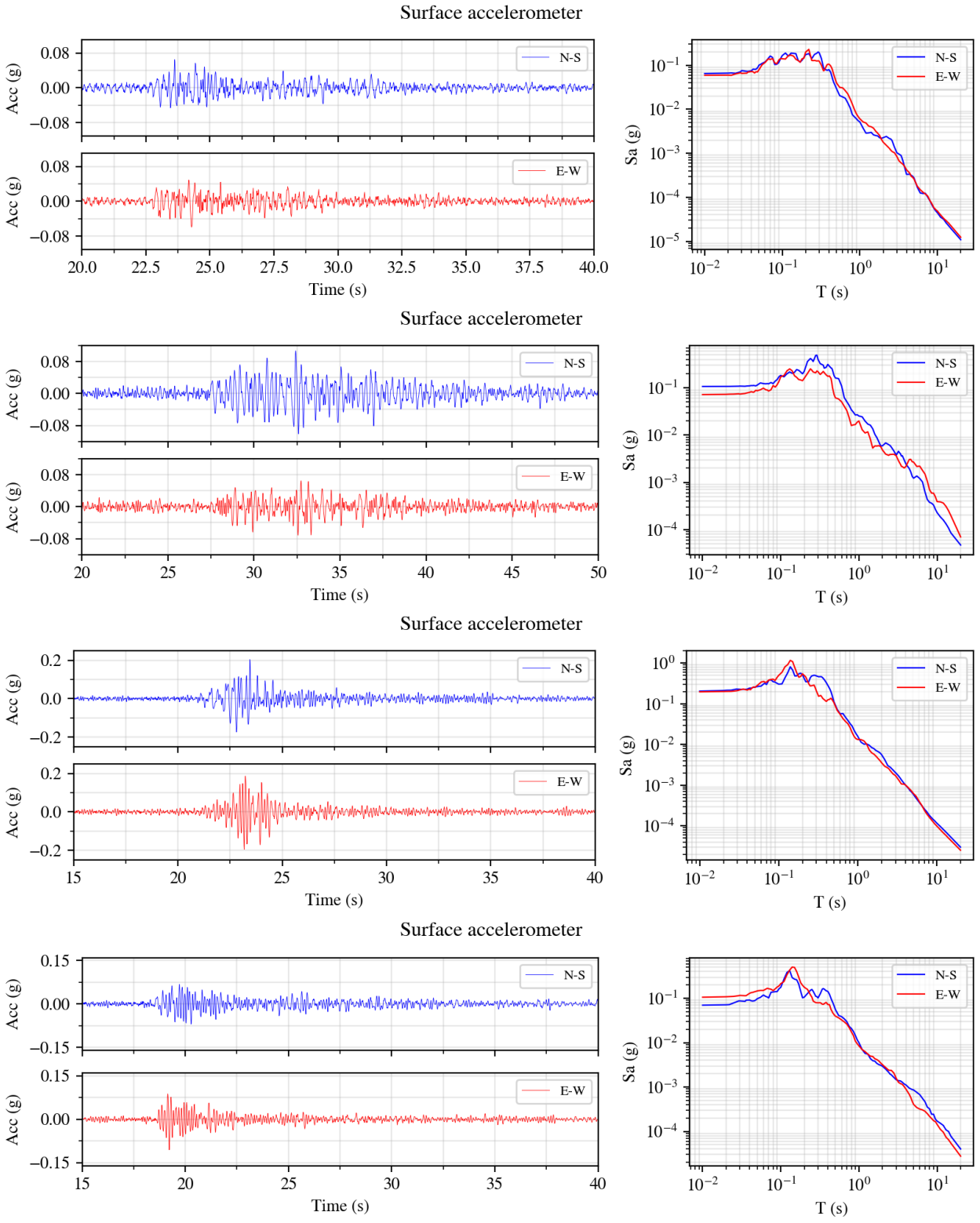


Figure 4.43 Acceleration time series recorded during event 11, 12, 15 and 16

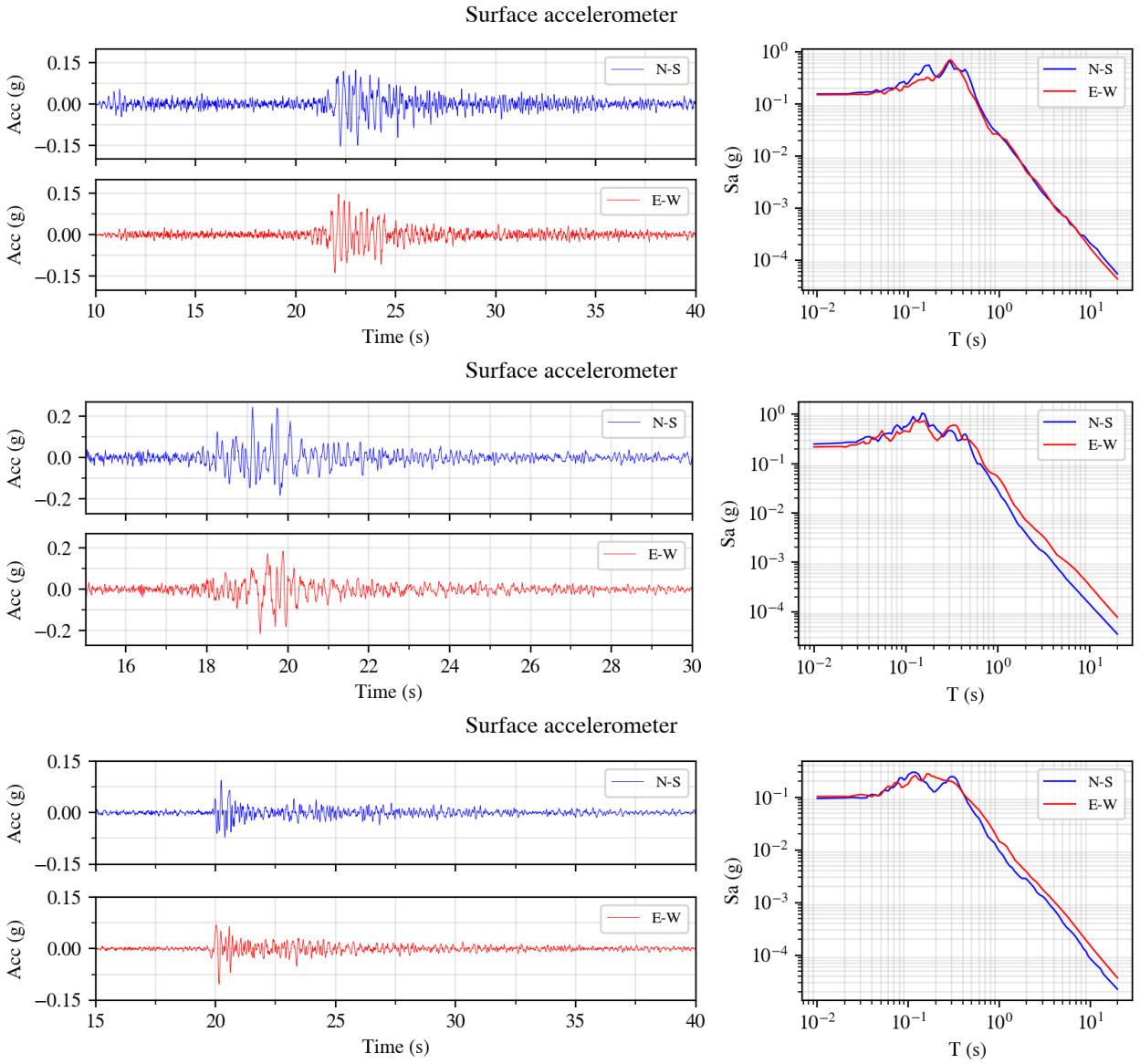


Figure 4.44 Acceleration time series recorded during event 22, 24 and 25

4.4.3 **Finite Element Model Setup**

Figure 4.44 shows the generated mesh after integrating information such as the geometry and material boundaries obtained from cross-section profile into GiD. The two thick columns on either side of the model are two free-field columns. Similar to Yamzaki site, the phreatic surface beneath the crest was included when generating the mesh, which was shown as the material boundary between the yellow and dark blue layers. The ground water elevation was recorded in the boring logs and the site

exploration also reported that the ground water table was at 2m below the base of the levee fill, so it is reasonable to assume the water table beneath the crest of the levee is hydrostatic and the water table is near the top surface of layer 3.

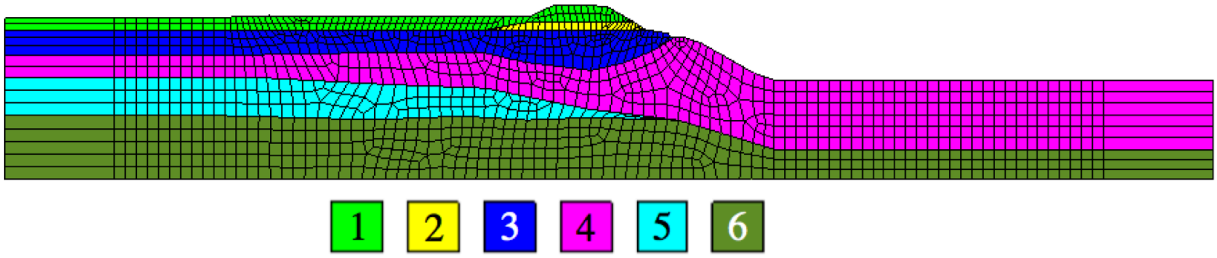


Figure 4.45 Mesh configuration using GiD

After creating the mesh, material properties need to be assigned to the elements. Table 4.11 summarizes some of the important parameters that are either directly used or related to material input parameters in OpenSees. Similar to the other two sites, the shear wave velocity is used to determine the small strain shear modulus, and the Poisson ratio is used to relate the shear modulus and bulk modulus. The relative density for the sand layer is based on the blow counts that exists at the boring log locations (Idriss and Boulanger, 2008), and the undrained shear strength was determined based on the overconsolidation ratio and vertical effective stress. The permeability for different layers are varied based on the soil type, and are summarized in the table as well.

Table 4.11 Material properties used based on available data and assumptions

Soil Type	MD	Layer Tag	ρ (g/cm^3)	υ	V_S (m/s)	D_R	OCR	k_x (m/s)	k_y (m/s)
Sand	PDMY03	1	1.9	0.35	102	46%	NA	$5x10^{-7}$	$5x10^{-7}$
Clay	PIMY	2	1.7	0.4	102	NA	2	$5x10^{-9}$	$5x10^{-9}$
Clay	PIMY	3	1.8	0.4	102	NA	2	$5x10^{-9}$	$5x10^{-9}$
Sand	PDMY03	4	2.2	0.35	136	45%	NA	$5x10^{-7}$	$5x10^{-7}$
Clay	PIMY	5	1.8	0.4	115	NA	2	$5x10^{-9}$	$5x10^{-9}$
Bedrock	PIMY	6	2.7	0.25	534	NA	NA	$5x10^{-11}$	$5x10^{-11}$

The last step is to apply the right ground motion to the base of the model. No dashpot is used since the motions recorded by the downhole accelerometers are within motions. As mentioned earlier, the time series recorded by the downhole accelerometer (CG827420903a) seem to only contain noise and could not be used at all. The approach I am adopting herein is to use recordings by sensor CG827420904a (most events are recorded by this sensor) and perform a deconvolution analysis. The two horizontal components need to be firstly combined to be rotated to the direction transverse to the cross-section. Then the ground motions recorded by sensor CG827420904a were applied to the base of the model, and the acceleration time series was recorded at the same location of the sensor. A transfer function can be determined by taking the ratio of the Fourier amplitude of these two motions. Then the actual ground motion at the base can be back calculated by using the actual sensor recording and the computed transfer function. This is very similar to what was performed at the Nakashimo site. For events that are not recorded by sensor CG827420904a, the ground motions recorded by the surface accelerometer at the toe (CG827420901a) were then used for this deconvolution analysis instead. Figures 4.46-48 show the acceleration time series that should be applied at the base of the model after the deconvolution analysis.

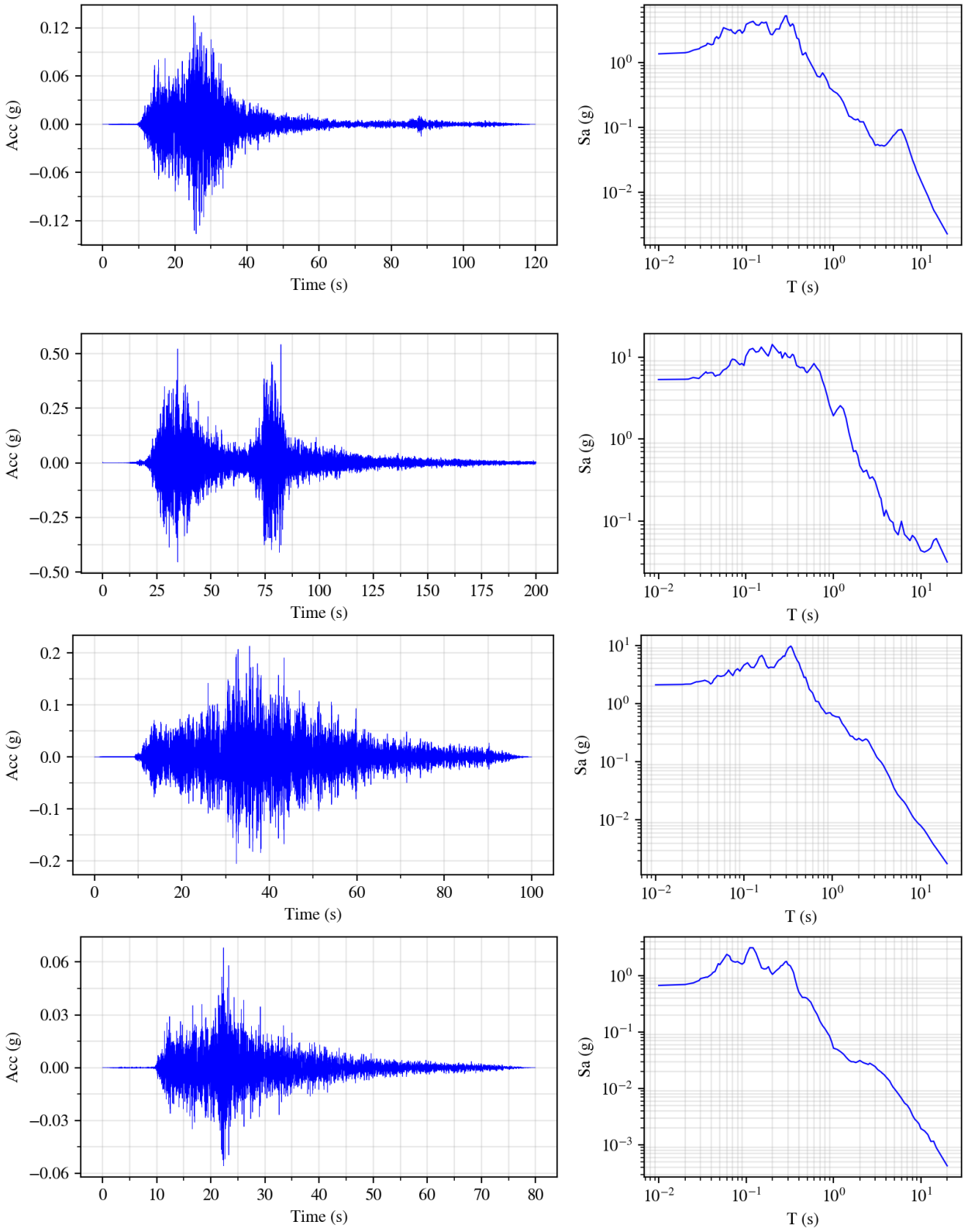


Figure 4.46 Acceleration time series to be applied at the base of the model and respective response spectrum for event 3, 4, 9 and 10

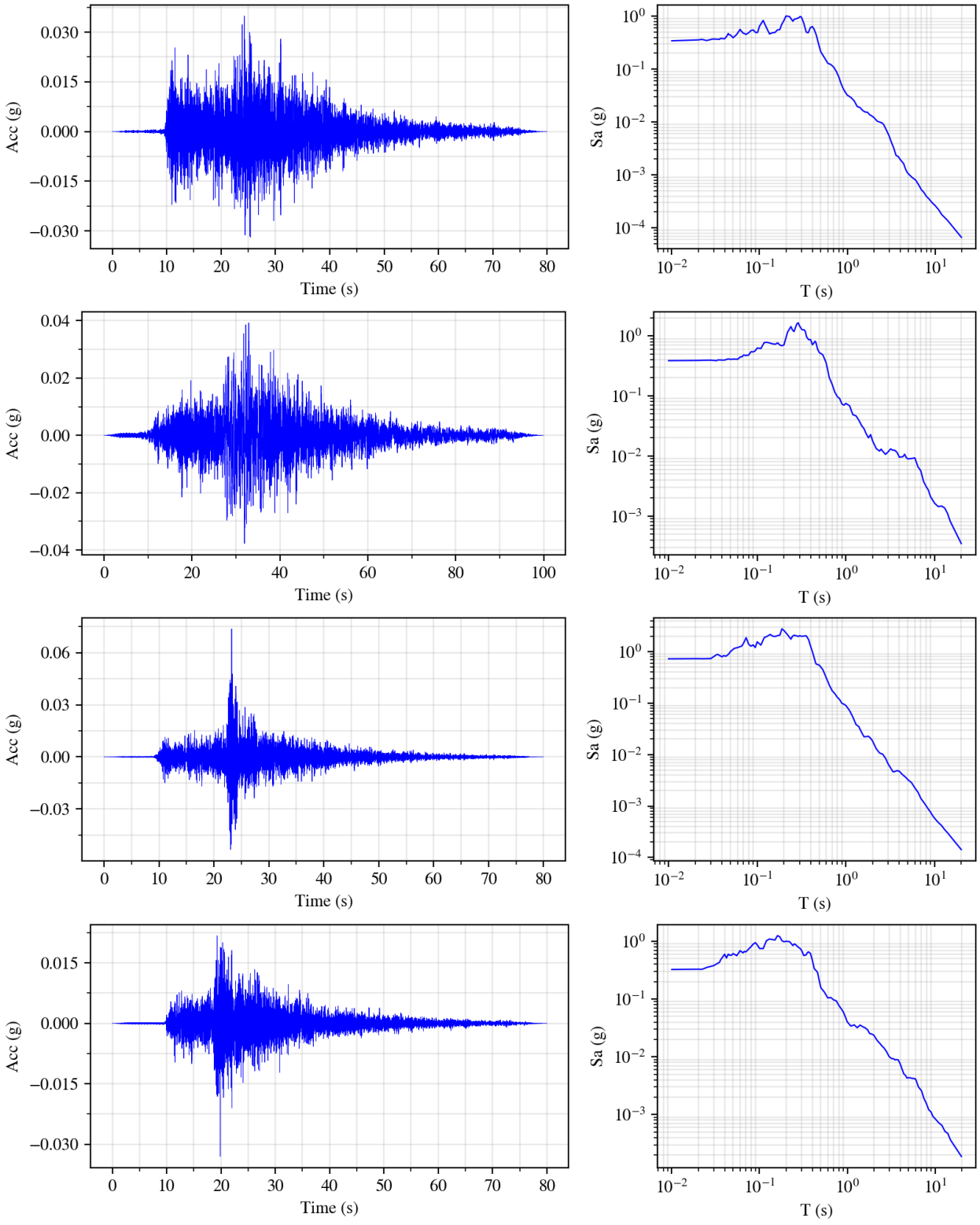


Figure 4.47 Acceleration time series to be applied at the base of the model and respective response spectrum for event 11, 12, 15 and 16

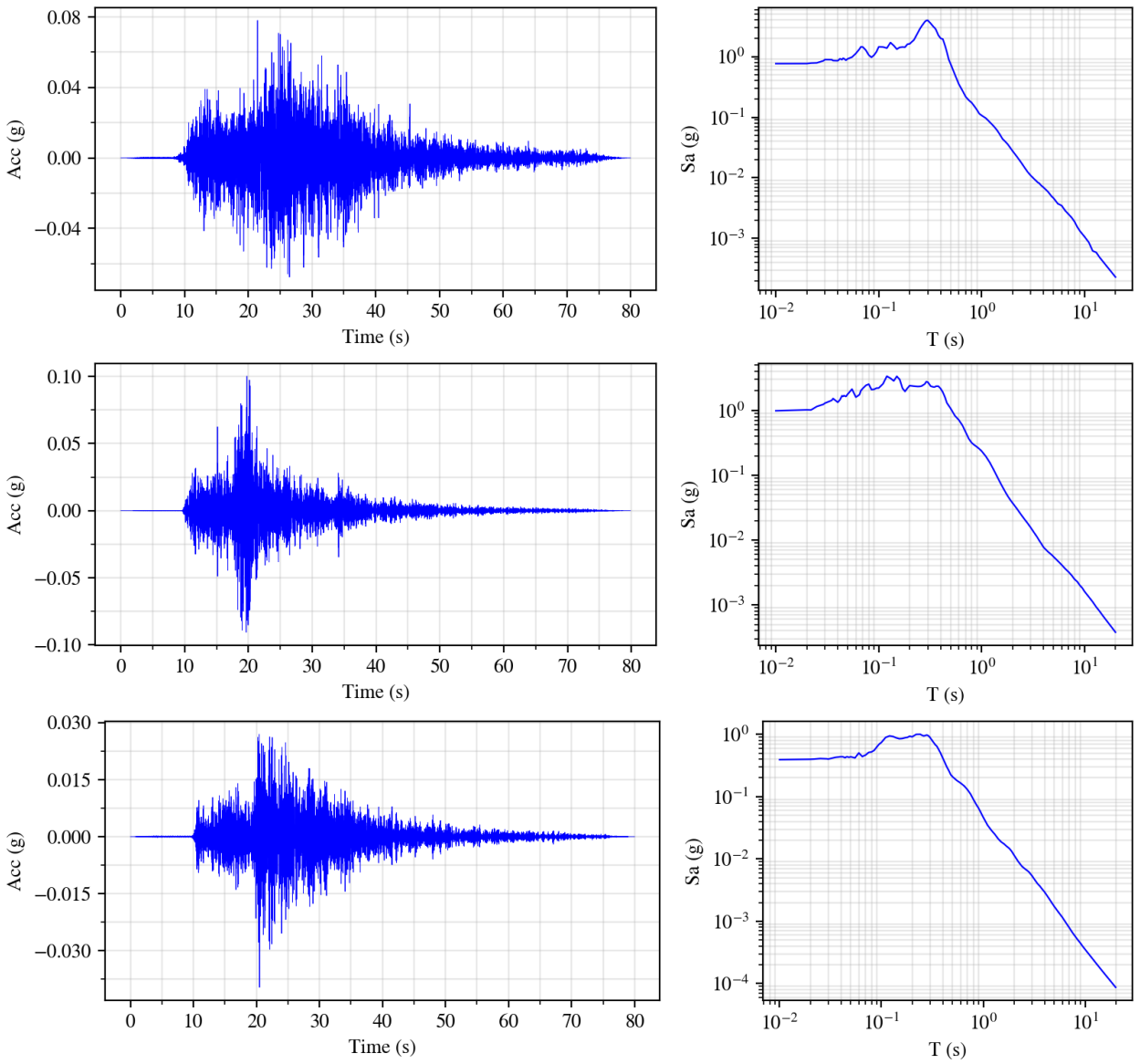


Figure 4.48 Acceleration time series to be applied at the base of the model and respective response spectrum for event 22, 24 and 25

4.4.4 **Analysis Results**

Similar to what was performed at the other two sites, this section presents results for the finite element simulations compared with recorded response and reported performance data. The predicted and recorded surface motion time series together with their respective response spectrum are first compared. Profiles of peak acceleration, velocity and shear strain at the location of boring logs are plotted for

each ground motion. Lastly, I also compared the predicted levee crest settlement with reported damage observations.

4.4.4.1 Comparison of Surface Motions

At the Kozuka site, I compared the surface crest motions at the location of sensor CG827420902a. As shown in Figures 4.49-4.33, the blue curve stands for the recorded response at Kozuka site, and the red curve represents the predicted response from finite element simulation results. Their response spectra are also plotted in the same figures. A residual term defined by Eq. 4.3 was computed to assess how well the response spectrum matches with each other, and all the residual terms are summarized in Table 4.9. Table 4.9 also summarized the peak acceleration (PGA) and peak velocity (PGV) values for both measured and predicted surface motion.

Again, the similar shape of response spectrum indicates that the response produced by finite element model matches quite well with the recorded response. The peaks of the response spectrum are also close to each other between the measurement and prediction. The finite element model was able to predict a similar value of PGA and PGV at the levee crest for most of the events compared with the measurements. However, for the 2011 Tohoku-oki event, the model seemed to have under-predicted the motion at the crest. Considering that this event is a very extreme event, and the response of the levee may get more nonlinear and complicated.

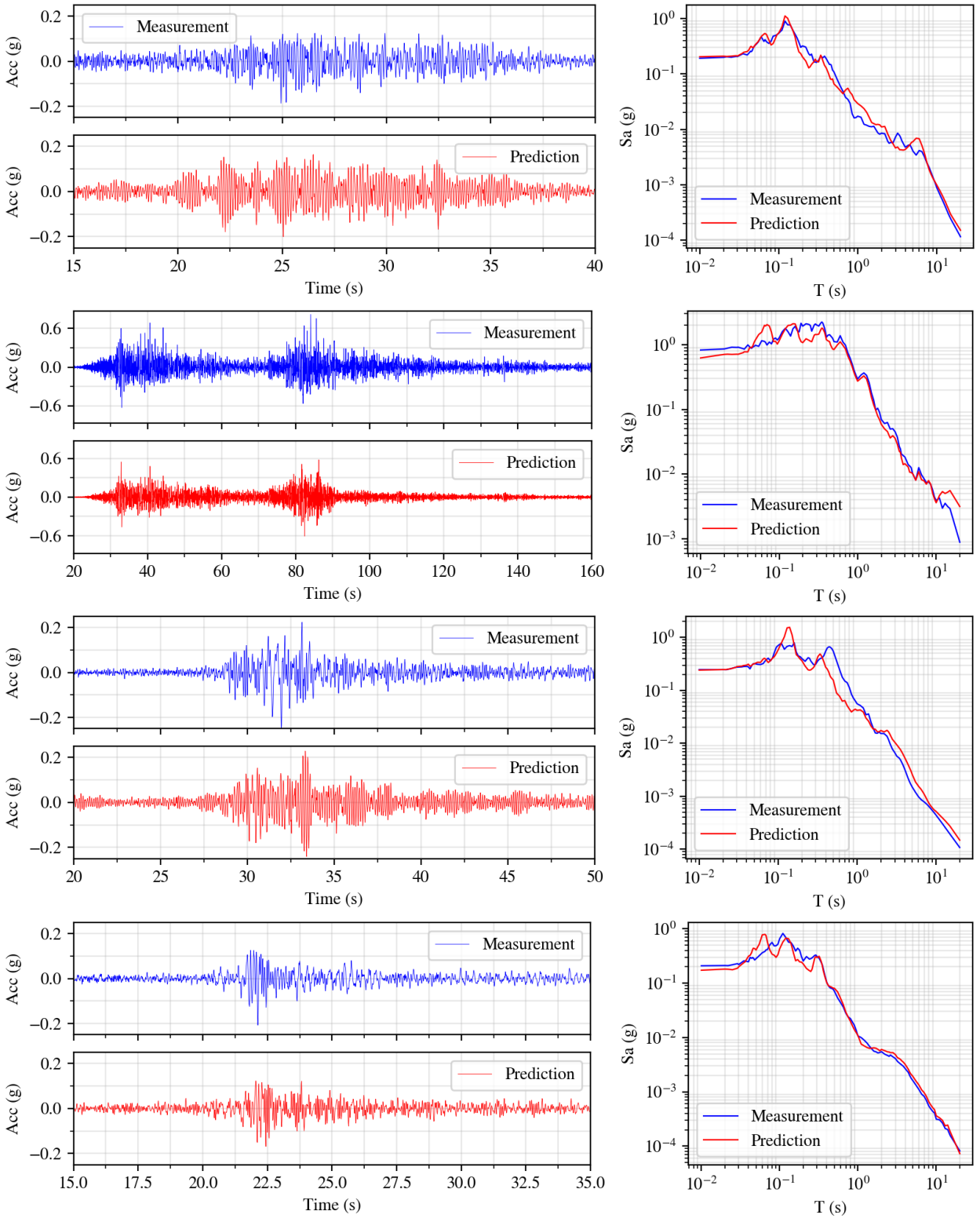


Figure 4.49 Predicted and measured surface motion at crest comparison for event 3, 4, 9 and 10

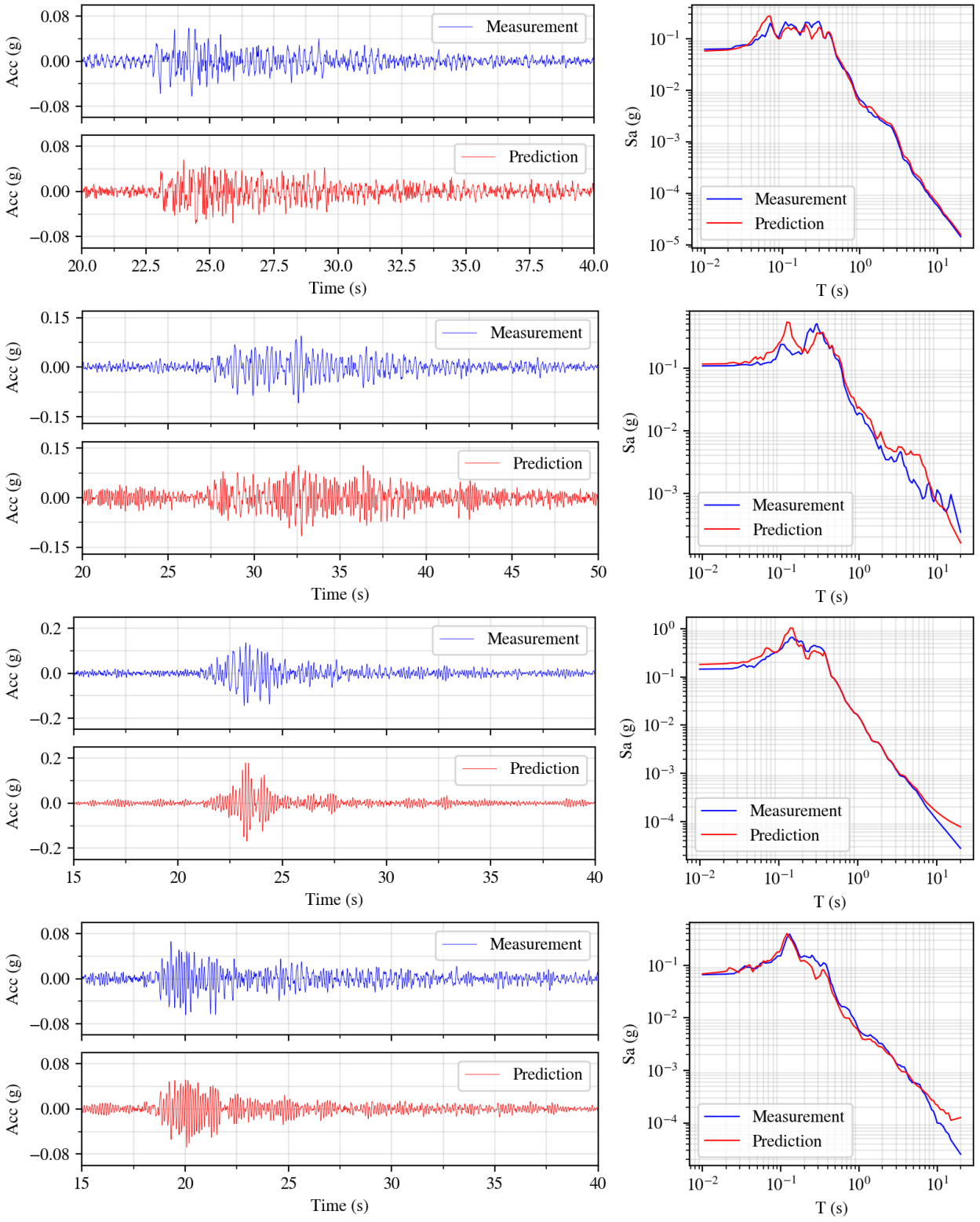


Figure 4.50 Predicted and measured surface motion at crest comparison for event 11, 12, 15 and 16

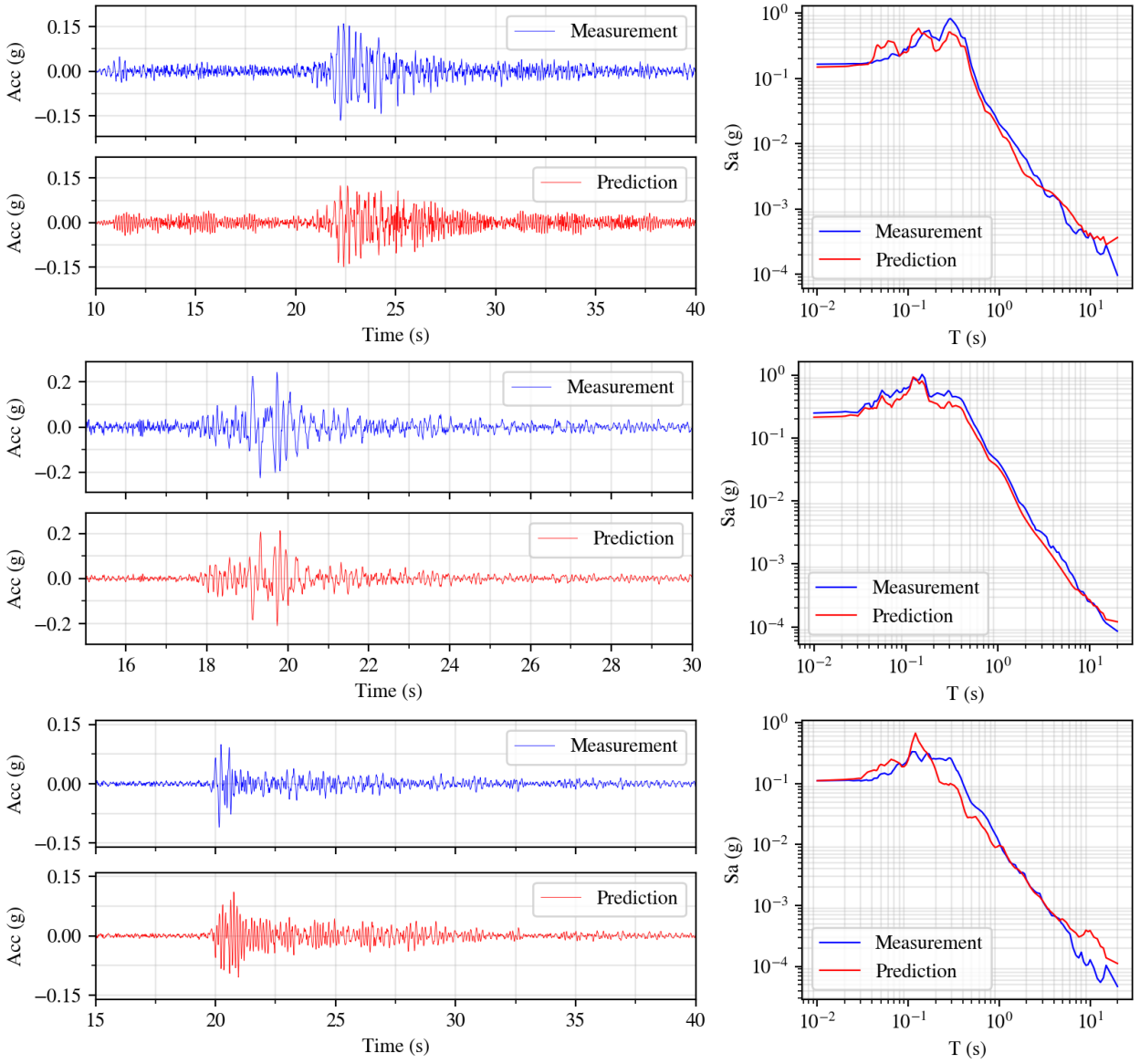


Figure 4.51 Predicted and measured surface motion at crest comparison for event 22, 24 and 25

Table 4.12 PGA and PGV of measured and predicted surface motion at levee crest and residuals

Event ID	Year	Measured PGA at Crest (g)	Measured PGV at Crest (m/s)	Predicted PGA at Crest (g)	Predicted PGV at Crest(m/s)	ε
3	2008	0.187	0.043	0.201	0.045	0.105
4	2011	0.817	0.187	0.602	0.156	0.198
9	2008	0.246	0.087	0.241	0.075	0.235
10	2010	0.208	0.045	0.169	0.045	0.067
11	2010	0.062	0.026	0.057	0.025	0.042
12	2011	0.109	0.046	0.123	0.048	0.203
15	2011	0.145	0.048	0.18	0.041	0.068
16	2011	0.066	0.016	0.068	0.013	0.121
22	2011	0.165	0.036	0.151	0.028	0.126
24	2013	0.243	0.026	0.197	0.022	0.078
25	2013	0.11	0.008	0.108	0.018	0.261

4.4.4.2 Profiles of Peak Acceleration, Velocity and Shear Strain

Similar to what was performed at the other two sites, I recorded the response of a vertical array of elements at the location of the boring log at the crest, and plotted them versus depth. Figure 4.34-4.37 are the profiles of peak acceleration (PGA), velocity (PGV) and shear strain for elements right under levee crest during these ten events, where the blue triangles represent the actual measurement from accelerometer recordings. A profile of shear strength is also plotted in the figures, where the shear strength is computed as $\sigma_v'\tan(\phi')$ for sand layers and undrained shear strength shown for clay layers. It is obviously observed from these figures that shear strain occurs the most at bottom clay layer, and the sand layer right above it. What seems to be interesting is that even the strong events didn't cause that much strain for this model. And it is also interesting to see that the PGV in the bedrock layer didn't change much while the PGA in the bedrock layer usually will fluctuate a little.

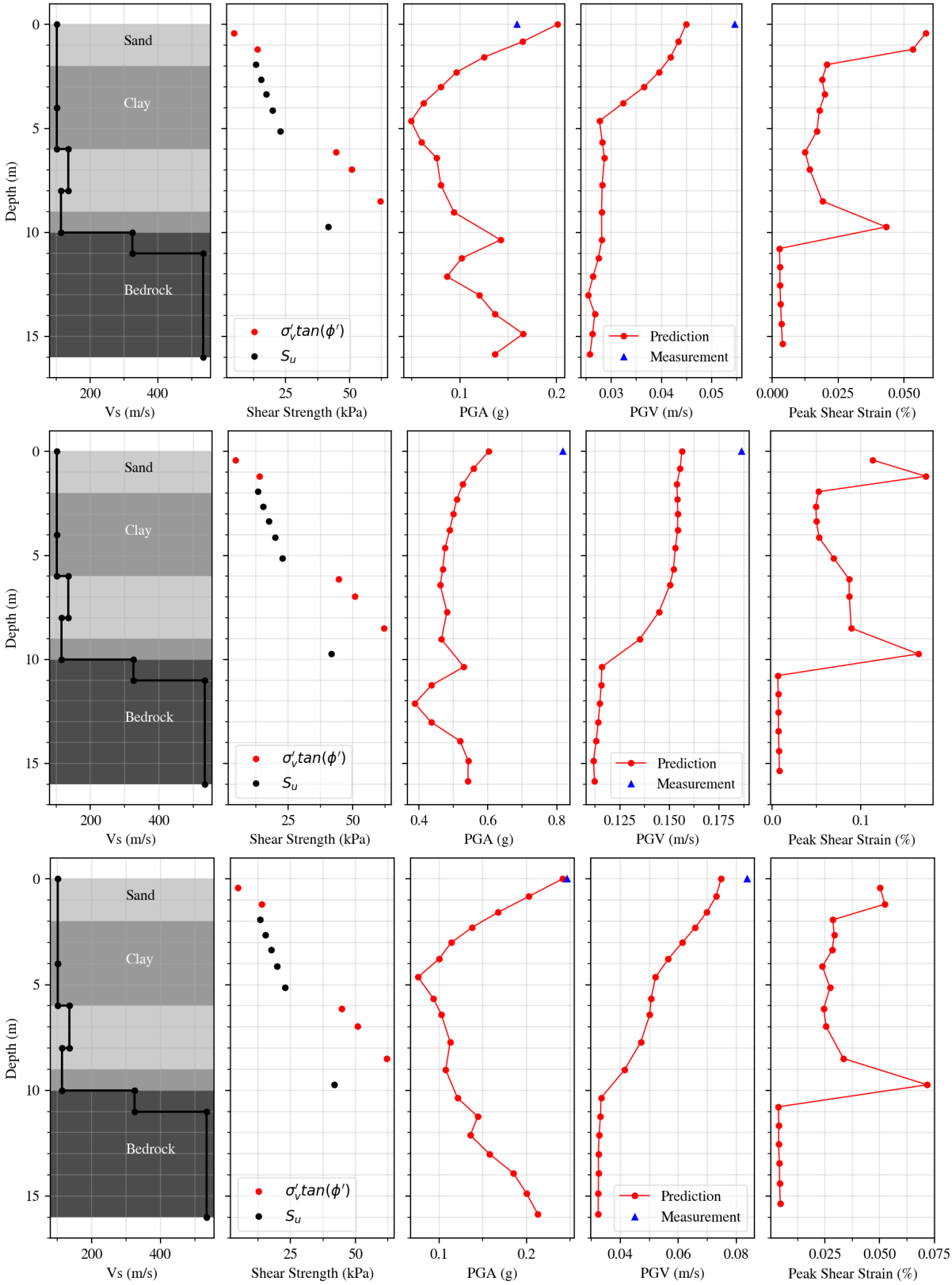


Figure 4.52 Profiles of PGA, PGV and peak shear strain for event 3, 4 and 9

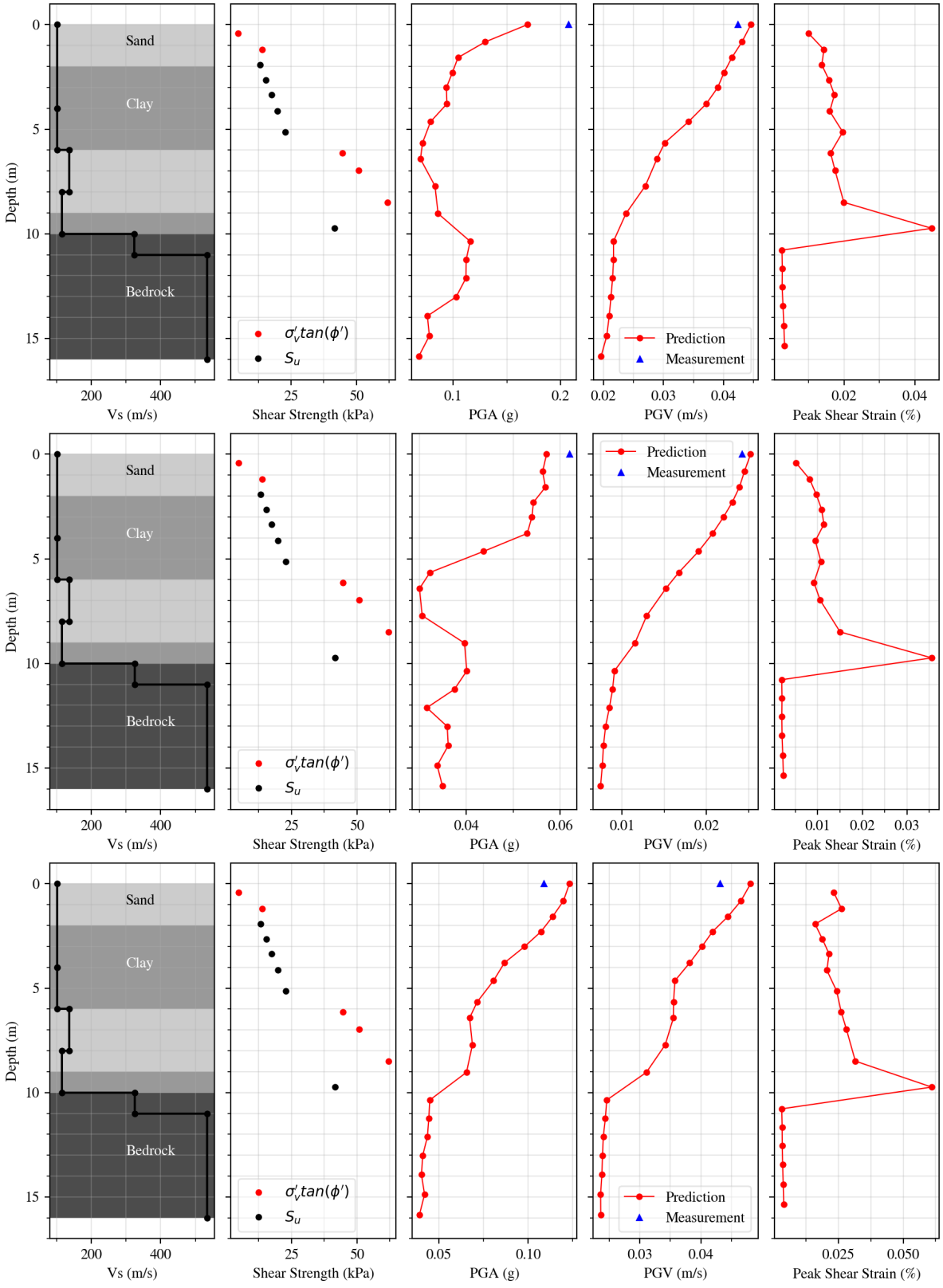


Figure 4.53 Profiles of PGA, PGV and peak shear strain for event 10, 11 and 12

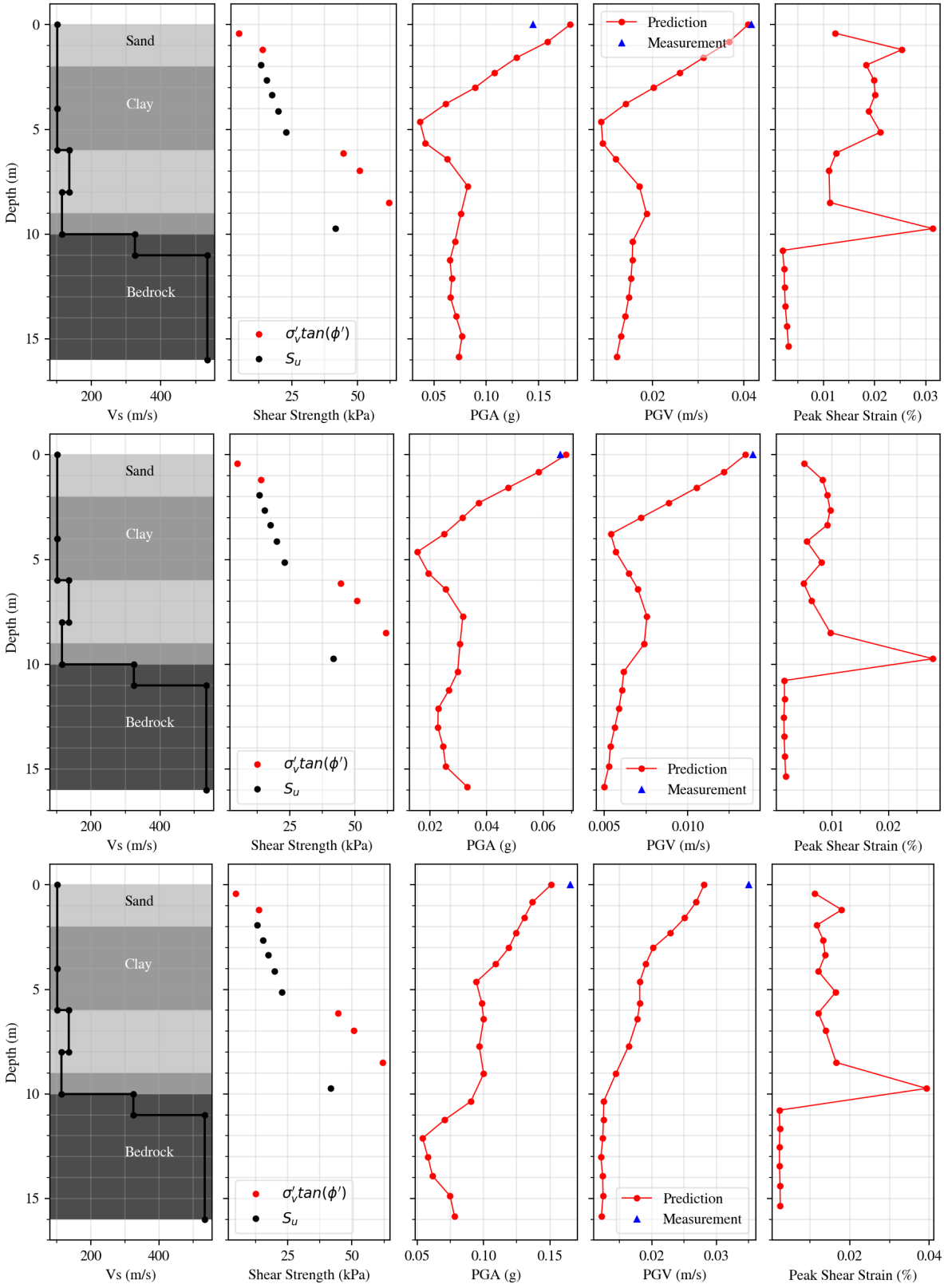


Figure 4.54 Profiles of PGA, PGV and peak shear strain for event 15, 16 and 22

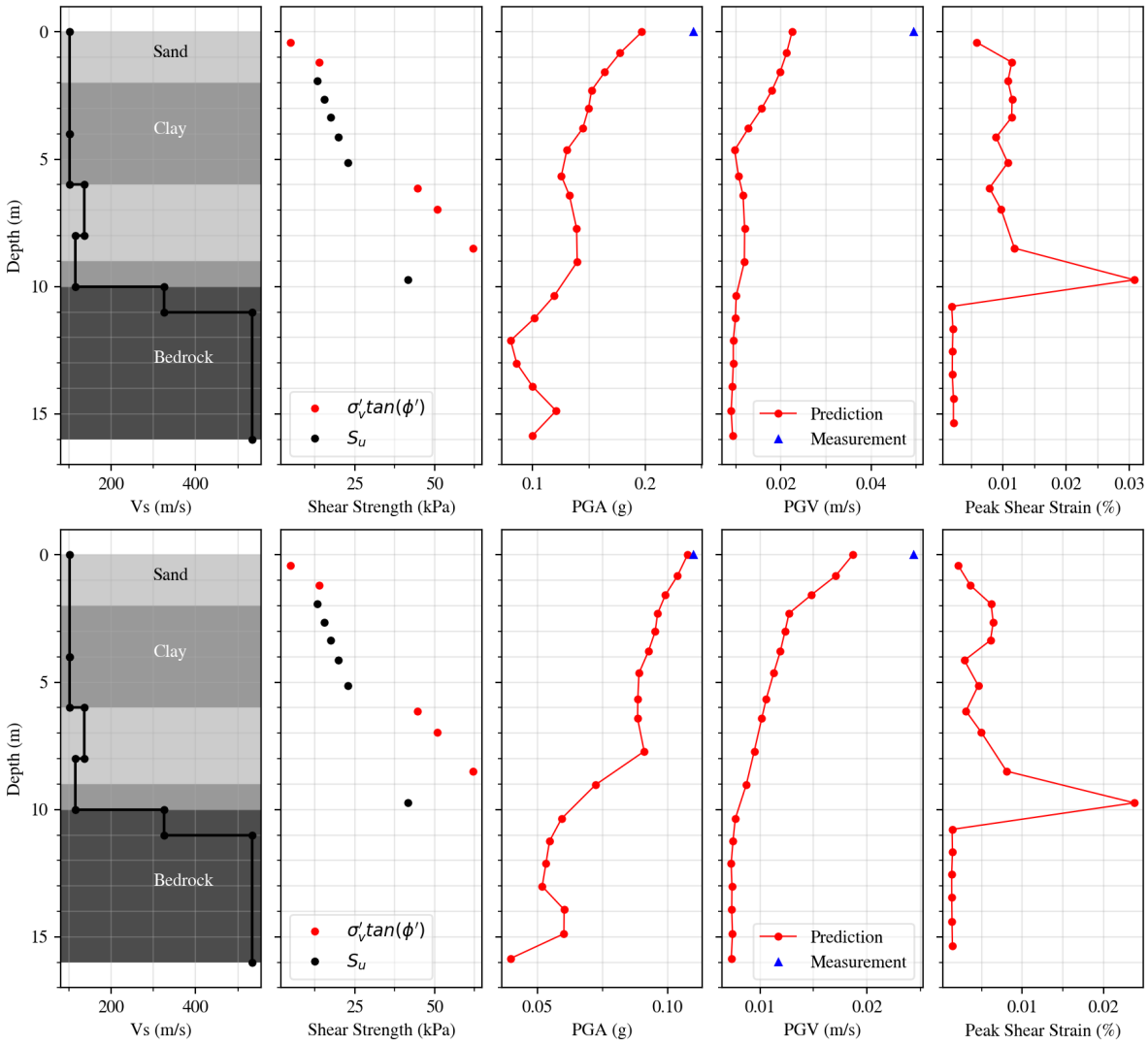


Figure 4.55 Profiles of PGA, PGV and peak shear strain for event 25 and 26

4.4.4.3 Observed Damage versus Predicted Damage

Although there was no reported damage for any of the events, I still recorded the average crest settlement in the finite element analysis, which are all summarized in Table 4.13. Table 4.13 shows that the finite element model predicted less than 1cm of settlement for all the earthquake events that were analyzed, even for the 2011 Tohoku-oki event.

Table 4.13 also summarizes the damage level that is determined based on the damage level classification shown in Table 4.7. Figure 4.56 shows how the crest settlement changes with the

measured PGV at levee crest, and all of the points lie in the region of DL = 0 because the settlements are all less than 1cm.

Table 4.13 Settlement and damage level comparison

Event ID	Year	Damage Observation	Measured PGV at Crest (m/s)	Observed Damage level	Predicted Settlement (cm)	Predicted Damage level
3	2008	No damage reported	0.043	0	0.17	0
4	2011	No damage reported	0.187	0	0.72	0
9	2008	No damage reported	0.087	0	0.18	0
10	2010	No damage reported	0.045	0	0.06	0
11	2010	No damage reported	0.026	0	0.03	0
12	2011	No damage reported	0.046	0	0.1	0
15	2011	No damage reported	0.048	0	0.07	0
16	2011	No damage reported	0.016	0	0.02	0
22	2011	No damage reported	0.036	0	0.06	0
24	2013	No damage reported	0.026	0	0.03	0
25	2013	No damage reported	0.008	0	0.01	0

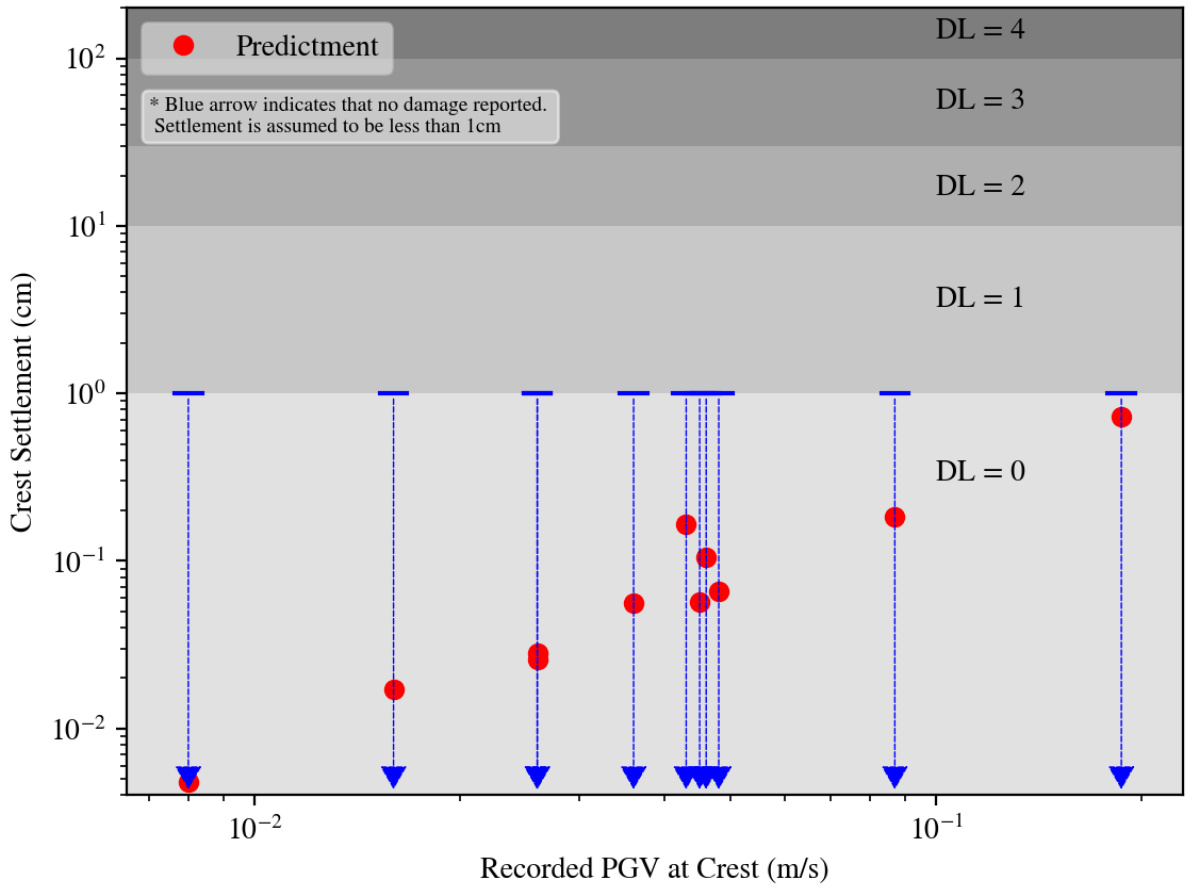


Figure 4.56 Crest settlement versus recorded PGV at levee crest

4.5 FRAGILITY FUNCTIONS

In this section, I will first describe the ground motions that are selected and the fragility curves that are developed for Nakashimo site using these ground motions and the approach proposed in Chapter 2. A comparison with fragility functions proposed by Kwak et al. (2016) is provided. Then the effect of magnitude is investigated. The spatial variability of soil is incorporated by implementing spatially correlated random fields into the finite element analysis, and the relative density of the sand material is varied, which all have an impact on the fragility curves.

4.5.1 **Ground Motion Selection**

Baker et al. (2011) proposed a ground motion selection algorithm that allows the user to select a set of ground motions whose response spectra match a target mean and variance. Four sets of ground motions were also developed using this algorithm for the PEER transportation research Program (Baker et al. 2011).

I used Set #1A among the four sets, which consists of 40 unscaled three-component ground motions whose response spectra match the median and log standard deviations predicted for a magnitude 7 strike slop earthquake at the rupture distance of 10 km. Another important reason for selecting this set of ground motion is that Kwak et al. (2016) utilized field performance data from two M 6.6 shallow crustal earthquakes, and this set of ground motions has a similar magnitude. Figure 4.57 shows the response spectra of the selected ground motions.

Although three components are included for these 40 ground motion records, only two horizontal components are used in this study. In addition to the original unscaled motions, I also scaled this set of motions by a factor of 2 to have a bigger range of intensity levels.

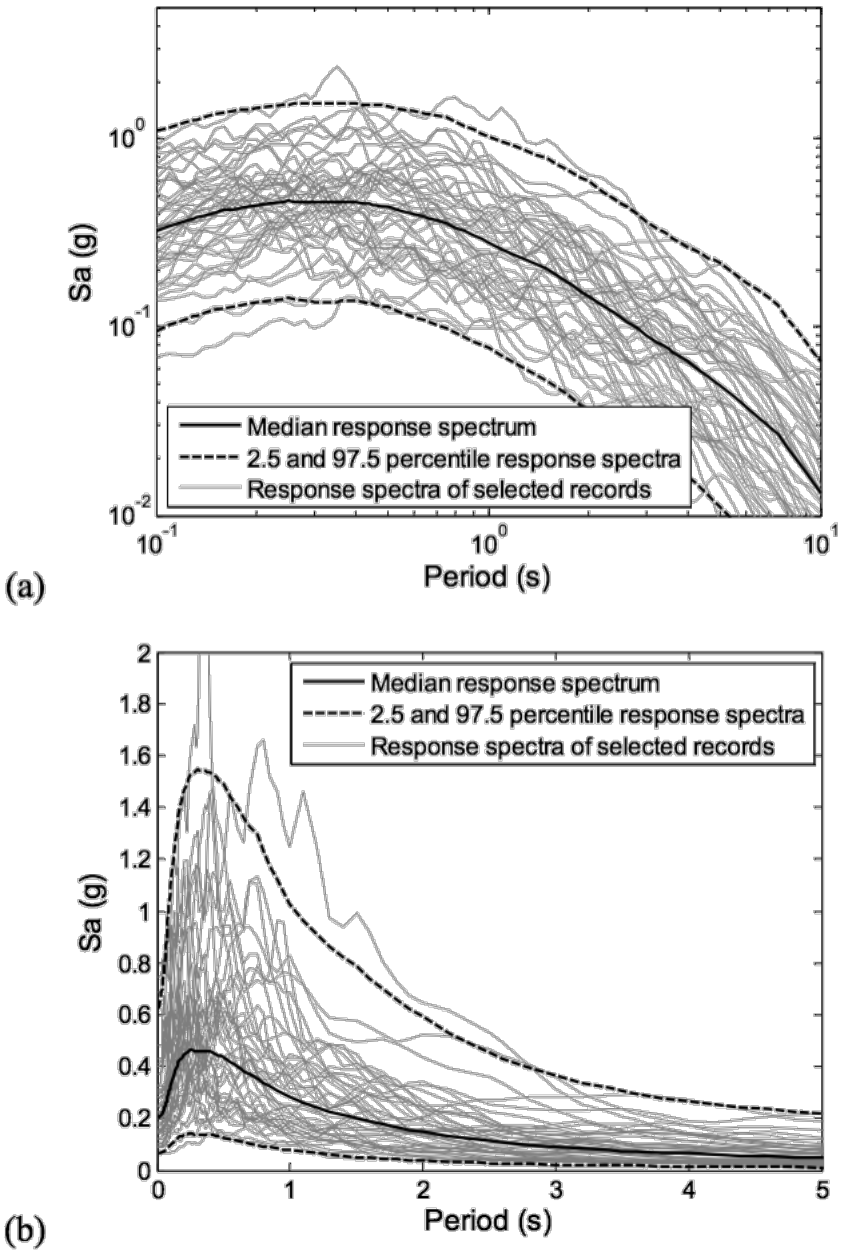


Figure 4.57 Response spectra of 40 ground motions, compared to the target response spectra predicted by GMM (Boore and Atkinson 2008: (a) log-log scale (b) linear scale (Baker et al. 2011)

4.5.2 **Two Groundwater Cases**

As shown in Figure 4.58, the water table on the riverside of the levee is slightly above the base of the levee fill, and it was reported that phreatic surface within the fill is approximately at the base of the fill, which is referred to as the low groundwater (LGW) case. However, the water table on the riverside sometimes will fluctuate, and it would be interesting to see how an increase of river water elevation will impact levee performance. Therefore, I raised the water table to approximately 1m below the levee crest on the riverside of the levee model, referred to as the high groundwater (HGW) case. The phreatic surface is obtained by conducting a seepage analysis in RocScience Phase2. Figure 4.59 shows the location of the raised water table, and the light purple line in Figure indicated the location of phreatic surface after a steady-state seepage analysis in RS2.

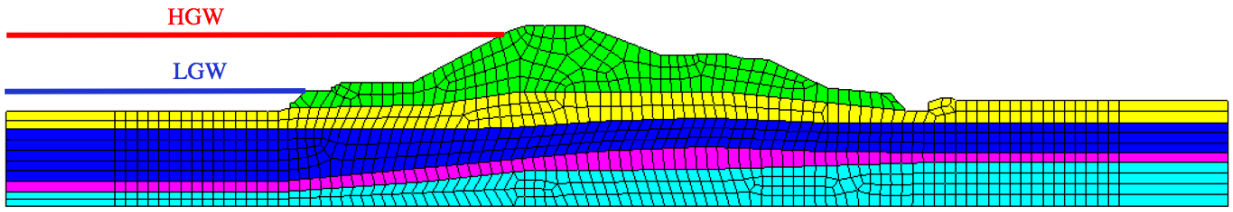


Figure 4.58 River table location for two cases: LGW and HGW

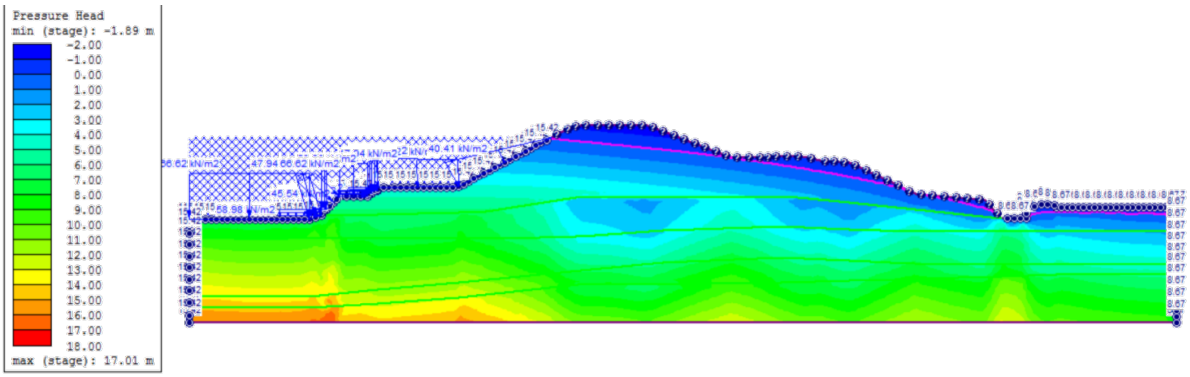


Figure 4.59 Phreatic surface from Phase 2 for the HGW case

4.5.3 **Fragility Curves**

As mentioned in Chapter 2, dynamic analysis can be performed on the Nakashimo levee model with the selected set of ground motions to build fragility functions. For each ground motion, the average crest settlement is recorded together with an intensity measure of the ground motion (i.e. PGV in this study). Note that a Lysmer-Kuhlemeyer (1969) dashpot is added at the base of the model for these analyses since all the motions I used are considered as outcrop motions. By using a dashpot, it is assumed that the model is underlain by an elastic half-space, which allows part of the energy caused by the motion to be removed from the underlying layer beneath the base of the model. The average shear wave velocity of the underlying medium is found to be around 430m/s.

Figure 4.60 shows how the average crest settlement changes with the PGV of the input motion for both the low groundwater (LGW) case and the high groundwater (HGW) case. Overall, the levee model settles more in the high groundwater case, which makes sense because more soil become saturated if the river water table is raised, which causes more of the levee fill to be liquefiable. The results in Figure 4.60 suggest that the crest settlement has a linear relationship with the PGV of the input motion in the log scale.

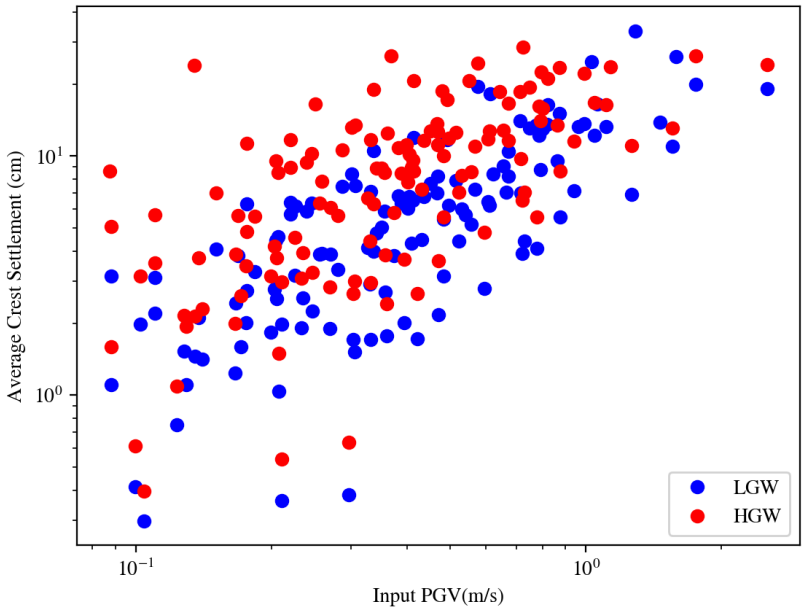


Figure 4.60 Crest settlement versus PGV of input motion for both LGW and HGW cases

To construct a fragility function based on these settlements and PGV values, it is important to follow the procedures described in Chapter 2. Following Eq. 2.7 (and assuming the natural log standard deviation of the error term is constant), a straight line is regressed between the crest settlement and PGV in the natural log scale for both the LGW and HGW cases, which are shown in Figure 4.61 and Figure 4.62.

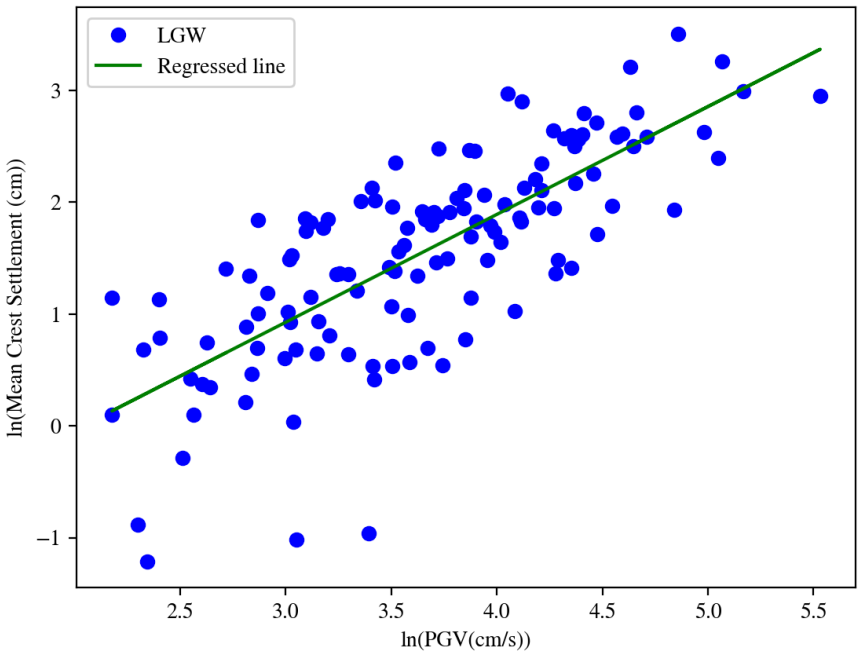


Figure 4.61 Crest settlement versus PGV of input motion for LGW case and regressed straight line (axis in natural log)

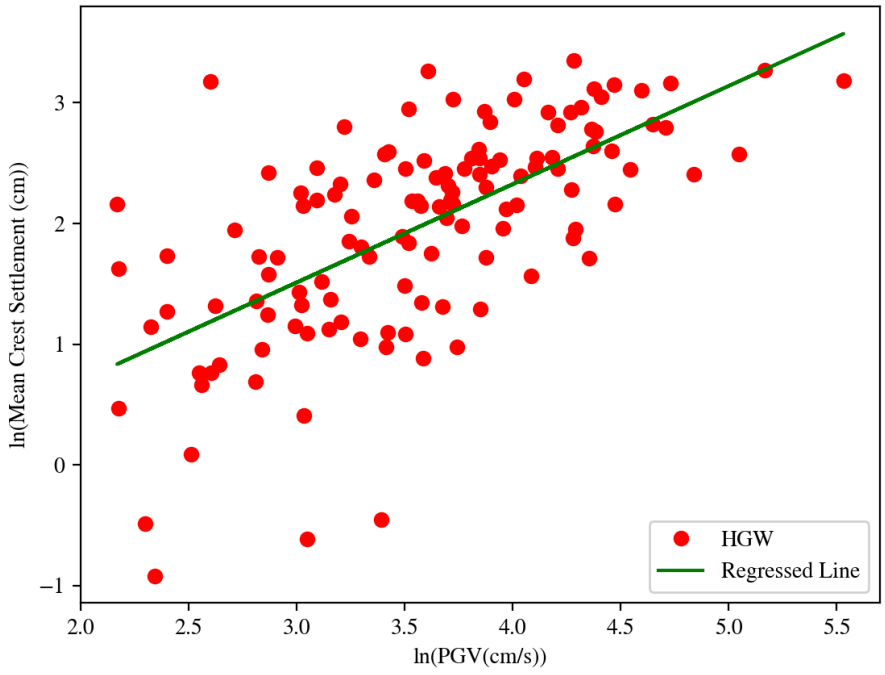


Figure 4.62 Crest settlement versus PGV of input motion for HGW case and regressed straight line (axis in natural log)

Table 4.14 summarized the intercept of the regressed line (m_0), slope (m_1) and the standard deviation of the residuals (σ) for both LGW and HGW cases. An interesting issue here is that the slope of the LGW case is slightly larger than the slope of the HGW case, which means that the fragility functions will cross at some high PGV values, which will not make sense physically. This can be solved by regressing the data together to constrain both cases to have the same slope, but for the interest of this study and also considering the fact that the slopes are pretty similar, it is not considered here.

Using Eq. 2.11 and Eq. 2.12, the moments of the log-normal CDFs for PGV-based fragility curves can be calculated, and are summarized in Table 4.15. Table 4.15 also included the moments of the log-normal CDFs proposed by Kwak et al. (2016) for comparison. Note that both the LGW and HGW cases belong to the categrory of D_W > -1m as defined by Kwak et al. (2016). The results in Table 4.15 show that the standard deviation predicted by the finite element analyses are smaller than those proposed by Kwak et al. (2016). This can be explained by the fact that this analyses summarized in Table 4.14 only account for motion-to-motion variability and other sources of variable and uncertainty that exist under field conditions have not yet been considered.

Table 4.14 Slope, intercept and standard deviation of the regressed line for both cases

Case	LGW	HGW
m_0	-1.962	-0.932
m_1	0.964	0.814
σ	0.350	0.434

Table 4.15 Moments of log-normal CDFs of exceeding different damage levels for both LGW and HGW cases, and results from Kwak et.al. 2016

Case	LGW			HGW			Kwak et al. 2016 (D_W > -1m)		
Moments	μ	e^{μ}	β	μ	e^{μ}	β	μ	e^{μ}	β
DL > 0	2.04	8	0.36	1.14	3	0.53	4.43	84	0.80
DL > 1	4.43	84	0.36	3.97	53	0.53	4.62	101	0.80
DL > 2	5.57	261	0.36	5.32	205	0.53	5.15	172	0.80
DL > 3	6.82	912	0.36	6.80	898	0.53	5.89	361	0.80

Figure 4.63 shows the PGV-based fragility curves for DL > 1. The vertical axis is probability of exceedance of DL>1, which implies a crest settlement is larger than 10cm. It is clearly seen from Figure 4.63 that raising the water table (from LGW to HGW) shifts the fragility curves to the left. The median of the fragility curve for the LGW case, on the other hand is quite close to the median of the fragility curve proposed by Kwak et al. (2016), even though the standard deviation is smaller.

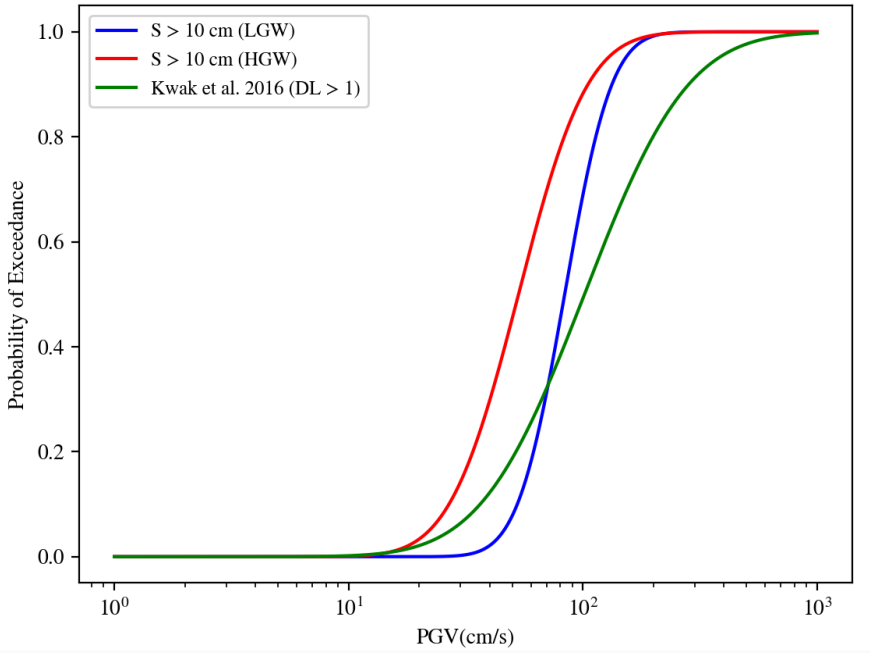


Figure 4.63 Fragility curve for DL>1 comparisons

4.5.4 **The Effect of Magnitude**

As described in Chapter 2, the effect of the magnitude of the earthquake on the fragility curves can be included by simply adding a magnitude term (Eq. 2.10). To investigate whether there is magintude effect, I plot the residuals obtained from Figure 4.61 against the magnitude of the earthquake for the LGW case. The residuals are defined as the differences between the blue data points and the regressed line in the natural logarithm scale. Figure 4.64 shows how the residuals trend with magnitude along with a linear fit line. Figure 4.64 indicates that there is indeed a positive trend between crest settlement and magnitude, as anticipated.

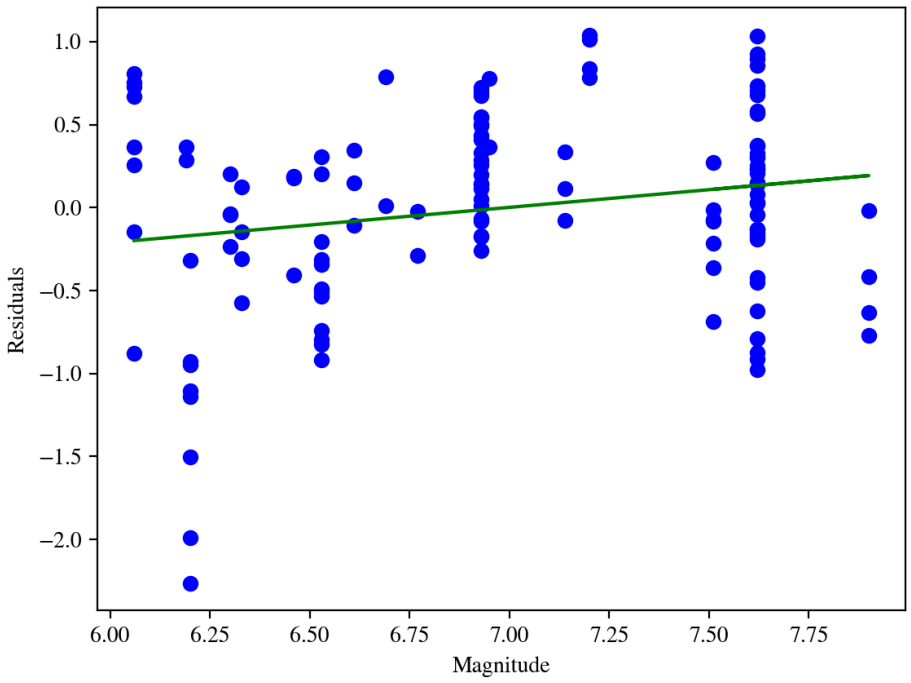


Figure 4.64 Residuals from regressed line versus Magnitude for LGW case

Now that it is clear that there is a positive trend between crest settlement and magnitude, the next step is to perform a multiple linear regression following Eq. 2.10 to set the coefficients for PGV and magnitude scaling of crest settlement as well as the standard deviation of the residuals. Table 4.16 summarized the intercept (m_0), PGV-scaling coefficient (m_1), magnitude-scaling coefficient (m_2) and

the standard deviation of the residuals (σ). Table 4.16 also lists m_0, m_1 and σ for the case when the magnitude effect is not included.

Table 4.16 Coefficients and standard deviation of residuals from multiple linear regression with and without accounting for magnitude effect

Case	M effect not included	M effect included
m_0	-1.962	-3.425
m_1	0.964	0.89
m_2	NA	0.248
σ	0.350	0.333

Using the coeffients that were just obtained, the fragility curves can be varied for different magnitudes by calculating the moments of the log-normal CDFs. Similar to Eq. 2.11, the mean of log-normal CDFs can be modified as follows,

$$\mu = \frac{\ln(S_t) - m_0 - m_2 \cdot M}{m_1} \tag{4.4}$$

while the standard deviation of the log-normal CDFs is kept the same as Eq. 2.12 (ratio of σ and m_1), and it is computed to be around 0.37. As also indicated in Table 4.15, the standard deviation of the log-normal CDFs without incorporating the magnitude effect is around 0.36. Figure 4.65 gives an example of fragility curves of DL > 1 for three different magnitude levels. It is clear from the figure that as the magnitude increases, the fragility curve shifts to the left, which also indicates that given the same PGV, larger magnitudes of events tend to cause more damage.

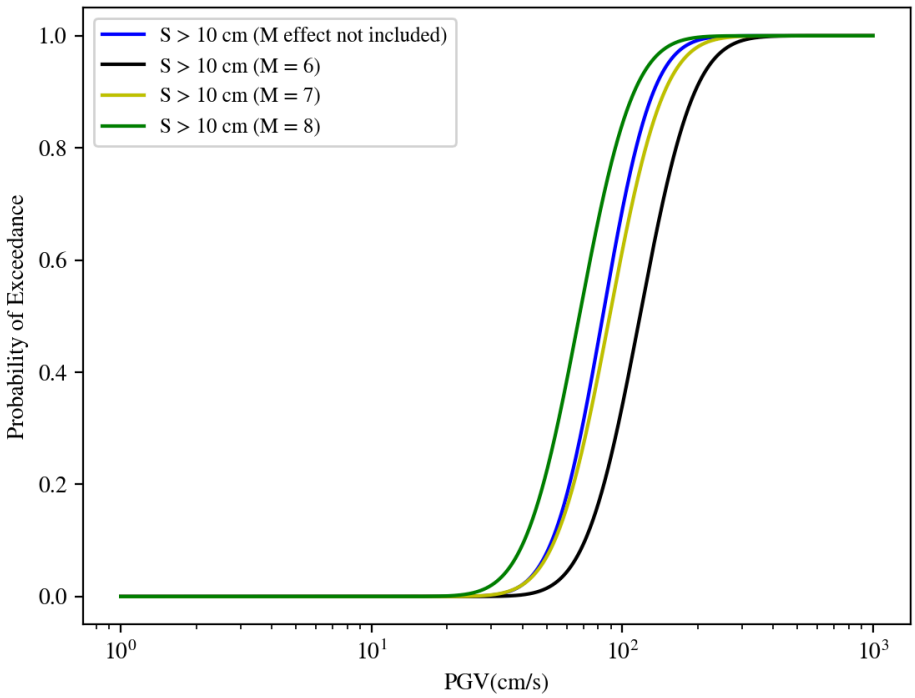


Figure 4.65 Fragility curves of DL > 1 for different magnitudes

4.5.5 **Heteroscedasticity**

The fragility curves calculated above are all based on the assumption that the standard deviation of the error term (σ) is constant. However, according to Figure 4.61 and Figure 4.62, it appears that σ is slowly decreases as the PGV of the motion increases. Changes in dispersion with predictor variables is referred to as heteroscedasticity. This is actually an interesting feature because I would expect the soil response to be more nonlinear when the PGV of the motion increases, and the standard deviation of the crest settlement might actually increase. A hypothesis is that the reason why σ slowly decreases is because of the fewer data points as the PGV of the motion gets really high. Nevertheless, I adopted the following approach to account for the heteroscedasticity and make corrections on the fragility curves.

To evaluate how σ changes with PGV, a bin method is used. The residuals obtained from Figure 4.61 and 4.62, together with PGV data are first sorted, and a bin size of 40 is selected to get the mean PGV

within that bin and the standard deviation of the residuals in that bin. Then I repeat this procedure while moving the location of the bin. Figure 4.66 shows the sorted PGVs and residuals for both LGW and HGW case, and Figure 4.67 shows how the computed standard deviations of the residuals within the bin changes with the computed mean PGV. Figure 4.67 also shows regressed curves using the following equation:

$$\sigma = a_0 * \left(\frac{1}{1+e^{a_1*(PGV)^{a_2}+a_3}}\right) + a_4 \tag{4.5}$$

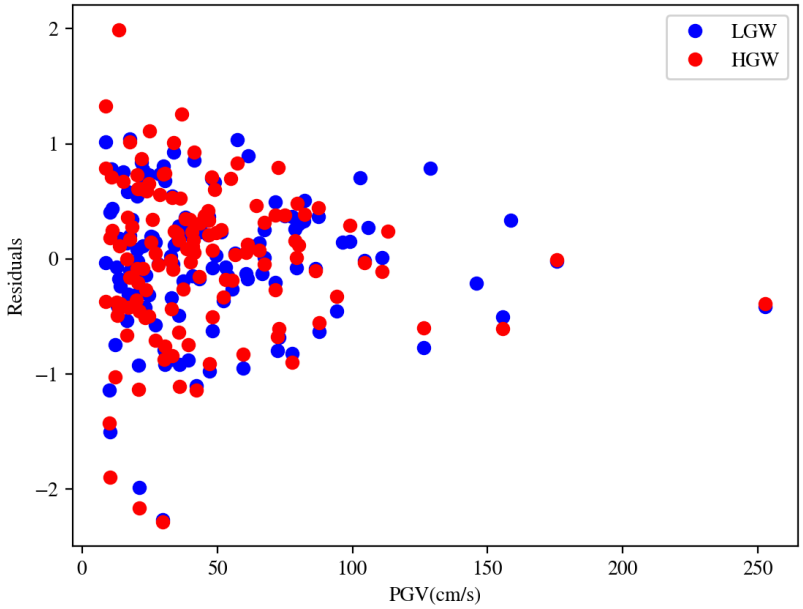


Figure 4.66 Residuals versus PGV for both LGW and HGW cases

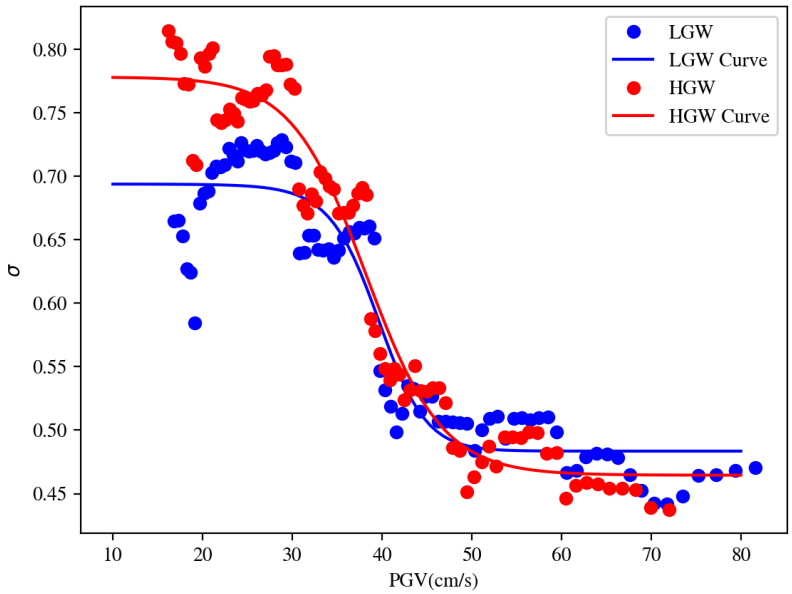


Figure 4.67 Standard deviation versus mean PGV from bin method and regressed curve

Table 4.17 lists the coefficients of the regressed curves shown in Figure 4.67. Now that the relationship between σ and PGV has been established, the next step is to use Eq. 2.8 and Eq. 2.9 to re-compute the probability of exceedance. Eq. 2.11 and Eq. 2.12 can no longer be directly used to get the moments of log-normal CDFs. Figure 4.68 gives an example of how the heteroskedastic fragility curves are different from the original fragility curves. It is observed from Figure 4.68 that the modified fragility curve for the LGW case is even closer to the fragility curve proposed by Kwak et al. (2016), especially when PGV is small. This is due to the fact that the standard deviation was around 0.4 before any correction, but now the standard deviation gradually decreases from 0.8 to 0.4.

Table 4.17 Coefficients of the regressed curve of standard deviation for two cases

Case	LGW	HGW
a_0	0.210	0.314
a_1	0.047	0.358
a_2	1.460	0.358
a_3	-9.998	-10.050
a_4	0.484	0.465

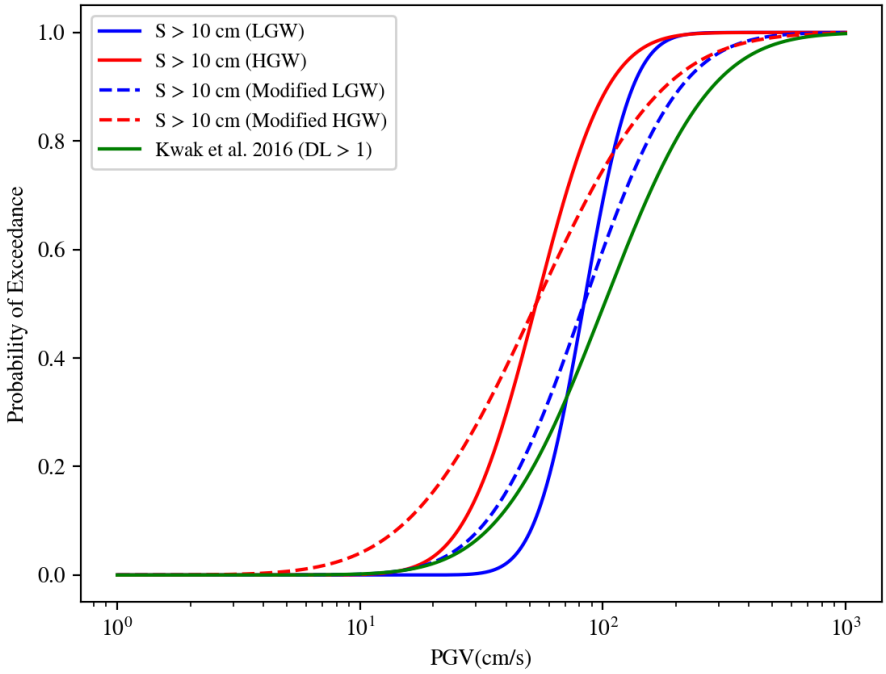


Figure 4.68 Fragility curves comparison after the heteroscedasticity correction

4.5.6 **The Effect of Within-Section Spatial Variability**

As described in Chapter 3, natural soils are rarely homogeneous, and heterogeneity is commonly found both in soil stratigraphy and within-layer properties. The spatial variability in soil properties can be modelled using random field theory. During the finite element analysis, elements within each layer were assigned with the same soil property parameters, which does not account for the spatial variability

of soil. By using the new random field generation algorithm proposed in Chapter 3, a spatially correlated random field of soil properties can be incorporated into the finite element analysis.

For the sand layers, the relative density can be regarded as the random variable, and all the other parameters used in the material model are related to relative density. For the clay layers, the undrained shear strength is the random variable. I assume that the relative density and undrained shear strength are both log-normally distributed. For each individual soil layer, a spatially correlated random field of soil properties is generated, which is shown in Figure 4.69. The mean values of the random field are based on the values listed in Table 4.4. The coefficient of variation of the relative density random field in the sand layer is selected to be 0.6 and the coefficient of variation of the undrained shear strength random field in the clay layer is selected to be 0.25, which are recommended by Phoon and Kulhawy (1999). The horizontal scale of fluctuation is 20m for both sand and clay layers, and the vertical scale of fluctuation is 1.5m, which are recommended by ISSMGE-TC304 (2021). The bottom layer is a bedrock layer, and it is not quite necessary to vary its property spatially.

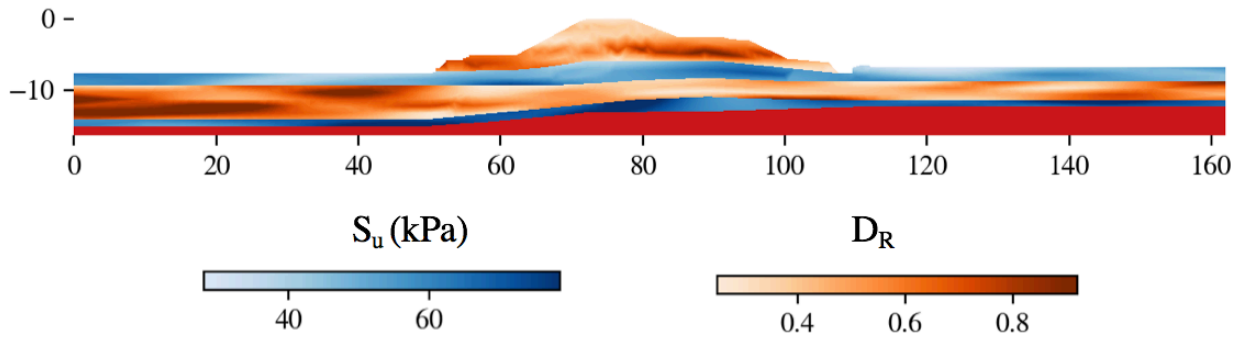


Figure 4.69 An example of spatially correlated random field of soil properties

Figure 4.69 gives one realization of such spatially correlated random field that can be incorporated into the finite element analysis. By repeating this procedure, 500 realizations are generated in total. Then I selected one ground motion record among the aforementioned 40 ground motion records, which is plotted in Figure 4.70 together with its response spectra. The PGA of this motion is approximately

0.21g, and the PGV is around 0.36m/s, thus this is a ground motion with a medium shaking intensity. The last step is to implement these 500 realizations of random fields into the finite element analysis together with the selected ground motion record and run dynamic analysis with the Nakashimo levee model. Crest settlement is recorded for each realization. The aim of these analyses is not to capture the overall variability in response (which would require running multiple ground motions through the model), but to isolate the effects of soil property variability on the response variability.

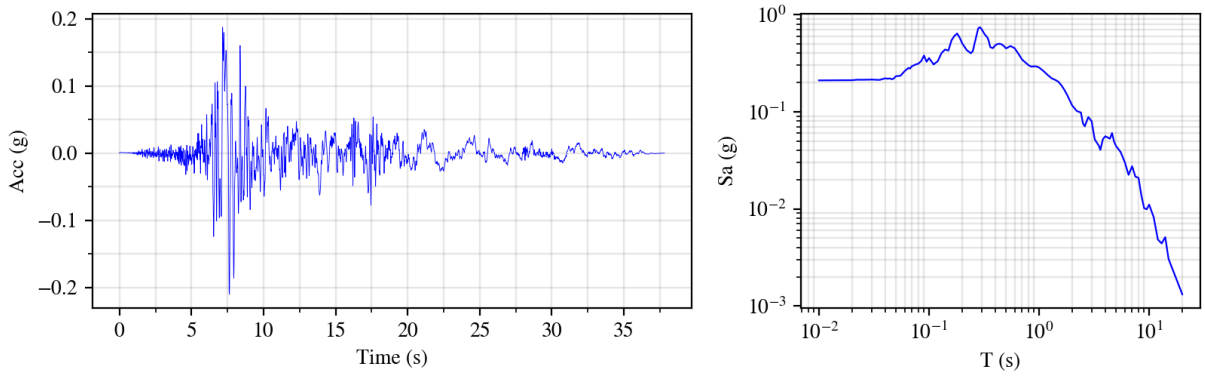


Figure 4.70 Ground motion record selected and its response spectra

Figure 4.71 plots the crest settlements for all the 500 realizations. The mean crest settlement is computed to be around 3.4cm, while the crest settlement predicted by the levee model with uniform soil properties is around 2.6cm. This indicates that by incorporating the spatial variability of soil, the levee model tends to be more fragile compared with levee model with uniform soil properties, which is consistent with the findings presented in Chapter 3.

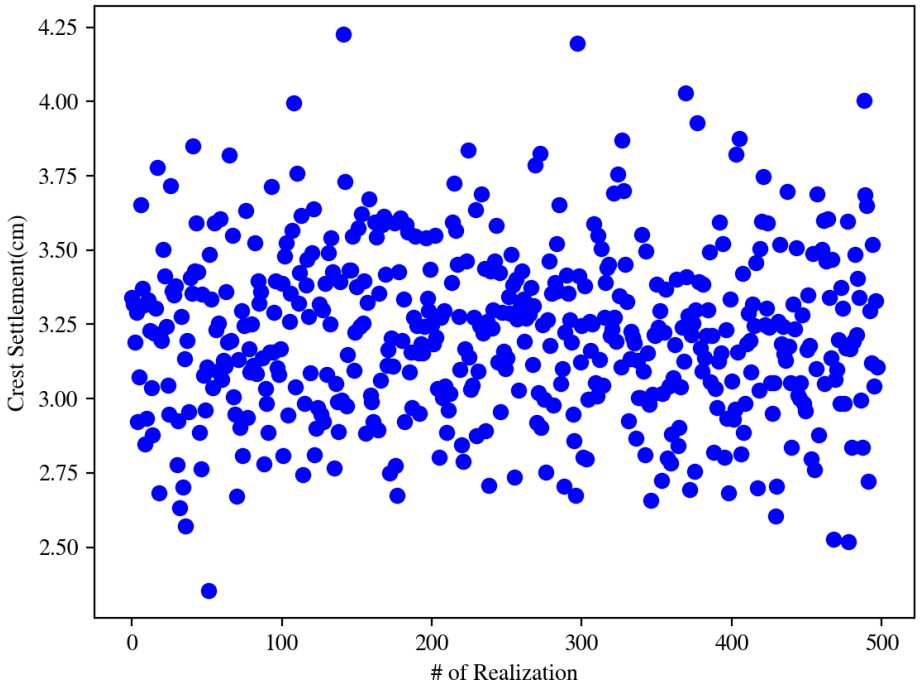


Figure 4.71 Crest settlement distribution over 500 realizations

A quantile-quantile (Q-Q) test was performed on the crest settlement data. The natural logs of the crest settlements were computed, the natural log mean was subtracted, and the difference normalized by the population standard deviation. The resulting normalized residual is plotted with its theoretical counterpart for a lognormal distribution to form the Q-Q plot shown in Figure 4.72. All the data points are close to the red line, which means the natural logarithm of crest settlements are normally distributed. Therefore, the crest settlements are actually log-normally distributed.

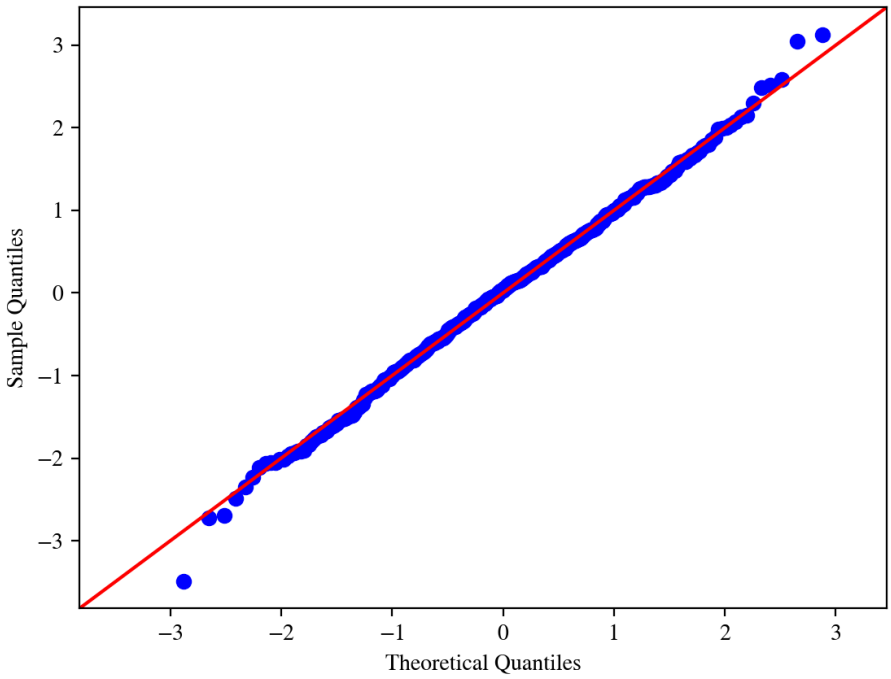


Figure 4.72 A Q-Q plot for the logged values of crest settlement

The standard deviation of the natural log of crest settlement is computed to be 0.13. As mentioned earlier, the standard deviation obtained from motion to motion variability is around 0.36 for the LGW case, which is lower than what Kwak et al. (2016) observed from field performance data. This mismatch occurs because the finite element analysis failed to account for all sources of uncertainty. Using results like those presented in this section, which likely vary with the intensity of shaking (this effects has not been investigated), the motion-to-motion variability can be increased to also include soil property variability.

4.5.7 **The Effect of Mean Relative Density**

So far, the response variability from motion-to-motion variability and from the soil's spatial variability within the cross-section have been discussed. As pointed out in Chapter 2, the average soil property also varies along the length of levee. Kwak et al. (2016) did not have adequate information to characterize the average soil properties, and therefore did not include average relative density of the

levee fill as a predictive variable in the fragility function formulation. This is a form of epistemic uncertainty because additional geotechnical information would permit refinement of the fragility functions. The approach I adopt here is to vary the sand layer's relative density, and to figure out how this will have an influence on the performance of the levees and the fragility curves.

The sand layers for the Nakashimo levee cross-section studied here have a mean relative density of approximately 55%, indicating that the sand is medium dense. To account for the influence of potential variations in the mean value of relative density along the length of the levee, I adjusted the relative density to be 35% and 75%. I then analyzed these levee models with looser sand materials and denser sand materials separately using the same set of motions.

Figure 4.73 shows how the average crest settlement changes with the PGV of the input motion for three different relative density cases. Intuitively the levee model with a lower relative density should settle more compared with the levee model that has a higher relative density. Similar to the investigation of magnitude effect, the relationship between crest settlement, PGV, D_R and magnitude now can be defined as,

$$\ln(S) = m_0 + m_1 \cdot \ln(PGV) + m_2 \cdot M + m_3 \cdot D_R + \varepsilon \tag{4.6}$$

Multiple linear regression is performed. Table 4.18 summarized the intercept (m_0), coefficient for PGV-scaling of crest settlement (m_1), coefficient for magnitude-scaling (m_2), coefficient of D_R-scaling (m_3) and the standard deviation of the residuals (σ). Similar to Eq. 4.4 and Eq. 2.12, the median and standard deviation of the log-normal CDFs of exceeding different damage levels can be computed using the following two equations,

$$\mu = \frac{\ln(S_t) - m_0 - m_2 \cdot M - m_3 \cdot D_R}{m_1} \tag{4.7}$$

$$\beta = \frac{\sigma}{m_1} \tag{4.8}$$

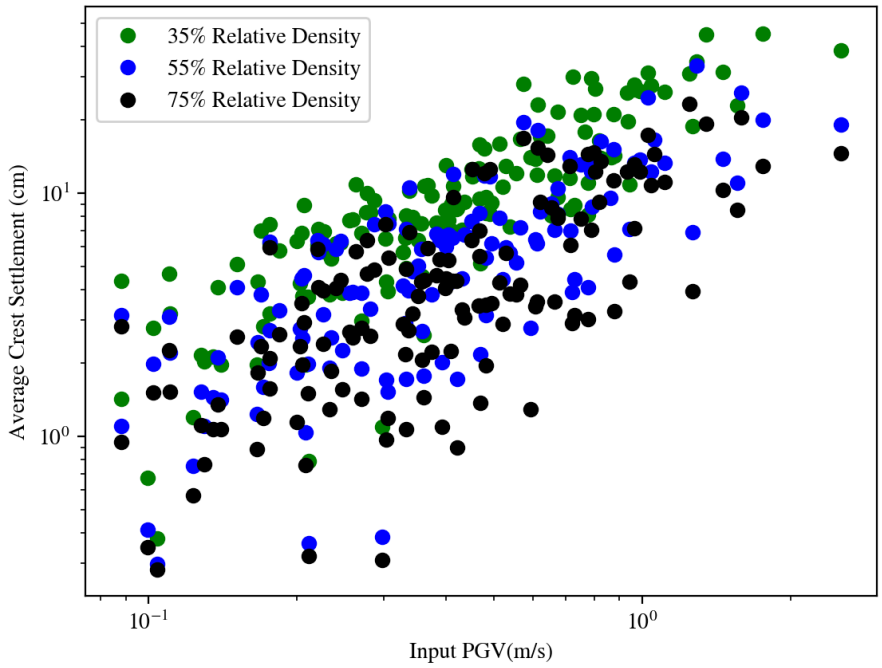


Figure 4.73 Crest settlement versus PGV of input motion for two different relative density cases

Table 4.18 Coefficients and standard deviation of residuals from multiple linear regression accounting for PGV, magnitude and relative density

Parameter	Value
m_0	-1.851
m_1	0.945
m_2	0.168
m_3	-2.036
σ	0.381

Table 4.19-4.21 listed the calculated moments of the log-normal CDFs for PGV-based fragility curves for three magnitudes (M = 6, 7 and 8) and three different relative density cases (D_R = 75%, 55% and 35%). Figure 4.74 also gives examples of fragility curves of DL > 1 given different relative density and magnitude. Apparently, given the same relative density, the increase of magnitude will shift the

fragility curve to the left, meaning the levee is more likely to fail under large magnitudes events. Moreover, for a given magnitude, if the relative density decreases, the fragility curve shifts to the left.

Table 4.19 Moments of log-normal CDFs of exceeding different damage levels for three different relative density cases for events with a magnitude of 6

D_R	35%			55%			75%		
Moments	μ	e^{μ}	β	μ	e^{μ}	β	μ	e^{μ}	β
DL > 0	1.65	5	0.40	2.08	8	0.40	2.51	12	0.40
DL > 1	4.08	59	0.40	4.51	91	0.40	4.94	140	0.40
DL > 2	5.25	190	0.40	5.68	292	0.40	6.11	449	0.40
DL > 3	6.52	678	0.40	6.95	1043	0.40	7.38	1605	0.40

Table 4.20 Moments of log-normal CDFs of exceeding different damage levels for three different relative density cases for events with a magnitude of 7

D_R	35%			55%			55%		
Moments	μ	e^{μ}	β	μ	e^{μ}	β	μ	e^{μ}	β
DL > 0	1.47	4	0.40	1.90	7	0.40	2.33	10	0.40
DL > 1	3.90	50	0.40	4.34	76	0.40	4.77	118	0.40
DL > 2	5.07	159	0.40	5.50	244	0.40	5.93	376	0.40
DL > 3	6.34	568	0.40	6.77	873	0.40	7.20	1344	0.40

Table 4.21 Moments of log-normal CDFs of exceeding different damage levels for three different relative density cases for events with a magnitude of 8

D_R	35%			55%			75%		
Moments	μ	e^{μ}	β	μ	e^{μ}	β	μ	e^{μ}	β
DL > 0	1.29	4	0.40	1.72	6	0.40	2.15	9	0.40
DL > 1	3.73	42	0.40	4.16	64	0.40	4.59	98	0.40
DL > 2	4.89	133	0.40	5.32	205	0.40	5.75	315	0.40
DL > 3	6.16	475	0.40	6.59	731	0.40	7.03	1125	0.40

It is clearly seen from Table 4.18 that the levee model with a lower relative density of sand materials becomes more fragile, and all the mean and medians of the log-normal CDFs for different damage levels decreased. Figure 5.44 also gives examples of fragility curves of DL > 1 given different relative density and magnitude. The results show that for a given relative density, the increase of magnitude will shift the fragility curve to the left, meaning the levee is more likely to fail under large magnitudes events. Moreover, for a given magnitude, if the relative density decreases, the fragility curve will also shift to the left.

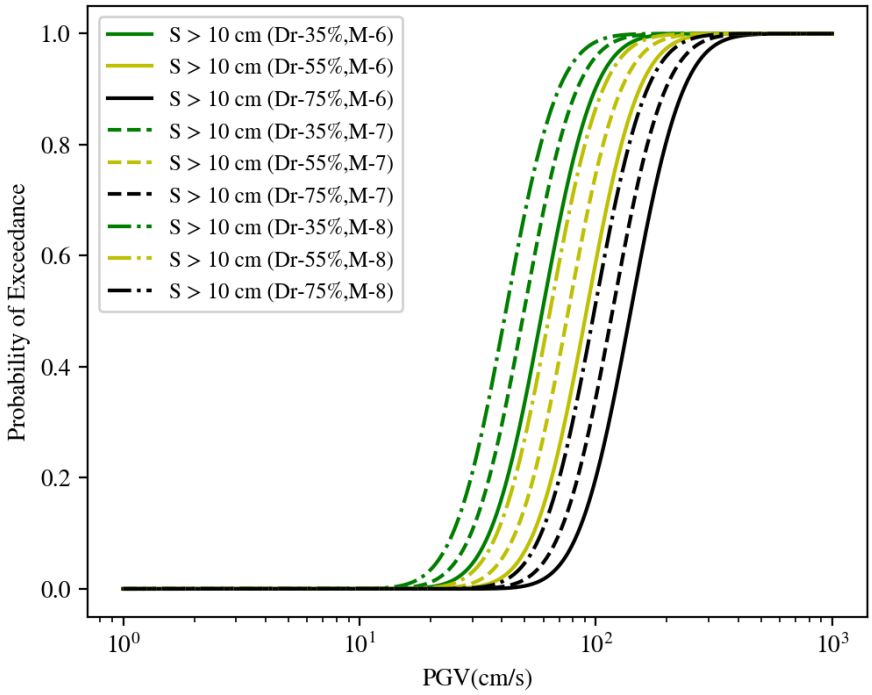


Figure 4.74 Fragility curves of DL > 1 for three different relative density

4.6 CONCLUSIONS

In this section, an overview of seven Japanese instrumented sites is first introduced. This database of seven sites includes not only cross-sections showing levee geometry and instrument layouts, but also geotechnical data, damage observation and processed ground motion time series. Among the seven

instrumented site, the Nakashimo site, Yamazaki site and Kozuka site were selected for the validation of analysis using OpenSees considering that they will have available information available.

With a detailed cross-section and stratigraphy profile, a finite element mesh can be generated using GiD. By properly assigning material properties based on available geotechnical data, and applying the correct ground motion, dynamic analysis was performed on all these three sites. To find out how well the finite element model can predict compared with the actual measurement, I first compared the predicted surface motion at levee crest with recordings. By plotting and comparing the response spectrum of the ground motions, it is obviously observed that the response produced by finite element model matches quite well with the recorded response. At the Nakashimo site, a pore water pressure response was also compared, and the finite element model was able to capture the overall trend of pore water pressure building-up and dissipation as the actual recording indicated.

Vertical profiles of PGA and PGV and profiles of shear strain for the finite element model were also plotted to investigate how they trend over depth. Predicted crest settlements from the finite element model were compared with the reported performance data, and they agreed quite well. Damage level were also evaluated based on the amount of crest settlement that the earthquake event caused.

Fragility curves are developed for Nakashimo site using a set of ground motions and the new approach proposed in Chapter 2. A comparison study shows that the mean and median of the log-normal CDFs for the fragility curve obtained finite element analysis are quite close to the mean and median of the fragility functions proposed by Kwak et al. (2016). The standard deviation, on the other hand is smaller because the finite element analysis does not incorporate all sources of uncertainty.

Then the magnitude effect is investigated, and a group of fragility curves are developed based on the magnitude of the events. Spatially correlated random fields are implemented into the finite element analysis so that the within-section spatial variability is accounted for, and this will also increase the

standard deivation of the log-normal CDFs of the fragility curves. Lastly, the relative density of the sand material is varied, which produced another group of fragility curves that accounted for additional uncertainty. All things considered, the standard deviation of the log-normal CDFs for fragility function obtained from finite element model is still smaller than what was proposed by Kwak et al. (2016) after incorporating motion-to-motion variability,within-section spatial variability and section-to-section variability. I believe that modeling uncertainty is another important source of uncertainty that is not incorporated in this study, and can be attributed to several factors. For example, the vertical component of the ground motion is not considered, which will also have impact on the crest settlement. There is newer material model available such as PM4 Sand material model that can be used to model sand materials. This might also result in differences in model response.

5 MCDONALD ISLAND LEVEES

This chapter focuses on developing fragility functions for McDonald Island levees using finite element simulations. McDonald Island is in the central Delta as shown in Fig. 5.1. We chose to focus on McDonald Island because it contains important natural gas infrastructure that is owned by Pacific Gas and Electric (PG&E). This research was funded by the California Energy Commission to study impacts of levee failures on gas pipelines, so McDonald Island was a natural choice for performing this study. I first discuss characterization of McDonald Island levees, including geometry based on LiDAR and bathymetry surveys. I then focus on stratigraphy and soil properties using available boring logs and geophysical surveys. I then select ground motions for the finite element study in a manner that is broadly consistent with seismic hazard in the region. Finite element models of various levee cross-sections are then developed and shaken with the ground motions. Finally, fragility functions are derived by relating predicted levee settlement to ground motion intensity measures, earthquake magnitude, and soil properties.



Figure 5.1 Map of the Sacramento and San Joaquin Delta Region (USGS)

5.1 CHARACTERIZATION OF MCDONALD ISLAND LEVEES

5.1.1 Levee Geometry

LiDAR data (obtained by California DWR in 2017) and bathymetry data are used to define the levee geometry, which are shown in Figure 5.2. The LiDAR data is available across the whole Island, while the bathymetry data is available only at the north of the island (Columbia Cut) and the east of the island (Turner Cut).

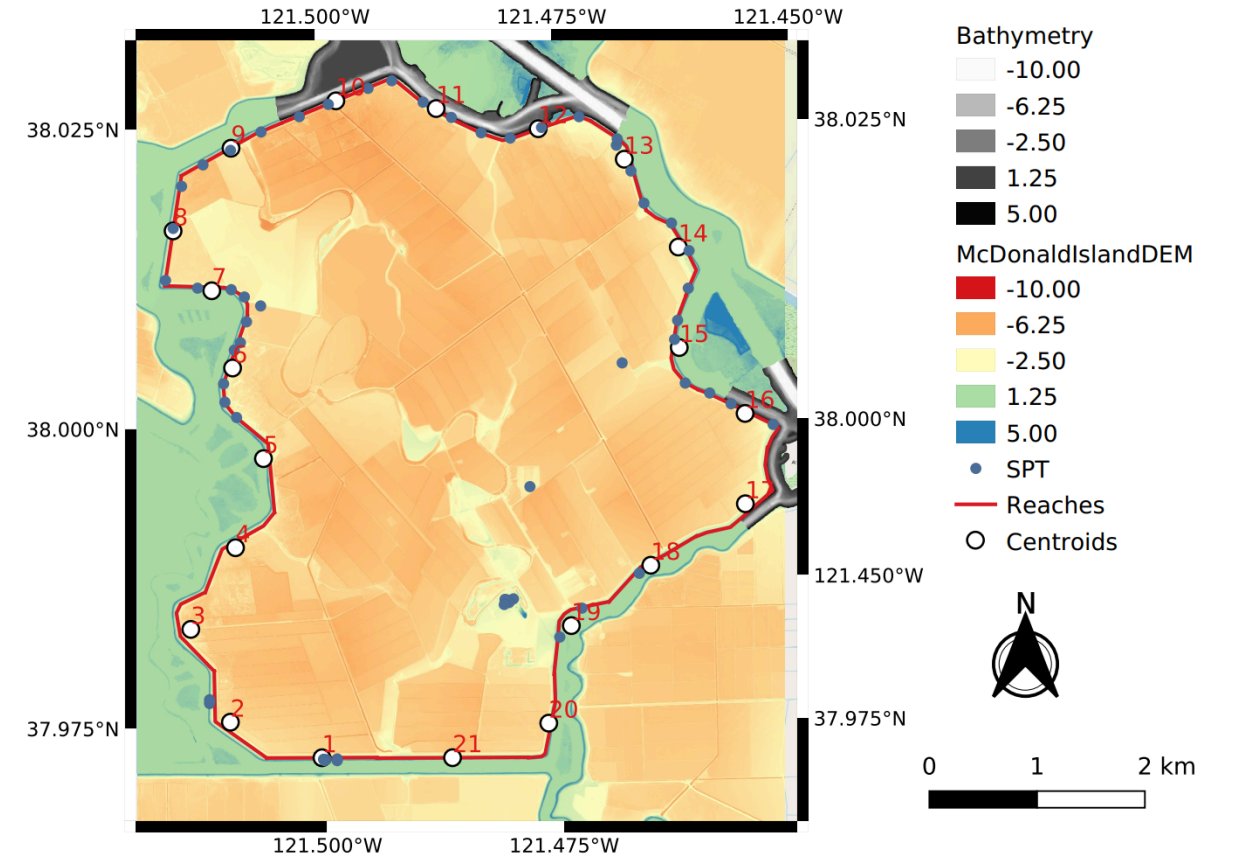


Figure 5.2 Bathymetry and LiDAR data at McDonald Island, location of boring logs and reaches

As is also shown in Figure 5.2, McDonald Island is divided into 21 "reaches", which are displayed red lines with white circles denoting the centroid of each reach. A reach is defined as a length of levee for which the limit state function is a stationary random field, meaning that the capacity and demand are also stationary random fields (Kwak et al. 2016). Following this definition, the reach can be represented by analysis of a single cross-section. Soil properties and seismic demands may vary within a reach, but their mean, standard deviation, and spatial correlation structure must be constant within the reach. As for McDonald Island, I selected 1km as the reach length based on analysis of levee geometry and spatial variability of shaking demands from seismic hazard analysis. My colleague, Zehan Liu, performed a seismic hazard analysis for neighboring Bacon Island, and found that mean shaking demands were essentially constant with 1km reaches.

At each centroid location, I was able to obtain a cross-section profile that represents that particular reach. Figures 5.3, 5.4 and 5.5 plot the LiDAR profiles for all 21 reaches. Only the LiDAR data are used here for geometry comparison due to the limited bathymetry data. As is indicated in these three Figures, the cross-section profiles look quite similar despite the minor differences of the locations of the toe drain at the land side. It is reasonable to conclude that these reaches have similar geometry profiles, and I herein select a single cross-section geometry for analysis.

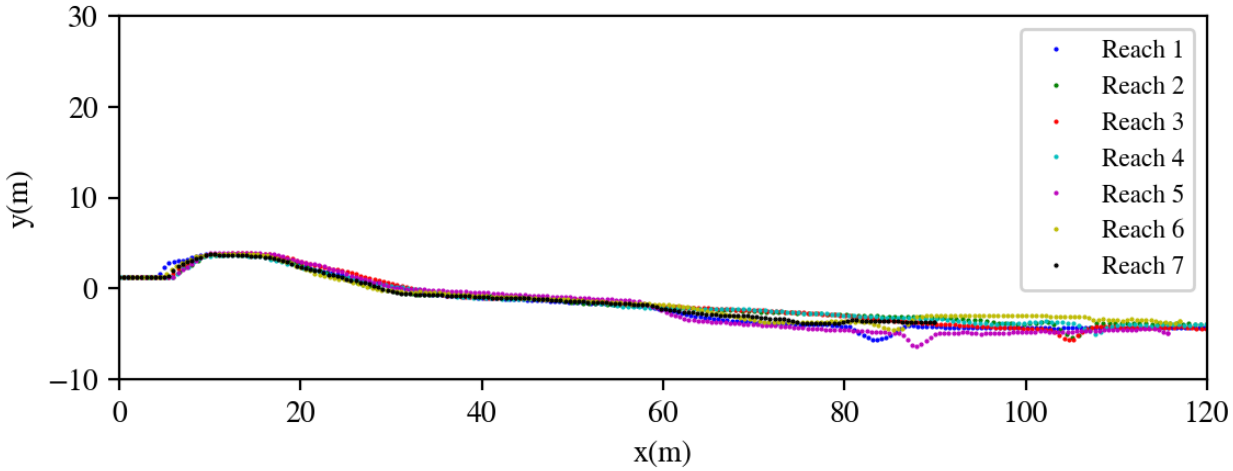


Figure 5.3 Geometry profiles of reaches 1-7 (LiDAR data only)

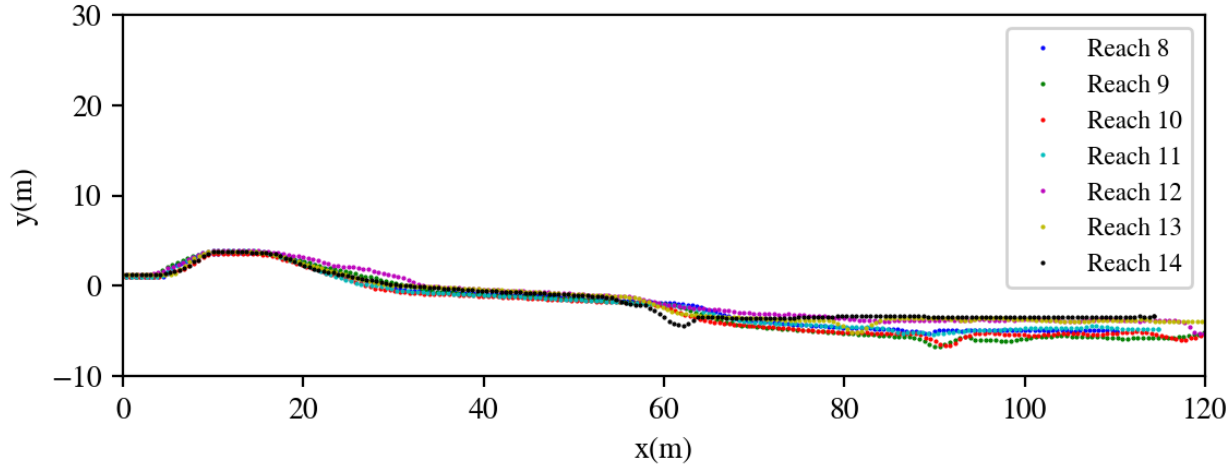


Figure 5.4 Geometry profiles of reaches 8-14 (LiDAR data only)

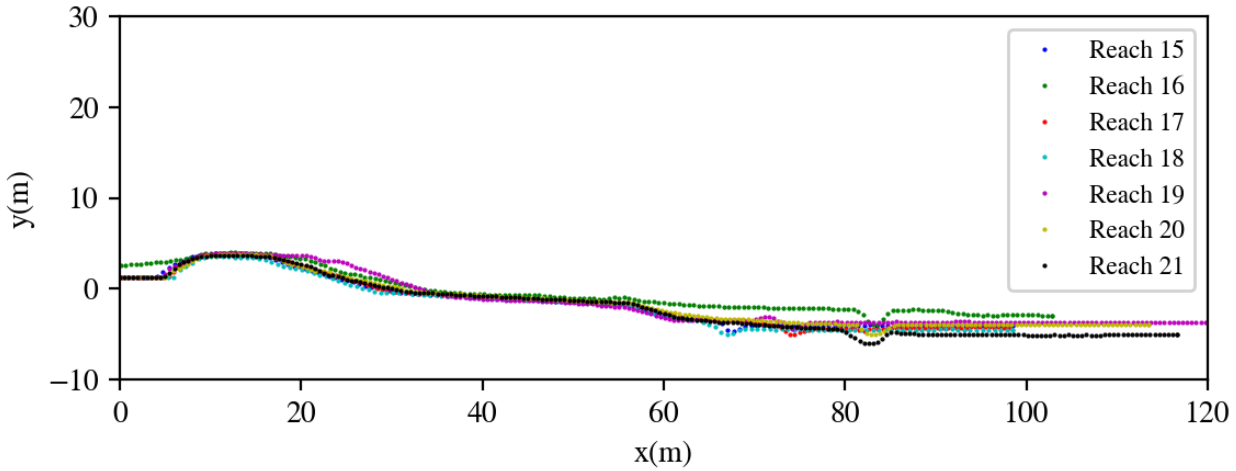


Figure 5.5 Geometry profiles of reaches 15-21 (LiDAR data only)

In order to build a complete geometry profile, both LiDAR and bathymetry data will need to be incorporated. Figure 5.6 points out the locations of two boring logs that I will use to construct the geometry profile. The location of boring log Mcd-Tra-22 will have both LiDAR and bathymetry data while the location of Mcd-Tra-24 only has LiDAR data. However, the location of Mcd-Tra-24 is still preferred because it also has shear wave velocity measurement at that location, which will be addressed in the next section. Using QGIS, the geometry profiles at boring logs Mcd-Tra-22 and Mcd-Tra-24 are obtained and shown in Figure 5.7 and Figure 5.8, respectively. The horizontal line in the LiDAR data indicated the location of the water table in the channel. The next step is to combine the bathymetry

data from cross-section at boring log Mcd-Tra-22 with LiDAR data from cross-section at boring log Mcd-Tra-24, and the resulting geometry profile is shown in Figure 5.9.

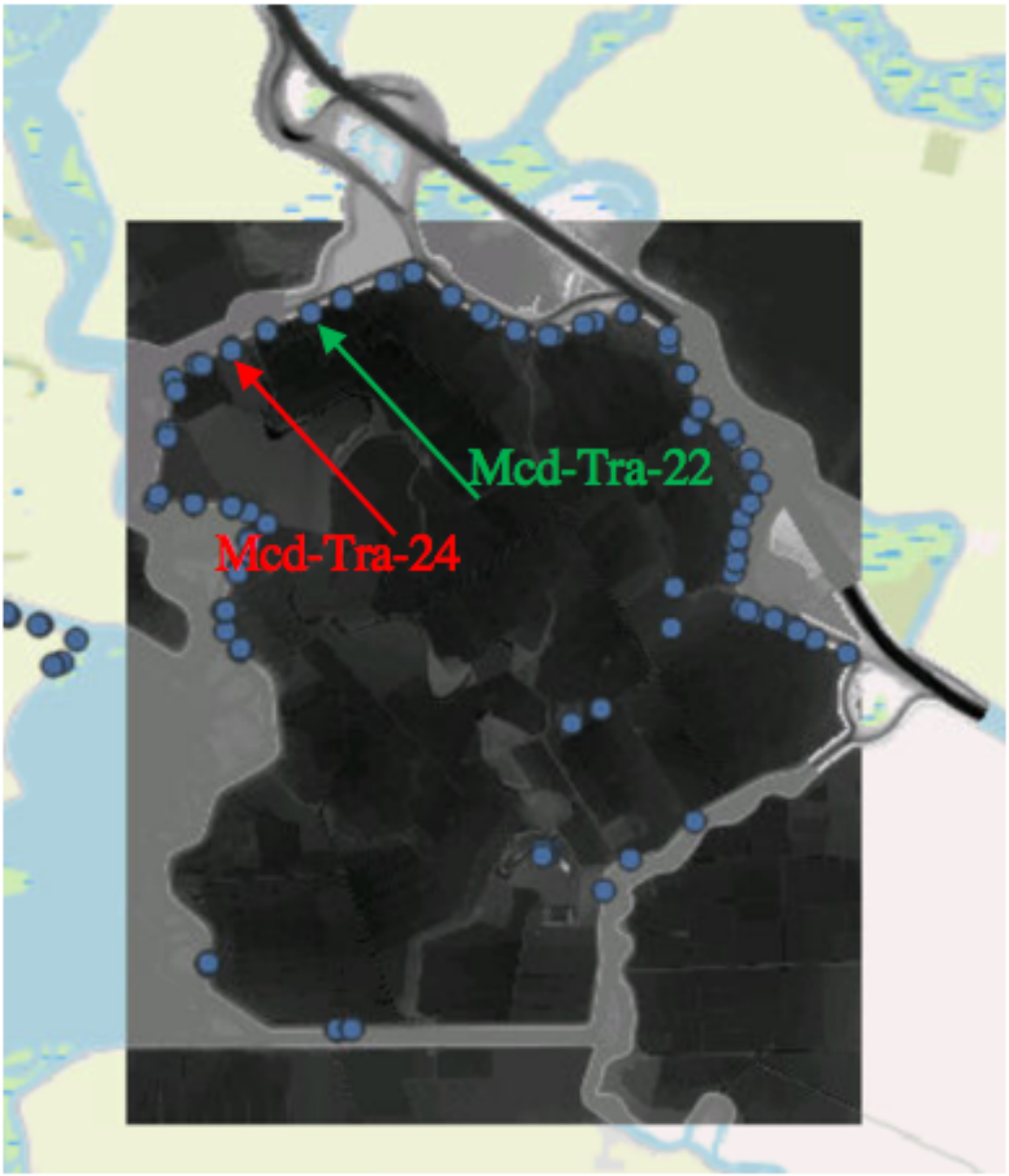


Figure 5.6 Map of two boring logs locations at McDonald Island

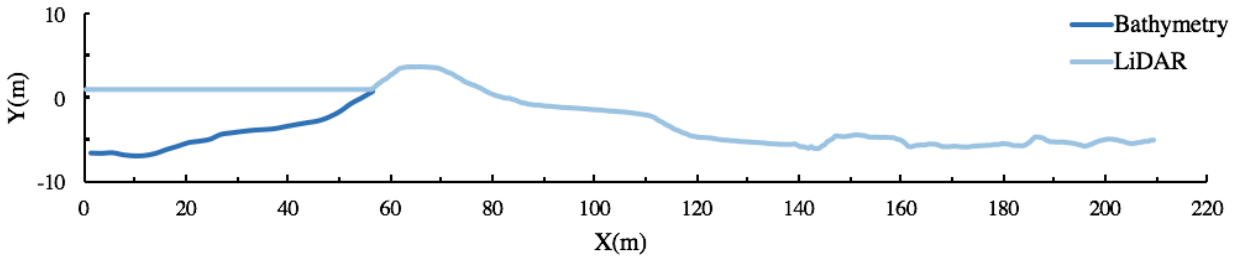


Figure 5.7 Geometry profiles at boring log Mcd-Tra-22

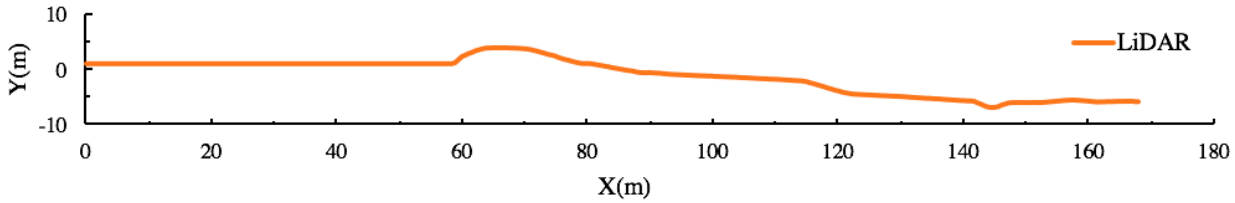


Figure 5.8 Geometry profiles at boring log Mcd-Tra-24

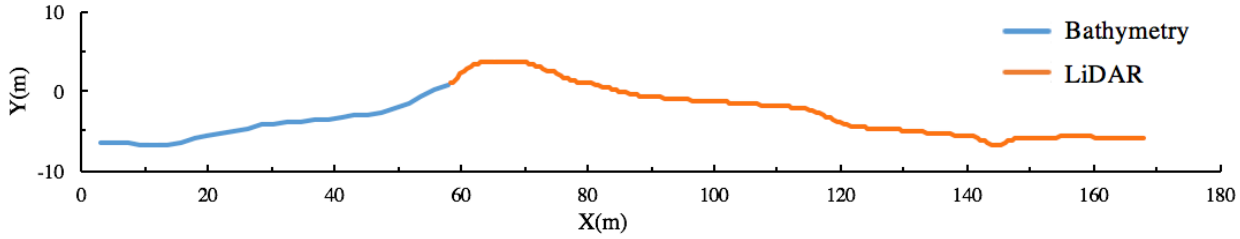


Figure 5.9 Combined geometry profile using both LiDAR and bathymetry data

5.1.2 **Stratigraphy and Soil Properties**

Now that I have constructed a generic geometry profile for the McDonald Island levees, I turn to the issue of developing stratigraphic cross-sections that reasonably represent these levees. Ideally, the cross-section will have multiple site investigations along the cross-section, laboratory tests to determine soil properties, and groundwater measurements to assess seepage conditions. This density of data is not available, but there are a couple of boring logs available for McDonald Island, which are shown as the blue points in Figure 5.2.

Some geophysical measurements of shear wave velocity are also available at the McDonald Island. Figure 5.10 shows the approximate locations of the three survey sites where Dr. Mitchell Craig and Dr.

Koichi Hayashi have performed geophysical measurements of shear wave velocity as part of the CEC-sponsored research effort. At each of the three survey sites, a pair of parallel lines 300 meters long were recorded, one along the crown (crest) of the levee and one at the toe (base) of the levee on the island interior side, with a spacing of about 30 meters between the two lines. The line on the levee crown was recorded using the MASW method, while the line at the toe of the levee was recorded using individual seismographs with geophones, where ambient noise was recorded and processed using the Microtremor Array Method (MAM).



Figure 5.10 Map of locations of three survey sites that have shear wave velocity measurement

I focused first on Site 1 to develop a levee cross-section because it has both boring logs nearby and shear wave velocity measurements, and it's close to the Columbia cut where there is bathymetry data. Figure 5.11 plots the stratigraphy information indicated by three boring logs (Mcd-Tra 23, Mcd-Tra 24 and Mcd-Tra 25) at or near Site 1. Although these three boring logs are not at the same cross-section, here I am integrating all the information to build a stratigraphic cross-section based on stratigraphy profiles from these boring logs, which is shown in Figure 5.12. The approximate location of these three boring logs are also indicated in Figure 5.12.

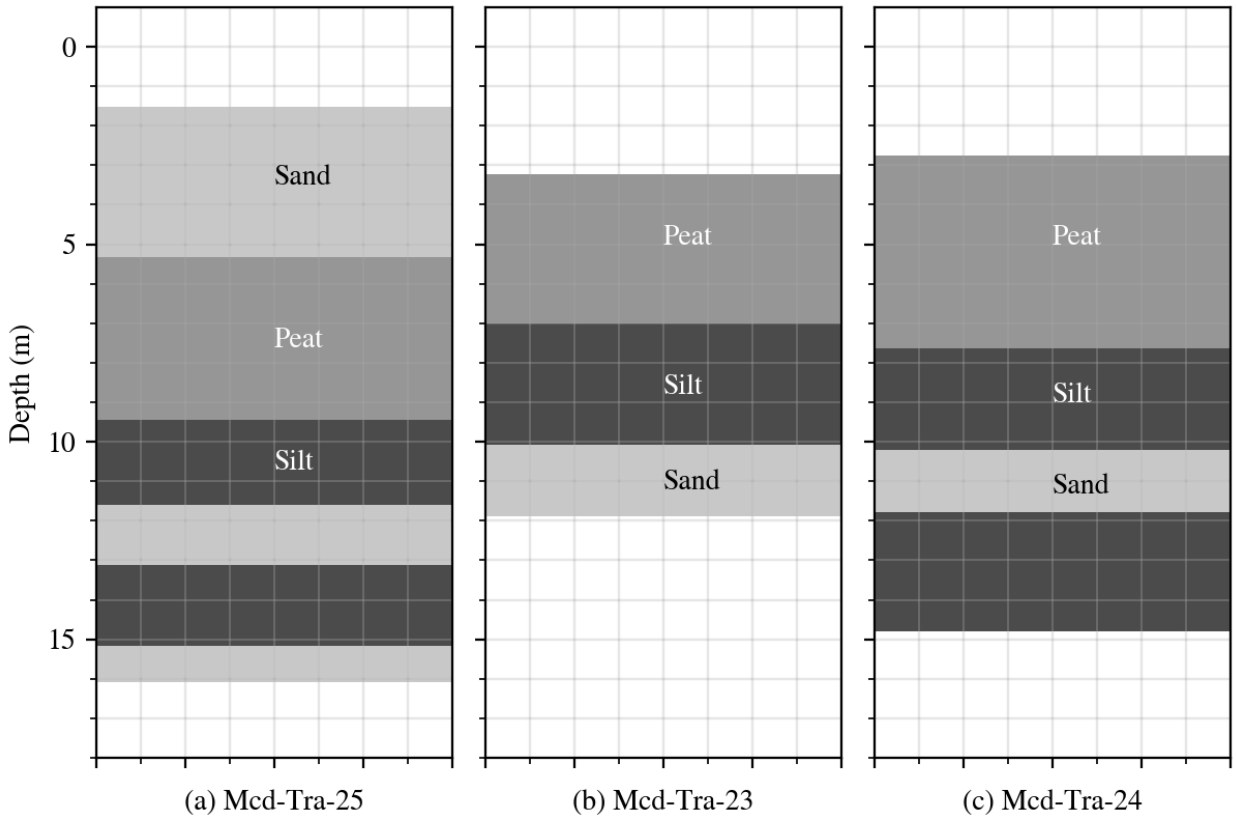


Figure 5.11 Stratigraphy profile of boring log (a) Mcd-Tra-25, (b) Mcd-Tra-23, (c) Mcd-Tra-24

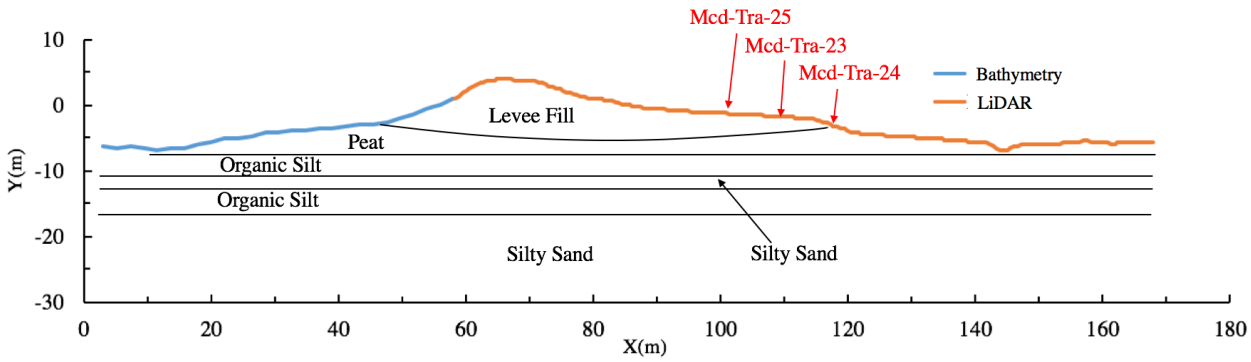


Figure 5.12 A complete cross-section layout including the stratigraphy

Since this cross-section is within Site 1, a shear wave velocity profile at the levee crest is also available. Figure 5.13 shows the shear wave velocity profile from the crest of levee cross-section where boring log mcd-tra-24 is located, and it is clearly seen that the region where the shear wave velocity gets as low as 80m/s is consistent with the presence of peat materials beneath the levee body, which is indicated in Figure 5.12. Unfortunately, the three boring logs used to determine the stratigraphy of the cross-section do not contain blow counts that can be utilized for the soil properties. Therefore, other boring logs available at McDonald Island need to borrowed to define the soil properties. Figure 5.13 shows four raw blow count profiles at McDonald Island. After a correction for $(N_1)60$, it turns out the relative density of the levee fill ranges from 55% to 80%, and the two sand layers beneath the levee fill seems to be even denser. Therefore, I decide to use the average $(N_1)60$ about 23, which yields a relative density of around 71% for all the sand layers. For the peat and silt layer, since blow counts are not really helpful for the strength determination, a strength normalization method is used to determine the undrained shear strength. See Eq. 4.2. For instance, an overconsolidation ratio of 2 is assumed for peat layers, because peat soils are unknown for significant secondary compression, and the void ratio might decrease over time. A shear strength profile is also shown in Figure 5.13.

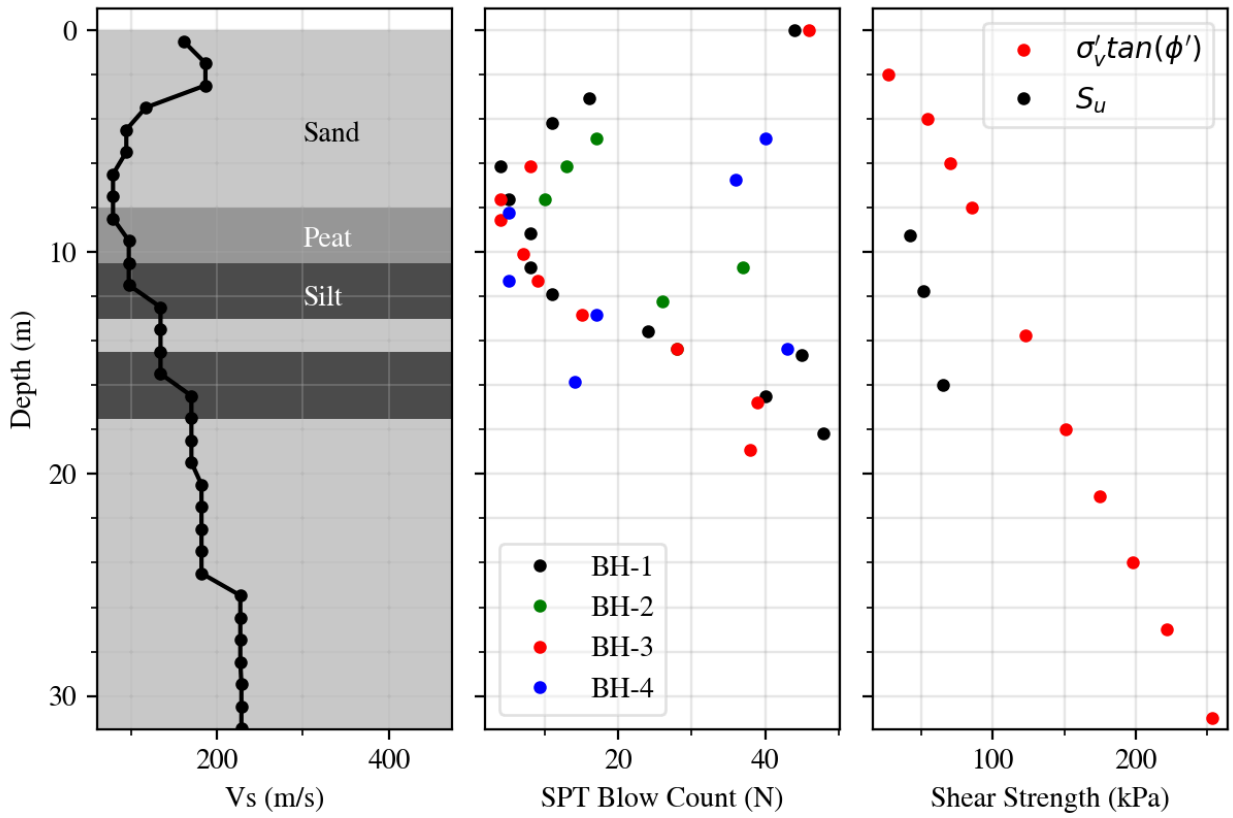


Figure 5.13 A shear wave velocity profile at levee crest including stratigraphy, four SPT blow count profile and shear strength profile over depth

In addition, Dr. Mitchell Craig and Dr. Koichi Hayashi processed data separately from two parallel lines at each site, but then combined the data together to produce a single two-dimensional shear wave velocity section for each site. Figures 5.14-5.16 shows the combined shear wave velocity profiles at these three sites. A low shear wave velocity zone in the shallow depth is found at all three sites, and shear wave velocities at shallow depth tend to be under 100m/s due to the presence of the peat. Velocities deeper than about 10m are then higher than 100m/s and tend to increase with depth.

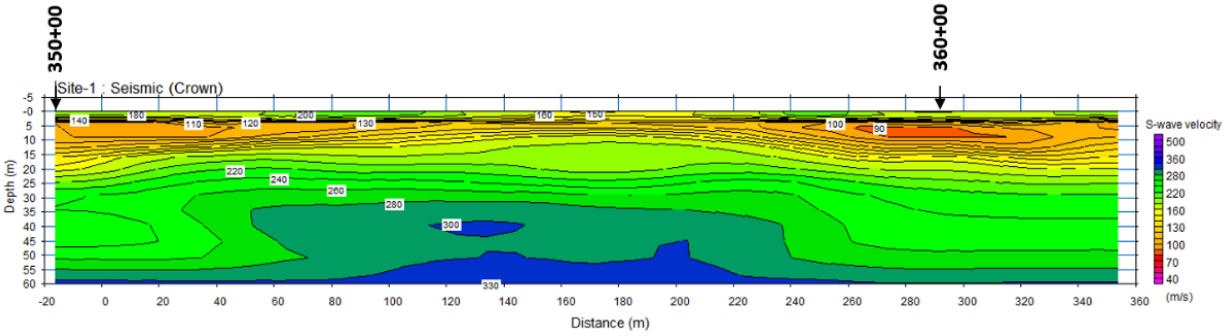


Figure 5.14 Seismic velocity profile at Site 1 from combined active and passive surveys (M.Craig and K.Hayashi)

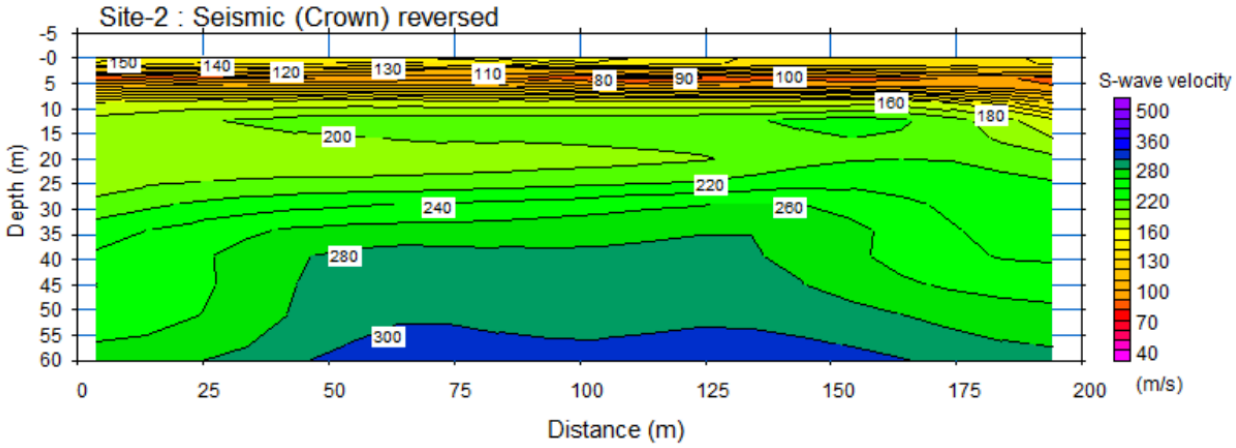


Figure 5.15 Seismic velocity profile at Site 2 from combined active and passive surveys (M.Craig and K.Hayashi)

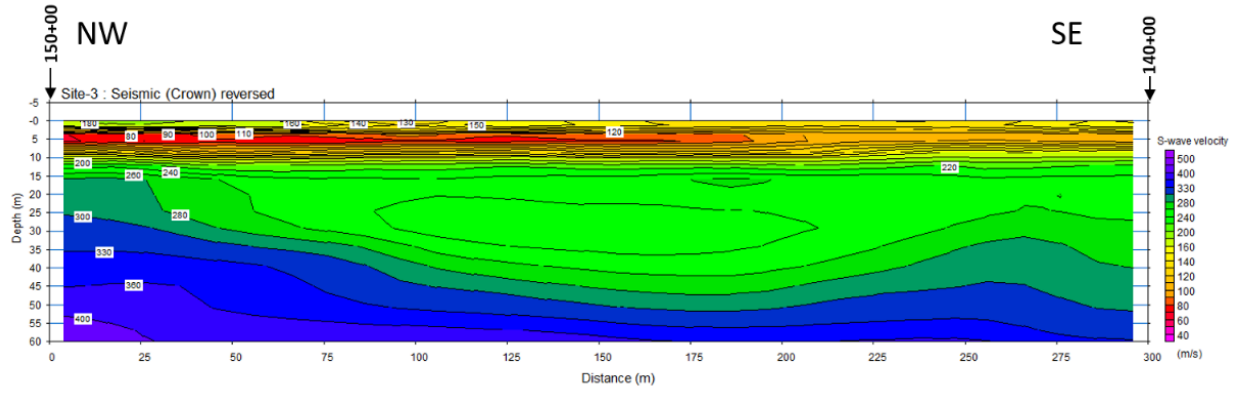


Figure 5.16 Seismic velocity profile at Site 3 from combined active and passive surveys (M.Craig and K.Hayashi)

Figure 5.17 plots the time-averaged shear wave velocity for the upper 3m at Site 1 as a function of distance along the levee crest. Variations in the velocity follow a spatial correlation structure that is clearly apparent in the data. Figure 5.18 shows the variogram obtained from the average shear wave velocity profile. The variogram is fitted with Gaussian variogram model, with a nugget of 0, sill of 5.91 $(m/s)^2$ and an effective range of 117 m. The horizontal scale of fluctuation for the shear wave velocity is 58.5 m, which is a half of the effective range. Repeating this process for the other two sites, and the computed horizontal scale of fluctuation for Site 2 and Site 3 are 59m and 60m, respectively. I was not able to compute the vertical scale of fluctuation for shear wave velocity using these data because the data does not have enough resolution in the vertical direction.

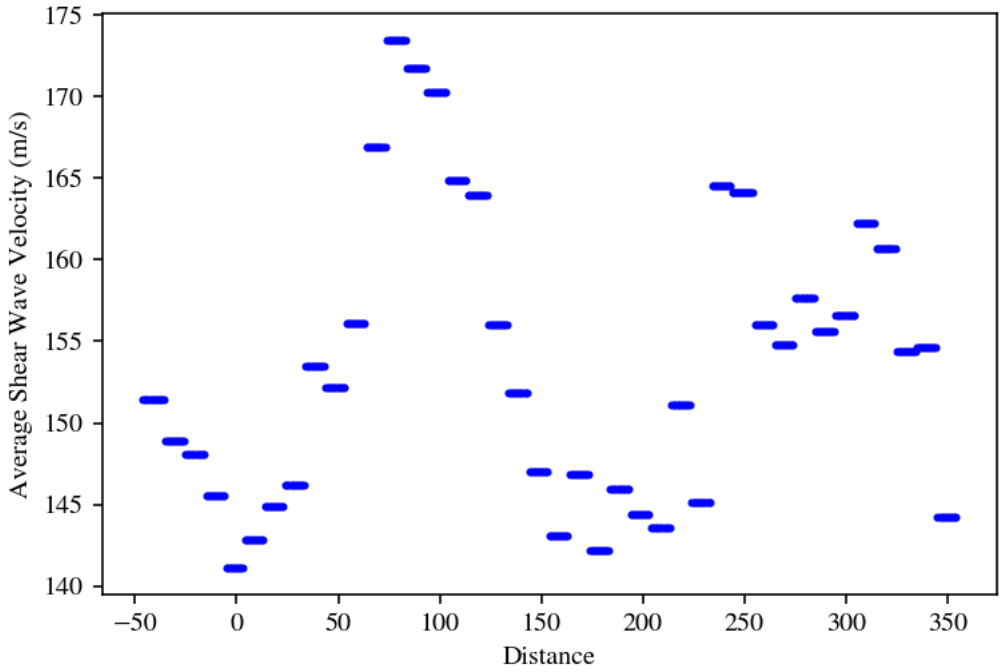


Figure 5.17 Time-averaged shear velocity profile of upper 3m at Site 1

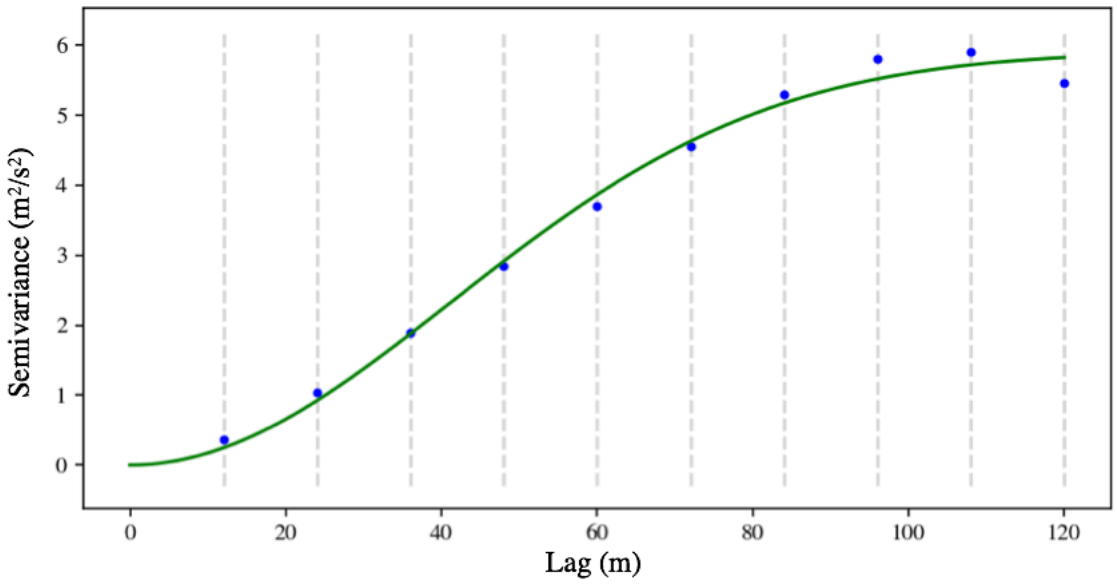


Figure 5.18 Variogram of the average shear wave velocity profile for upper 3m at Site 1

5.1.3 **Ground Motion Selection**

This section presents procedures applied to select ground motions that are consistent with the results of seismic hazard analyses in the Delta (specifically at McDonald Island) for application in finite element simulations. Key considerations in selecting the ground motions are:

1. Intensity measures (such as PGA and PGV) must cover the range of intensities identified from seismic hazard analyses for a range of return periods (or exceedance rates) relevant in engineering applications
2. The distribution of magnitude and distance should be reasonably consistent with PSHA disaggregation
3. Earthquake mechanisms should be consistent with seismic hazard in the region

These goals are attained by first performing Probabilistic Seismic Hazard Analysis (PSHA) at various locations within McDonald Island. Four sites are selected individually in the North, South, East and West direction of McDonald Island. The reference V_{S30} used in these analyses are around 200m/s. The

PSHA was performed using USGS nshmp-haz code (https://github.com/usgs/nshmp-haz). The Third Uniform California Earthquake Rupture Forecast (UCERF3) seismic source model (Field et al. 2014) and the NGA-West 2 ground motion model (Boore et al. 2014) were used in these analyses.

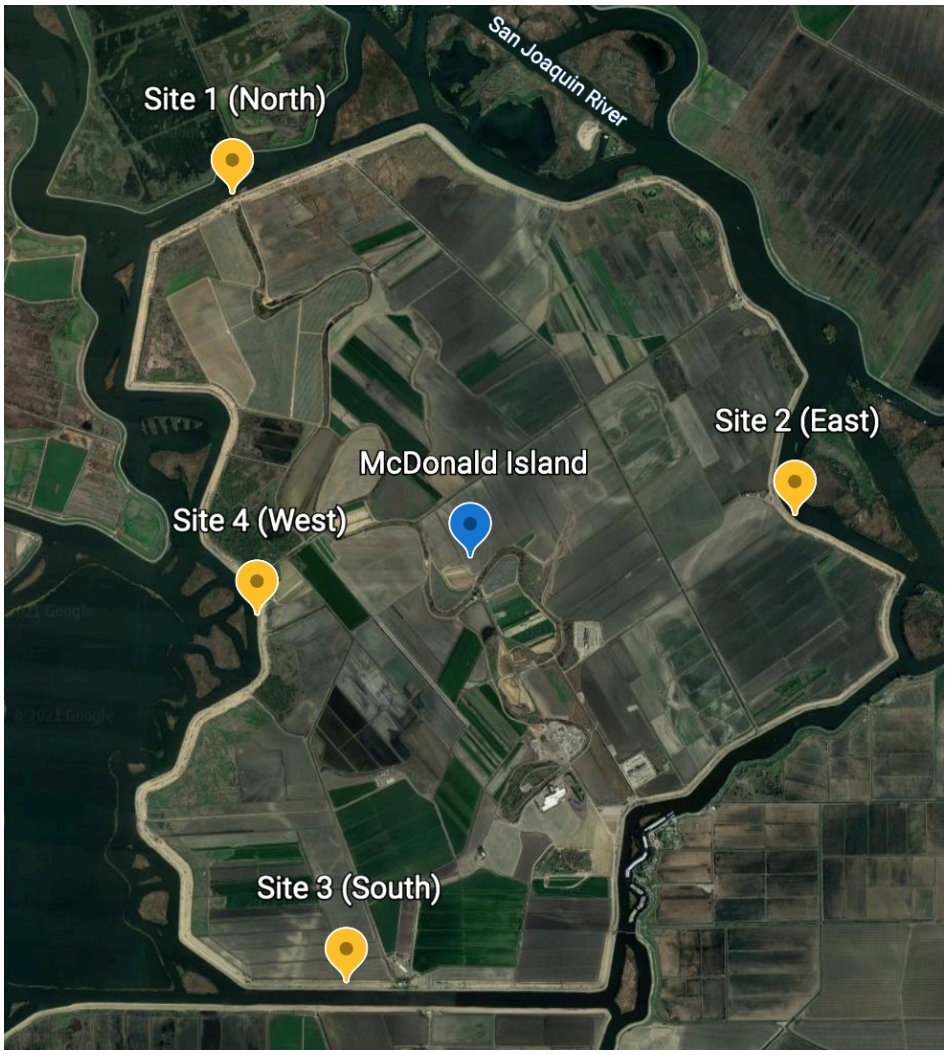


Figure 5.19 The location of four representative sites at McDonald Island

Hazard curves obtained from PSHA are plotted in the Figure 5.20. Figure 5.20 (a) shows the hazard curve in terms of PGA, and Figure 5.20(b) shows the hazard curve in terms of PGV. The hazard curves at these four sites are essentially identical, which is most likely due to the fact that the McDonald Island is relatively small.

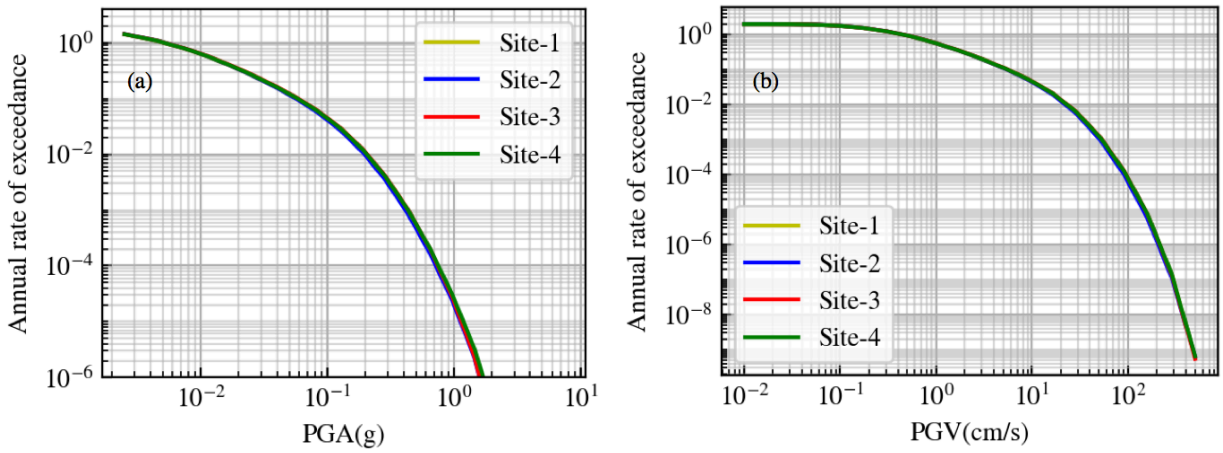


Figure 5.20 Hazard curve in terms of (a) PGA and (b) PGV

While PSHA computes the total seismic hazard using total probability theorem, PSHA deaggregation (Bazzurro and Cornell 1999; Harmsen 2001; McGuire 1995) computes the relative contribution of earthquake parameters to the total hazard using Bayes' rule (Benjamin and Cornell 1970). When hazard is computed using different faults that produce a range of magnitudes at different source-to-site distances, deaggregation of seismic hazard will provide information about contributions to the overall hazard from each magnitude-distance bin. Note that seismic hazard in the Delta is controlled by moderate magnitude nearby earthquakes, and larger magnitude more distant earthquakes on the San Andreas and Hayward faults. The sources at close distance are combinations of background grid sources and known faults like the Great Valley Midland fault about 14km away from the McDonald Island.

Figure 5.21 is an example of the deaggregation result of magnitude and distance at site 1 for a return period of 10 years. Since four sites have similar deaggregation results, the result is only plotted for site 1 here. There are six return periods analyzed including 10 years, 50 years, 225 years, 475 years, 975 years and 2475 years. The deaggregation plot for the other 5 return periods are shown in Figures 5.22-5.26.

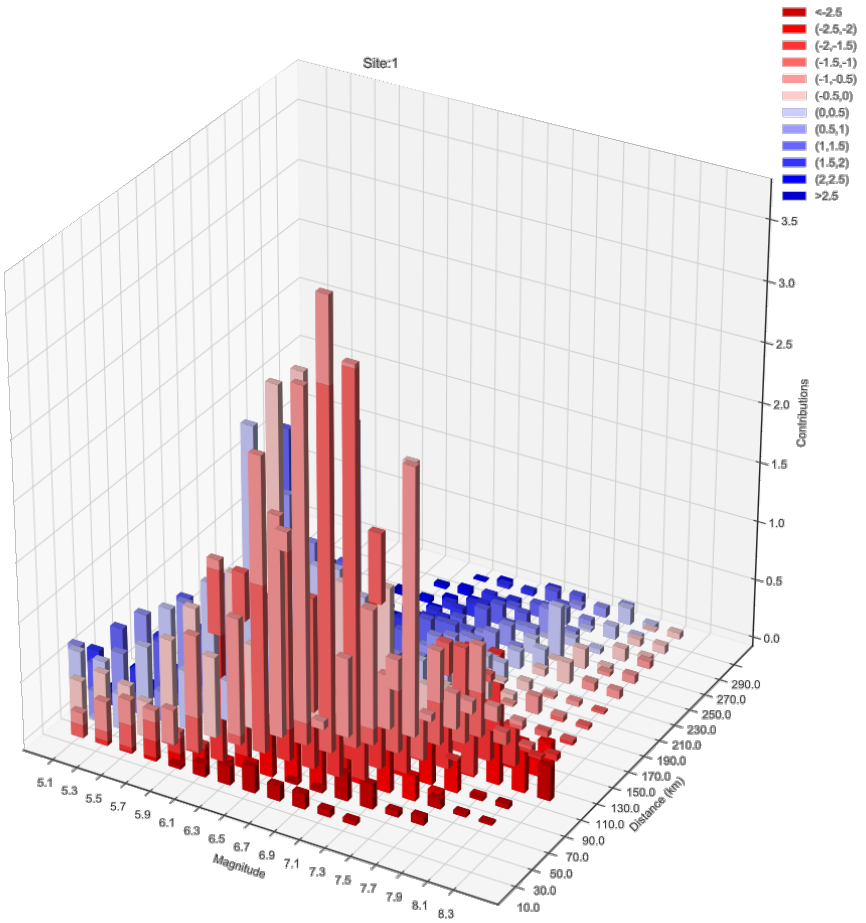


Figure 5.21 Deaggregation results at site 1 for a return period of 10 years

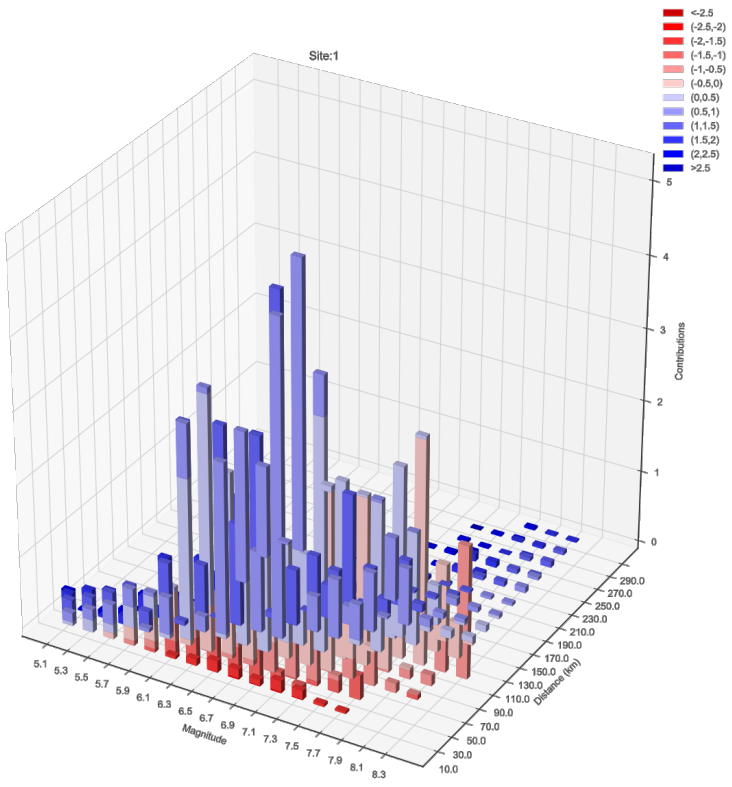


Figure 5.22 Deaggregation results at site 1 for a return period of 50 years

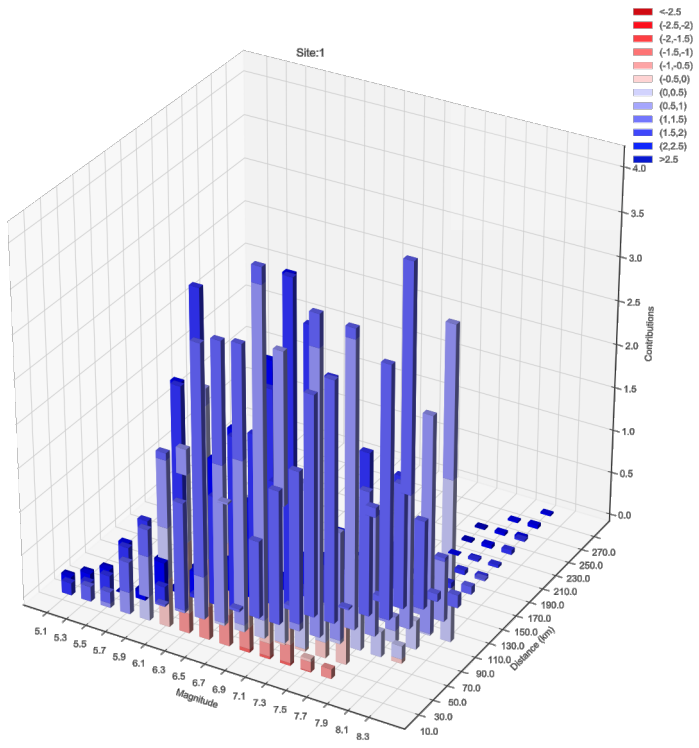


Figure 5.23 Deaggregation results at site 1 for a return period of 225 years

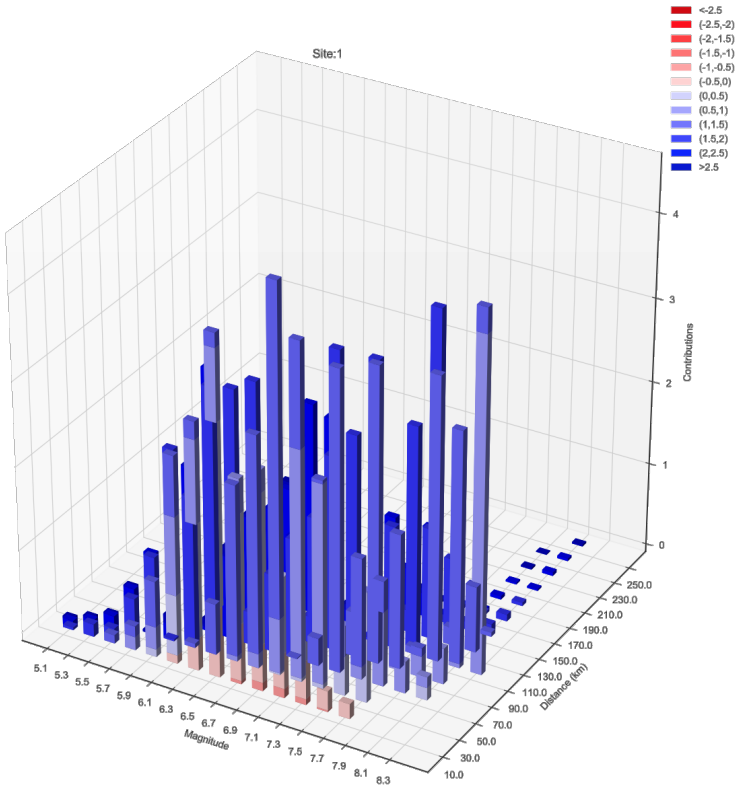


Figure 5.24 Deaggregation results at site 1 for a return period of 475 years

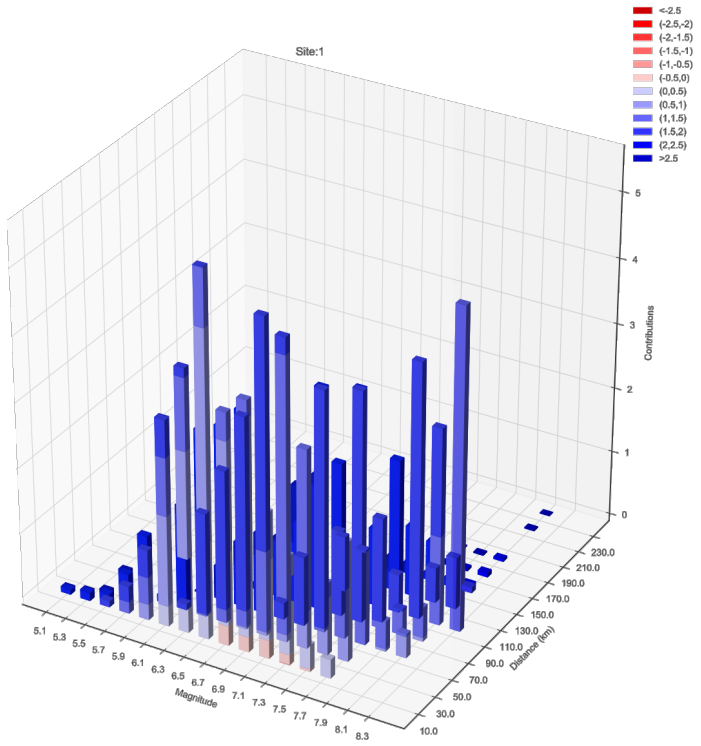


Figure 5.25 Deaggregation results at site 1 for a return period of 975 years

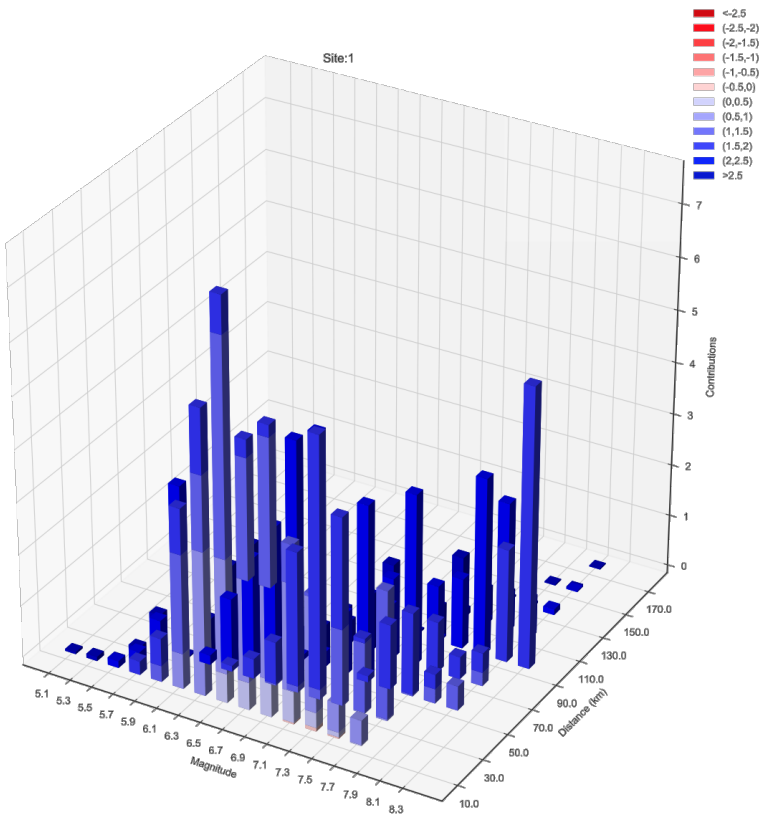


Figure 5.26 Deaggregation results at site 1 for a return period of 2475 years

Based on deaggregation results for all the return periods at all four sites, I selected scenarios of magnitude and distance combinations that contributed to the total seismic hazard for more than 1%. And among all these scenarios, I selected the minimum and maximum distance given each magnitude of interest, which resulted in a total of 27 scenarios of magnitude and distance. These 27 scenarios are plotted in Figure 5.27.

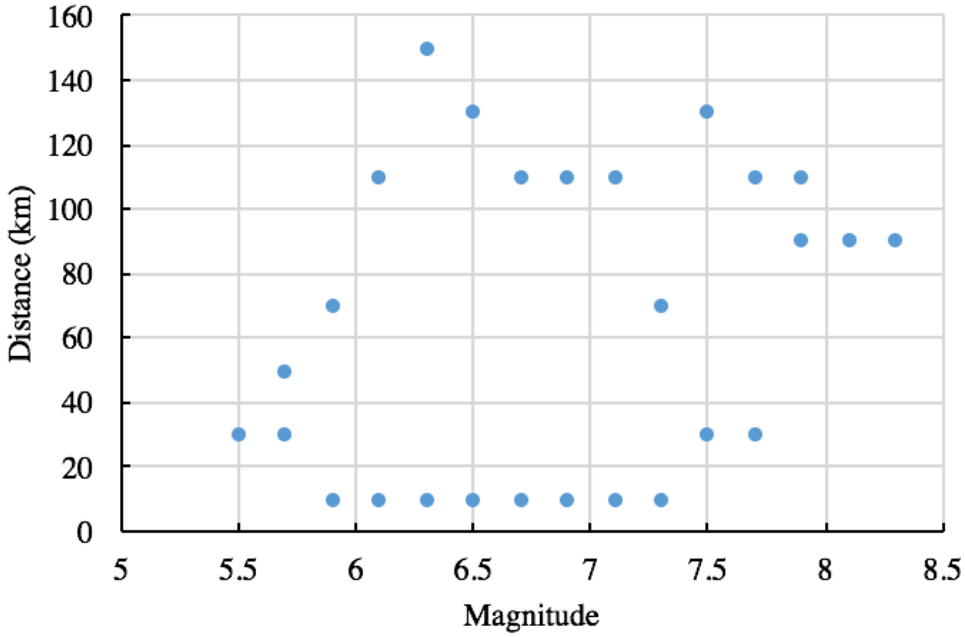


Figure 5.27 Scenarios of magnitude and distance combinations from deaggregation results

After obtaining 27 scenarios of magnitude and distance, a ground motion selection algorithm proposed by Baker and Lee (2018) is applied to select a group of ground motions that match an unconditional response spectrum associated with each combination of magnitude and distance. The ground motion model used in the algorithm is BSSA14 (Boore et al. 2014), which is consistent with what was done in the PSHA. All the ground motions selected are from the NGA-West2 database. Subduction events are not considered. The magnitude of events ranges from 5 to 8.3, and the rupture distance is less than 200km. V_{S30} is specified to be less than 500m/s. For each scenario of magnitude and distance, 30 scaled ground motion records are selected by running this algorithm. Figure 5.28 shows an example of the response spectra of 30 selected ground motion compared to the target response spectra where the magnitude is 6.5 and the rupture distance is 10km.

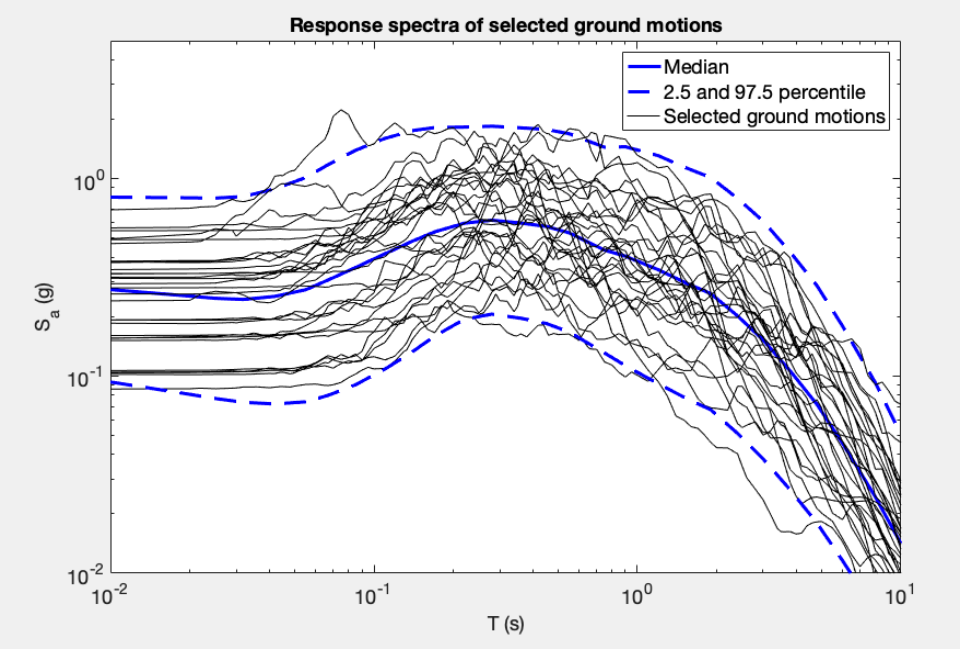


Figure 5.28 Response spectra of 30 ground motions, compared to the target response spectra predicted by GMM model (M = 6.5, R= 10km)

Overall, I managed to obtain approximately 760 scaled ground motion records with the distribution of PGV shown in Figure 5.29 It is clearly seen from Figure 5.29 that these ground motion records do cover a good range of PGV which is beneficial to the construction of fragility functions.

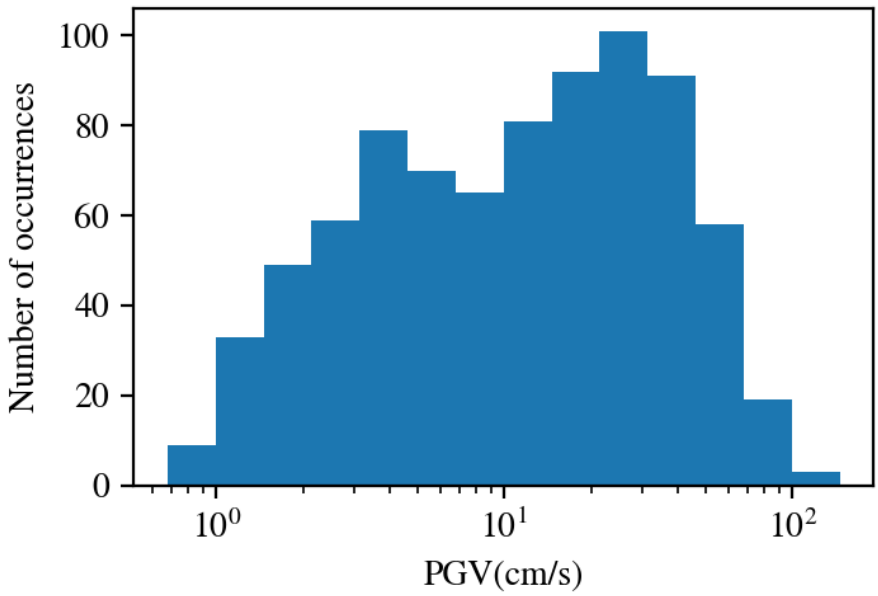


Figure 5.29 Histogram of PGV for the selected ground motions

5.2 SIMULATIONS

5.2.1 Finite Element Model Setup

As mentioned in Chapter 2, in cases where the phreatic surface is unknown, and there is no recorded groundwater elevation inside the levees, it is better to conduct a steady state seepage analysis in RocScience Phase 2 first to determine the location of the phreatic surface so that the phreatic surface can also be included in the mesh generation. Pre-defining the phreatic surface also makes it easier to create zero pressure conditions for nodes on and above the phreatic surface. I adopt this approach for the McDonald Island levees.

Figure 5.30 shows the model setup in Phase2. As indicated by the figure, the water in the channel is pretty high and close to the levee crest, and the groundwater is at the elevation of the toe on the landside of the levee. Figure 5.31 shows the pressure head distribution after seepage analysis is finished, and the purple line indicates the location of the phreatic surface.

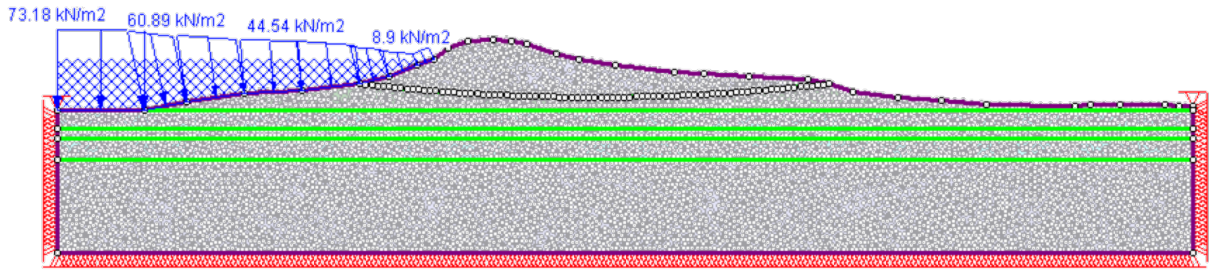


Figure 5.30 Model setup in Phase2 for seepage analysis

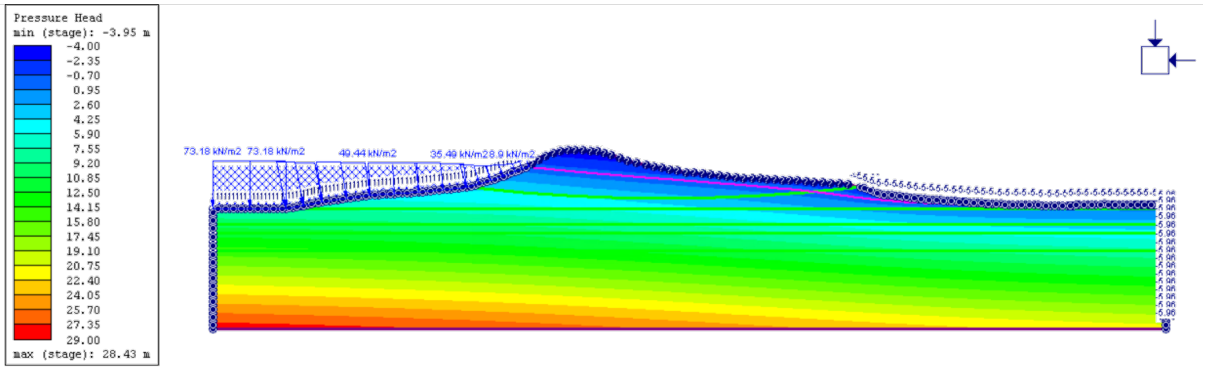


Figure 5.31 Pressure head distribution after seepage analysis in Phase2

After getting the phreatic surface through Phase 2, it is now easy to define that as a material boundary in GiD, which is indicated in Figure 5.32. Figure 5.32 shows the generated mesh after integrating information such as the geometry and material boundaries from Figure 5.12 into GiD. Similar to the levee models analyzed in Chapter 4, two thick columns on either side of the model are added as free-field columns, which ensures that free-field conditions exist at the horizontal boundaries of the model. After creating the mesh, the next step is to assign material properties to the elements. Table 5.1 summarizes some of the important parameters that are either directly used or related to material input parameters in OpenSees.

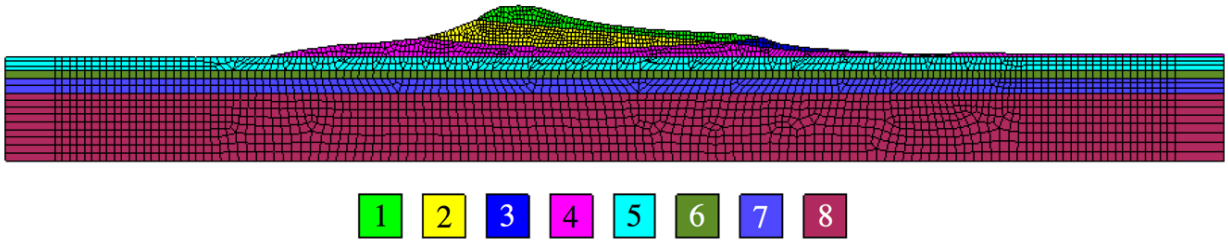


Figure 5.32 Mesh configuration using GiD for McDonald Island levee

Table 5.1 Material properties used based on available data and assumptions

Soil Type	MD	Layer Tag	ρ (g/cm^3)	υ	V_S (m/s)	D_R	OCR	k_x (m/s)	k_y (m/s)
Sand	PDMY03	1	1.9	0.35	161	71%	NA	$5x10^{-7}$	$5x10^{-7}$
Sand	PDMY03	2	2.1	0.35	192	71%	NA	$5x10^{-7}$	$5x10^{-7}$
Peat	PIMY	3	1.1	0.35	80	NA	2	$5x10^{-8}$	$5x10^{-9}$
Peat	PIMY	4	1.1	0.35	80	NA	2	$5x10^{-8}$	$5x10^{-9}$
Silt	PIMY	5	1.8	0.4	101	NA	2	$5x10^{-9}$	$5x10^{-9}$
Sand	PDMY03	6	2.2	0.35	154	71%	NA	$5x10^{-7}$	$5x10^{-7}$
Silt	PIMY	7	1.8	0.4	163	NA	2	$5x10^{-9}$	$5x10^{-9}$
Sand	PDMY03	8	2.2	0.35	211	71%	NA	$5x10^{-7}$	$5x10^{-7}$

Similar to what I did with Japanese levees, the shear wave velocity is used to determine the small strain shear modulus, and the Poisson ratio is used to relate the shear modulus and bulk modulus. Some of the boring logs data contain the dry density and moisture content data obtained from the laboratory testing, which can provide guidance on the density of soil. The relative density for the sand layer is based on the blow counts from the boring log locations, and is discussed in previous sections. It was found that the sand layers for the Mcdonald Island levees are generally from medium-dense to dense. The undrained shear strength for the peat and silt layers was determined based on the overconsolidation ratio and vertical effective stress. The permeability for different layers are varied based on the soil type, and are summarized in Table 5.1 as well.

Lastly, a Lysmer-Kuhlemeyer (1969) dashpot is added at the base of the model since all the motions I used are considered as outcrop motions. As discussed in Chapter 2, the dashpot coefficient is defined as the product of the mass density and shear wave velocity of the underlying medium. The average shear wave velocity of the underlying medium is obtained from the shear wave velocity profile shown in earlier section, and is computed to be around 280m/s.

5.2.2 **Example Realizations**

Unlike the case histories in Japan, there is no recorded response or reported performance to make a comparison, so I choose to show the simulation results for two cases: one realization where the levee model did not deform much during and after shaking (referred to as event 1) and one realization where a significant amount of deformations occurred (referred to as event 2). A post-processor tool, STKO, is used to visualize the analysis results.

Figure 5.33 shows the acceleration time series of event 1 together with its response spectra. The PGA of this motion is approximately 0.19g, and the PGV is around 0.15m/s. Figure 5.34 shows the crest motion time series under the shaking of event 1 as well as its response spectra. The PGA of the crest motion is approximately 0.43g, and the PGV is around 0.34m/s.

It was found that the levee crest settled about 0.015m during gravity stage, and the imposed ground motion caused the levee crest to settle an additional 0.037m. After the earthquake loading, the levee model was also allowed to reconsolidate, in which the excess pore water pressure will gradually dissipate. During this stage, the levee crest settled 0.005m. The post-shaking settlement is relatively small, which is expected because the plasticity model adopted herein assumes reconsolidation is purely elastic, whereas post-cyclic reconsolidation of liquefied sand is elasto-plastic. Figure 5.35 also shows the contour plots of vertical displacement during these three stages superposed on a deformed mesh with deformations amplified by 25. Figure 5.35(b) and Figure 5.35(c) are very similar, which also indicates that the levee model did not settle much during the post-shaking reconsolidation stage.

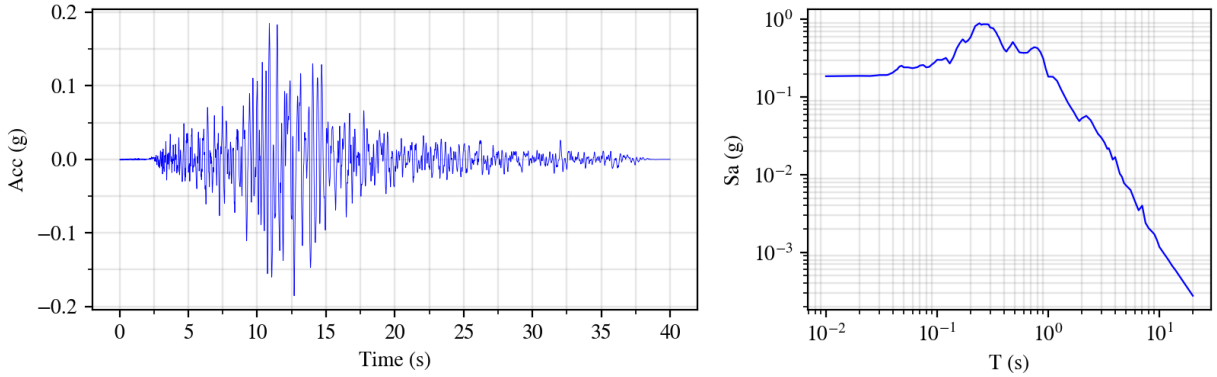


Figure 5.33 Input ground motion record of event 1 and its response spectra

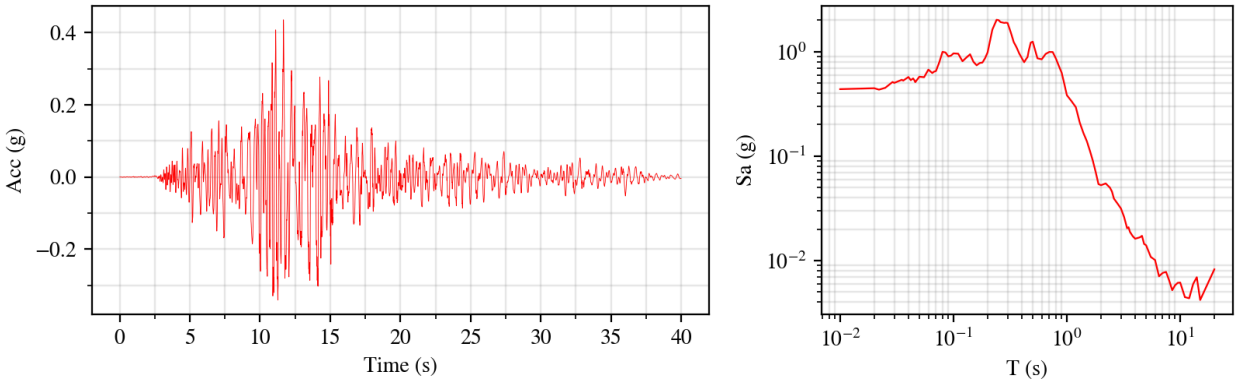


Figure 5.34 Crest motion time series under the shaking of event 1 and its response spectra

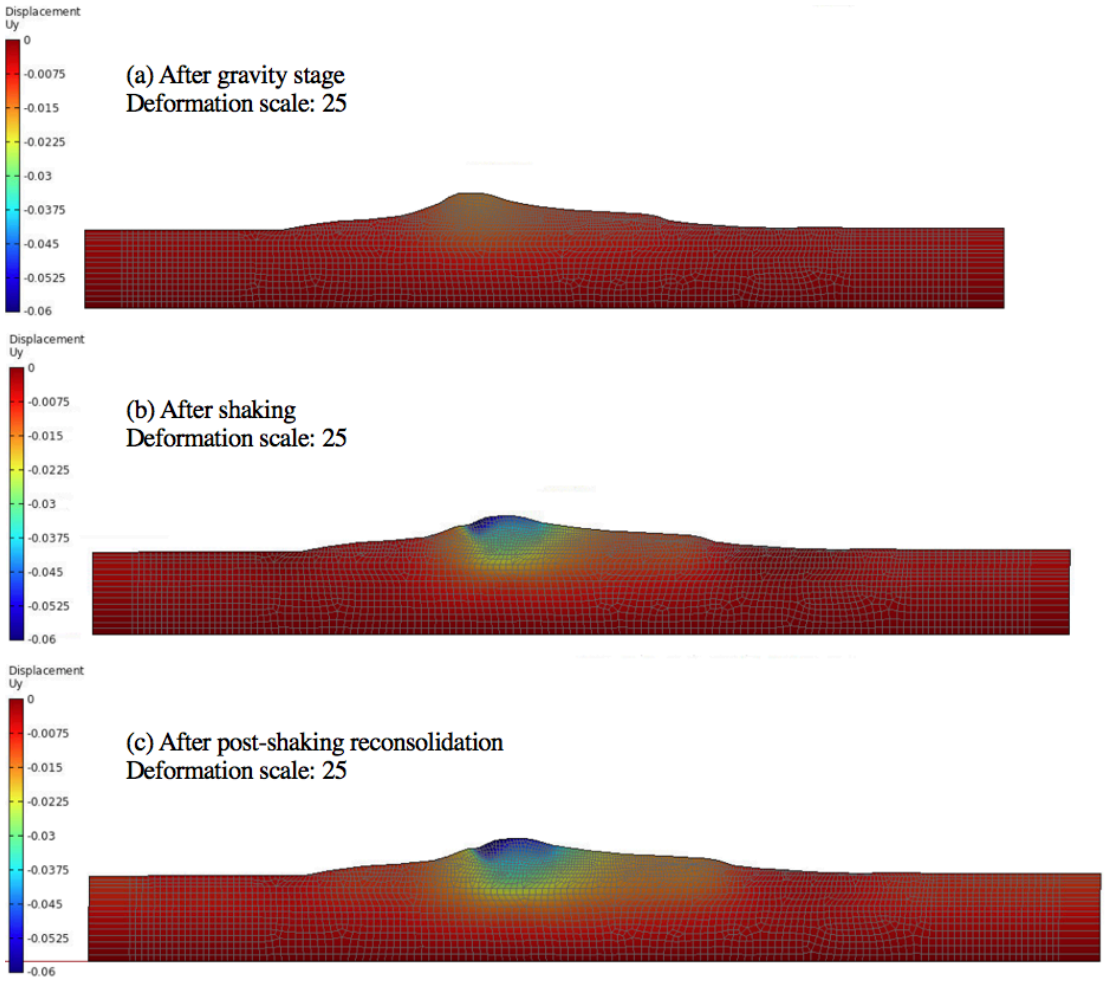


Figure 5.35 Vertical displacement contour plots after (a) gravity (b) shaking (c) post-shaking reconsolidation under event 1

Furthermore, Figure 5.36 shows the pore water pressure distribution during three different stages. Note that although the legend title in Figure 5.36 says angular velocity, it actually represents the pore water pressure due to OpenSees' implementation of pore water pressure as the velocity in the 3rd DOF. It is clearly seen from Figure 5.36 that excess pore pressure did build up during shaking, and those excess pore water pressure dissipated during the post-shaking reconsolidation stage as water pressure returned to its pre-event steady state condition. In addition, Figure 5.37 shows how the excess pore water pressure ratio at the center of the levee fill changes over time during shaking, and it is clear that the levee fill did not liquefy under event 1. Figure 5.38 indicates that the crest settlement gradually increases as the shaking continues.

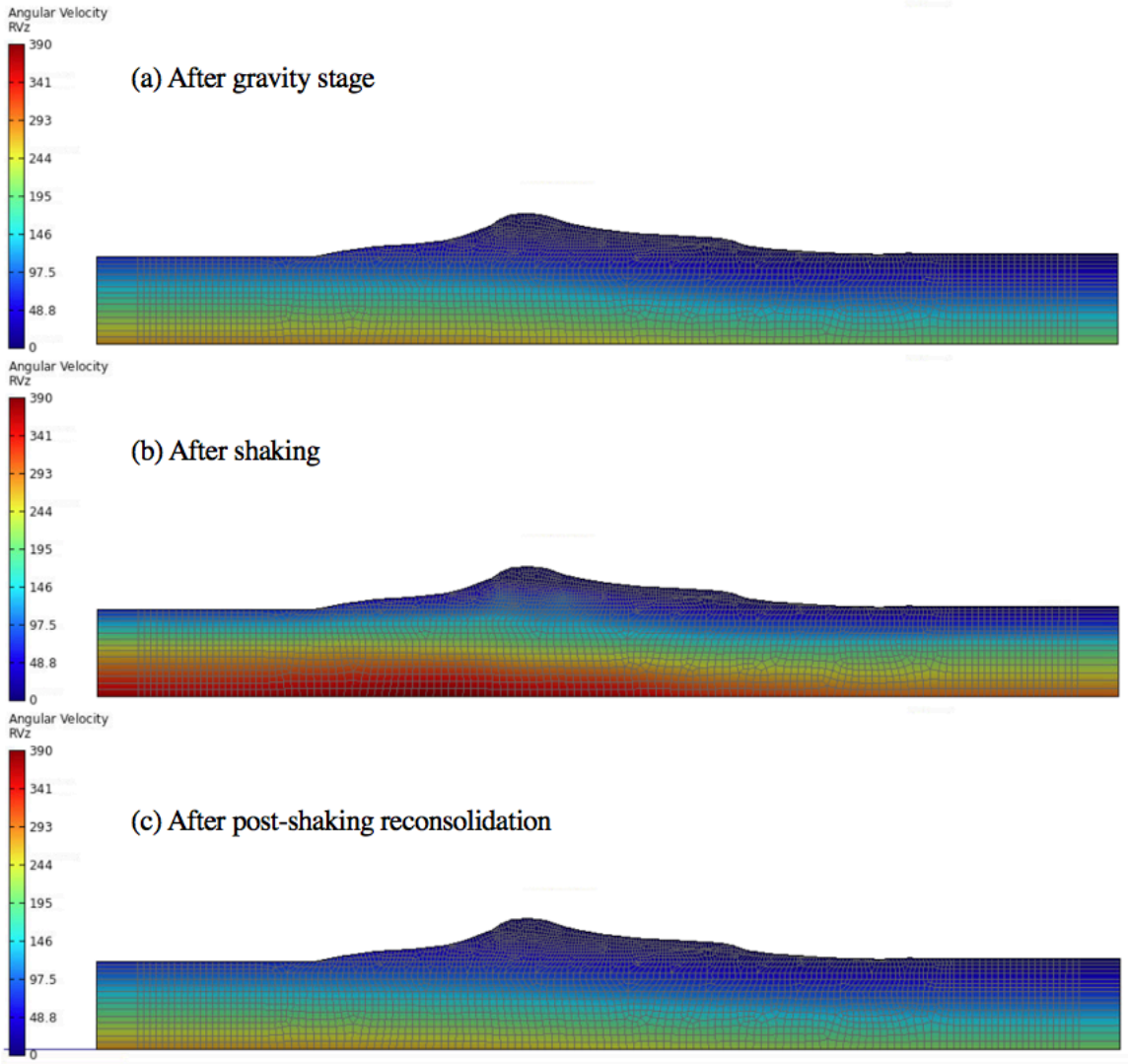


Figure 5.36 Pore water distribution plots after (a) gravity (b) shaking (c) post-shaking reconsolidation under event 1

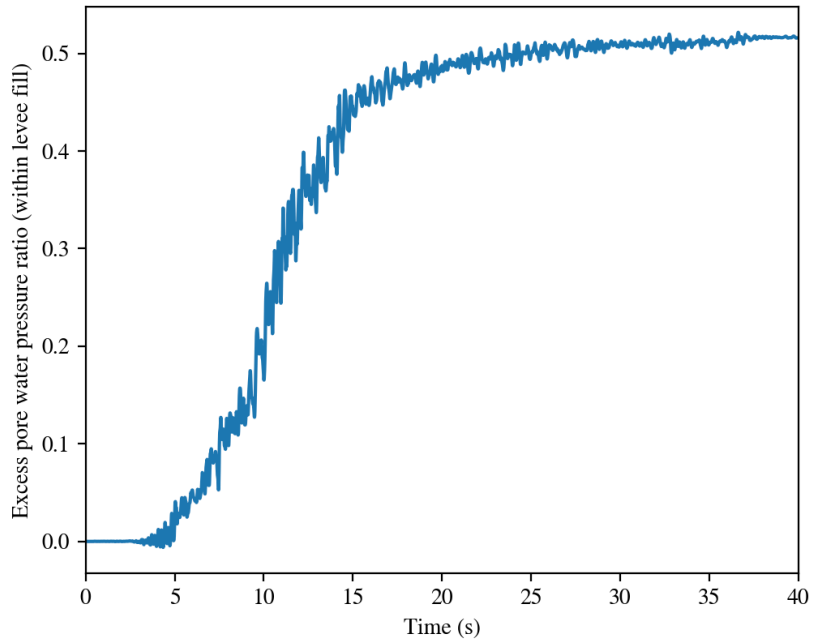


Figure 5.37 Excess pore water pressure ratio over time during shaking event 1

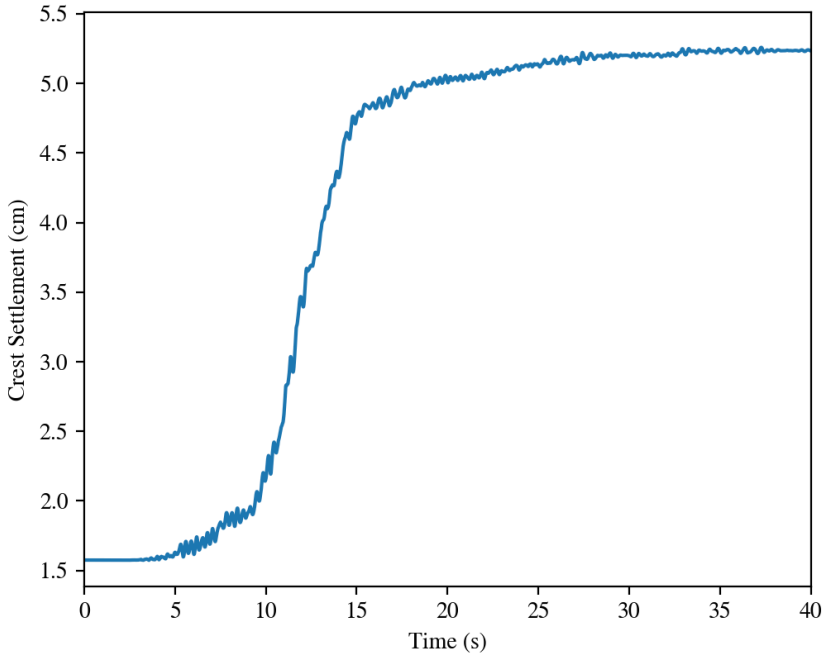


Figure 5.38 Crest settlement over time during shaking event 1

The levee crest only settled 0.037m during the shaking of event 1. It would also be interesting to see how the levee model performs under another event that has stronger shaking than this event. Therefore, event 2 is selected for the second case where more deformations were observed. Figure 5.39 shows the

acceleration time series of event 2 together with its response spectra. The PGA of this motion is approximately 0.49g, and the PGV is around 0.39m/s. Figure 5.40 shows the crest motion time series under the shaking of event 1 as well as its response spectra. The PGA of the crest motion is approximately 0.5g, and the PGV is around 0.5m/s.

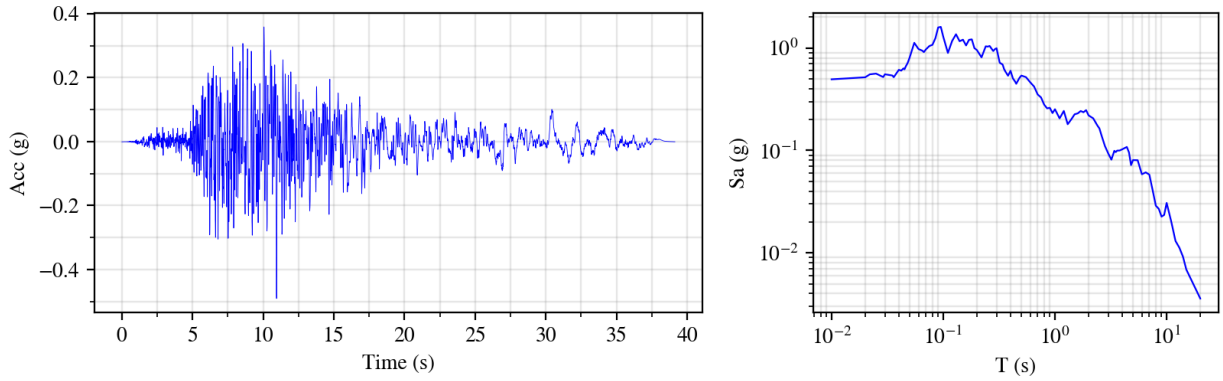


Figure 5.39 Input ground motion record of event 2 and its response spectra

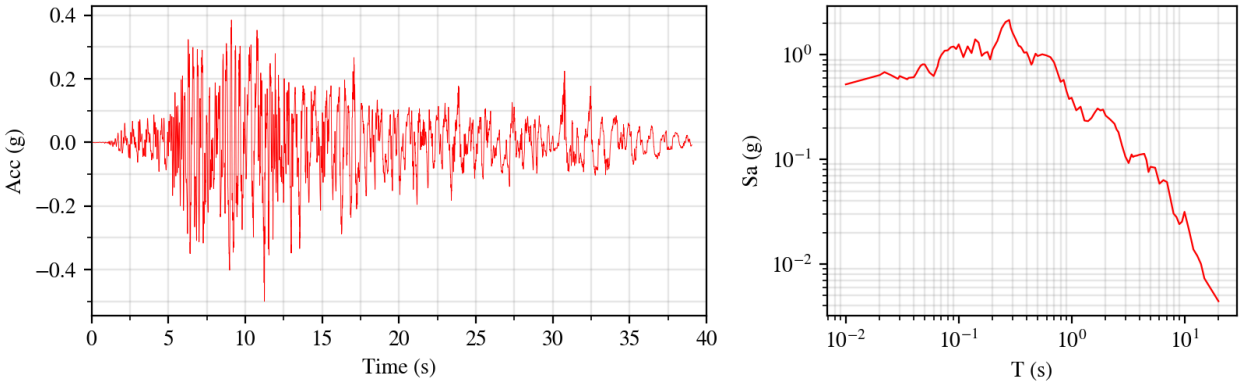


Figure 5.40 Crest motion time series under the shaking of event 2 and its response spectra

It was found that the levee crest under this event settled an additional of 0.17m during shaking, and during the post-shaking reconsolidation stage, the levee crest settled 0.01m more. Figure 5.41 shows the contour plots of vertical displacement during these three stages. The deformation scale is 10. Again, the plots indicate that the levee model did not settle much during the post-shaking reconsolidation stage. Figure 5.42, on the other hand, shows the pore water pressure distribution during three different stages for event 2. The levee model apparently built up more excess pore water pressure under event 2

compared with the excess pore water pressure that was generated during event 1. Figure 5.43 also shows how the excess pore water pressure ratio at the center of the levee fill changes over time during shaking, and it was indicated that the levee fill was close to liquefaction during this strong event since the excess pore water pressure gradually increases towards 1. Figure 5.44 shows how the crest settlement gradually increases over time as shaking continues.

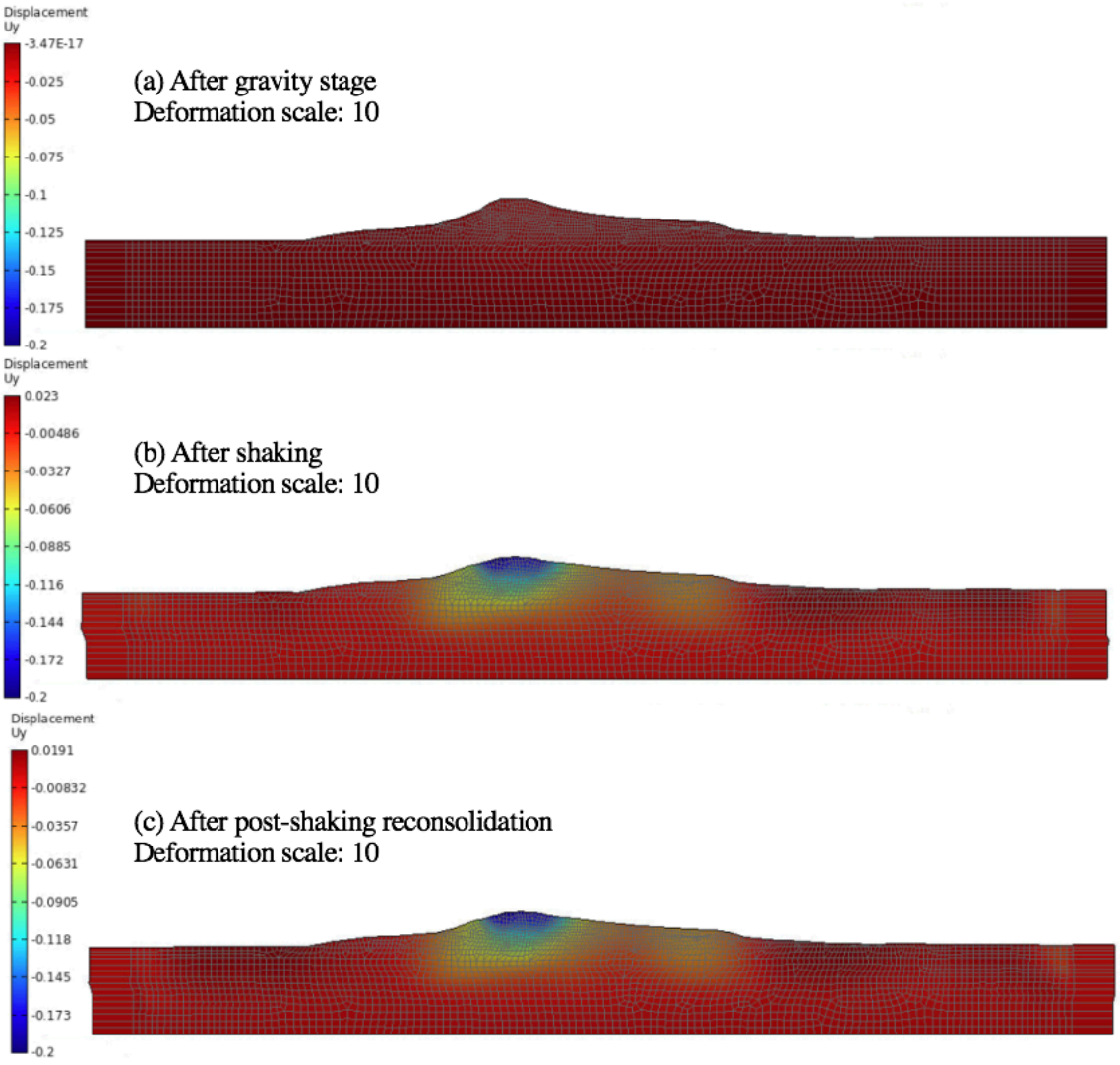


Figure 5.41 Vertical displacement contour plots after (a) gravity (b) shaking (c) post-shaking reconsolidation under event 2

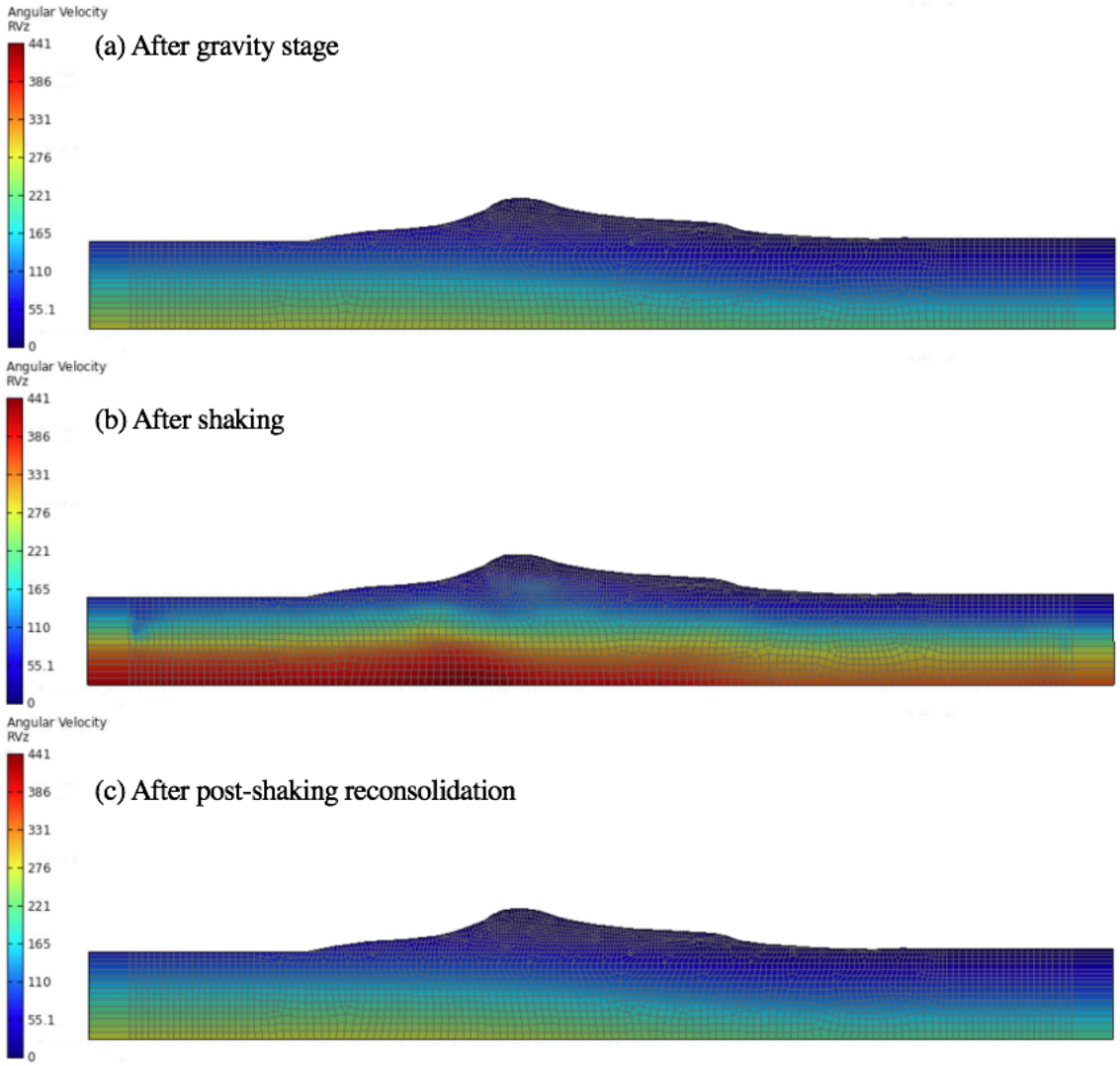


Figure 5.42 Pore water distribution plots after (a) gravity (b) shaking (c) post-shaking reconsolidation under event 2

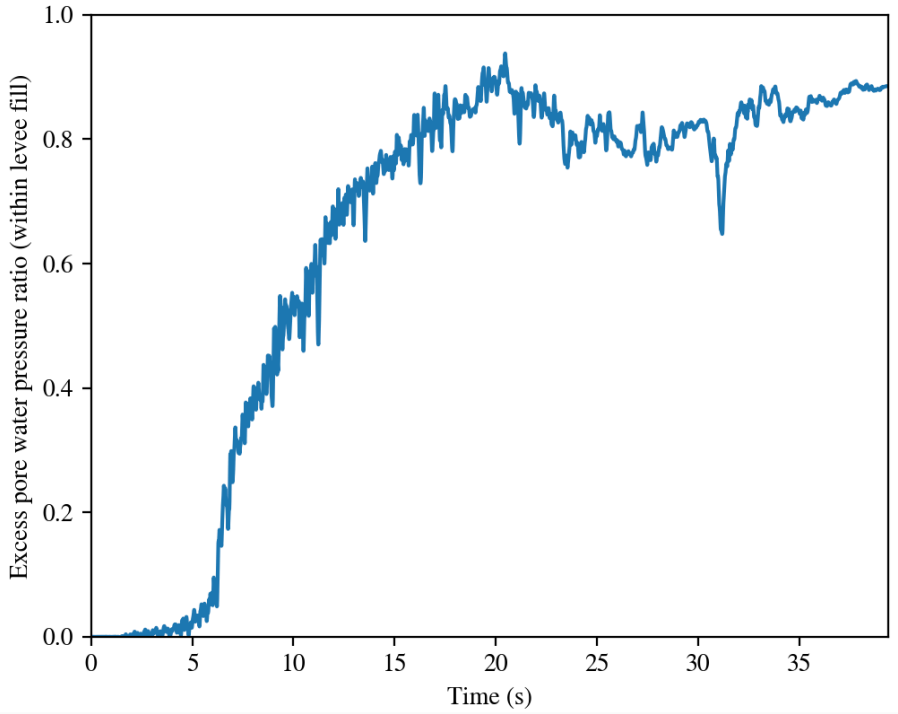


Figure 5.43 Excess pore water pressure ratio over time during shaking event 2

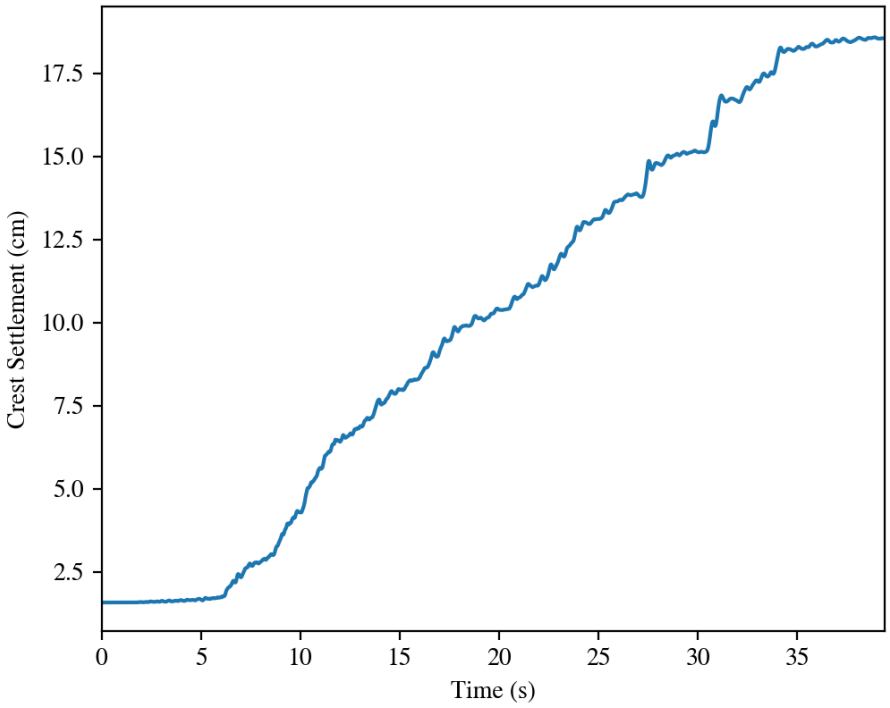


Figure 5.44 Crest settlement over time during shaking event 2

5.3 FRAGILITY FUNCTIONS

In this section I compute fragility functions for the McDonald Island levees using Monte Carlo simulations in which the selected ground motions are applied to levees with various soil properties. The previous section presented selection of ground motions that were imposed on the base of the numerical models. However, ground motion intensity measures generally correspond to free-field surface shaking conditions. Furthermore, the numerical models involve soil liquefaction, whereas free-field surface demands are generally for a condition in which liquefaction does not occur. I therefore first use one-dimensional site response simulations on soil profiles taken vertically through the levee crest, and run simulations without liquefaction to develop values of the intensity measures that appear on the x-axis of the fragility functions.

I then turn my attention to defining the y-axis of the fragility functions by running Monte Carlo simulations on the Stampede2 high performance computing cluster at the University of Texas, Austin through the DesignSafe cyberinfrastructure (Rathje et al. 2017). Parallel computing was performed using OpenSeesMP.

Variability of levee crest settlement for a given value of the ground motion intensity measure results in dispersion in the fragility relationship. The fragility function is the cumulative distribution function of levee capacity, and the distribution has variance that can be attributed to three factors: motion-to-motion variability, within-cross-section soil variability and section-to-section variability

All three sources of variability are considered in the sections that follow.

5.3.1 Ground Motion Intensity Measure Selection

The x-axis of the fragility function is a ground motion intensity measure that must be consistent with seismic hazard analysis at the site of interest. Specifically, the intensity measure should correspond to a ground surface motion with the same V_{S30} as the site of interest, should be a free-field motion (i.e., at the surface of a horizontally layered profile), and should not be influenced by liquefaction. These conditions arise because they match conditions corresponding to ground motions utilized to develop the ground motions models commonly used in seismic hazard analysis.

The ground motions selected in Section 5.2 are imposed on a dashpot at the base of the numerical models, and therefore represent an outcropping motion. This outcropping motion is therefore consistent with a surface motion, but not for site conditions corresponding to the site of interest. The soft soils beneath the levee alter the ground shaking, resulting in a levee crest motion that differs from the input motion. For example, the levee crest motions differed significantly from the input motions in Figure 5.33 and Figure 5.34. The levee crest motion is not an appropriate intensity measure because the crest motion is altered by (1) liquefaction of levee fill and underlying soils and (2) topographic amplification due to the 2D levee geometry.

The intensity measure utilized on the x-axis of the fragility functions is obtained by extracting a vertical soil column through the levee crest, and performing one-dimensional ground response analysis on the profile with liquefaction suppressed. In order to turn off the liquefaction effect in the finite element model, the bulk modulus of water is set to be equal to the bulk modulus of air, rendering the soil drained during shaking. Figure 5.45 illustrates the one-dimensional soil column.

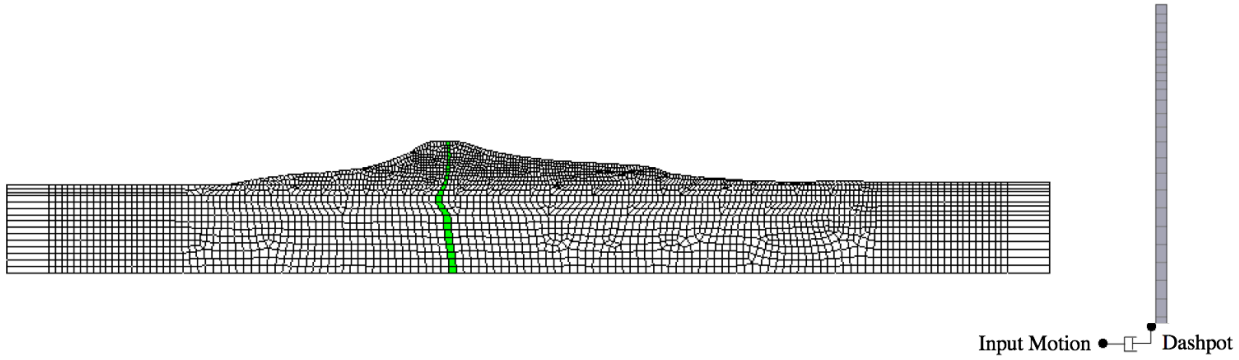


Figure 5.45 Vertical column from 2D model and reconstructed 1D model

The influence of intensity measure selection on levee response is shown in Figure 5.46, where levee crest settlement is plotted versus PGV for three different IM's. The range of PGV is largest for the input motion because the system tends to amplify small input motions, and de-amplify large input motions. Therefore, the slope of the relationship is shallower when using the input motion as the IM. The crest motion from 2D model exhibits the steepest slope, which I attribute to competing effects of topographic amplification and liquefaction. The 2D levee geometry tends to amplify the input ground motion, which is apparent at small shaking intensity. Liquefaction tends to de-amplify the ground motion, which is apparent at high input shaking intensity. Therefore, using the crest motion results in the steepest relationship between settlement and IM. The one-dimensional soil profile without liquefaction is intermediate between the other two selections. De-amplification of strong motions is similar between the one-dimensional soil profile and the 2D finite element model. This is somewhat surprising because the 2D profile involved liquefaction, and would therefore be expected to de-amplify the input motion more. I attribute this to two factors: (1) the peak motion may occur before liquefaction triggers, and (2) dilatancy in the constitutive model may result in propagation of significant ground motion after liquefaction triggers.

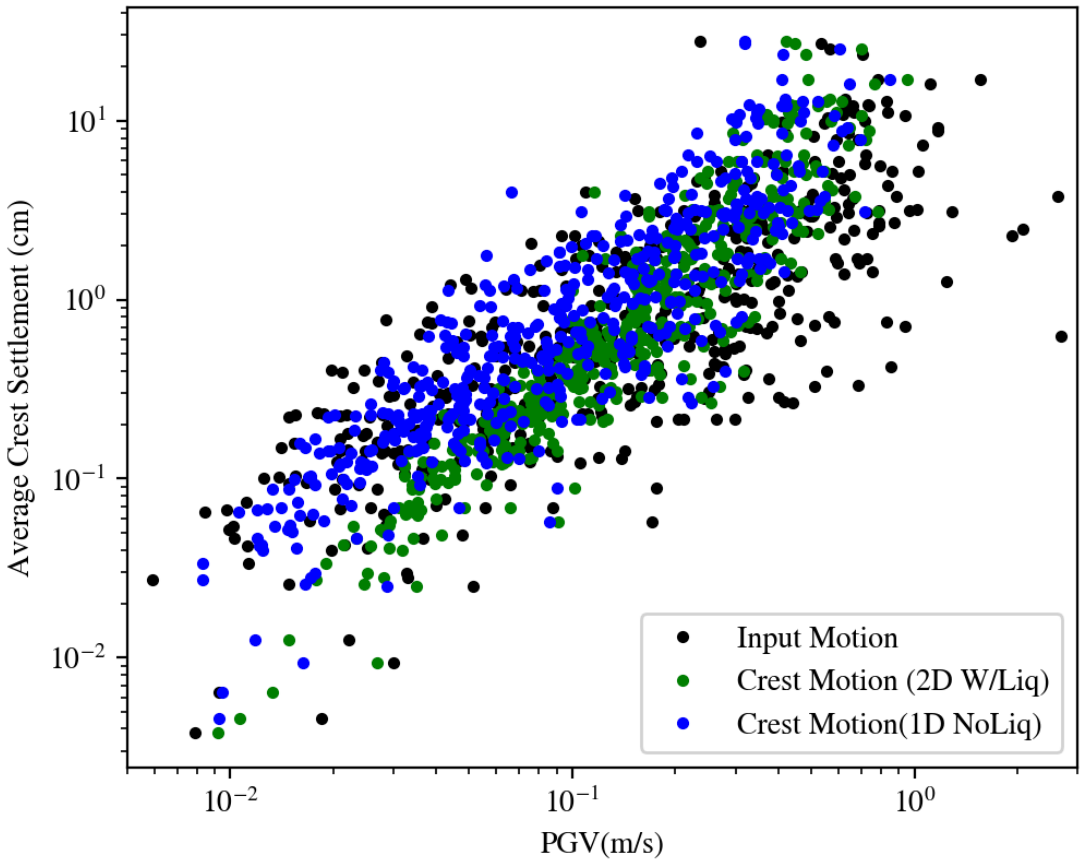


Figure 5.46 Crest settlement versus PGV of reference motion

5.3.2 **Motion-to-Motion Variability**

To assess the influence of motion-to-motion variability, I select the baseline profile and shake it with the 760 selected ground motions. The relationship between levee crest settlement and PGV is then regressed using the functional form in Eq. 5.1, where m_0 and m_1 are regression constants, and ε is a normally distributed random variable with standard deviation σ_{m2m}, where m2m denotes motion-to-motion.

$$\ln(S) = m_0 + m_1 \cdot \ln(PGV) + \varepsilon \tag{5.1}$$

Table 5.2 summarizes m_0, m_1, and σ_{m2m}. Using Eq. 2.11 and Eq. 2.12, the moments of the log-normal CDFs for PGV-based fragility curves are calculated, and are summarized in Table 5.3. Table 5.4 included the moments of the log-normal CDFs proposed by Kwak et al. (2016) to make a comparison.

Table 5.2 Slope, intercept and standard deviation of the regressed line for three reference motions

Reference motion	Input Motion		Crest Motion (2D W/Liq)		Crest Motion (NoLiq)	
Type	coef	std error	coef	std error	coef	std error
m_0	-2.863	0.098	-4.671	0.082	-3.261	0.076
m_1	0.937	0.034	1.623	0.03	1.287	0.031
σ_{m2m}	0.889	NA	0.323	NA	0.507	NA

Table 5.3 Moments of log-normal CDFs of exceeding different damage levels for three reference motions

Reference Motion	Input Motion			Crest Motion			Crest Motion (NoLiq)		
Moments	μ	e^{μ} (cm/s)	β	μ	e^{μ} (cm/s)	β	μ	e^{μ} (cm/s)	β
DL > 0	3.06	21	0.95	2.88	18	0.20	2.53	13	0.39
DL > 1	5.51	248	0.95	4.30	73	0.20	4.32	75	0.39
DL > 2	6.69	801	0.95	4.97	145	0.20	5.18	177	0.39
DL > 3	7.97	2894	0.95	5.72	304	0.20	6.11	451	0.39

Table 5.4 Moments of log-normal CDFs of exceeding different damage levels from Kwak et al. (2016)

Case	Kwak et al. 2016 (D_W > -1m)		
Moments	μ	e^{μ} (cm/s)	β
DL > 0	4.43	84	0.80
DL > 1	4.62	101	0.80
DL > 2	5.15	172	0.80
DL > 3	5.89	361	0.80

It is observed that the standard deviation using crest motion is smaller than 0.8, which is the standard deviation proposed by Kwak et al. (2016). The medians of the log-normal CDF for exceeding damage level 1, 2, and 3 using crest motion are all slightly smaller than the median proposed by Kwak et al. (2016). However, if the reference motion is the crest motion from one-dimensional model, the standard deviation is smaller than 0.8 as well, but the medians of the log-normal CDF for exceeding damage level 2, and 3 are slightly larger than the median proposed by Kwak et al. (2016). What also seems interesting is that the standard deviation using input motion is even higher than 0.8, and the medians of the log-normal CDF for exceeding damage level 1, 2, and 3 are all higher than what was proposed by Kwak et al. (2016). This further indicates that input motion might not be a good reference motion to use.

In order to have a better idea of how different the fragility curves are, Figure 5.47 gives an example of the PGV-based fragility curves for DL > 1. The vertical axis is probability of exceedance of DL>1 or the crest settlement is larger than 10cm. It is clearly seen from Figure 5.47 that fragility curves from crest motions have smaller medians compared with the fragility curve proposed by Kwak et al. (2016), which could be due to the fact that McDonald levees have a relatively higher river table compared with Japanese levees. And this will most likely cause the levees to settle more during earthquake loading. And the smaller standard deviation can be explained by the fact that the numerical simulations only accounted for the motion to motion variability so far.

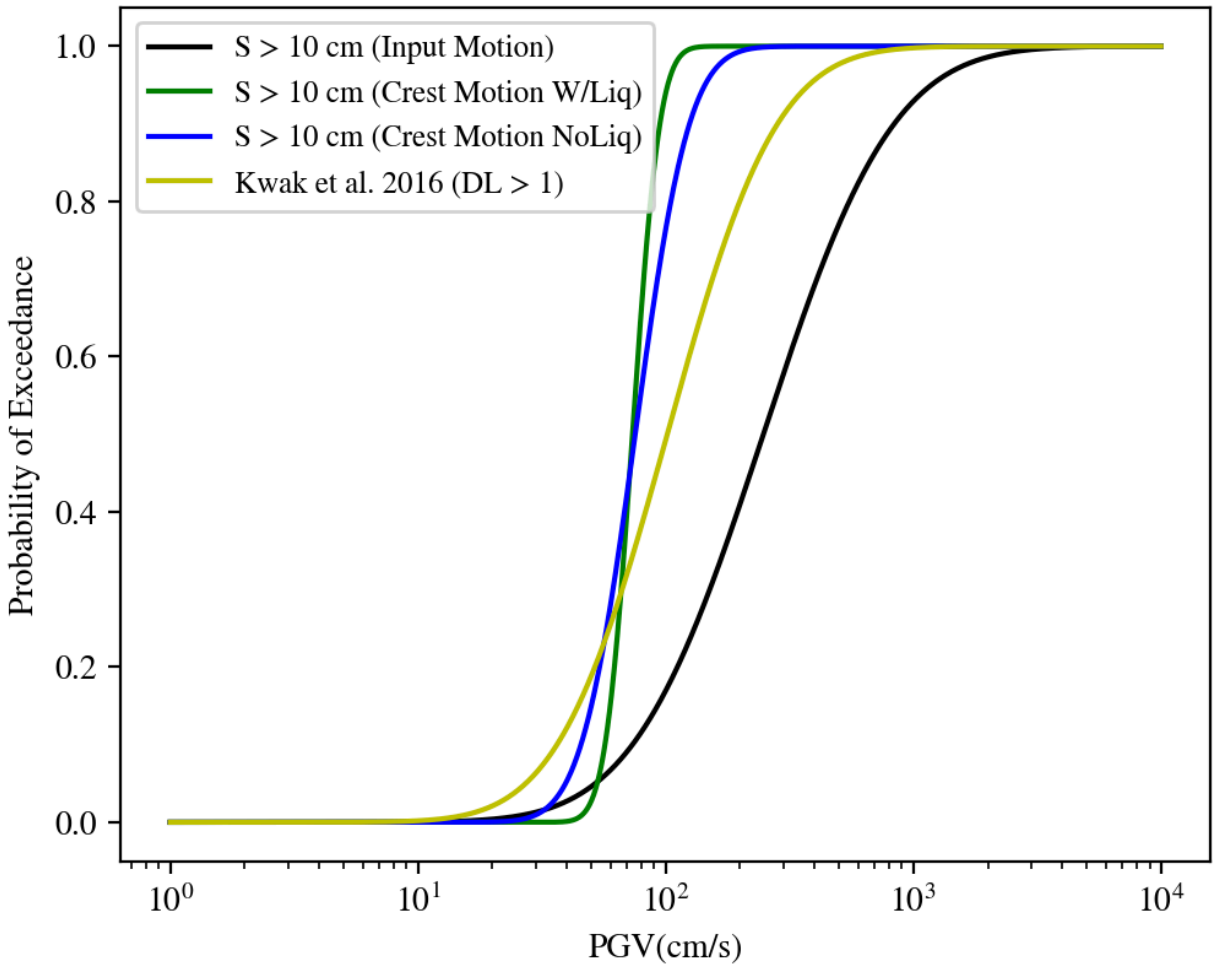


Figure 5.47 Fragility curve for DL>1 comparisons with different reference motions

5.3.3 **The Effect of Magnitude**

The motion-to-motion variability is for earthquakes with various magnitudes, and I anticipate that for a given intensity, a higher magnitude earthquake will induce more settlement due to its longer duration. To explore the magnitude effect, I plot the residuals obtained from Figure 5.46 versus the magnitude of the earthquake. Since the crest motion from one-dimensional is favored in this study, so the residuals used here are defined as the differences between the blue data points and its corresponsding regressed line. Figure 5.48 shows how the residuals are distributed for different magnitudes.

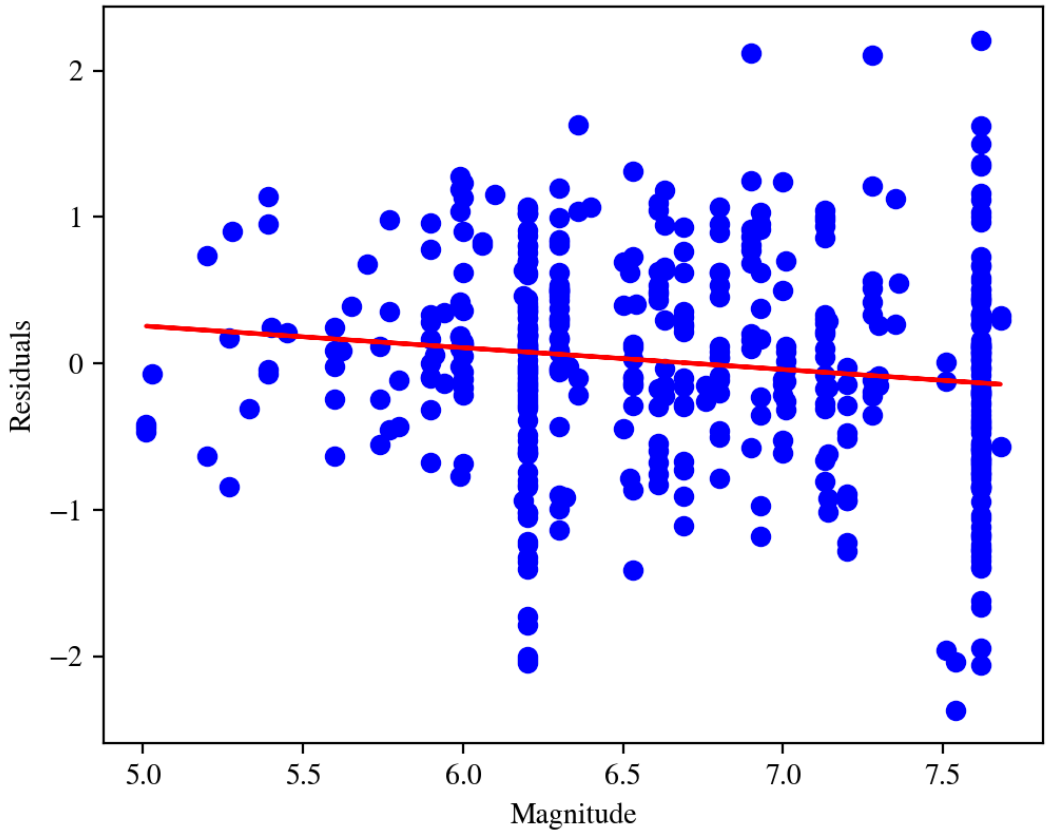


Figure 5.48 Residuals from regressed line versus magnitude using crest motion 1D NoLiq as the reference motion

A straight line is also regressed between the residuals and the magnitudes. A negative trend is found between crest settlement and magnitude, which doesn't make sense because large magnitude earthquakes have a longer duration, and therefore should induce more levee settlement. My hypothesis regarding this negative trend is thatthe ground motions used for the analysis are scaled by different scaling factors to match the target spectra, and these scale factors may be biased with respect to magnitude, thereby obscuring the magnitude effect. Figure 5.49 plots scaling factor versus magnitude, and it indicates that there is indeed a negative trend between scaling factor and magnitude.

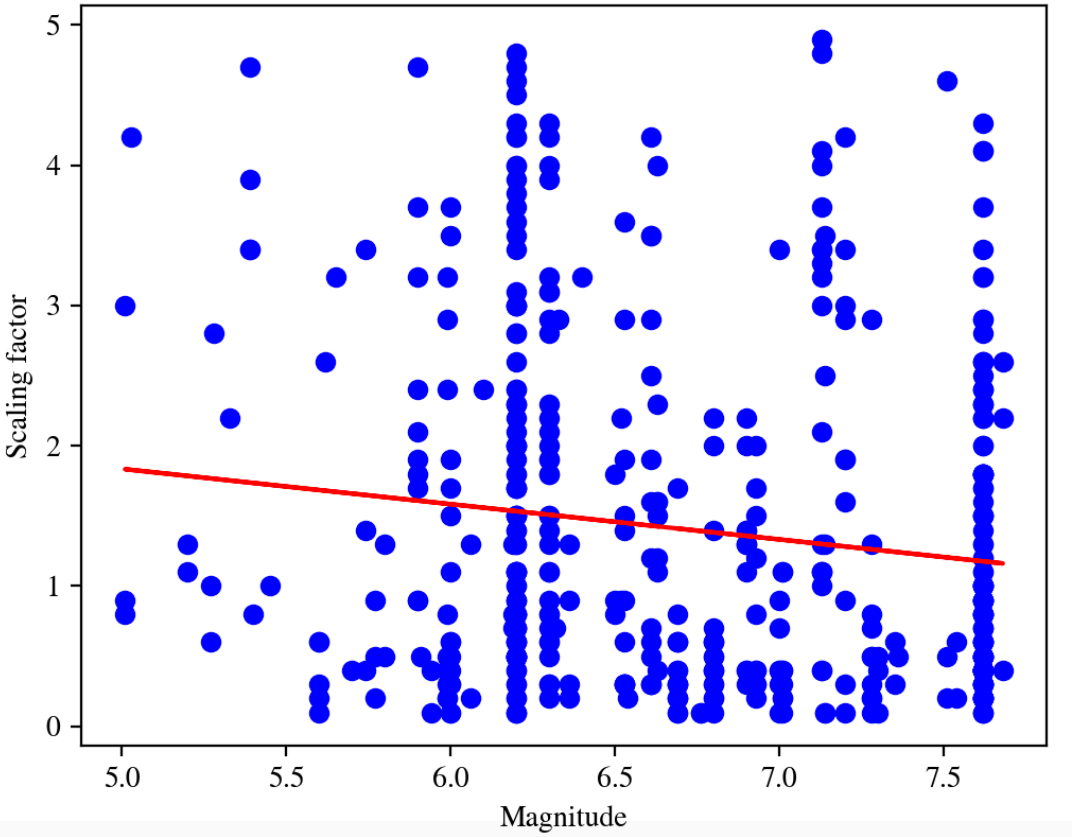


Figure 5.49 Scaling factor versus the magnitude for the selected scaled ground motions

To evaluate the effect of scaling, I re-ran the numerical simulations using unscaled ground motions. Figure 5.50 shows how the average crest settlement changes with the PGV of the crest motion from the one-dimensional model in the natural logarithm scale. I then regressed crest settlement vs PGV, and plotted the residuals versus magnitude. Figure 5.51 plots the regressed straight line between crest settlement and PGV of crest motion from one-dimensional model, and Figure 5.51 shows that there is indeed a positive trend between crest settlement and magnitude, as anticipated. A key conclusion from this work is that ground motions should not be scaled in a manner that is biased with respect to magnitude when deriving fragility functions. Unscaled motions are used for all subsequent fragility function derivation presented in this thesis.

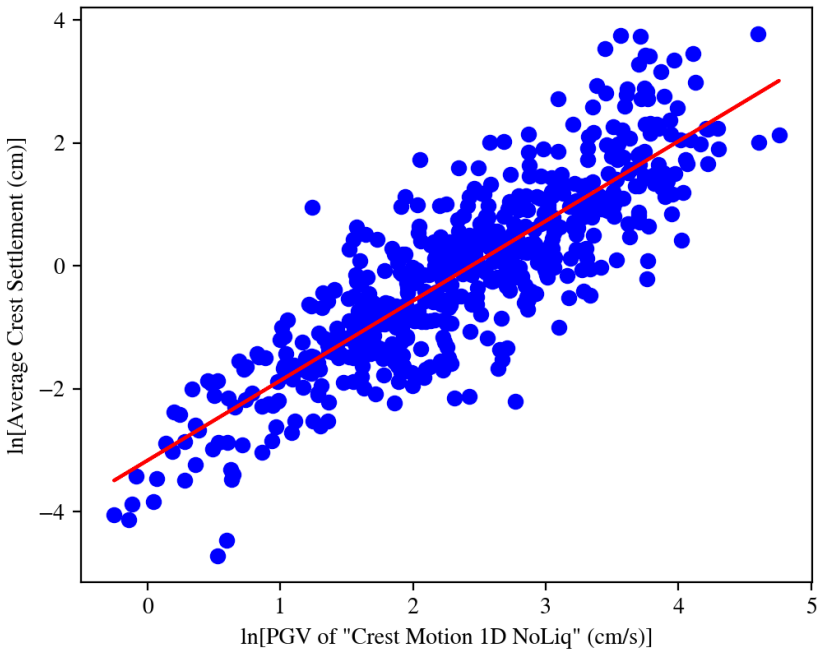


Figure 5.50 Crest settlement versus PGV in the natural logarithm scale using unscaled motions

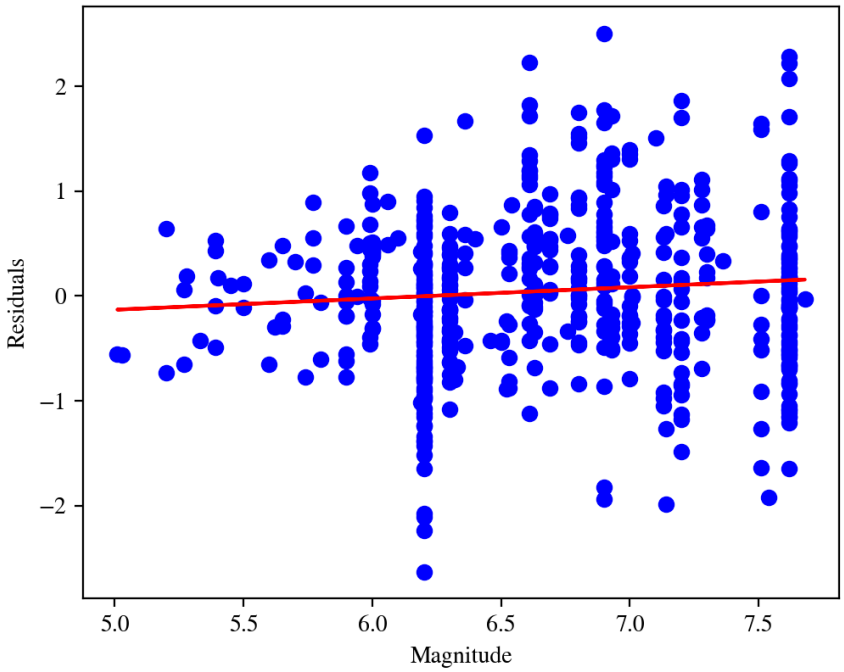


Figure 5.51 Residuals from regressed line versus magnitude using unscaled motions

Now that it is clear that there is a positive trend between crest settlement and magnitude, the next step is to perform a multiple linear regression following Eq. 5.2 to figure out the coefficients of PGV and magnitude as well as the standard deviation of the residuals. Table 5.5 summarized the intercept (m_0),

coefficient of PGV (m_1), coefficient of magnitude (m_2) and the standard deviation of the residuals (σ). Table 5.5 also listed m_0, m_1 and σ for the case when the magnitude effect is not included.

$$\ln(S) = m_0 + m_1 \cdot \ln(PGV) + m_2 \cdot M + \varepsilon \tag{5.2}$$

Table 5.5 Coefficients and standard deviation of residuals from multiple linear regression with and without accounting for magnitude effect

Case	M effect not included		M effect included	
Type	coef	std error	coef	std error
m_0	-3.185	0.085	-3.825	0.374
m_1	1.327	0.033	1.301	0.036
m_2	NA	NA	0.105	0.060
σ	0.562	NA	0.559	NA

Now that the relationship between the settlement and magnitude is expressed by this new term m_2, the fragility curves can be varied for different magnitudes. The mean of log-normal CDFs can be computed using Eq. 4.4, while the standard deviation of the log-normal CDFs is computed to be around 0.43 using Eq. 2.12. Figure 5.52 gives an example of fragility curves of DL > 1 for three different magnitude levels. It is clear from the figure that as the magnitude increases, the fragility curve shifts to the left, which also indicates that given the same PGV, larger magnitudes of events tend to cause more damage. However, the effect of magnitude is rather weak as the fragility functions are all fairly similar.

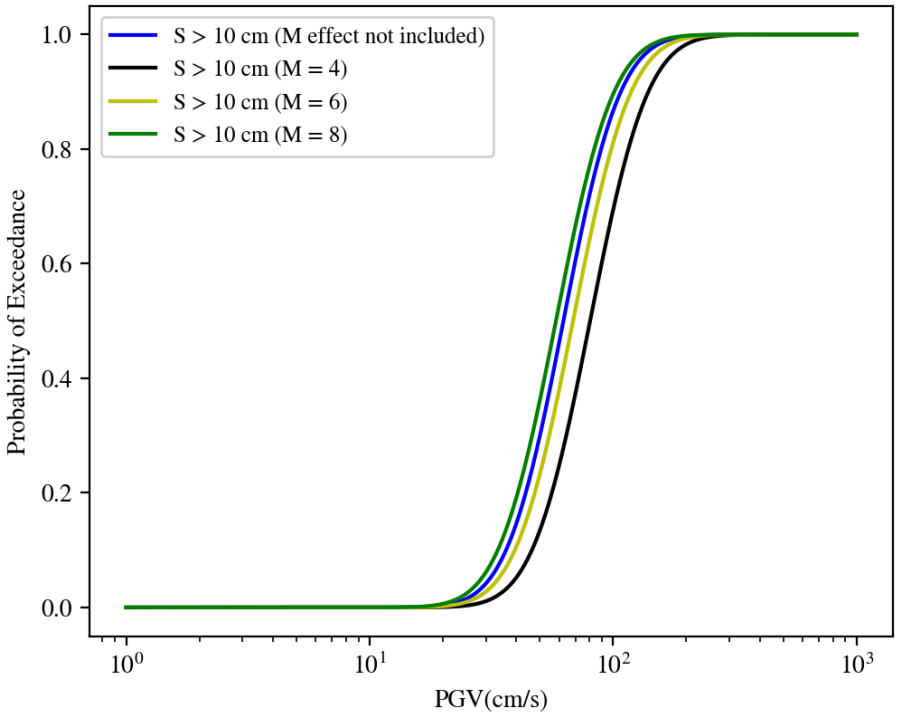


Figure 5.52 Fragility curves of DL > 1 for three different magnitudes

5.3.4 **The Effect of Within-Section Spatial Variability**

During all the previous simulations that were discussed, elements within each layer were assigned with the same soil property parameters, which failed to incorporate the within-section spatial variability of soil. By using the new random field generation algorithm proposed in Chapter 3, a spatially correlated random field of soil properties has been incorporated into the finite element analysis to assess the influence of within-section variability.

Similar to what was performed on the Japanese levees, the relative density is regarded as the random variable for the sand layers, and all the other parameters used in the material model are related to relative density. The undrained shear strength is varied for the silt and peat layers. Assume that the relative density and undrained shear strength are both log-normally distributed. For each individual soil layer, a spatially correlated random field of soil properties is generated, which is shown in Figure 5.53. The mean values of the random field are based on the values listed in Table 5.1. The coefficient

of variation of the relative density random field in the sand layer is selected to be 0.6, and the coefficient of variation of the undrained shear strength random field in the peat and silt layer is selected to be 0.25, which are recommended by Phoon and Kulhawy (1999). The horizontal scale of fluctuation is 20m for all soil layers, and the vertical scale of fluctuation is 1.5m, which are recommended by ISSMGE-TC304 (2021). Figure 5.53 shows one of 500 realizations of the spatially correlated random field that were analyzed to assess the influence of within-section variability on fragility. Then I selected one ground motion record among all the ground motion records mentioned earlier, and the acceleration time series is plotted in Figure 5.54, together with its response spectra. The PGA of this motion is approximately 0.4g, and the PGV is around 0.31m/s, thus this is an earthquake event that has medium to strong shaking intensity. The last step is to implement these 500 realizations of random fields into the finite element analysis together with the selected ground motion record and run dynamic analysis with this model. Crest settlement is recorded for each realization.

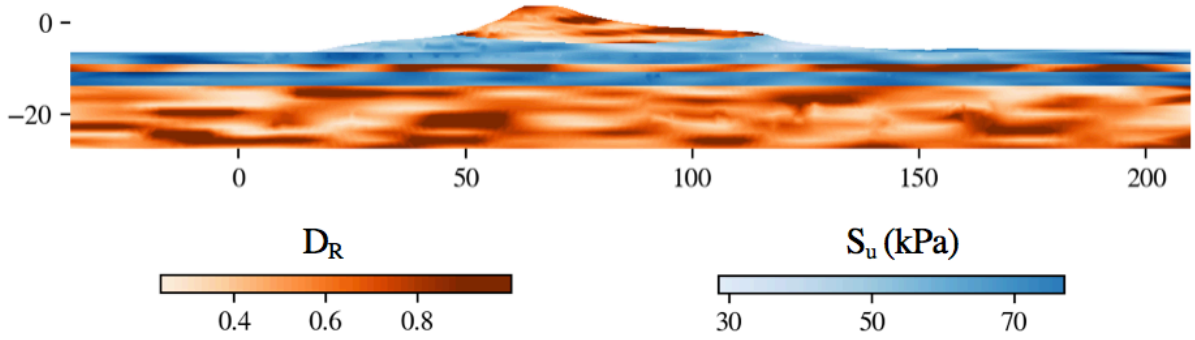


Figure 5.53 An example of spatially correlated random field of soil properties

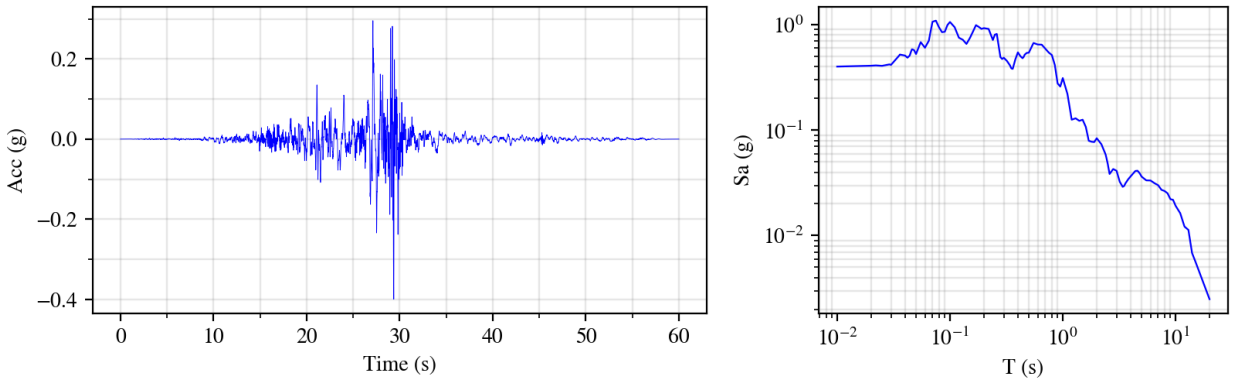


Figure 5.54 Ground motion record selected and its response spectra

Figure 5.55 shows the crest settlements for all the 500 realizations. The mean crest settlement is computed to be around 13.3cm, while the crest settlement predicted by the levee model with uniform soil properties is around 5.3cm. Again, this indicates that the levee model with spatially varied soil properties tends to settle more compared with levee model with uniform soil properties.

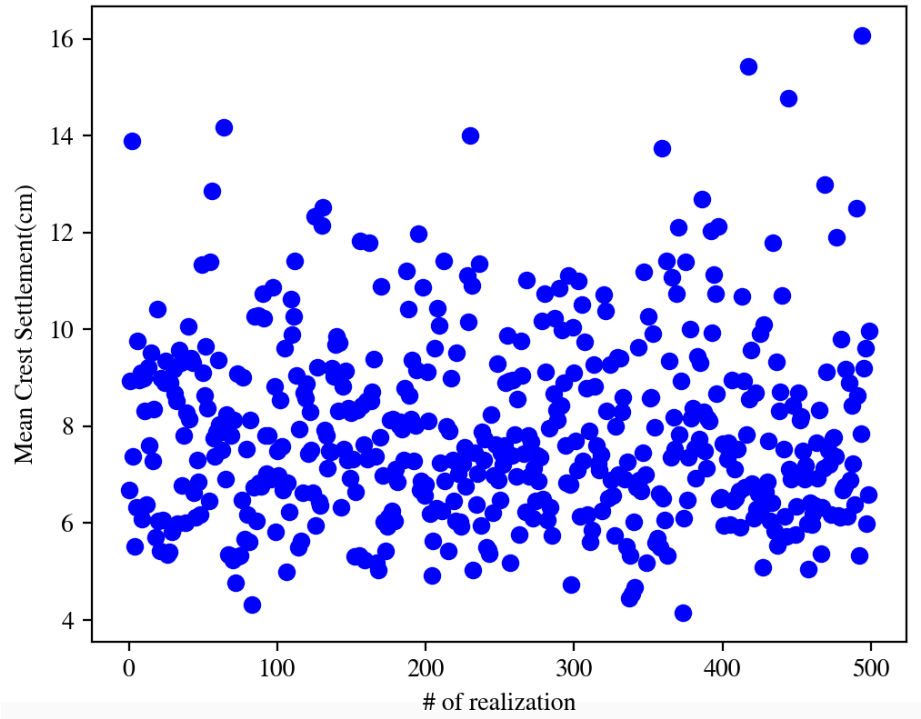


Figure 5.55 Crest settlement distribution over 500 realizations

A quantile-quantile (Q-Q) test was also performed on these crest settlement data. The crest settlements were taken the logarithm first, and then the Q-Q test was performed, which is shown in Figure 5.56. All the data points are close to the red line, and I conclude that crest settlement is log-normally distributed. The standard deviation of crest settlement (denoted as σ_{sv}) is 0.24. In addition to the standard deviation obtained from motion to motion variability (σ_{m2m} =0.56), this indicates that spatial variability is indeed an importance source of uncertainty and needs to be accounted for in the deriving of fragility functions.

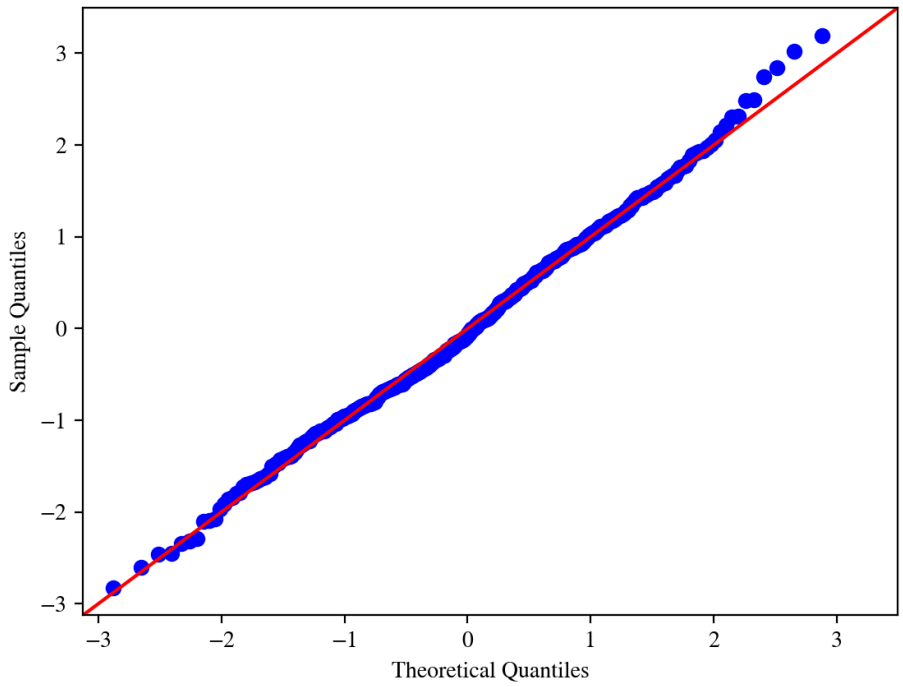


Figure 5.56 A Q-Q plot of crest settlement with the natural logarithm taken

Another important question here is whether the increase in settlement will depend on the relative density. Therefore, I repeated such procedures by varying the relative density to be 55% and 35%, respectively. 500 realizations of spatially correlated random field of soil properties are generated for each case. And the computed mean crest settlements and standard deviation of crest settlements are summarized in Table 5.6.

Table 5.6 Settlement from uniform model, mean and standard deviation of settlement from 500 realizations

D_R	71%	55%	35%
Settlement obtained from uniform model (cm)	5.2	9.0	22.4
μ (cm)	13.3	22.3	39.9
σ_{sv}	0.24	0.25	0.25

As indicated in Table 5.6, the crest settlement did all increase when the soil properties are spatially varied compared with the settlement obtained from levee model that has uniform soil properties. And it appears that the increase in settlement does not vary in terms of the relative density in the natural logarithm scale. The average increase of settlement in the natural logarithm scale is computed to be around 0.81. And this increase in settlement can be included as an adjustment term for the intercept (m_0), defined as Δm_0. And this adjusted term will shift the mean of the log-normal CDFs, which is computed as follows,

$$\Delta\mu = \frac{\Delta m_0}{m_1} = \frac{0.81}{1.301} = 0.62 \tag{5.3}$$

and the standard deviation of the log-normal CDFs can also be updated as follows by including the standard deviation from motion to motion variability and the within-section spatial variability,

$$\sigma' = \sqrt{\sigma_{m2m}^2 + \sigma_{sv}^2} = \sqrt{0.56^2 + 0.24^2} = 0.61 \tag{5.4}$$

$$\beta' = \frac{\sigma'}{m_1} = \frac{0.61}{1.301} = 0.47 \tag{5.5}$$

where the standard deviation from motion to motion variability and the standard deviation from the within-section spatial variability are assumed to be independent from each other.

5.3.5 **The Effect of Mean Relative Density**

As mentioned in Chapter 4, the mean relative density for the sand layers can be varied to account for the average soil variability along the length of the levee systems. Section 5.1.2 also shows that although the sand layers for McDonald Island levees have a mean relative density of approximately 70%, the relative density does vary to a certain extent. Apparently, not every levee site will have such dense sand layers. Therefore, I varied the relative density of sand layers to be 55% and 35% instead, and then dynamic analysis was performed on this levee model using the same set of unscaled ground motions.

Figure 5.57 shows how the average crest settlement changes with the PGV of the crest motion from the one-dimensional model for three different relative density cases. It is obviously observed from Figure 5.57 that the levee model with a lower relative density of sand materials will have more deformations, especially when the PGV gets high. It also appears that for the levee model with 35% relative density, the slope of settlement gets slightly steeper when the PGV exceeds 20cm/s compared with the slope before 20cm/s, which could be due to the fact that the effect of liquefaction comes into place as the shaking intensity increases. Nevertheless, it is still reasonable enough to assume that the crest settlment is linearly related to PGV in the logarithm scale.

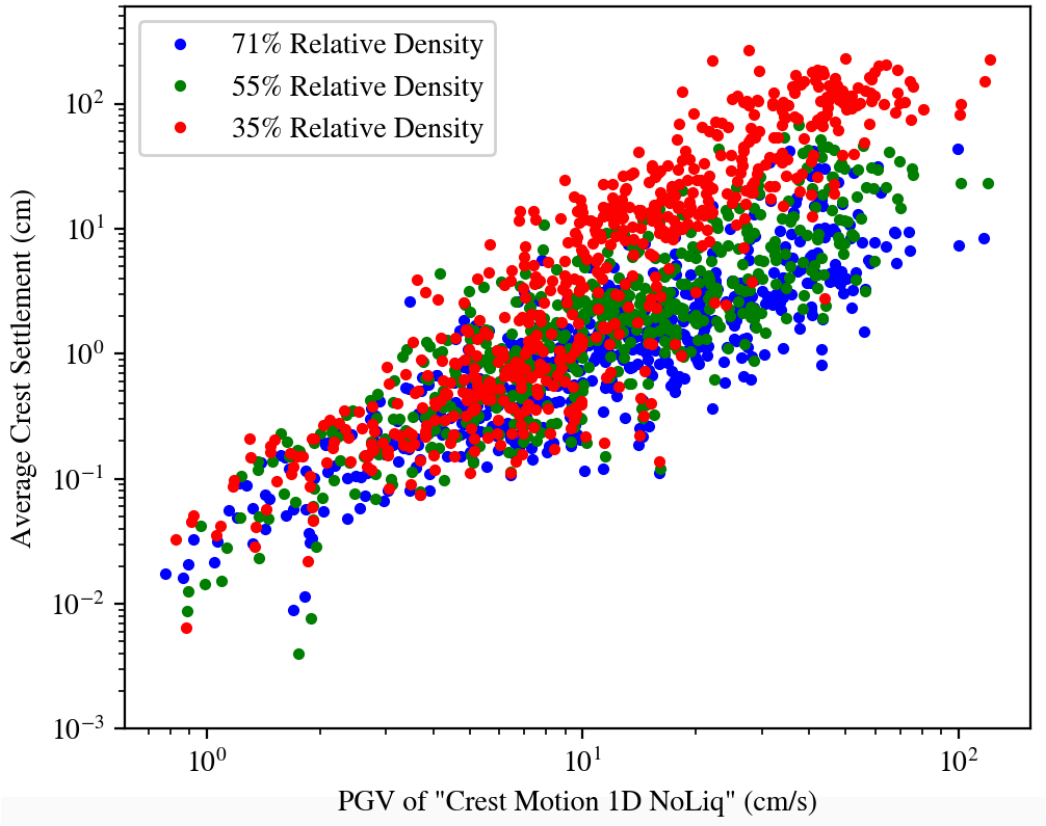


Figure 5.57 Crest settlement versus PGV for three different relative density using crest motion from 1D model

If the magnitude effect is not considered, then the relationship between crest settlement, PGV and D_R can be expressed as,

$$\ln(S) = m_0 + m_1 \cdot \ln(PGV) + m_3 \cdot D_R + \varepsilon \tag{5.6}$$

Multiple linear regression is performed on crest settlement with PGV and D_R. Table 5.7 summarized the intercept (m_0), coefficient of PGV (m_1), coefficient of D_R (m_3) and the standard deviation of the residuals (σ). Using the coefficients, it is very straightforward to determine the median and standard deviation of the log-normal CDFs of exceeding different damage levels using the following two equations,

$$\mu = \frac{\ln(S_t) - m_0 - m_3 \cdot D_R}{m_1} \tag{5.7}$$

$$\beta = \frac{\sigma}{m_1} \tag{5.8}$$

Table 5.7 Coefficients and standard deviation of residuals from multiple linear regression accounting for both PGV and relative density

Parameter	Value	Std Error
m_0	-1.314	0.108
m_1	1.660	0.024
m_3	-4.250	0.160
σ	0.941	NA

Table 5.8, on the other hand, listed the calculated moments of the log-normal CDFs for PGV-based fragility curves for three different relative density. Figure 5.58 also gives an example of fragility curves of DL > 1 given these three different relative density. And it is clearly seen from Figure 5.58 that increasing the relative density will shift the fragility curve to the right, which makes the levee more resistant with earthquake loading.

Table 5.8 Moments of log-normal CDFs of exceeding different damage levels for three different relative density cases accounting for both PGV and relative density

D_R	71%			55%			35%		
Moments	μ	e^{μ}(cm/s)	β	μ	e^{μ}(cm/s)	β	μ	e^{μ}(cm/s)	β
DL > 0	2.61	14	0.57	2.20	9	0.57	1.69	5	0.57
DL > 1	4.00	54	0.57	3.59	36	0.57	3.07	22	0.57
DL > 2	4.66	105	0.57	4.25	70	0.57	3.74	42	0.57
DL > 3	5.38	218	0.57	4.97	145	0.57	4.46	87	0.57

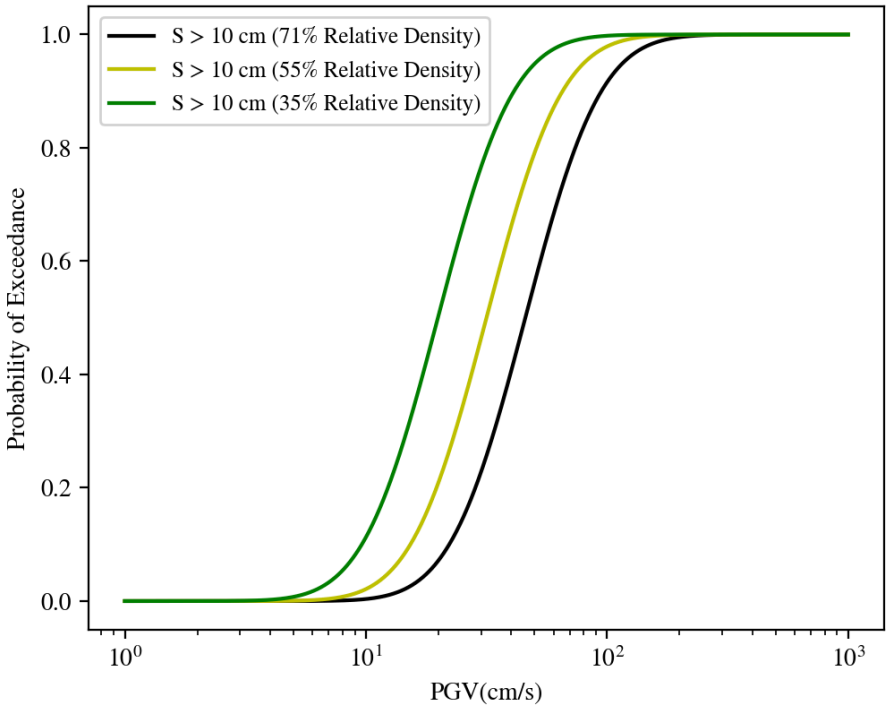


Figure 5.58 Fragility curves of DL > 1 for three different relative density

However, if the magnitude effect is accounted for, then the relationship between crest settlement, PGV, D_R and magnitude should be defined as,

$$\ln(S) = m_0 + m_1 \cdot \ln(PGV) + m_2 \cdot M + m_3 \cdot D_R + \varepsilon \tag{5.9}$$

Multiple linear regression is also performed. Table 5.8 summarized the intercept (m_0), coefficient of PGV (m_1), coefficient of magnitude (m_2), coefficient of D_R (m_3) and the standard deviation of the residuals (σ). Similar to Eq. 5.7 and Eq. 5.8 the median and standard deviation of the log-normal CDFs of exceeding different damage levels can be computed using the following two equations,

$$\mu = \frac{\ln(S_t) - m_0 - m_2 \cdot M - m_3 \cdot D_R}{m_1} \tag{5.10}$$

$$\beta = \frac{\sigma}{m_1} \tag{5.11}$$

Table 5.9 Coefficients and standard deviation of residuals from multiple linear regression accounting for PGV, magnitude and relative density

Parameter	Value	Std Error
m_0	-2.156	0.278
m_1	1.625	0.027
m_2	0.136	0.041
m_3	-4.260	0.16
σ	0.935	NA

Table 5.10-5.12 listed the calculated moments of the log-normal CDFs for PGV-based fragility curves for three magnitudes (M = 4, 6 and 8) and three different relative density cases (D_R = 75%, 55% and 35%). Figure 5.59 also gives examples of fragility curves of DL > 1 given different relative density and magnitude. Apparently, given the same relative density, the increase of magnitude will shift the fragility curve to the left, meaning the levee is more likely to fail under large magnitudes events. And given the same magnitude, if the relative density decreases, the fragility curve will also shift to the left.

Table 5.10 Moments of log-normal CDFs of exceeding different damage levels for three different relative density cases for events with a magnitude of 4

D_R	71%			55%			35%		
Moments	μ	e^{μ}(cm/s)	β	μ	e^{μ}(cm/s)	β	μ	e^{μ}(cm/s)	β
DL > 0	2.85	17	0.58	2.43	11	0.58	1.91	7	0.58
DL > 1	4.27	72	0.58	3.85	47	0.58	3.33	28	0.58
DL > 2	4.95	141	0.58	4.53	92	0.58	4.00	55	0.58
DL > 3	5.69	295	0.58	5.27	194	0.58	4.74	115	0.58

Table 5.11 Moments of log-normal CDFs of exceeding different damage levels for three different relative density cases for events with a magnitude of 6

D_R	71%			55%			35%		
Moments	μ	e^{μ}(cm/s)	β	μ	e^{μ}(cm/s)	β	μ	e^{μ}(cm/s)	β
DL > 0	2.69	15	0.58	2.27	10	0.58	1.74	6	0.58
DL > 1	4.10	61	0.58	3.68	40	0.58	3.16	24	0.58
DL > 2	4.78	119	0.58	4.36	78	0.58	3.84	46	0.58
DL > 3	5.52	250	0.58	5.10	164	0.58	4.58	97	0.58

Table 5.12 Moments of log-normal CDFs of exceeding different damage levels for three different relative density cases for events with a magnitude of 8

D_R	71%			55%			35%		
Moments	μ	e^{μ}	β	μ	e^{μ}	β	μ	e^{μ}	β
DL > 0	2.52	12	0.58	2.10	8	0.58	1.57	5	0.58
DL > 1	3.94	51	0.58	3.52	34	0.58	2.99	20	0.58
DL > 2	4.61	101	0.58	4.19	66	0.58	3.67	39	0.58
DL > 3	5.35	211	0.58	4.93	139	0.58	4.41	82	0.58

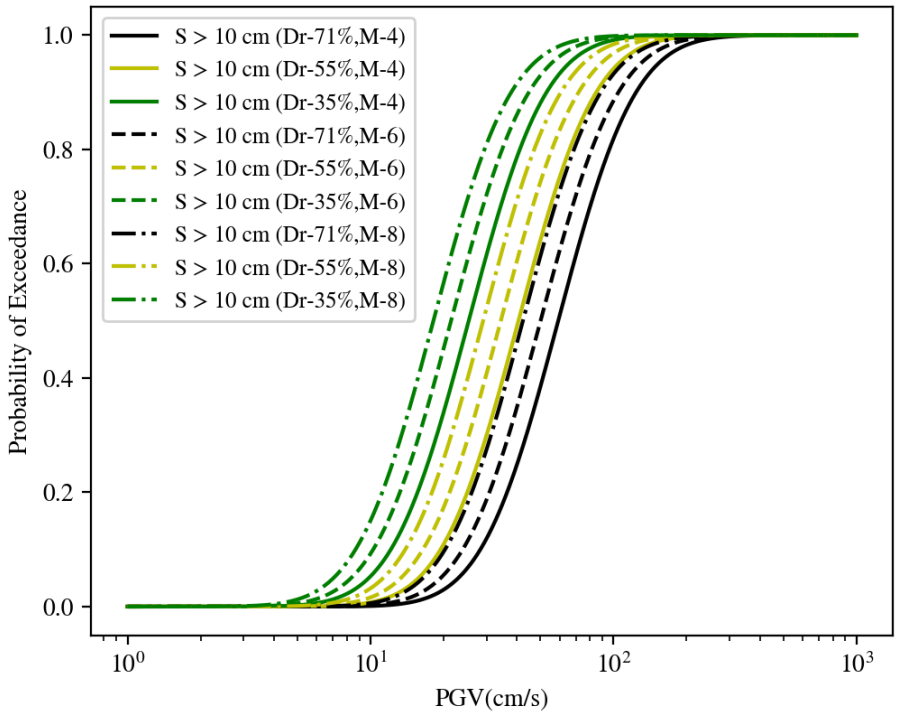


Figure 5.59 Fragility curves of DL > 1 for three different relative density cases and three different magnitudes

Another point I would like to point out is that now that we have all the crest settlement data from different ground motions and also from levee models with different mean relative densities, it will also be interesting to see overall standard deviation if PGV is considered only. Figure 5.60 shows the average crest settlement from Figure 5.50 versus PGV of crest motion from 1D model in the natural logarithm scale. The relationship between levee crest settlement and PGV is then regressed using the functional form in Eq. 5.1, where m_0 and m_1 are regression constants. The regressed line is also shown in Figure 5.53. Table 5.13 summarizes m_0, m_1, and the standard deviation of the residuals as well as the standard errors associated with the regression constants. Then the standard deviation of log-normal CDFs is computed to be around 0.776. And if spatial variablity is also included here, then the adjusted overall standard deviation is computed to be around 0.79, which is almost the same as what Kwak et al. (2016) proposed.

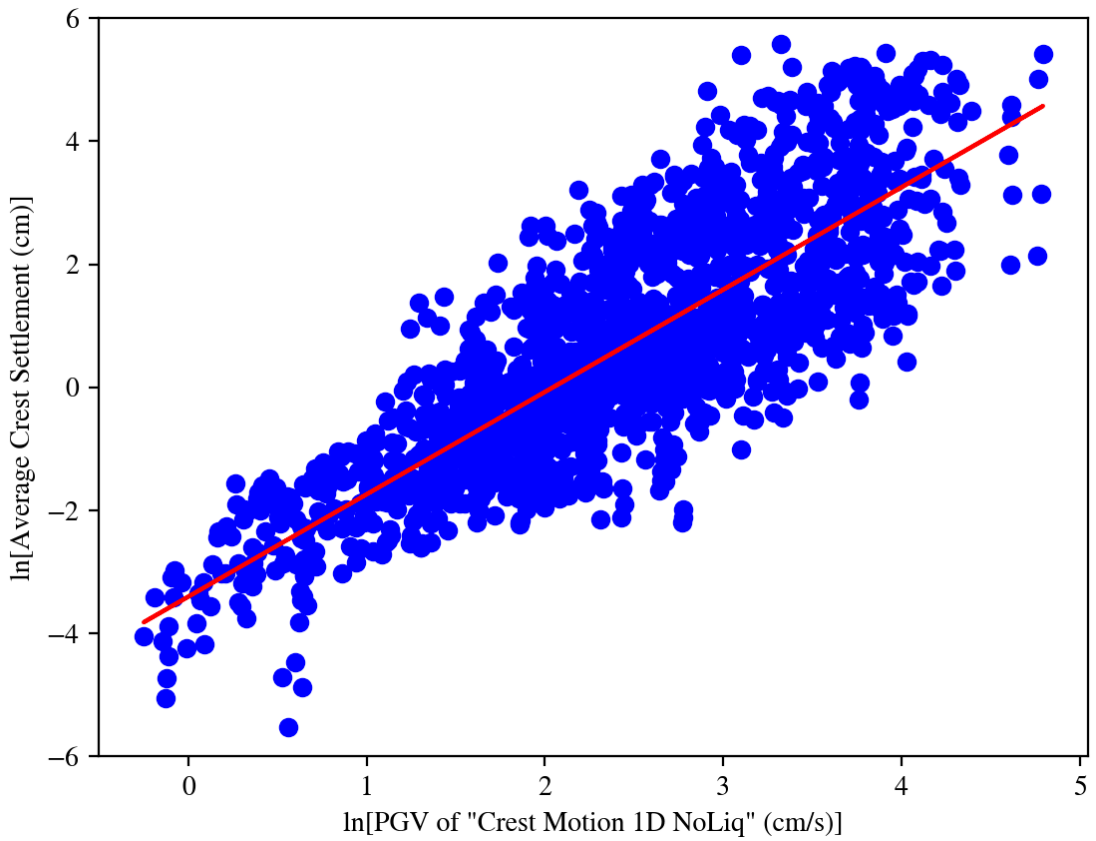


Figure 5.60 Integrated crest settlement data versus PGV of crest motion from 1D model in the natural logarithm scale

Table 5.13 Regression constants, their standard errors and standard deviation of the residuals

Type	Coef	Std Error
m_0	-3.401	0.073
m_1	1.663	0.038
σ	1.29	NA

5.3.6 **Recommended Fragility Functions**

Among all the fragility functions that have been developed in this section, it will be a choice of the user to select the suitable fragility function given different conditions. For example, when doing the system reliability analysis of the levees, it is common to divide the levee system into various reaches.

The simplest approach is to assign the same fragility functions to all the reaches, which could be problematic because the performance of reaches could vary spatially depending on different site conditions. And this study will provide guidance on how to vary the fragility functions given the mean relative density of the levee site. This is when Table 5.9, Eq. 5.10 and Eq. 5.11 will become extremely useful.

The study also investigated how the magnitude has impact on the fragility curves, which can be very helpful if the user already knows what magnitudes of event will contribute to the most to the total hazard. Correction can be made on the fragility curves given different target magnitudes by using coefficients from Table 5.5.

As for the standard deviation associated with the fragility curve, since the numerical simulations won't capture all sources of uncertainty, the standard deviation solely from motion-to-motion variability is usually much smaller than the standard deviation from empirical fragility functions. However, adjustments can be made on the standard deviation from motion-to-motion variability by also incorporating the spatial variability within a cross-section and the average soil variability along the length of the levee system. For instance, the standard deviation is about 0.43 from motion-to-motion variability. By varying the mean relative density of the sand layers, the standard deviation increases to 0.58, and by incorporation the standard deviation from spatial variability of soil within a cross-section, the overall standard deviation of the log-normal CDFs of the fragility curve turns out to be quite close with what Kwak et al. (2016) proposed.

6 CONCLUSIONS AND RECOMMENDATIONS

6.1 CONCLUSIONS

In this study, the main goal is to evaluate the seismic performance of levees in the Delta region using finite element analysis, specifically for levees at McDonald Island because it contains important natural gas infrastructure that is of great importance to PG&E. PGV-based fragility functions are derived from the finite element simulations using a calibrated numerical approach.

Considering that soils are naturally rarely homogeneous, the inherent spatial soil variability is often characterized and incorporated through random field implementation. A new algorithm of combining both Cholesky decomposition method and Kriging interpolation technique is proposed, which helps save the computational cost. A finite element analysis of a simple levee model is analyzed, and it is found that spatial variability decreases the factor of safety, rendering a structure less safe than a model using uniform mean properties. A comparison study with Fenton and Griffiths (2003) also validates the proposed algorithm.

Case histories of Japanese levees are utilized to validate the analysis approach. Among the seven instrumented sites about which Zimmaro et al. (2019) documented instrumental data and related field performance data, three levees sites (Nakashimo site, Yamazaki site and Kozuka site) are selected for the validation of analysis via finite element simulations. A two-dimensional (2D) levee model for each site is constructed using the cross-section and stratigraphy profile, and soil properties are assigned based on available geotechnical data. By running the 2D model with recorded earthquake events, predicted response is compared with the recorded response. It is found that the predicted surface motion at the levee crest matches quite well with the recorded surface motion to a certain extent, and the

predicted crest settlement also agrees decently with the reported performance data. At the Nakashimo site, a pore water pressure response is also compared, and the finite element model is able to capture the overall trend of pore water pressure building-up and dissipation as the actual recording indicates.

PGV-based fragility curves are developed at Nakashimo site using a set of ground motions and following the calibrated approach of developing fragility function. Motion-to-motion variability, within-cross-section-section soil variability and section-to-section variablity are considered separately. A comparison study shows that the mean and median of the log-normal CDFs for the fragility curve obtained from finite element analysis are quite close to the mean and median of the fragility functions proposed by Kwak et al. (2016), while the standard deviation is slightly smaller. The magnitude effect is also investigated, which will shift the PGV-based fragility curves differently based on the magnitude of earthquake events.

The levee at the McDoanld Island is analyzed in a similar manner. A generic levee cross-section is developed uisng LiDAR data and bathymetry data since the geometry profiles of levees at McDonald Island are essentially very similar. A 2D levee model is constructed and soil properties are assigned based on available geotechnical data and geophysical measurements. A group of ground motions are then selected to be consitent with seismic hazard in the Delta (specifically at McDonald Island) for the purpose of developing fragility functions. A ground motion intensity measure selection study shows that PGV of the crest motion from a one-dimensional (1D) model without liquefaction is favored in terms of the x-axis of the fragility function.

PGV-based fragility curves are derived from finite element simulation results, with motion-to-motion variability, within-cross-section-section soil variability and section-to-section variablity acccounted for as well. The magnitude effect is also investigated. It is found that levees at McDonald Island are significantly more fragile then Japanese levee sites that are analyzed since the former have much higher

water and are more susceptible to liquefaction-induced deformations during earthquakes. Peat materials are found in the foundation of the levees at McDonald Island, which also have an impact on the performance of the levees. The mean and medians of the log-normal CDFs for PGV-based fragility curves are found to be smaller than what was proposed in Kwak et al. (2016). The standard deviation of the log-normal CDFs of the fragility curve, after accounting for motion-to-motion variability, within-cross-section variability, and section-to-section varaibility, corresponds quite well with what was proposed by Kwak et al. (2016).

This study provides guidance on the choice of fragility function based on the site conditions. For example, when doing the system reliability analysis of the levees, it is common to divide the levee system into various reaches. Instead of assigning the same fragility functions to all the reaches, different fragility curves can be determined and assigned to each reach given the mean relative density of each reach.

6.2 RECOMMENDATIONS FOR FUTURE WORK

This study has been focused on deriving the fragility function for levees in the Delta region, specifically at McDonald Island, using finite element simulation results. Future work regarding the development and implementation of fragility functions can be summarized as below:

1. Zimmaro et al. (2019) proposed a levee system reliability analysis framework by considering the spatial correlations and distributions of demand and capacity between reaches for seimic and high-water demands. The probability of failure of the reach is first determined using level-crossing stastistics, and the probability of the failure of the levee system can be calculated by combining the reach failure probabilies. This framework can also be applied for the levees at McDonald Island. The spatial distributions of capacity can be determined from the fragility

curves proposed in this study. Also, my colleague, Zehan Liu, has been working on developing the spatial distributions of the demand in a neighboring island of McDonald Island. I anticpate that the spatial distributions of the demand for these two islands will be very similar.

2. My colleagues, Tristan Buckreis and Pengfei Wang, are currently developing a site response model for the soft soil conditions in the Delta. They are also modifying path models for different regions in northern California. Their work will result in improved seismic hazard analysis for the Delta, and will be an input to the system reliability model that utilizes the fragility functions developed in my thesis.
3. Considering that this study proposed a numerical approach of deriving fragility functions using finite element analysis, it can also be applied to other levee sites that are of interest in the Delta region. For example, fragility functions can be derived for levees at Bacon Island, which will not only validate the fragility curves proposed in the study, but can also be used for the levee system reliability analysis for Bacon Island.
4. I was recently informed that there might be more geotechnical data available at McDonald Island. This will be useful in terms of better constraining the soil properties in the levee model and also for providing guidance on the selection of fragility curves for different reaches in the system reliability analysis.
5. When deriving the fragility functions, a linear relationship is assumed between the crest settlement and PGV in the logarithm scale, and a constant standard deviation is assumed for the log-normal CDFs for the fragility curves. However, as mentioned in Chapter 5, it is likely that a nonlinear function might be better to characterize the relationship between the crest settlement and PGV, which will complicate the construction of fragility function, but can be included for future research. A non-constant standard deviation of the log-normal CDFs for the fragility curves can be incorporated through a heteroscedasticity study, but this will complicate the implementation of fragility functions as well.

6. All the fragility curves in this study are derived using PGV, as recommended by Kwak et al. (2016). In addition to PGV, the fragility functions also utilize magnitude because PGV is an insufficient intensity measure. Tsai (2018) derived fragility functions for levees using PGA, including levees with peat in the foundation. However, PGA is also an insufficient intensity measure. Intensity measures such as Arias intensity and cumulative absolute velocity inherently account for duration, and therefore may be sufficient. However, they are also less predictable compared with PGV and PGA. Additional research is needed to study optimal intensity measures.
7. Ground motions in this study were selected by performing deaggregation at a range of return periods, and selecting the magnitude and distance values that contribute the most to hazard. A ground motion model was then used to compute a median response spectrum for this M, R pair, and the algorithm by Baker (2015) was used to select ground motions. An alternative approach is multiple stripe analysis, in which deaggregation is not necessary. Rather, the uniform hazard spectrum at a particular return period is input to Baker's algorithm. I suggest that multiple stripe analysis should be utilized to ascertain sensitivity of the fragility functions to ground motion selection.
8. Considering that large long-period ground motions can be generated by large earthquake events by the Cascadia subduction zone, the DRMS study (URS/JBA 2007b) incorporated it into the PSHA when evaluating the seismic hazard of the Delta (Wong et al. 2008). However, I believe that the Cascadia suduction zone is sufficiently far away from the region I am studying, so subduction events are not considered in this study. But additional research can be performed regarding the effect of these subduction events.
9. I believe that modeling uncertainty is an important issue in this study, and was inferred based on the difference between the standard deviation of the empirical fragility functions and that from the numerical modeling based fragility functions. Modeling uncertainty can be attributed

to several factors. For example, the vertical component of the ground motion is not considered, which will have impact on the performance of the levee model. Furthermore, other material models such as PM4sand would likely produce different results, but only a single material model was used herein. Additional work could potentially clarify modeling uncertainty beyond the efforts performed herein.

10. This study utilized the standard deviation of the empirical fragility functions by Kwak et al. (2016) as a target. However, those fragility functions were derived from only two earthquakes, and therefore represent primarily section-to-section variability and within-section variabliy, with only a reduced amount of motion-to-motion variability. By contrast, the finite element analysis incorporated a large portion of motion-to-motion variablity and within-section variablity, but less section-to-section variability by only considering three different mean relative densities within a single cross-section. Therefore, the total uncertainty is likely higher than reflected by the empirical fragility functions and by the numerical fragility functions. Future work could clarify this issue.

REFERENCES

ASCE. (2017). 2017 infrastructure report card. In *American Society of Civil Engineers*.

Bachmann, P. (1894). *Die analytische zahlentheorie* (Vol. 2). Teubner.

Baker, J. W. (2015). Efficient analytical fragility function fitting using dynamic structural analysis. *Earthquake Spectra*, *31*(1), 579-599.

Baker, J. W., & Lee, C. (2018). An improved algorithm for selecting ground motions to match a conditional spectrum. *Journal of Earthquake Engineering*, *22*(4), 708-723.

Baker, J. W., Lin, T., Shahi, S. K., & Jayaram, N. (2011). New ground motion selection procedures and selected motions for the PEER transportation research program. *PEER report*, *3*.

Bathe, K. J. (2007). Finite element method. *Wiley encyclopedia of computer science and engineering*, 1-12.

Boore, D. M., Stewart, J. P., Seyhan, E., & Atkinson, G. M. (2014). NGA-West2 equations for predicting PGA, PGV, and 5% damped PSA for shallow crustal earthquakes. Earthquake Spectra, 30(3), 1057-1085.

Boulanger, R. W., & Montgomery, J. (2016). Nonlinear deformation analyses of an embankment dam on a spatially variable liquefiable deposit. *Soil Dynamics and Earthquake Engineering*, *91*, 222-233.

Burton, C., & Cutter, S. L. (2008). Levee failures and social vulnerability in the Sacramento-San Joaquin Delta area, California. *Natural hazards review*, *9*(3), 136-149.

California Energy Commission. (2020). "Natural gas pipelines", https://www.energy.ca.gov/sites/default/files/2020-10/Natural_Gas_Pipelines_ADA.pdf Last accessed 24th Nov 2021.

Darendeli, M. B. (2001). *Development of a new family of normalized modulus reduction and material damping curves*. The university of Texas at Austin.

Electric Power Research Institute (1993). Guidelines for site specific ground motions, Rept. TR102293, 1-5, Pala Alto, California.

Elgamal, A., Yang, Z., Parra, E., & Ragheb, A. (2003). Modeling of cyclic mobility in saturated cohesionless soils. *International Journal of Plasticity*, *19*(6), 883-905.

Elkateb, T., Chalaturnyk, R., & Robertson, P. K. (2003). An overview of soil heterogeneity: quantification and implications on geotechnical field problems. Canadian Geotechnical Journal, 40(1), 1-15.

Fenton, G. A., & Griffiths, D. V. (2003). Bearing-capacity prediction of spatially random c ϕ soils. *Canadian geotechnical journal*, *40*(1), 54-65.

Fenton, G. A., & Vanmarcke, E. H. (1990). Simulation of random fields via local average subdivision. *Journal of Engineering Mechanics*, *116*(8), 1733-1749.

Field, E. H., Arrowsmith, R. J., Biasi, G. P., Bird, P., Dawson, T. E., Felzer, K. R., ... & Zeng, Y. (2014). Uniform California earthquake rupture forecast, version 3 (UCERF3)—The time-independent model. Bulletin of the Seismological Society of America, 104(3), 1122-1180.

Griffiths, D. V., & Fenton, G. A. (2001). Bearing capacity of spatially random soil: the undrained clay Prandtl problem revisited. *Geotechnique*, *51*(4), 351-359.

Griffiths, D. V., Fenton, G. A., & Manoharan, N. (2002). Bearing capacity of rough rigid strip footing on cohesive soil: probabilistic study. *Journal of Geotechnical and Geoenvironmental Engineering*, *128*(9), 743-755.

Harder Jr, L. F., & Boulanger, R. (1997). Application of K and K correction factors. In *Proceeding of the NCEER workshop on evaluation of liquefaction resistance of soils* (pp. 167-90).

Idriss, I. M., & Boulanger, R. W. (2008). *Soil liquefaction during earthquakes*. Earthquake Engineering Research Institute.

ISSMGE-TC304 (2021). "State-of-the-Art Review of Inherent Variability and Uncertainty in Geotechnical Properties and Models." *Technical Committee TC304 - Engineering Practice of Risk Assessment and Management*, International Society of Soil Mechanics and Geotechnical Engineering (ISSMGE), 2 March 2021.

Johnson, M. E. (1987). *Multivariate statistical simulation: A guide to selecting and generating continuous multivariate distributions* (Vol. 192). John Wiley & Sons.

Journel, A. G., & Journel, A. G. (1989). *Fundamentals of geostatistics in five lessons* (Vol. 8). Washington: American Geophysical Union.

Joyner, W. B., & Chen, A. T. (1975). Calculation of nonlinear ground response in earthquakes. *Bulletin of the Seismological Society of America*, *65*(5), 1315-1336.

Khatibinia, M., Chiti, H., Akbarpour, A., & Naseri, H. R. (2016). Shape optimization of concrete gravity dams considering dam–water–foundation interaction and nonlinear effects. *Iran University of Science & Technology*, *6*(1), 115-134.

Khosravifar, A., Elgamal, A., Lu, J., & Li, J. (2018). A 3D model for earthquake-induced liquefaction triggering and post-liquefaction response. *Soil Dynamics and Earthquake Engineering*, *110*, 43-52.

Kishida, T., Boulanger, R. W., Abrahamson, N. A., Wehling, T. M., & Driller, M. W. (2009). Regression models for dynamic properties of highly organic soils. *Journal of geotechnical and geoenvironmental engineering*, *135*(4), 533-543.

Krige, D. G. (1951). A statistical approach to some basic mine valuation problems on the Witwatersrand. *Journal of the Southern African Institute of Mining and Metallurgy*, *52*(6), 119-139.

Kwak, D. Y., Stewart, J. P., Brandenberg, S. J., & Mikami, A. (2016). Characterization of seismic levee fragility using field performance data. *Earthquake Spectra*, *32*(1), 193-215.

Kwak, D. Y., Stewart, J. P., Brandenberg, S. J., & Mikami, A. (2016). Seismic levee system fragility considering spatial correlation of demands and component fragilities. *Earthquake Spectra*, *32*(4), 2207-2228.

Lysmer, J., & Kuhlemeyer, R. L. (1969). Finite dynamic model for infinite media. *Journal of the Engineering Mechanics Division*, *95*(4), 859-877.

Maps, F. I. R. (2012). Federal Emergency Management Agency (FEMA).

Mazzoni, S., McKenna, F., Scott, M. H., & Fenves, G. L. (2006). OpenSees command language manual. *Pacific Earthquake Engineering Research (PEER) Center*, *264*, 137-158.

McGann, C. R., Arduino, P., and Mackenzie-Helnwein, P. (2012). "Stabilized single-point 4-node quadrilateral element for dynamic analysis of fluid saturated porous media." *Acta Geotechnica*, 7(4), 297-311.

McKenna, F., Fenves, G. L., & Scott, M. H. (2000). Open system for earthquake engineering simulation. *University of California, Berkeley, CA*.

Mejía, J. M., & Rodríguez-Iturbe, I. (1974). On the synthesis of random field sampling from the spectrum: An application to the generation of hydrologic spatial processes. *Water Resources Research*, *10*(4), 705-711.

Moehle, J., & Deierlein, G. G. (2004, August). A framework methodology for performance-based earthquake engineering. In *13th world conference on earthquake engineering* (Vol. 679).

Myers, D. E. (1989). Vector conditional simulation. In *Geostatistics* (pp. 283-293). Springer, Dordrecht.

Petracca, M., Candeloro, F., & Camata, G. (2017). "STKO user manual". ASDEA Software Technology, Pescara Italy.

Phoon, K. K., & Kulhawy, F. H. (1999). Characterization of geotechnical variability. *Canadian geotechnical journal*, *36*(4), 612-624.

Porter, K., Kennedy, R., & Bachman, R. (2007). Creating fragility functions for performance-based erthquake engineering. *Earthquake Spectra*, *23*(2), 471-489.

R.W.Boulanger, K.Ziotopoulou. "PM4Sand(Version 3.1): A Sand Plasticity Model for Earthquake Engineering Applications". Report No. UCD/CGM-17/01 2017

Rice, S. O. (1944). "Mathematical analysis of random noise". Bell System Tech. J. 23: 282–332.

Rocscience Inc. 2008, Phase2 Version 7.0 - Finite Element Analysis for Excavations and Slopes. www.rocscience.com, Toronto, Ontario, Canada.

Rosidi, D. (2007). Seismic risk assessment of levees. *Civil Engineering Dimension*, *9*(2), 57-63.

Tompson, A. F., Ababou, R., & Gelhar, L. W. (1989). Implementation of the three-dimensional turning bands random field generator. *Water Resources Research*, *25*(10), 2227-2243.

Tsai, Y. T. (2018). *Characterizing Seismic Performance of Levees on Peaty Organic Soils from Case Histories and Simulations*. University of California, Los Angeles.

U.S. Geological Survey. (2021). "Map of the Sacramento-San Joaquin Delta", https://www.usgs.gov/media/images/map-sacramento-san-joaquin-delta Last accessed 24th Nov 2021.

URS/JBA. (2008). "Delta risk management strategy (DRMS), phase 1, draft 4." *Risk Analysis Rep*., URS Corporation.

Vanmarcke, E. (2010). *Random fields: analysis and synthesis*. World scientific.

Wong, I., Thomas, P., Unruh, J., Hanson, K., & Youngs, R. (2008). Characterizing the earthquake ground shaking hazard in the Sacramento-San Joaquin Delta, California. In *Geotechnical Earthquake Engineering and Soil Dynamics IV* (pp. 1-11).

Wood, A. T., & Chan, G. (1994). Simulation of stationary Gaussian processes in [0, 1] d. *Journal of computational and graphical statistics*, *3*(4), 409-432.

Yang, Z., Lu, J., & Elgamal, A. (2008). OpenSees soil models and solid-fluid fully coupled elements. *User's Manual. Ver*, *1*, 27.

Zienkiewicz, O. C., & Shiomi, T. (1984). Dynamic behaviour of saturated porous media; the generalized Biot formulation and its numerical solution. *International journal for numerical and analytical methods in geomechanics*, *8*(1), 71-96.

Zimmaro, P., Stewart, J. P., Brandenberg, S. J., Kwak, D. Y., & Jongejan, R. (2019). Multi-hazard system reliability of flood control levees. *Soil Dynamics and Earthquake Engineering*, *124*, 345-353.